Laser-Doped Selective Emitter and Local Back Surface Field Solar Cells with Rear Passivation

Ziv Hameiri

Centre for Photovoltaic Engineering

The University of New South Wales

Sydney

Australia

A thesis submitted to the University of New South Wales in fulfilment of the requirements for the degree of Doctor of Philosophy

August 2010

To my hero – my grandma
And in memory of her family who was murdered in the Holocaust

"One sees clearly only with the heart.
Anything essential is invisible to the eyes."

The Little Prince, Antoine de Saint-Exupéry

Abstract

In order to make solar energy a viable solution for the energy challenges facing humankind in the coming years, the cost of solar cells must be reduced. The single sided laser-doped solar cell has been shown to provide high efficiency without an increased manufacturing cost. However, the peak efficiency of this structure has previously been limited by basic design issues. This thesis examines two different ways to improve the performance of single sided laser-doped solar cells. The first is replacing the aluminum rear contact with localised contacts and a high-quality passivation layer. The second is optimising the laser processing to minimise any detrimental effects.

The first part of the thesis focuses on rear surface passivation. It begins with a review of different passivation methods and then investigates the influence of annealing on the obtained passivation. It is demonstrated that annealing in the 600-820°C range significantly improves the passivation of different SiN_x films on different silicon surfaces. An optimal annealing temperature is identified in the 680-700°C range. A surface recombination velocity value in the range of 2-7 cm/s is calculated for 1 Ω.cm *p*-type substrate. Significant bulk lifetime enhancement is seen when SiN_x-passivated CZ wafers are annealed. Using an optimal annealing condition, the implied open-circuit voltage of CZ silicon substrates increased to a value comparable to that of FZ wafers - almost 720 mV.

The second part of this thesis focuses on the laser doping process and in particular the impact of dielectric films on defect formation. Laser-induced defects are investigated using a wide range of characterisation techniques. It is found that laser doping degrades the electrical performance of the device. This degradation is more pronounced when a dielectric layer is present during the laser process, possibly due to the thermal expansion mismatch between the silicon and the overlying dielectric layer. However, no crystalline disorientation resulting from the epitaxial regrowth process is observed. Near-surface defects caused by laser doping are observed and a higher density of defects is revealed by Yang etch when a dielectric film is present on the surface prior to laser doping. An electron beam induced current system is extensively employed to analyse the laser-doped junctions. It is found that although a uniform *p-n* junction is formed even when ablation occurs, junction discontinuities are more frequently observed for high laser powers. It is shown that a SiO_2/SiN_x stack is able to reduce the defect density. An efficiency of 18.4% on commercial-grade CZ substrates demonstrates that high efficiencies are achievable despite the laser-induced defects, provided an optimum dielectric layer and laser power are used.

The influence of laser parameters on the electrical performance of laser-doped solar cells is then investigated. It is demonstrated that a wide range of laser diode currents can be used to create a *p-n* junction by laser doping. Grooves formed through intermediate levels of ablation can be used to improve the adhesion between the silicon and the metal without significantly degrading the cell performance. It is shown that similar open-circuit voltage (V_{oc}), short-circuit current (J_{sc}) and fill factor (FF) values are obtained for a wide range of laser diode currents. At intermediate levels of silicon ablation, the V_{oc} is the first cell parameter to be reduced, primarily due to the large silicon-metal interface. This reduction decreases the efficiency, although efficiencies above 18.1% are still achievable. At higher levels of ablation, shunts reduce the FF and V_{oc}. Under these conditions significant efficiency degradation is observed. An efficiency of 18.7% is achieved on a large area commercial grade *p*-type CZ industrial size substrate. Electroless and photo-plating are compared; higher pseudo-*FF*s are achieved for photoplated laser-doped solar cells. If the photoplating technique is combined with well-optimised Ni sintering, the pseudo-*FF* is almost independent of the laser diode current.

At the end of the thesis, a new double sided laser-doped structure is developed. This structure is based on silicon nitride passivation of the rear surface and the formation of a selective emitter and local back-surface field by laser doping. One-sun implied V_{oc} above 680 mV is achieved using the double sided laser-doped structure on commercial grade CZ *p*-type wafers when measured after laser doping and prior to metallisation. This is ~50 mV higher than the V_{oc} obtained for the single-sided laser-doped cell at the same stage. This high V_{oc} demonstrates the potential of this structure to achieve efficiencies exceeding 20%.

Acknowledgement

Firstly I want to thank my family and friends back home for making everything much easier by making me feel close, despite the enormous physical distance between us.

More traditionally:

I am grateful to my supervisor Prof. Stuart Wenham for the many hours of fruitful discussions and for sharing with me some of his endless knowledge of solar cells. I have learned so much from each of our conversations. His numerous ideas and amazing creativity have kept me motivated throughout the entire PhD.

I would like to express my deepest gratitude to my co-supervisor Associate Prof. Alistair Sproul (the "Boss") for the wise advices he gave me throughout these past years. His enthusiasm for fighting global warming has always inspired me and truly changed my life. Thank you very much for the many discussions regarding water pumps, energy efficiency, solar cells, optics and much more. Thank you for sharing with me the secrets of WVASE and for helping me to develop different models using this software package. Huge thanks for your guidance in negotiating the UNSW administration system. Most of all, thank you so very much for always being there for me. Thank you.

I want to thank my un-official co-supervisor Dr. Tom Puzzer, one of the smartest people that I have ever met. I have learned so much from his encyclopedic knowledge, not only regarding microscopic and PECVD systems, but also regarding scientific writing, culture in the Balkan region and many other interesting topics. One of my main regrets is that I did not meet him at an earlier stage of my PhD studies. Thank you very much for introducing me to the abilities of the EBIC system and for so many imaging hours.

I do not have enough words to thank my dear friend Craig Johnson for so many interesting conversations (however not enough) and for the very careful proof-reading/editing of this thesis. Craigi, you made this thesis much better – thank you.

Huge thanks to Nino (Habibi) for so many silicon nitride depositions. The work of Chapter 5 could not have been done without his amazing support. I hope that you know how much I appreciate your help and the fact that you did everything with such a big smile.

I also want to thank Budi Tjahjono for the initial training in the labs and for many discussions regarding solar cells and laser doping in the early stages of my work. Many thanks to Ly Mai for sharing with me her large knowledge and experience in solar cell fabrication and for proof-reading this thesis. Linfei Gu worked

with me on developing the mathematical modeling of the laser beam during her summer taste of research. I want to thank her not only for the assistance, but also for the opportunity she gave me to explain what I am doing. Thank you also to Kalai Valliappan who took some of the FIB images presented in Chapter 7, to Shahla Zamani Javid and Anahita Karpour who assisted with device processing at different stages of my research. Although these samples were not included in this thesis, I would like to thank them both for their help. I also want to thank Ned Western for reading and commenting on Chapters 3-5 and for providing the low–quality wafer, which was used in Section 8.3.6.

Special thanks to Dr. Andreas Fell for performing the heat transfer simulations presented in Chapters 6 and 7. Although we have never met and have only spoken to one another via email, and despite his very busy schedule, Andreas was very kind to run these simulations for me. Thank you so very much for that. Thank you also to Associate Prof. Thorsten Trupke for developing the amazing PL-based systems. His systems were used widely during this thesis and gave me invaluable information. Thank you very much for all the conversations regrading these systems. I would also want to thank Dr. Daniel Inns for organising some of the SIMS measurements at IBM New-York.

Some of the work presented in this thesis was carried out at Suntech Power in Wuxi, China. I am very grateful to Dr. Shi for giving me this very special opportunity and for the financial support in the last months. I want to thank the members of Suntech's R&D team for all the help, especially Dr. Ji for leading such a unique team and Mr. Zhu Fan for always being so efficient at solving any problem that I had.

Back at UNSW, I would like to say a huge thank you to the LDOT team, especially Nick Shaw for running the labs so smoothly, Kian Chin for so many working hours on the laser system, for solving so many big and small crises and for all the SHALOM SHABAT. To Alan Yee for helping with the fabrication of different measurement devices and Lawrence Soria for trying to make my old computer a bit faster. I also want to thank Jill Lewis, Julie Kwan and Danny Chen for all the help with a variety of administrative paper work. Special thanks to Julie for not including me too many times in her "These People" list and to Danny for his long friendship. Thank you also to Phil for keeping the office area so clean and tidy and mostly for all the early-morning chats.

I would also want to thank the EMU staff at UNSW, especially Dr. Quadir Zakaria for the help with the EBSD measurements and Dr. Warren McKenzie and Mr. Sean Lim for their enormous help with the TEM measurements.

I was inspired by many of the papers and books that I read during my PhD study. It is impossible to thank all the authors of these studies, however I want to thank some of these "giants" who influenced me so much, though I may have never or have only briefly met them: Prof. Martin Green, Prof. Armin Aberle, Prof. Andres Cuevas, Prof. Stefan Glunz, Dr. Jan Schmidt, Dr. Mark Kerr and Dr. Keith McIntosh.

I want to thank my dearest friend Nancy for her endless support and kindness. To Raul for so many weekend dinners, for always offering me a better option instead of spending time at uni and for being such a good friend. To Nonie for the opportunity to speak Hebrew and for always providing a friendly face. For the special "464 group" – Binesh, Craigi, Henner, Jeana and Sarale - for so many short and long chats, lunches and coffee/hot chocolate breaks. You all have filled my time here with joy, thank you. Special thanks to MY FRIEND Sarah, which gave this thesis the last touch. Her "delete/obvious/cut/kill" comments improved it.

Many huge thanks to my friends back home. It was impossible to finish this thesis without your support. I especially want to thank Hersko for his big heart. You are not *like* my brother – you *are* my brother. To Tatouse for her weekly phone calls and for an infinite number of supportive SMSs, I am so lucky to have a friend like you and I hope that I have told you that enough times. To Shoushan and to the Kapachit for keeping me close to their hearts and for remembering that friendship is based not only on the big things, but also on all the day-to-day events. Thank you for sharing your life with me. To Anat and Gadi for just being awesome, it was worth coming all the way to Australia if only to meet you two. To Mikmik for the long journey that we did together, it made me a better person – thank you.

Last but not least, I want to thank my family, especially to my wonderful parents for their endless love and support. For always giving me the freedom to choose my own way and for providing me with the tools to do it wisely. To Einav, Nitsan, Adi, Dor, Tal, Amiti and Noya for being so special, each of you in your unique way. I am looking forward to spending more time with you and watching you grow into the great people you all will be. And to Napo, who chose me more than nine years ago and filled my heart with happiness.

Contents

Chapter 1 : Introduction

Humankind faces three main energy-related problems today. The first is *global warming*, which refers to the effect of human activities on the climate, especially due to burning fossil fuels (coal, oil and gas) and deforestation [1]. The basic mechanism of global warming can be understood by considering the radiation from the sun that warms the Earth and the infrared radiation from the Earth and the atmosphere that is emitted to space. On average, these two radiation streams must balance for the Earth's temperature to remain constant. The *greenhouse effect* arises from the presence of so-called "greenhouse gases", such as carbon dioxide (CO_2) and methane, in the atmosphere. These gases absorb part of the thermal radiation emitted by Earth; an excess of these gases in the atmosphere alters the basic energy balance. The balance is restored by an increase in the Earth's surface temperature. It is estimated that doubling the current concentration of CO_2 would increase the global average temperature by 5-6°C [1]. The clear correlation between atmospheric CO_2 concentration and the polar temperature over the last 160,000 years is presented in Figure 1-1.

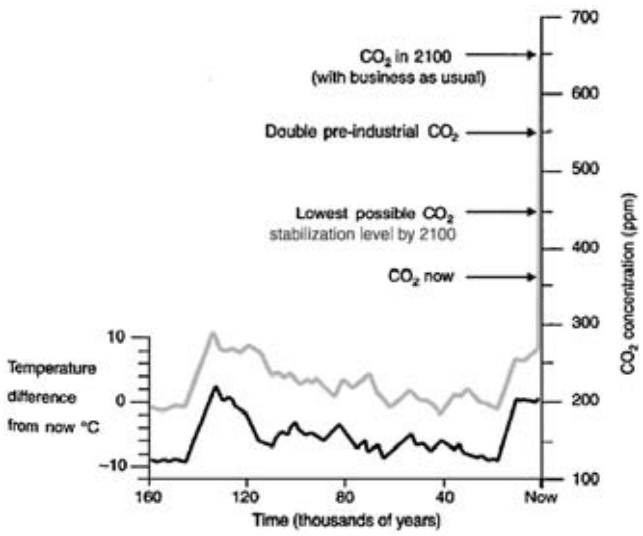

Figure 1-1: Variation over the last 160,000 years of polar temperature (black line) and atmospheric CO_2 concentration (gray line) [1].

Increases in global surface temperature would have catastrophic impacts both on human communities and on natural ecosystems. Recent satellite photos indicate that the global sea level is rising by 3.4 mm/year, and it is estimated that by 2100 the total rise will exceed one metre [2]. Furthermore, disasters such as tropical cyclones, floods, wind-storms and droughts are all climate-related. Figure 1-2 shows the

variation in the global near-surface temperature over the last 140 years. It clearly demonstrates that global warming is an *existing* problem that must be promptly addressed. If global warming is to be limited to a maximum of 2°C above pre-industrial values, global emission of greenhouse gases needs to peak between 2015 and 2020 and then decline rapidly [2].

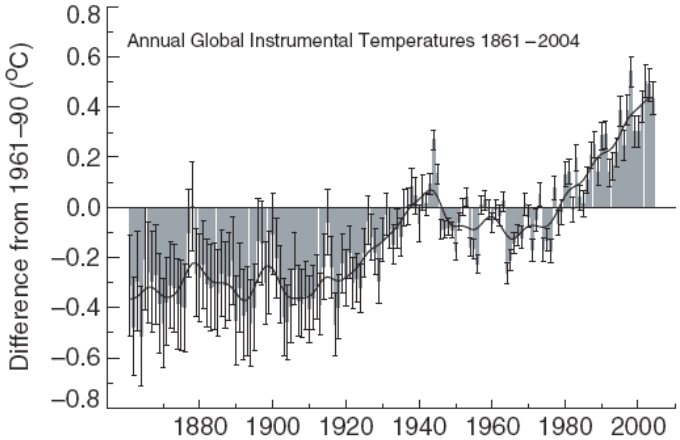

Figure 1-2: Variations in the global average near-surface temperature over the last 140 years [1].

The second problem humankind is facing is exhaustion of our energy resources. Today, humans collectivity consume 13 terawatts (TW) of power and it is estimated that 30 TW will be required by 2050 due to global population growth and economic development [3]. As shown in Figure 1-3, almost 80% of the total energy consumed in 2008 was provided by fossil fuels [4]. Geologists have estimated that at the 1998 level of energy use, only half a century worth of oil is available [3]. Although gas and coal reserves would last longer, new energy sources need to be developed.

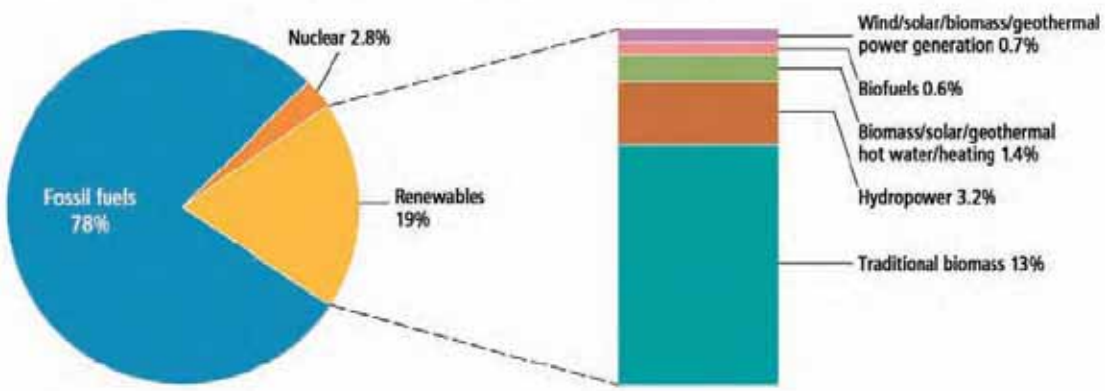

Figure 1-3: Renewable energy share of total final energy consumption at 2008 [4].

The third energy-related problem is *energy poverty*. According to a United Nations report, at least 1.6 billion people do not have access to electricity [5], mostly

due to the fact that it is too expensive to distribute electricity to their rural communities by conventional means, such as extending the transmission line network. Due to the lack of energy, these communities suffer from a very low standard of living. Since a reliable source of electricity is essential for generating jobs and sustaining industrial activity, it is almost impossible for members of these communities to improve their standard of living above current levels. Indoor pollution from traditional fuels and stoves and the lack of electricity in local clinics contribute to poor health conditions in these regions. Furthermore, the report indicates severe social impacts of this poverty, especially on women and children. In many of these communities children do not attend schools and instead must work to meet their family's subsistence needs. Women are responsible for most of the household cooking and water boiling activities, which limit their ability to pursue other productive activities, education and social participation [5]. Improving the opportunities for people living in poor communities should be a primary goal for the global community, especially for those of us who are fortunate to live in developed countries.

There are several well-known alternatives to fossil fuels that can be employed to generate electricity. Nuclear energy is often suggested as a non-emitting large-scale source of electric power. However, this is only a short-term solution for a long-term problem. Beside issues surrounding waste disposal, security, the limited supply of uranium and the health concerns related to this energy source, it was shown recently that nuclear power generation is not an economical solution compared to other alternatives such as solar energy [6]. Furthermore, ten to fifteen years are required to build and commission modern nuclear plants [7], so they cannot impact global emissions within the 2015-2020 window mentioned earlier.

Renewable energy sources can provide clean energy and can replace fossil fuels in many applications. However, the use of most renewable energy technologies is limited. Wind and hydroelectric generation are effective only in certain locations and cannot meet the future 30 TW demand. Biomass - the burning of organic material - is limited by the availability of water and arable land, while geothermal is limited by the high drilling cost. Exploitation of the ocean's energy is a relatively new technology and is probably the least mature renewable energy alternative [4]. Although a global solution for energy problems must include a combination of all the mentioned renewable energy alternatives (together with improvements in design and changes in usage patterns to encourage *energy efficiency*), **solar energy** is the only technology that can effectively address all three problems raised above.

Solar energy is essentially unlimited: every hour the Earth's surface receives more energy from the sun than humans use in a year [3]. There are hardly any limitations on the location where this energy can be used; solar energy can potentially

provide electricity whenever there is a sun. Photovoltaic (PV) - the direct conversion of sunlight into electricity by separation of charge in an electronic material - is almost an entirely maintenance-free technology. When properly designed and manufactured, photovoltaic modules are durable and easy to transport, making PV an ideal solution for rural and inaccessible regions. Photovoltaic power generation produces no pollutants, no waste products and does not liberate toxic chemicals into the environment, so its basic operation is inherently environmentally friendly. The fact that it can be installed at the point of use saves the cost of developing a transmission network and prevents any associated environmental damage.

The main limitation of PV is cost. At present, the price of one kilowatt hour of electricity from PV in the United States ranges between $US0.19 (for industrial use) and $US0.35 (for residential use), much more expensive than the fossil fuel alternatives - between $US0.04 and $US0.08 [8]. Although silicon (Si) makes up 25.7% of the Earth's crust by weight and is the second most abundant element (being exceeded only by oxygen), it does not appear as a pure element in nature [9]. Solar cell fabrication requires pure Si as a starting material; unfortunately the purification process is very expensive. Bruton estimated that 40% of the final module cost arises from the silicon wafer [10], while Jester estimated it as 50%, where 30% is due to the purification process and 20% is due to the wafering [11]. It is clear that in order to make solar energy cost-competitive, reduction in the solar cell cost is essential. One path to reduce the cost is to reduce the raw material cost. While this can be done by reducing the wafer thickness or by employing a lower quality of Si, for example, fabrication processes must be modified to suit these substrates. The second path is increasing the solar cell efficiency without significantly increasing the manufacturing cost. Like any other manufacturing process, decreasing the fabrication cost is desirable. In solar cell fabrication this can be done mainly by reducing the thermal budget and the use of expensive materials.

This thesis explores a new fabrication approach based on laser processing and rear surface passivation that increases the solar cell efficiency and aims to do so without increasing the manufacturing cost. Additionally it is very suitable for low-quality and thin substrates.

1.1 Thesis Objectives

This thesis examines possible improvements of the single-sided laser-doped solar cell, in order to enhance its efficiency. It focuses on two different aspects. The first is replacing the aluminum rear contact of this structure by localised contacts and a high-quality passivation layer. The second is optimising the laser processing and the

laser operation condition in order to minimise any detrimental effects. The objectives of this thesis are therefore:

1. To analyse loss mechanisms in single sided laser-doped solar cell, in order to identify paths of improvement.

2. To verify published results regarding surface passivation of low-resistivity *p*-type substrates and to identify the best method compatible with existing equipment in order to establish baseline processes.

3. To identify and examine potential improvements in the passivation process in order to achieve high voltages using relatively low quality substrates. To assess the suitability of the chosen passivation method for subsequent fabrication steps of the laser-doped solar cell.

4. To investigate the formation of laser-induced defects and their impact on the electrical parameters of the device. To understand the influence of the presence of a dielectric layer on defect formation. To develop methods to minimise the impact of these defects on the solar cell.

5. To investigate the impact of the laser operating conditions on the solar cell performance, in order to maximise the obtained performance.

6. To develop a novel double sided laser-doped solar cell structure, in order to increase the solar cell efficiency without increasing the fabrication cost. To identify potential problems and to provide possible solutions.

1.2 Thesis Outline

This thesis consists of two main parts; the first (Chapters 3-5) deals with surface passivation, while the second (Chapters 6-8) focuses on device fabrication including laser processing and the improvement of laser-doped solar cells with self-aligned metallisation.

Chapter 2 reviews different structures of solar cells. It starts with describing the most common commercial solar cell – the screen-printed solar cell. The limitations of this structure are analysed and compared to the performance of the most efficient laboratory solar cell – the passivated emitter and rear locally-diffused (PERL) solar cell. The concept of the selective emitter is explained and its commercial applications, such as the “buried contact” and “semiconductor finger”

solar cells, are presented. Different applications of lasers in solar cell fabrication are then reviewed, together with solar cell structures that incorporate laser processing.

Chapter 3 reviews the different recombination mechanisms in solar cells. The concept of effective lifetime is explained and different methods to measure it are presented. Special attention is given to describing methods to separate the influence of different recombination mechanisms in order to determine the impact of each of them on the device.

Chapter 4 reviews three main surface passivation methods: silicon dioxide, silicon nitride and a stack layer of silicon dioxide/silicon nitride. The interface properties and the impact of annealing on each of the methods are presented in order to assess advantages and limitations. Voids in the published studies are identified, especially in relation to the influence of annealing on the obtained passivation.

At the beginning of **Chapter 5**, available equipment is utilised to establish baseline processes. Passivation results reported in the literature are verified by comparing different passivation methods for the surfaces of low-resistivity *p*-type substrates. As silicon nitride is found to provide the highest passivation quality, the influences of refractive index and film thickness on the passivation quality are investigated. The chapter then studies the dependence of silicon nitride passivation quality on annealing in the temperature range 600-820°C, using a variety of films and surfaces. Focus is given to the influence of annealing on the bulk lifetime of Czochralski (CZ) grown Si wafers. At the end of the chapter, the suitability of silicon nitride passivation to the fabrication sequence of laser-doped solar cells is evaluated.

Chapter 6 investigates laser-induced defects. The influence of different dielectric films on defect formation is highlighted, as this is the basis for the laser doping method employed in this thesis. A wide variety of characterisation methods are used to obtain insights into the nature of these defects. Following these investigations, laser-doped solar cells with different dielectric films are fabricated and their electrical parameters are compared and analysed. At the end of the chapter a novel method is introduced to minimise laser-induced defects by modifying the laser pulse, in order to reduce the cooling rate of the Si after laser-induced melting.

Chapter 7 investigates the influence of laser power on solar cell electrical parameters. The discussion is divided into three major parts. The first part investigates the influence of laser power on the electrical parameters of the laser-doped junction. The second part studies the impact of laser power on the performance of completed solar cell, in order to examine possible use of induced ablation to improve metal

adhesion to laser-doped regions. The relationship and the trade-off between surface roughness and electrical performance are ascertained. The third part of this chapter investigates the influence of laser power and plating techniques on the device shunt resistance.

Chapter 8 investigates the loss mechanisms of the single-sided laser-doped structure and discusses possible improvements. The main part of this chapter presents a novel solar cell structure: the double sided laser-doped solar cell. This structure is based on silicon nitride passivation of the rear surface and the formation of selective emitter and local back-surface field by laser doping. The fabrication sequence of this new structure is outlined and preliminary results are presented. Some problems in the metallisation process are identified and possible solutions are given.

Finally, **Chapter 9** summarises the important results discussed in this thesis, as well as suggestions for possible future work.

Chapter 2 : Review – Solar Cells and Laser Applications

At present the main limitation of solar cells is their relatively high cost. In order to make solar cells competitive, their efficiency must be improved without increasing the manufacturing costs. This chapter evaluates both the most common and the most efficient types of solar cells, in order to identify the main limitations of the former and possible commercial applications of the latter. In addition current laser applications in solar cell fabrication are reviewed, with focus on its potential to replace a variety of expensive processes.

2.1 History

The operation of solar cells is based on the *photovoltaic effect*, which is defined as the "*generation of electric current by light incident on an interface between certain pairs of substrates*" [12] or more generally "*providing a source of electric current under the influence of light or similar radiation*" [13]. The photovoltaic effect was first demonstrated by Bequerel in 1839 [14] by illuminating coated platinum electrodes inserted into an acidic solution [15].

The first solar cell was fabricated by Fritts in 1883 [16-17]. It was made of selenium coated with a very thin layer of gold and achieved an efficiency of ~1%. The first semiconductor *p-n* junction solar cell was described and patented by Ohl in 1941 [18]. However, the first operating solar cell was developed only in 1954 by Chapin, Fuller and Pearson [19]. The junction was formed by a *p*-type emitter diffusion on an *n*-type silicon substrate and achieved 6% efficiency [19]. The cell's efficiency was quickly improved to 10% and it soon found its first application, to power satellites in space [20].

The efficiency continued to improve, reaching 14.5% in 1961 [21]. The change to boron doped substrates, which occurred during this period of time, lowered the efficiency, but improved the tolerance to radiation in space [22]. Efficiencies above 14.5% in boron doped substrates were only achieved in the early 1970s by the 'violet' solar cell [23]. Figure 2-1 presents the evolution of crystalline and multicrystalline silicon solar cell efficiencies over the last 60 years. The record efficiency of 25%, which approaches the Shockley-Queisser limit for a *p-n* junction [24], was obtained by the University of New South Wales (UNSW) [22, 25] with the passivated emitter and rear locally diffused (PERL) solar cell. However, efficiencies

of commercial solar cells are well below this value, in the range of 16.5 % [26]. This highlights the need to develop commercial processes that utilise some of the high efficiency features of the PERL cell. One possible pathway is using lasers to achieve lower cost, higher performance commercial solar cells.

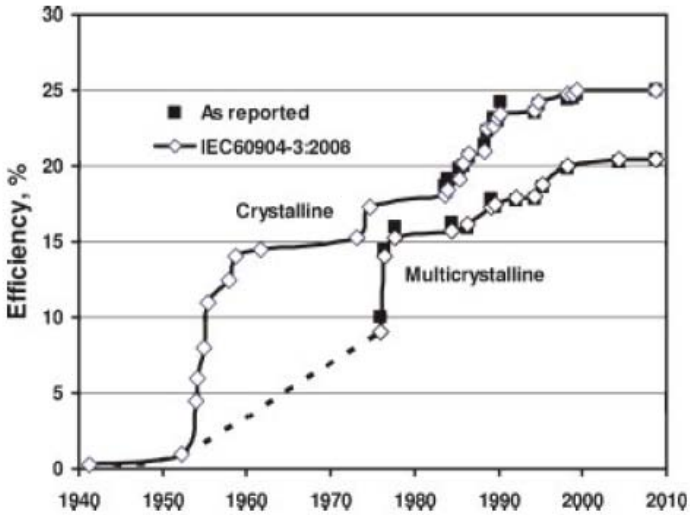

Figure 2-1: Evolution of crystalline and multicrystalline silicon solar cells efficiency [22].

2.2 Screen-Printed Solar Cells

Screen-printed solar cells have dominated the PV market over the last 30 years [27], despite suffering from well-known limitations. The prevalence of this technology is mainly due to it being robust, simple and requiring relatively inexpensive equipment that can be easily automated. Furthermore, the manufacturing process produces relatively low amounts of chemical waste and has little environmental impact [28]. This section describes the structure of screen-printed solar cells and highlights their limitations.

Figure 2-2 presents a schematic of a *p*-type screen-printed solar cell. Its main features are a front-surface homogenous emitter, a full-area rear contact and wide, metallic front finger contacts. Due to the width of the front fingers, the fingers are spaced 2.5-3 mm apart in order to reduce shading losses. This relatively large distance requires high lateral conductivity within the emitter layer, hence a heavily-diffused emitter is needed. Furthermore, a high surface concentration of dopant is required to reduce the contact resistance of the Si-metal interface. Therefore, a conventional screen-printed solar cell, typically has a 40-45 Ω/□ emitter [26]. In order to minimise the formation of shunts, which can occur during contact firing, the emitter depth is in the range of 0.3-0.4 μm [26].

However, this heavily-doped, relatively deep emitter is one of the main limitations of the screen-printed solar cell. Auger recombination (see Chapter 3) and the high concentration of phosphorus atoms result in a high recombination rate within

the emitter layer. These recombination processes significantly reduce the solar cell's response to short wavelength photons, which are absorbed in the first few nanometres from the surface. Carriers that are generated by these photons must travel to the junction for collection, though most of them recombine prior to collection and do not contribute to the light generated electrical current. Therefore, this heavily-doped layer is often called a *dead layer*. In addition to the current loss, the large emitter dark saturation current (I_0) reduces the device voltage. Furthermore, the high surface doping concentration increases the surface state density, increasing the surface recombination velocity, and further reducing both the current and voltage of the solar cell.

Another limitation of the screen-printed structure is the high shading loss. Due to the large finger width, between 7-10% of the front surface is shaded. In addition to the current loss, the high recombination rate at this large Si-metal interface reduces the solar cell voltage. The relatively low conductivity of the metal pastes and high Si-metal contact resistance introduce another loss mechanism, resulting in relatively low values for the fill factor (*FF*), which is in the 75-76% range [28].

The dead layer and high recombination rate at the front surface, greatly reduce the importance of the rear surface design, as the front side dominates cell performance. Typically the rear surface passivation is based on the formation of an aluminium (Al) back surface field (BSF) [29-30], which provides only a moderate level of passivation. An in-depth review of the fabrication sequence of a screen-printed solar cells can be found in Ref. [26].

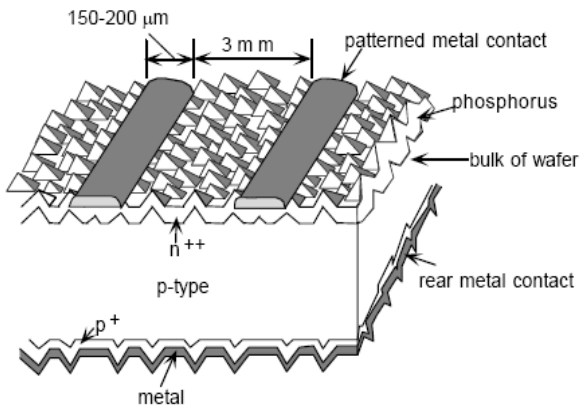

Figure 2-2: Screen-printed solar cell schematic [31].

2.3 The PERL Solar Cell

The PERL solar cell structure has held the record for highest efficiency single-junction silicon solar cell since the beginning of the 1990s, with a current record of 25% [22, 25]. This section reviews the PERL structure in order to identify features which can be adapted for mass production.

Figure 2-3 presents a schematic of the PERL structure. One of its main advantages is the use of a *selective emitter*. The front surface consists of two levels of doping: a lightly-doped emitter (150 Ω/□ for a 1 Ω.cm substrate [32]) and heavily-doped regions immediately beneath the metal contacts. The light emitter provides a good response to short wavelengths and reduces the contribution of this layer to the total dark saturation current, while the heavily-doped regions beneath the metal reduce the Si-metal contact resistance and suppress recombination at the Si-metal interface, by reducing minority carrier concentration in these areas [33]. Further reduction is achieved by minimising the contact areas on both surfaces by using photolithography.

The passivation of both surfaces is based on dry oxidation followed by aluminium-annealing (see Chapter 4) which provides a very low surface recombination velocity and allows the use of a thin oxide without degrading the obtained passivation [34].

Reflection loss from the front surface is reduced to below 3.5% by using thin front metal fingers (~25 μm wide), inverted pyramids and a double layer antireflection coating [34].

In addition to its near-perfect response to short wavelengths, the PERL cell also responds well to long wavelengths. This is attributed to the thick (400-450 μm), high quality float zone (FZ) substrate, very good rear passivation and minimal heavily-doped regions [22]. An effective light-trapping scheme is used, consisting of 'tiler's pattern' inverted pyramids and a metallic rear Al reflector. This reflector also contributes to the long wavelength response of the device by enhancing the average path length of weakly absorbed light by up to 40 times [34].

Fill factor loss is minimised by an improved front metallisation process [32], a heavily doped region beneath the metal and the well-optimised spacing between the finger (on the front) and the contact holes (at the rear).

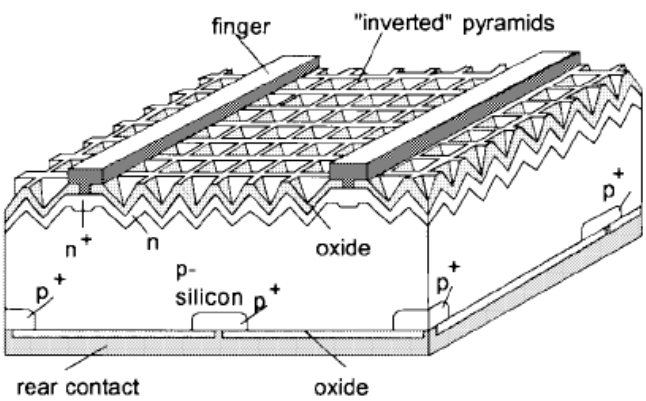

Figure 2-3: PERL solar cell schematic [35].

Table 2-1 compares the electrical parameters of screen-printed and PERL solar cells under standard AM1.5 spectrum (100 mW/cm^2, 25°C). Although the efficiency of the PERL structure is 8.5% absolute (~5.5% for PERL on a CZ substrate) higher than that of screen-printed solar cells, the high fabrication cost prevents its acceptance into mass production. Besides the cost, the fabrication of PERL solar cells involves at least five different photolithographic processes, eight high temperature processes and the evaporation of metal contacts and two layers of antireflection coating (ARC), which results in a lengthy fabrication time [36]. However, the superiority of the PERL solar cell highlights the need to develop comparable commercial methods of forming selective emitters, well defined front metal fingers and high quality rear passivation.

Table 2-1: Electrical parameters of screen-printed and PERL solar cells (AM1.5 spectrum, 100 mW/cm^2, 25°C).

	Resistivity [Ω.cm]	**Area [cm^2]**	**J_{sc} [mA/cm^2]**	**V_{oc} [mV]**	***FF* [%]**	**Efficiency [%]**	**Ref**
Screen-printed	2.0	155	35.1	614	76.3	16.5	[26]
PERL CZ	1.2	4	38.7 [a]	628	79.4	19.3 [a, b]	[37]
PERL FZ	1.0	4	42.7	706	82.8	25.0	[22]

[a] No ARC. The J_{sc} and efficiency are expected to increase by 15% with the application of an ARC.

[b] As measured after 8 days of storage.

2.4 Laser Grooved Solar Cells

One of the main advantages of the PERL structure is the use of a selective emitter to enhance device performance. In the PERL solar cell, the selective emitter is defined by photolithography. However, this method cannot be adapted to commercial applications due to its high cost. This section reviews two commercial realisations of the selective emitter concept, using laser processing to form grooves.

2.4.1 Buried Contact Solar Cell

The buried contact (BC) solar cell was introduced by Wenham and Green in 1986 [38-39]. As can be seen in Figure 2-4, its front surface design is similar to that of the PERL, while the rear surface is identical to that of the conventional screen-printed solar cell.

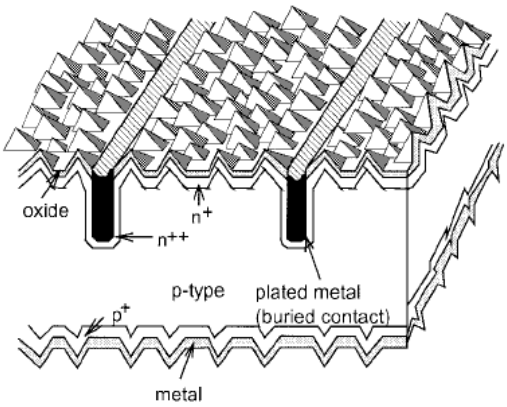

Figure 2-4: Buried-contacts solar cell schematic [35].

The fabrication sequence of this structure consists of surface texturing and light-emitter diffusion (100-120 Ω/□), followed by an oxidation step. Besides being a passivation layer, the silicon dioxide film acts as a diffusion-barrier and as a mask for subsequent groove-diffusion and metallisation processes. The selective emitter is formed by laser ablation, which creates 20 μm wide, 50 μm deep grooves. After removing laser-induced defects, a heavy groove-diffusion is carried out. The rear contact is formed by a full-area Al-alloyed layer, while the front metal fingers are electrolessly plated [40].

Similar to the PERL structure, the use of a selective emitter improves the device's response to short wavelengths (*blue response*), thereby increasing the light generated current. The voltage is enhanced by the reduced dark saturation current (due to the lightly-diffused emitter), and the shielding of the Si-metal interface from the active area of the cell (by the heavy diffusion). If CZ wafers are used as a substrate, the heavy phosphorus groove-diffusion improves the material quality by gettering of impurities [41-43]. The relatively narrow and deep grooves provide an excellent aspect ratio, which decreases the shading loss and - together with the high conductivity of the plated metal and low Si-metal contact resistance - improves the *FF*.

Due to the nearly-optimised front surface design, the rear surface is the main limitation of this structure [44]. In order to improve the performance of the standard BC solar cell, a double-sided BC (DSBC) [45-48] and an interdigitated buried backside contact (IBBC) [49] structures were developed. However, the performances of these advanced structures seem to be limited by the increased fabrication complexity.

Table 2-2: Electrical parameters of different buried contact solar cells (AM1.5 spectrum, 100 mW/cm^2, 25°C).

	Resistivity [Ω.cm]	Area [cm^2]	J_{sc} [mA/cm^2]	V_{oc} [mV]	*FF* [%]	Efficiency [%]	Ref
Standard BC	1.0	12	39.7	646	79.4	20.4	[43]
DSBC	1.0	8	36.5	662	76.8	18.5	[50]
IBBC (*n*-type)	1.0	8	37.9	664	76.5	19.2	[51]

The BC structure was successfully transferred to industry [52-53], demonstrating impressive efficiency of 18.3% [54]. It was shown in addition to the improved performance, the production cost is similar or even lower than the traditional screen-printed solar cell [55]. However, due to the long high-temperature processes, this structure is not suitable for multi-crystalline silicon (mc-Si) substrates.

2.4.2 Semiconductor Finger Solar Cell

Another commercially available selective-emitter structure is the semiconductor finger (SCF) solar cell, which was developed by Mai [26, 56]. It is based on the BC structure with one main modification: the laser grooves in this structure are perpendicular to the metal fingers (see Figure 2-5). This permits screen-printed metal contacts to be applied to the front and rear surfaces. Note that the dielectric layer (silicon nitride) allows the metal to contact the Si only in the heavily-doped finger regions [57].

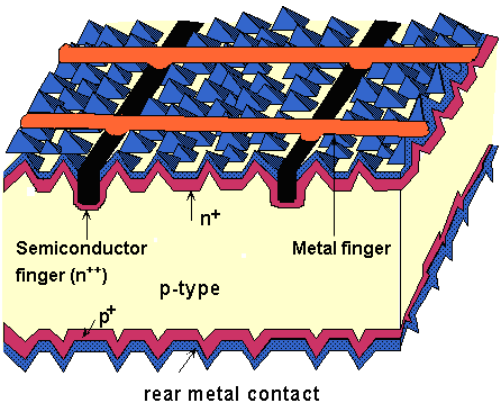

Figure 2-5: Semiconductor finger solar cell schematic [26].

The fabrication sequence of the SCF is fairly similar to that of BC solar cells. After texturing and light-emitter diffusion, a silicon dioxide layer is thermally grown. This layer serves as a diffusion barrier for subsequent heavy groove-diffusion. Similar to the BC, laser ablation is used to create 20 µm deep grooves. Laser-induced defects are then etched prior a heavy groove-diffusion. Next, the silicon dioxide is removed

before silicon nitride deposition. Besides an ARC layer, the silicon nitride serves as a passivation layer and isolates the metal from the silicon surface. Screen-printed Al is employed to create a BSF and rear contact, while screen-printed silver paste is used to form the front metal fingers. Due to the high conductivity of the heavily-diffused grooves, the spacing between the metal fingers can be increased by 50% [58] without degrading the *FF,* even though the cell design makes use of a lightly-diffused emitter. An efficiency of 18.4% was achieved by this structure using only production-line equipment.

The main advantage of the SCF is that only minimal modification of existing screen-printed production lines is required. However, similar to the BC structure, this structure is less suitable for mc-Si substrates due to the long high-temperature processes.

Table 2-3: Electrical parameters of semiconductor finger solar cell fabricated on CZ *p*-type substrate (AM1.5 spectrum, 100 mW/cm^2, 25°C) [26].

Area [cm^2]	J_{sc} [mA/cm^2]	V_{oc} [mV]	*FF* [%]	Efficiency [%]
155	36.9	638	78.3	18.4

2.5 Laser Applications in Solar Cell Fabrication

Except for grooving, lasers have been used for decades in a variety of other solar cell manufacturing applications. Lasers are often used to isolate edges [59-60] and shunted areas [61], for ablating dielectric layers [62-64], texturing surfaces [65-67] and micro-structuring [68]. Some research groups have employed lasers to reactivate inactive dopants subsequent to heavy thermal diffusion to improve the overall result of the diffusion [69]. Given their wide application, this section briefly reviews laser-based solar cell structures.

2.5.1 Laser Drilled Solar Cells

Laser drilling is used to create holes through the silicon wafer. The shape of the holes can be either cylindrical or conical. Conical holes were found to be more suitable for solar cell fabrication since they are easier to plate [70]. There are a number of cell designs that utilise this process and these will be described below.

Emitter Wrap-Through

The emitter wrap-through (EWT) solar cell, which is presented in Figure 2-6 utilises laser drilled holes (vias) to connect the front junction with rear metal contacts [71]. This is a back-contact structure, where all the metal contacts are placed on the

rear surface; therefore, shading loss is almost eliminated. Other benefits of the back-contact structure are the simplified module assembly [71] and a homogenous optical appearance, which is desirable for some applications [72].

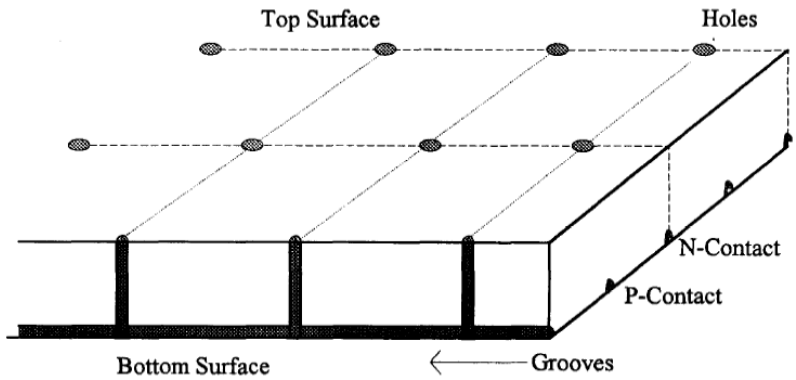

Figure 2-6: Emitter wrap-through solar cell schematic [71].

Different versions of this structure, with different metallisation methods and fabrication sequences, were developed over time [73]. However, most of these sequences are based on the BC structure [74] and use a dielectric layer as a diffusion barrier. In all structures, the vias are doped and filled with metal and are therefore highly conductive. The vias diffusion forms a rear junction, which improves the carrier collection, especially when a low-quality substrate is used. The EWT solar cells are characterised by high current density and a relatively low *FF* value, mostly due to metallisation problems. Table 2-4 summarises key results obtained by this structure.

Table 2-4: Electrical parameters of EWT solar cells.

Resistivity [Ω.cm]	Area [cm^2]	J_{sc} [mA/cm^2]	V_{oc} [mV]	*FF* [%]	Efficiency [%]	Ref
N/A (CZ)	25	37.7	591	74.6	16.6	[72]
1.4 (CZ)	6.23	40.9	616	74.1	18.7	[75]

Metal Wrap-Through

The metal wrap-through (MWT) is a variation of the EWT structure, which was suggested by Van Kerschaver *et al.* in 1998 [70]. Similar to the EWT, this structure is based on laser-drilled holes. However, in this solar cell, only the busbars are transferred to the rear, while the metal fingers are kept on the front. This reduces the fabrication complexity, by reducing the number of required vias. However, it preserves the simplified module assembly and the formation of the rear junction, which increases the collection volume [70]. Recently, an efficiency of 18.6% was demonstrated using this cell structure on an FZ substrate [76].

2.5.2 Laser-Fired Contacts

The laser-fired contact (LFC) was proposed by Schneiderlochner *et al*. in 2002 as a method to create rear, localised contacts [77]. The method is based on the known ability of a laser to alloy Al into Si in order to form *p*-type Si regions [78]. In the LFC structure, the rear surface is well passivated by a dielectric film, coated with evaporated Al. Laser pulses are then applied to locally alloy Al into Si, creating an effective p^+ BSF [79]. Similar to the PERL structure, this structure eliminates the large rear Si-metal interface. The contact area is minimised to localised regions, improving the device voltage and the response for long wavelengths [80]. The LFC method has been combined with different solar cell structures, such as BC solar cells [81], with a high degree of success [80].

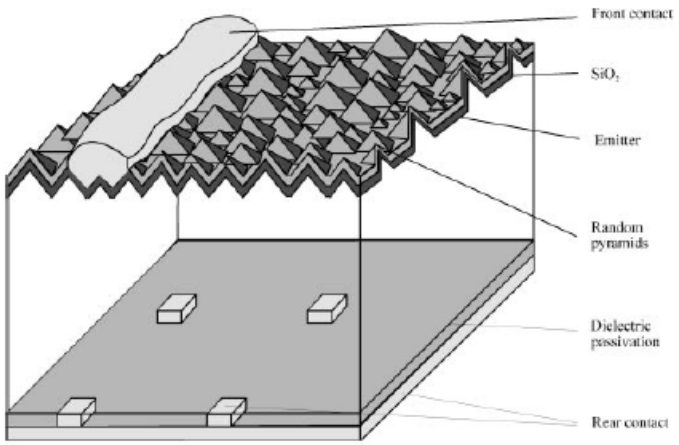

Figure 2-7: Schematic of solar cell with rear laser-fired contacts [77].

Table 2-5 summarises key results obtained with LFC solar cells. High *FF* values demonstrate the ability of the laser to form good ohmic contact between the Si and Al. As can be seen in the table, a variety of dielectric films can be applied to the rear surface for passivation. The achieved efficiency of 20.3% on a mc-Si wafer was the first cell to achieve an efficiency above 20% using this type of substrate.

Table 2-5: Summary of key results obtained by LFC solar cells.

Dielectric	Resistivity [Ω.cm]	Area [cm^2]	J_{sc} [mA/cm^2]	V_{oc} [mV]	*FF* [%]	Efficiency [%]	Ref
Si dioxide	0.6 (mc-Si)	1	37.7	664	80.9	**20.3**	[82]
Si nitride	0.5 (FZ)	4	38.5	670	79.8	20.6	[83]
Si dioxide	0.5 (FZ)	N/A	39.1	678	81.4	21.6	[79]
Amorphous Si	0.5 (FZ)	4	39.5	677	81.1	21.7	[83]
Si dioxide	0.5 (FZ)	4	39.7	685	80.9	22.0	[83]

2.5.3 Rear Interdigitated Single Evaporation Solar Cell

Another rear contact design is the rear interdigitated single evaporation (RISE) solar cell, introduced by Engelhart *et al*. [84-85]. The rear surface of this structure consists of two height levels. The ~40 μm height difference is created by laser ablation and subsequent crystal damage etching. The upper level is boron-diffused in order to form a BSF, while the lower level is phosphorus-diffused to create an emitter [86]. Both of the levels are passivated by silicon dioxide. The local opening for the electrical contacts is performed by laser ablation of an etch resist. The ohmic contact is achieved by growing a thin tunnel oxide (~1.5 nm), prior to Al evaporation, onto the entire rear. Note that the type of substrate wafer may be changed from *p*-type to *n*-type without changing the processing sequence or the cell design. An efficiency of 22% was achieved by the RISE structure on a FZ *p*-type substrate [86]. The high *FF* value demonstrated by this cell design (see Table 2-6) indicates that good ohmic contact was formed at the silicon-silicon dioxide-Al interface. Furthermore, this high value indicates no shunt, which occasionally characterises rear contact structures, was created.

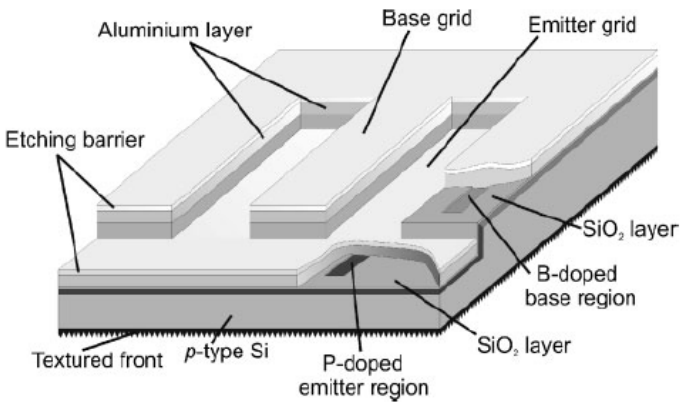

Figure 2-8: Schematic of the RISE back junction solar cell [86].

Table 2-6: Electrical parameters of RISE solar cells.

Resistivity [Ω.cm]	Area [cm^2]	J_{sc} [mA/cm^2]	V_{oc} [mV]	*FF* [%]	Efficiency [%]	Ref
1.5 (FZ)	4	40.5	660	80.6	21.5	[85]
1.5 (FZ)	4	41.7	662	79.9	22.0	[86]

2.6 Laser-Doped Solar Cells

Fairfield and Schwuttke in 1968 were the first to create a *p-n* junction with a laser. They used focused irradiation from a pulsed laser to scan a polished surface coated with phosphorus. This formed a diode with parameters similar to a

conventionally diffused junction [87]. Different methods were then developed to form a junction with the assistance of lasers. One method involved laser annealing of ion-implanted silicon. In this process, a dopant film is ion-implanted into the surface, after which a laser is used to remove crystallographic defects by melting the surface and allowing it to epitaxially resolidify. During this process, redistribution of the implanted dopants occurs and a junction is formed [88-90]. Another method forms the junction by recrystallising a doped amorphous silicon layer deposited onto a silicon substrate [88].

In recent years, much attention has been given to the laser doping process, also known as laser-induced diffusion. In this method, dopants are driven into the surface region by laser-induced melting and diffusion in the liquid phase. A wide variety of dopant sources can be used in gas, liquid or solid form. Doping from gaseous sources, often called gas immersion laser doping (GILD), is based on laser-induced melting of silicon in an environment that contains a high concentration of dopant atoms – for example, gaseous species such as PH_3 [91] or PCl_3 [67, 92] are used as a phosphorus source. Another option is to employ a laser to produce dopant molecules by gas-phase photolysis and to simultaneously heat the substrate to allow incorporation of dopants [93]. An interesting alternative is gas discharge implantation and XeCl laser annealing, which was used by Young *et al*. to achieve efficiencies up to 16.5% [94]. Liquid dopant sources can be used as well. In this case the wafer is immersed in organic solutions [95] or laser chemical processing (LCP – see below) can be done [96]. If solid sources are used, the process is often called *laser induced melting of pre-deposited impurities doping* (LIMPID). In this process, the dopant source can be evaporated [97-98] or sputtered [99] onto the surface. More recently it seems that a spin on dopant (SOD) source is the preferred option. In this approach, a solution with a high dopant concentration is spun onto the surface. The film is then solidified by a short bake to create a solid dopant source [100-101]. High efficiencies using a variety of substrates and SODs have been obtained using this method [102-104]. The laser doping process has broad applications, including the formation of large area emitters [103, 105], selective emitters [67, 102, 106-107] and BSF [90, 108]. Formation of selective emitters using the laser doping approach is very promising, as it offers the ability to create heavily-doped regions without additional high temperature processes. This is a significant benefit when mc-Si substrates are used.

This section reviews three main laser doping techniques. More information regarding laser doping is provided in Chapters 6 and 7.

Table 2-7: Classification of different laser doping techniques using liquid phase diffusion.

Gas Source (GILD)		Liquid Source		Solid Source (LIMPID)	
Dopant Gas	[67, 92]	Solution Bath	[95]	PSG	[109-111]
Gas Photolysis	[93]	LCP	[96]	Evaporation	[97-98]
				Sputtering	[99, 112]
				SOD	[100-101]

2.6.1 Laser Chemical Processing

Laser chemical processing (LCP) was first proposed by Willeke and Kray in 2001 [113] (initially referred to as laser chemical etching (LCE) [114]). It is based on the laser light-guiding water jet, which was developed by Richerzhagen in the middle of the 1990s [115]. In this laser system, the beam is focussed in a nozzle inside a pressurised water chamber, so that a hair-thin laminar water jet is emitted from the nozzle and carries the laser beam [113]. Similar to glass fibre, the beam is directed to the work-piece by total reflection at the water-air interface (see Figure 2-9). The laser system was patented and commercialised by the Swiss company Synova under the name LaserMicroJet [116]. Since it is possible to replace the water with different chemicals as a liquid jet; the applications of the LCP system can be extended beyond the original use of wafer cutting. As examples, damage-free micro-structuring can be performed by adding potassium hydroxide to the liquid jet [68, 96], while deep cutting can be done by adding appropriate chemicals and solvents to enhance ablation via chemical reactions [117]. If the liquid jet contains dopants atoms, laser doping is possible [118-120]. Efficiencies exceeding 20% were demonstrated by Kray *et al.* using this approach, though microelectronics grade processing was used such as photolithography to define metal contacts and FZ wafers were required [121].

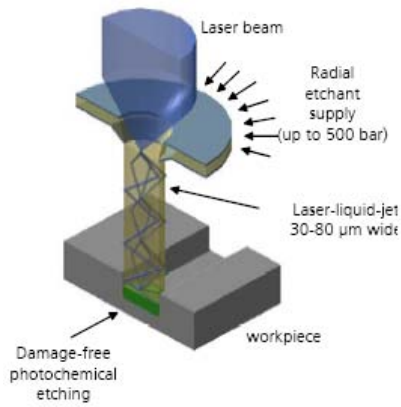

Figure 2-9: Schematic of LCP system [68].

2.6.2 Line Beam

The line-beam system presented in Figure 2-10 has been developed at the University of Stuttgart over the past few years [122]. As the name indicates, it uses a line-beam shaped laser focus with very narrow short axis focus (< 10 μm) and a wide long axis (~200 μm) [123]. The intensity in both directions is Gaussian distributed [105]. Initially, the system was designed for the creation of a full-area emitter [103]. Extremely homogeneous doping profiles have been demonstrated by this approach [124], especially when sputtered phosphorus precursors were used [99, 112]. Furthermore, a laser-doped emitter was fabricated on textured surfaces, without significant degradation of the reflectance properties of the device [125]. An efficiency of 18.9% was achieved recently on FZ substrate by large area emitters fabricated by this method [104]. More recently, this approach was extended into selective emitter formation [109, 126].

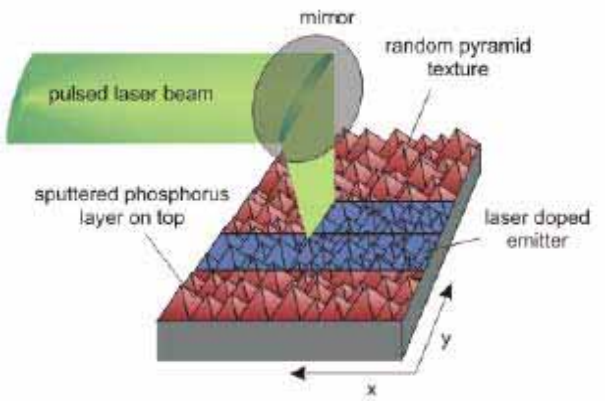

Figure 2-10: Schematic of the 'line beam' laser system [126].

2.6.3 The UNSW Approach

A different laser doping method for creating selective emitters has been developed at UNSW [127]. In this method, the dopant source (SOD) is applied onto the dielectric film, which is employed not only as an ARC and passivation layer for the surface, but also as a mask for the subsequent metallisation process. A laser beam scanning over the areas where metallisation will be applied locally melts the silicon, removes the dielectric film and induces diffusion of dopants in liquid phase. In this way, a selective emitter and self-aligned metallisation pattern are formed simultaneously. High-efficiency solar cells, both on *n*-type and *p*-type substrates, were achieved by this technique [128-130]. The electrical parameters of these solar cells are summarised in Table 2-8.

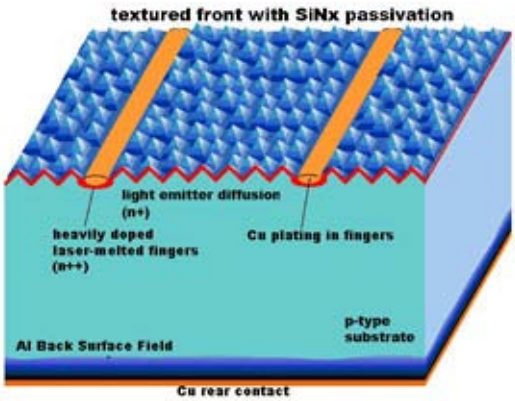

Figure 2-11: Single sided laser-doped solar cell schematic [128].

2.7 Chapter Summary

The main limitation of screen-printed solar cells is the heavily doped emitter and the large surface coverage by the front metal fingers. It has been demonstrated by a variety of solar cell structures that selective emitters and well defined front fingers significantly enhance device performance. However, the formation of selective emitters typically includes high temperature processes. High temperature processes are not desirable, as they are expensive, require a long cleaning process, can degrade wafer quality (due to contamination) and are not suitable for mc-Si substrates.

Formation of selective emitters by laser doping is a promising method. Due to the localised nature of the laser beam, selective emitters can be created without suffering from the afore-mentioned limitations. A wide variety of laser processes both in laboratory and industrial environments, demonstrate the high suitability of laser processing in solar cell fabrication. Chapters 6-8 of this thesis investigate different approaches to further improve the laser doping process and laser-doped solar cell structures in order to make solar cells more cost-effective.

Table 2-8: Summary of electrical parameters of laser-doped selective emitter solar cells.

Method	Resistivity [Ω.cm]	J_{sc} [mA/cm^2]	V_{oc} [mV]	*FF* [%]	Efficiency [%]	Ref
UNSW	1.0 (FZ) [a]	33.2	672	78.0	17.4	[66]
UNSW	2.5 (CZ) [a]	35.9	642	79.1	18.2	[130]
----	1.0 (FZ)	33.3	619	80	16.5	[107]
----	1.0 (FZ)	34.8	633	78.2	17.2	[111]
LCP	0.5 (FZ)	38.5	664	78.0	20.0 [b]	[131]
LCP	0.5 (FZ)	38.7	665	79.2	20.4 [b]	[121]
UNSW	mc-Si	35.0	623	73.0	15.9	[132]
UNSW	1.0 (CZ)	37.1	629	75.0	17.5	[128]

[a] On *n*-type substrate.

[b] Photolithographically defined front metal contacts.

Table 2-9: Summary of electrical parameters of full area laser-doped emitter solar cells.

Resistivity [Ω.cm]	Area [cm^2]	J_{sc} [mA/cm^2]	V_{oc} [mV]	*FF* [%]	Efficiency [%]	Ref
1.5 (CZ)	1.0	35.0	560	72.0	14.1	[69]
1.5 (CZ)	0.4	35.6	536	73.0	14.3	[98]
(FZ)	4.0	34.1	618	67.7	14.4	[103]
0.35	4.0	31.56	623.2	78.4	15.4	[124]
0.2 (FZ)	4.0	35.2	677	79.1	18.9	[104]

Chapter 3 : Review - Recombination and Effective Lifetime

Electron-hole pairs are created in semiconductors in a process called *generation*. In solar cells the energy source for this process is typically the absorption of incident light, although thermal processes can provide this energy as well. In the reverse process of *recombination*, electron-hole pairs are annihilated, emitting photons or phonons [133]. Recombination is therefore a limiting process which reduces solar cell performance, impacting especially the voltage, current and efficiency, but also the fill factor (when occurring within the depletion region). It is desirable to minimise the recombination processes within the device, although it is impossible to eliminate them completely.

Recombination at the rear surface has been identified as the main limitation of a number of commercial solar cell structures. The development of high quality passivation for this surface that is also suitable for commercial applications is the main focus of the following chapters. However, since surface recombination occurs in parallel with other recombination processes, analysis of surface passivation quality requires an understanding of other recombination mechanisms and their combined influence on the effective minority carrier lifetime. This chapter considers these topics and reviews effective lifetime measurement techniques.

3.1 Recombination in Solar Cells

Recombination processes are commonly classified as *intrinsic* or *extrinsic* processes [134]. Intrinsic recombination processes, including radiative and Auger recombination, occur even in ideal semiconductors. The influence of these mechanisms depends mainly on the amount of carrier injection. In contrast, extrinsic recombination occurs due to the presence of defect levels that provide a recombination path for minority carriers. This is the predominant recombination mechanism in Si devices under conditions of normal carrier injection [135]. Other recombination processes within the solar cell can be viewed as a manifestation of one of these fundamental mechanisms. For example, surface recombination can be seen as a particular case of recombination through defect levels created by dangling bonds [136]. For any recombination mechanism it is possible to define the associated *recombination lifetime* or the *minority carrier lifetime*. This value can be defined as the average time for an electron-hole pair to recombine after generation [135]:

3-1) $$\tau \equiv \frac{\Delta n}{U}$$

where τ is the carrier lifetime, Δn is the excess minority carrier concentration and U is the net recombination rate. Due to the fact that the different recombination processes occur in parallel, the influences of the different recombination processes on the carrier lifetime are usually lumped together into the *effective minority carrier lifetime* τ_{eff}, such that:

3-2) $$\frac{1}{\tau_{eff}} = \sum_i \frac{1}{\tau_i}$$

3.1.1 Radiative Recombination

Radiative recombination is the reverse process of absorption. An electron in the conduction band falls to an empty state in the valance band, emitting all or some of its excess energy as a photon. In direct band-gap semiconductors this process usually involves only three particles (an electron, a hole and a photon), while in indirect band-gap material four particles are often involved (an electron, a hole, a photon and a phonon) as dictated by the conservation of energy and momentum [133]. Radiative recombination is the dominant recombination mechanism in direct semiconductors [135] and is the basis of semiconductor lasers and light-emitting diodes (LED). However, due to the involvement of an additional particle, radiative recombination is suppressed in indirect materials such as Si. The net recombination rate for radiative recombination is given by [135]:

3-3) $$U_{rad} = B(np - n_i^2)$$

where B is the radiative recombination coefficient for the given semiconductor, n (p) is the electron (hole) concentration and n_i is the Si intrinsic carrier concentration (between 9.65×10^9 cm^{-3} [137] and 1.01×10^{10} cm^{-3} [138] at 300 K). The value of B for Si has been calculated to be 5×10^{-15} cm^3/s, at 300 K [139], while experimental measurements give a value of 9.5×10^{-15} cm^3/s [140]. The difference is attributed to excitonic effects which enhance the recombination rate and high value of n_i which was used during the measurement [31]. The corresponding carrier lifetime is given by [135]:

3-4) $$\tau_{rad} = \frac{1}{B(n_0 + p_0 + \Delta n)}$$

where n_0 (p_0) is the electron (hole) thermal equilibrium concentration. Note that under low injection conditions, the carrier lifetime has a constant value that depends on the doping level of the substrate (see Figure 3-1).

A possible side effect of radiative recombination is photon recycling or photon re-absorption. In this process, a photon that is emitted during the radiative recombination process is re-absorbed somewhere else in the semiconductor to generate an electron-hole pair [141]. This effect does not seem to have an important role in Si photovoltaics due to low radiative recombination rates and weak absorption in the wavelength range of interest.

3.1.2 Band-to-Band Auger Recombination

In band-to-band Auger recombination, an electron recombines with a hole and the excess energy is given to a third charge carrier which can be either an electron or a hole. This third carrier is excited to higher energy level in the appropriate band and can return to the initial energy state by emitting phonons [31]. From the traditional view, it is assumed that the charge carriers are non-interacting free particles [142]. Auger recombination is very effective in heavily doped material and under high injection level conditions [31]. In the case where the third charge carrier is an electron the process is denoted by *eeh*, while *ehh* labels a process where a hole is the excited carrier. The net recombination rates for these processes are given by [31]:

3-5) $$U_{eeh} = C_n(n^2 p - n_0^{\,2} p_0) \quad and \quad by \quad U_{ehh} = C_p(np^2 - n_0 p_0^{\,2})$$

where C_n and C_p are the Auger coefficients. Dziewior and Schmid determined their values to be: C_n = 2.8×10^{-31} cm^6/s and C_p = 0.99×10^{-31} cm^6/s [143]. The corresponding carrier lifetime is given for a *p*-type material by inserting Eq. (3-5) into Eq. (3-1):

3-6) $$\tau_{Auger} = \frac{1}{C_n n^2 + C_p n \Delta n}$$

However, a significant deviation from equations (3-5) and (3-6) has been experimentally observed [136]. Coulomb-enhanced Auger recombination, which accounts for the Coulomb interaction between the involved electron and hole has been proposed to explain these deviations [144]. Modified Auger recombination coefficients can be used to fit the experimental results [145]. Kerr and Cuevas

introduced a general parameterization of Auger recombination that was shown to accurately fit the available experimental data [146]:

3-7) $$U_{Auger} = np(1.8\times10^{-24} n_o^{0.65} + 6\times10^{-25} p_0^{0.65} + 3\times10^{-27} \Delta n^{0.8})$$

Similar to radiative recombination, the Auger carrier lifetime is steady at low injection level. Due to the strong dependence of the lifetime on the excess carrier concentration (as a result of the "*n*" squared in the denominator), Auger recombination becomes the dominant recombination mechanism in high injection condition.

Figure 3-1 presents the calculated radiative and Auger recombination carrier lifetimes for *p*-type (1 Ω.cm) Si. For the radiative lifetime Eq. (3-4) was used (B = 9.5×10^{-15} cm^3/s), while for Auger recombination both the non-interacting free particle lifetime (Eq. (3-6)) and the Coulomb-enhanced lifetime (Eq. (3-7)) were calculated. The figure also shows the intrinsic lifetime, the effective lifetime due to both recombination processes (Eq. (3-2)). For this substrate Coulomb-enhanced Auger recombination is the limiting mechanism for the entire injection range, while if non-interacting free particle Auger recombination is used, radiative recombination limits the lifetime at low and medium injection (below 1×10^{16} cm^{-3}). The intrinsic lifetime value of 2.3 ms, as calculated using the Coulomb-enhanced Auger recombination, is used in this thesis as the upper lifetime bound for 1 Ω.cm *p*-type Si wafer.

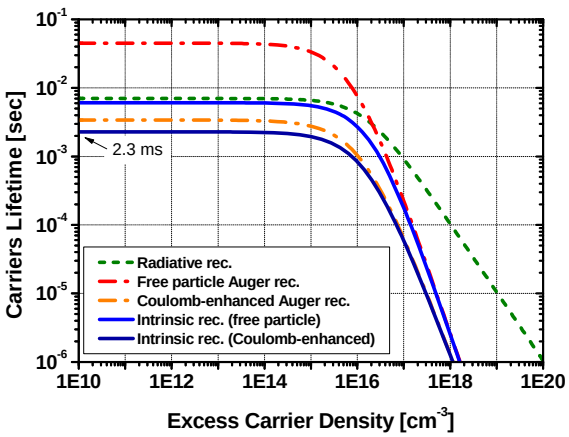

Figure 3-1: Calculated radiative lifetime, Auger lifetime and the intrinsic carrier lifetime for *p*-type (1 Ω.cm) Si.

3.1.3 Recombination through Defect Levels

Crystallographic defects and impurities incorporated into the crystal generate discrete energy levels within the otherwise forbidden band-gap. The presence of these levels allows for a two-step recombination process in which an electron from the conduction band relaxes to the defect level before recombining with a hole in the

valence band. The excess energy is usually released in the form of phonons [133]. The statistical physics of this process were independently developed by Shockley and Read [147] and by Hall [148] and therefore it is often called Shockley-Read-Hall recombination (SRH recombination). Following their approach, the recombination rate is given by [147]:

3-8)
$$U_{SRH} = \frac{np - n_i^2}{\tau_{p0}(n + n_1) + \tau_{n0}(p + p_1)}$$

where τ_{p0} and τ_{n0} are the capture time constants and are related to the capture cross section $\sigma_{p/n}$, the carriers' thermal velocity υ_{th}, and the defect concentration N_t:

3-9)
$$\tau_{p0} \equiv \frac{1}{\sigma_p v_{th} N_t} \quad and \quad \tau_{n0} \equiv \frac{1}{\sigma_n v_{th} N_t}$$

and the symbols n_1 and p_1 are the so-called SRH densities, which are defined as:

3-10)
$$n_1 \equiv N_c \exp(-\frac{E_c - E_t}{kT}) \quad and \quad p_1 \equiv N_v \exp(-\frac{E_t - E_v}{kT})$$

where k is the Boltzmann constant, T is the temperature in Kelvin, E_t is the energy level of the recombination centre, N_c and N_v are the effective densities of states in the conduction and valance bands and E_c and E_v are the energies of the conduction and the valance bands, respectively.

The corresponding carrier lifetime is given by [147]:

3-11)
$$\tau_{SRH} = \tau_{n0} \frac{p_0 + p_1 + \Delta n}{n_0 + p_0 + \Delta n} + \tau_{p0} \frac{n_0 + n_1 + \Delta n}{n_0 + p_0 + \Delta n}$$

Evaluation of Equations (3-8) - (3-11) reveals that the carrier lifetime is a function of the substrate resistivity, the carrier injection level and the properties of the recombination centre (energy level, capture cross section and defect concentration). It can be shown that the most effective recombination centres are the ones with energy level lying near the centre of the forbidden band-gap [135]. The dependence of the SRH lifetime on the excess carriers (Δn) is relatively complex, but examining the limiting cases of low and high injection levels can shine light onto the nature of this relationship [133]. The SRH lifetime for a p-type semiconductor is given for low and high injection, respectively, by:

3-12)

$$\tau_{SRH\_low} = \tau_{n0}(1+\frac{p_1}{p_0}) + \tau_{p0}\frac{n_1}{p_0}$$
$$\tau_{SRH\_high} = \tau_{n0} + \tau_{p0}$$

Equation (3-12) highlights the fact that under low and high injection conditions the SRH lifetime has a constant value (*not* injection level dependent). For deep defect levels (i.e. for defects lying near the centre of the band-gap) a further simplification of Eq. (3-12) is achieved for low injection. In such a case the SRH lifetime is simply equal to τ_{n0} (due to $n_1, p_1 << p_0$).

The effective lifetime due to the combined impact of intrinsic and SRH recombination mechanisms is often referred to as the *bulk lifetime*:

3-13)

$$\frac{1}{\tau_{bulk}} = (\frac{1}{\tau_{rad}} + \frac{1}{\tau_{Auger}}) + \frac{1}{\tau_{SRH}} = \frac{1}{\tau_{Intrinsic}} + \frac{1}{\tau_{SRH}}$$

Figure 3-2 presents the calculated intrinsic recombination lifetime, the SRH recombination lifetime and the bulk lifetime of *p*-type (1 Ω.cm) Si. Coulomb-enhanced Auger recombination was used to calculate the intrinsic lifetime, while a deep defect level (E_t - E_v = 0.6 eV) and moderate capture time constants (τ_{n0} = 100 µs and τ_{p0} = 2 ms) were used to calculate the SRH recombination lifetime. Note that under these conditions the SRH lifetime increases with increasing injection level. More information regarding SRH lifetimes under a variety of injection levels, defect energies, substrate doping concentrations and temperatures can be found in Ref. [149].

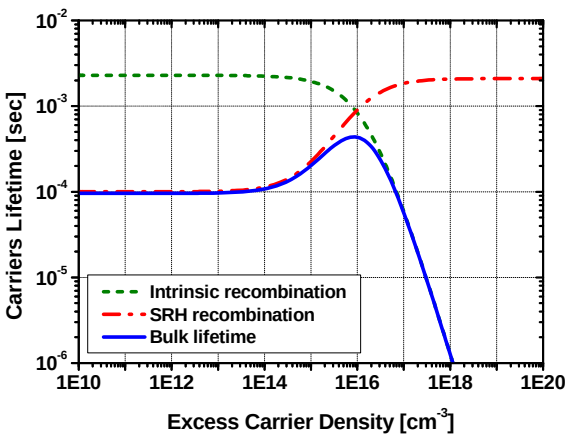

Figure 3-2: Calculated intrinsic lifetime (under Coulomb-enhanced Auger recombination), SRH recombination and the bulk lifetime of *p*-type (1 Ω.cm) Si.

3.1.4 Surface Recombination

The surface of a semiconductor is a severe interruption of the crystal symmetry [133]. Partially bonded Si atoms, often called *dangling bonds*, increase the density of defects within the band-gap. Even if the Si surface is not a bare surface, bonds between Si and other atoms can possibly create stress, which generates defect states [136]. SRH recombination statistics can be used to analyse surface recombination due to similarity of the processes at the surface to bulk recombination. However, a small modification must be made to convert the analysis from recombination per unit volume to recombination per unit surface area. In a fashion similar to Eq. (3-8), the surface recombination rate can be defined by [133]:

3-14)
$$U_s = \frac{n_s p_s - n_i^2}{\frac{(n_s + n_1)}{S_{p0}} + \frac{(p_s + p_1)}{S_{n0}}}$$

where n_s and p_s are the electron and hole concentrations at the surface and S_{n0} and S_{p0} are the *surface recombination velocity parameters* (SRV parameters) which are related to surface state density N_{st} and the capture cross section $\sigma_{n/p}$:

3-15)
$$S_{p0} \equiv \sigma_p v_{th} N_{st} \quad and \quad S_{n0} \equiv \sigma_n v_{th} N_{st}$$

Note that N_{st} has units of cm^{-2} and S_{x0} has units of velocity (cm/s) and not of time (sec). Similar to SRH recombination, surface recombination is strongly influenced by the surface states (defect energy, density and capture cross section), by the substrate resistivity and by the carrier injection level. It is important to mention that the above analysis is based on the assumption of no electric field at the surface that might affect the recombination (this assumption is often referred to as 'flat-band conditions' [133]). This assumption was found to be an over-simplification that causes large deviations between the predicted and the measured SRV values [133].

Eq. (3-14) is applied to a single surface state. However, a real surface contains a high density of defects in different energy levels, forming a continuum of surface states within the band-gap. The recombination rate must therefore be calculated by integrating over this continuum of energy levels. $D_{it}(E) \equiv N_{st}/dE$ denotes the interface state at given energy. The recombination rate is then given by the integral:

3-16)
$$U_s = v_{th} \int_{Ev}^{Ec} \frac{n_s p_s - n_i^2}{\frac{(n_s + n_1)}{\sigma_p(E)} + \frac{(p_s + p_1)}{\sigma_n(E)}} D_{it}(E) dE$$

The effective surface recombination velocity - S_{eff}, can then be defined by:

3-17) $$U_s \equiv S_{eff} \Delta n_s$$

where Δn_s is the excess minority carrier concentration at the surface. In this thesis the quality of the surface passivation is evaluated by S_{eff}.

Two fundamental methods to reduce the surface recombination rate can be concluded from Eq. (3-16) [133]:

1. Optimisation of the properties of the surface, mainly by reducing the surface states density, but also by modifying the capture cross sections. A common method for reducing surface states is growing a dielectric film on the surface to minimise the density of the dangling bonds.
2. Reducing the concentration of the charge carriers at the surface. The recombination process requires both an electron and a hole. Reducing the concentration of one carrier type will decrease the recombination rate significantly. Reduction of the surface concentration can be achieved by employing particular doping profiles (for example by creating a back surface field) or by electrostatic field effect. The highest recombination rate occurs when the electron and hole concentrations at the surface are similar (assuming identical capture cross sections).

The carrier lifetime due to recombination at the surface (τ_s) can be calculated by solving the following equation [150-151]:

3-18) $$\frac{1}{\tau_s} = \alpha_0{}^2 D$$

where D is minority carrier diffusion constant under low injection level and the ambipolar diffusion constant under high injection level and α_0 is the smallest eigenvalue solution of:

3-19) $$\tan(\alpha_0 W) = (S_1 + S_2) / \left(\alpha_0 D - \frac{S_1 S_2}{\alpha_0 D} \right)$$

where W is the wafer thickness and S_1 and S_2 are the SRV on either side of the sample. An example solution of this equation is given in Figure 3-3, for the case where W = 300 µm, D = 30 cm^2/s and $S_1 = S_2$ = 100 cm/s. The smallest value of α_0 which was found to solve the equation is 14.78 cm^{-1}, which leads to a surface lifetime τ_s = 150 µs when using Eq. (3-18).

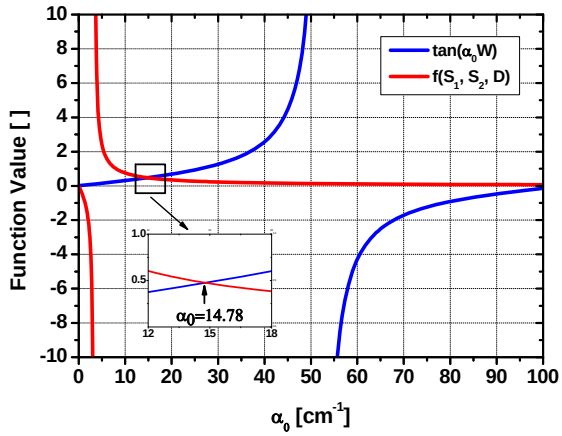

Figure 3-3: The graphs of the two terms of Eq. (3-19) for W = 300 µm, D = 30 cm^2/s and S_1=S_2=100 cm/s in the range 0 < α_0 < 100 cm^{-1}. The smallest value of α_0 that solves the equation is also shown.

Sproul has shown that for low values of S (S_1=S_2=S_{eff} < $D/(4W)$) the following expression can be used to calculate the surface lifetime with a high level of accuracy [152]:

3-20)
$$\frac{1}{\tau_s} = \frac{2S_{eff}}{W}$$

This expression will be employed, in this thesis, to calculate the surface lifetime. For very high values of S_{eff}, the surface lifetime is not limited by the SRV anymore; instead the surface lifetime is determined by the supply rate of minority carriers to the surface. Under this condition the surface lifetime is given by:

3-21)
$$\tau_{s\_\min} = \frac{1}{D}\left(\frac{W}{\pi}\right)^2$$

It was mentioned that the flat-band simplification leads to large deviations between the predicted and the measured SRV values. An extended SRH formalism, which includes the charge effect on the recombination rate, was introduced by Grove and Fitzgerald [153]. This theory has been discussed in detail by Aberle [133] and will not be discussed here. However, some conclusions from this theory are important for the following chapters:

1. Minimal SRV is achieved when the surface is under *inversion*.
2. *Depletion* of the surface region leads to maximal SRV.

3. The impact of wafer resistivity is more pronounced when considering band bending, due to the influence of sample resistivity on the transition point between depletion and inversion.
4. Two different effects lead to a strong injection level dependence of the SRV: electrostatic surface charge and asymmetrical capture cross section. Measurements of the surface states and the charge density are required to determine which effect dominates.

3.1.5 Emitter Recombination

Analysis of emitter recombination is relatively challenging due to a variety of effects related to a high dopant concentration. Firstly, the high dopant concentration enhances intrinsic recombination and raises the density of defects which increases the SRH recombination within the emitter and at the emitter's surface. Secondly, effects such as band-gap narrowing [154-155] and free carrier absorption [156] have an increased influence on the process within the emitter region. However, under these conditions Auger recombination is likely to be the dominant recombination mechanism. The recombination current (J_{rec}) into the emitter is given by [157]:

3-22)
$$J_{rec} = J_{0e} \frac{np}{n_i^2}$$

where J_{0e} is the emitter saturation current density, and n and p are the electron and hole concentrations on the base side of the space-charge region [136]. By averaging the recombination current across the entire volume of the sample, the recombination rate can be found:

3-23)
$$U_{emitter} = J_{0e} \frac{np}{qWn_i^2}$$

where q is the elementary charge of the electron. The emitter lifetime can now be defined for low and high injection levels by:

3-24)
$$\tau_{emitter-low} = \frac{qWn_i^2}{J_{0e}N_{A/D}} \quad and \quad \tau_{emitter-high} = \frac{qWn_i^2}{J_{0e}\Delta n}$$

where $N_{A/D}$ is the acceptor/donor concentration in the substrate.

3.2 Effective Lifetime

All these recombination processes occur simultaneously in the Si wafer. The carrier lifetime under the combined influence of these processes is described as *effective minority carrier lifetime* (hereafter, effective lifetime). Analysis of the effective lifetime is a powerful tool to study the different processes within the sample and is used throughout this work. Equation (3-2) can be written more specifically as:

$$\frac{1}{\tau_{eff}} = \left(\frac{1}{\tau_{rad}} + \frac{1}{\tau_{Auger}} + \frac{1}{\tau_{SRH}} \right) + \frac{1}{\tau_s} + \frac{1}{\tau_{emitter}} = \frac{1}{\tau_{bulk}} + \frac{1}{\tau_s} + \frac{1}{\tau_{emitter}} \quad \textbf{3-25)}$$

where τ_{bulk} is defined by Eq. (3-13). Although effective lifetime measurement is relative easy, it is challenging to separate the influence of the different mechanisms. Different methods and systems for measuring effective lifetime are discussed in the following section.

Surface Lifetime

Separation of the surface lifetime from the measured effective lifetime in order to evaluate the quality of the rear surface passivation is highly important for the study presented in the next chapters. There are two main methods to separate the surface lifetime from the effective lifetime, both are based on a test structure described in Figure 3-4. It was shown that this symmetrical structure gives the optimum sensitivity of the measured lifetime regarding variation of S_{eff} [158-159]. The main assumption regarding this structure is that both surfaces have similar SRV (S_1=S_2=S_{eff}). It is widely accepted that this assumption is reasonable if the surface preparation is done simultaneously for both surfaces and if the same system with identical parameters is used to form the passivation layer [158, 160], although some concern was raised regarding the cleanliness of the second surface to be deposited (when the passivation layer is deposited onto the surface) [161].

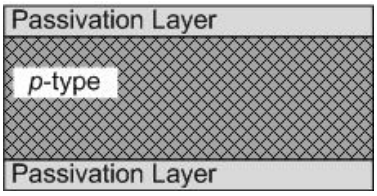

Figure 3-4: Schematic of test structure sample.

The first method is based on the dependence of the surface lifetime on wafer thickness. In this method, a number of wafers with a similar bulk lifetime, but with different thicknesses are used. A $1/\tau_{eff}$ vs $1/W$ plot is used to display the measured

effective lifetime. The slope of the linear fit to this graph represents $2S_{eff}$, while the intercept of the fit with the y-axis represents $1/\tau_{bulk}$. This method was used by Yablonovitch *et al*. to measure their unusually low S_{eff} of 0.25 cm/s [162] and by other researchers, with high level of accuracy [150, 163]. An example of this plot is shown in Figure 3-5.

The second method involves only one wafer and is based on an assumption regarding the bulk lifetime [164]. High quality wafers, such as FZ wafers, are mainly used in this method [158, 160]. It is assumed that these wafers are limited primarily by intrinsic recombination due to minimal SRH recombination rate; therefore under this condition S_{eff} can be calculated by:

3-26) $$\frac{1}{\tau_{eff}} = \left(\frac{1}{\tau_{Intrinsic}} + \frac{1}{\tau_{SRH}}\right) + \frac{2}{\tau_s} \cong \frac{1}{\tau_{Intrinsic}} + \frac{2S_{eff}}{W} \Rightarrow S_{eff} = \frac{W}{2}\left(\frac{1}{\tau_{eff}} - \frac{1}{\tau_{Intrinsic}}\right)$$

Note that the *upper* limit of S_{eff} is calculated by this equation. Due to the involved assumption regarding the bulk lifetime this method is probably less accurate for determining the value of S_{eff} when compared to the first method, especially for cases when very low values of S_{eff} are calculated. However, it still provides an adequate level of accuracy and is widely used [136, 158, 160]. This method was also employed in this thesis as it requires a significantly smaller number of wafers and provides sufficient information when comparing different passivation methods and different fabrication parameters.

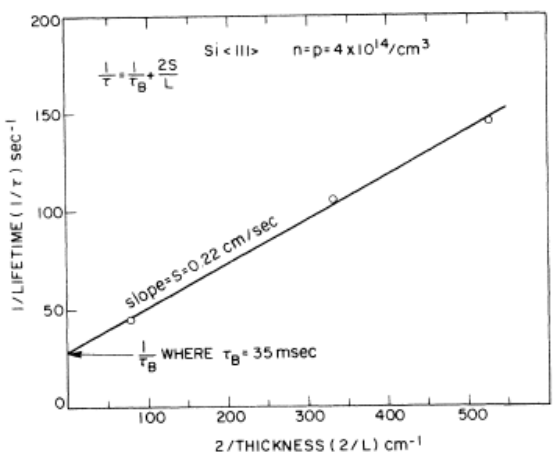

Figure 3-5: Example for calculation of S_{eff} using different thicknesses of similar wafers. The slope of the linear fit represents S_{eff} (0.22 cm/s), while the intercept with the y-axis represents $1/\tau_{bulk}$ [162].

Emitter Recombination

Investigation of the emitter recombination is often carried out at high injection levels. Under this condition, the injection level dependence of this recombination can be used to calculate the value of J_{0e}:

3-27) $$\frac{1}{\tau_{eff}} = \frac{1}{\tau_{rad}} + \frac{1}{\tau_{Auger}} + \frac{1}{\tau_{SRH}} + \frac{2}{\tau_{emitter}} \cong \frac{1}{\tau_{Auger}} + \frac{1}{\tau_{SRH}} + J_{0e}\frac{2\Delta n}{qWn_i^2}$$

3-28) $$\frac{1}{\tau_{eff}} - \frac{1}{\tau_{Auger}} = \frac{1}{\tau_{SRH}} + J_{0e}\frac{2\Delta n}{qWn_i^2}$$

In these equations, radiative recombination is ignored due to its negligible influence on the effective lifetime compared to other recombination processes in Si. When presenting the term ($1/\tau_{eff}$ - $1/\tau_{Auger}$) as a function of the excess carrier Δn, J_{0e} can be extracted from the slope of the linear fit to the graph. This method was first suggested by Kane and Swanson [157] and was shown to be a useful investigation tool [165]. It is employed in this thesis to study the influence of different fabrication processes on emitter recombination.

3.2.1 Measurement Methods

As effective lifetime is a very useful investigation tool for recombination processes within the solar cell, this section reviews the main methods to measure it and the basic principles behind the measurement systems.

Transient Decay Method

As mentioned before, there are different methods to measure effective lifetime. These methods differ mainly by the excitation condition used during the measurement. In the transient decay method the excess carriers are typically created by optical excitation from a laser or flash lamp. After terminating the excitation, the decay of the carrier density is monitored as a function of time. Due to the fact that no generation occurs after the excitation ceases, the change in the carrier density is only due to recombination processes. Using Eq. (3-1), the effective lifetime is given by:

3-29) $$-\frac{d(\Delta n)}{dt} = U = \frac{\Delta n}{\tau_{eff}} \Rightarrow \tau_{eff} = -\Delta n / \frac{d(\Delta n)}{dt}$$

This equation implies an exponential decay of the carrier density with time. The interpretation of effective lifetime in this case is the time taken for the carrier density to reduce to 37% of its initial value [166].

The most robust application of this method is the Photoconductance Decay (PCD) measurement, which was first proposed in 1955 [167]. In this application, the sample conductivity is sensed by an electrical circuit, mainly in contactless mode. The following expression can then be used to describe the conductivity, σ (note the difference between conductivity and capture cross section – $\sigma_{n/p}$) of the sample, as a function of Δn, assuming no traps [150]:

3-30) $$\sigma = q(\mu_n n + \mu_p p) \Rightarrow \Delta\sigma = q\Delta n(\mu_n + \mu_p)$$

where $\mu_{n/p}$ is the electron/hole mobility, which can be found in the literature [168-169]. From this equation Δn can be extracted easily, and thus τ_{eff} can be calculated using Eq. (3-29). The main advantage of this method is that only the *relative* change in Δn with time needs to be measured. Furthermore, the measurement is independent of the light intensity, the pulse shape and of the optical properties of the sample [170]. However, this method requires a steep "cut off" of the optical excitation and fast electronics to detect the excess carrier decay. These requirements limit the use of this method to relatively high lifetime samples (> 100 µs [170]).

Steady-State Method

In this method a steady and known generation rate is maintained. Under equilibrium conditions a balance exists between the rates of recombination and generation. The effective lifetime in this method is given by [166]:

3-31) $$U = G = \frac{\Delta n}{\tau_{eff}} \Rightarrow \tau_{eff} = \frac{\Delta n}{G}$$

where G is the generation rate. This expression assumes uniform generation and uniform carrier density across the sample, which is a good approximation if the wafer thickness is smaller than the carrier diffusion length. Unlike PCD, the absolute values of the excess carrier density, as well as the generation rate need to be measured. One advantage of the steady-state method is that the effective lifetime is measured under similar conditions to the operating condition of a solar cell. However, it is difficult to measure the effective lifetime as a function of Δn, as this measurement requires many well-stabilised light intensities and would potentially heat the sample [171].

Quasi Steady-State Method

In the Quasi Steady-State (QSS) method, an excitation source with a slow decay time (several ms) is employed. The sample is kept under QSS condition as the light intensity varies from maximum to zero. The QSS condition is maintained as long

as the decay time constant is longer than the effective lifetime [150], however it is advised that the decay constant time should be at least 10 times longer than the effective lifetime [170]. The QSS Photoconductance (QSS-PC) measurement was first proposed by Sinton *et al*. and typically employs a flash lamp, with an adjustable decay time as an excitation source [172-173]. Simpler electronics and light sources can be employed to measure even very low effective lifetimes with this method. The effective lifetime for a wide range of Δn (including under one-sun conditions) can be measured quickly and without sample heating. Similar to the steady-state method, this method requires measurement of the generation rate.

Good agreement was found between the measured effective lifetime obtained from the transient and QSS-PC methods for well-passivated samples [174]. However, these methods diverge for poorly-passivated samples (S_{eff} > 5700 cm/s). The difference increases for thicker samples and is dependent on the light source [175].

In 1999 Nagel *et al*. proposed the use of the *generalised analysis*, based on the continuity equation for excess carriers in semiconductor, to calculate the effective lifetime [176]:

3-32)
$$\tau_{eff} = \frac{\Delta n}{G - \frac{d(\Delta n)}{dt}}$$

This expression reduces to Eq. (3-29) under a transient condition (G=0), while under QSS condition ($d(\Delta n)/dt$=0), Eq. (3-31) is obtained. A wide range of effective lifetime values can be measured when this analysis is employed, with no limitation on the excitation decay time constant [176].

3.2.2 QSS-PC and PCD Measurements

In this thesis, two Sinton bridges (WCT-100 and WCT-120) were used to measure the effective lifetime under QSS and transient conditions. The Sinton bridge is based on a radio-frequency (RF) circuit with a coil [177] inductively coupled to the measured sample above it. When the RF generator is connected to the circuit, the coil produces electromagnetic radiation, which in turn induces an electromagnetic field within the measured wafer. Since the wafer is relatively thin, the resulting field is fairly constant within the wafer. Prior to each measurement the bridge needs to be balanced and the conductivity of the wafer under equilibrium conditions (i.e. the "background conductance"), needs to be measured. A flash lamp with adjustable decay time illuminates the sample. During illumination, the sample conductivity increases due to generated carriers. The output voltage of the unbalanced bridge is then recorded by an oscilloscope. It is important that the operating point of the bridge

be well within a region where the relationship between the sensed conductivity and the output voltage is linear. The generation rate is sensed by a calibrated detector and recorded by a second channel to the oscilloscope. To calculate the generation rate *in* the measured sample, an optical constant needs to be input. The value of this constant represents the difference between the optical properties of the detector and of the sample. The change in conductance is translated into Δn using Eq. (3-30) and mobility models. The effective lifetime is then calculated using the transient, the steady-state or the generalised equations. The measurement result is the *average* effective lifetime in the sample area bounded by the coil.

By adjusting the flash decay time, transient and QSS conditions can be achieved. Typically, a decay time constant of 10-20 µs is chosen for PCD measurements and 2 ms for QSS measurements [170]. These decay times limit the measurement accuracy in each operation mode. Table 3-1 summarises the recommended effective lifetime range for each setting.

Table 3-1: Recommended effective lifetime measurement setting [170].

Illumination mode	Analysis mode	Lifetime range
QSS	QSS	< 200 µs
	Generalised	Any
Transient	Transient	> 100 µs
	Generalised	> 100 µs

Optical Constant

As previously mentioned, an optical constant must be used to accurately calculate the generation rate within the sample. The generation rate is calculated by:

3-33)
$$G = G_0 \frac{J_{sc}}{qW} f_{abs}$$

where G_0 is the measured illumination in Suns (one-sun = 100 mW/cm^2), J_{sc} is the short circuit current density of the detector under one-sun illumination (38 mA/cm^2 for the WCT-100/120) and f_{abs} is the optical constant. The value of f_{abs} depends on the reflectance of the illuminated surface, light trapping properties of the sample, the sample thickness and the spectrum of the light source. Although guidelines for determining the constant value have been given [170, 178], some uncertainty still exists regarding the appropriate value of this constant. For high effective lifetime samples, the value can be determined by comparing the results of transient and QSS measurements [179]. The calculation of the effective lifetime when using the PCD method does not require measurement of the generation rate and therefore no optical constant is needed. The appropriate optical constant can be found by adjusting its

value until a good agreement between the transient and the QSS measurement results is obtained. Recently a self-consistent calibration method was proposed by Trupke and Bardos to accurately determine its value [180].

Measurement Accuracy

The uncertainty level in the effective lifetime measurement has been rarely studied, probably due to the complexity involved. McIntosh and Sinton carried out a preliminary investigation and identified a number of sources of uncertainty [181]. These sources include uncertainty in the measurement itself (hardware), but also in the input parameters. One of the main sources of uncertainty is the carrier mobility model employed for the calculations. From Eq. (3-30), Δn is extracted by using the sum of carrier mobilities, though the carrier mobility depends on Δn itself [168]. The WCT-100/120 uses an iterative process based on parameterisation of empirical results to obtain self-consistent mobilities and Δn values [170]. The parameterisation depends on Δn (but not on the temperature) and introduces another complexity to the uncertainty calculation [181]. Another possible source of uncertainty is the bridge calibration. As mentioned, the photoconductance method is based on linear relationship between the sensed voltage and the sample conductivity. The calibration constants are conventionally found by measuring the output voltage for wafers with known conductivities. However, the accuracy level of this procedure depends on the number of calibration wafers. Furthermore, McIntosh *et al*. found that this calibration procedure is not suitable for high resistivity wafers (> 30 Ω.cm) [182]. In their work, McIntosh and Sinton calculated uncertainty of 10.9% and 8.6% for QSS and PCD effective lifetime measurements, respectively [181].

Trapping and Depletion-Region Modulation

Two mechanisms have been identified that create artifacts in the measured effective lifetime at low injection levels. The first one is *trapping*, which is observed mostly in mc-Si wafers, but also in other low-quality samples [183-184]. Under this condition, extremely high effective lifetime values were measured using both PCD and QSS methods, at low injection levels. A defect level is described as a trap and not as a recombination centre if the captured minority carrier is more likely to return to its original energy band, rather than to recombine after the capture time. From neutrality demands, due to the trapped minority carriers, the majority carrier concentration increases. As a result, the photoconductance of the sample increases, which leads to higher calculated effective lifetime. The influence of this process is more prominent at lower intensity levels, where the trapping concentration is similar to the substrate doping concentration (background doping – $N_{A/D}$). Macdonald and Cuevas found that the trapping can increase the measured effective lifetime by 1-2 orders of magnitude

[183]. The influence of the trapping can be reduced by using a bias-light correction [185].

The second effect is *depletion-region modulation* (DRM) [186-187]. This effect was observed in samples with a depletion region, such as *p-n* junction or silicon nitride passivation. Similar to trapping, it results in very high effective lifetime at low injection levels. This increase is due to modulation of the depletion region width during illumination. As mentioned, the background conductivity is taken before each measurement; this measurement becomes a baseline for future calculations. During illumination, the generated carriers induce a voltage across the depletion region, which reduces its width. Hence, areas which were initially part of the depletion region with a negligible amount of charge changed to be part of the bulk region with carrier density of $N_{A/D}$. This transformation from depletion to bulk region causes a corresponding increase in the sample conductivity [187]. Again, the contribution of this process is more pronounced at low injection levels.

Implied V_{oc}

One of the advantages of the QSS method is the ability to predict the V_{oc} of solar cells – or the *implied* V_{oc} – at very early stages of the fabrication sequence. The calculation is based on the known excess carrier concentration and is given for a *p*-type wafer by [188]:

3-34)
$$Voc = \frac{kT}{q}\ln\left(\frac{\Delta n(0)[N_A + \Delta n(0)]}{n_i^2}\right)$$

where $\Delta n(0)$ is the carrier concentration at the junction. Note that this value in general is not identical to the *average* Δn (Δn_{ave}) calculated by Eq. (3-30). For well passivated, electrically thin samples (where the diffusion length is longer than the wafer thickness), the assumption of $\Delta n(0) \approx \Delta n_{ave}$ is acceptable. For other cases, adjustments are necessary. Cuevas and Sinton proposed the expression $\Delta n(0) \approx 2\Delta n_{ave}$ for the case of high rear surface recombination, while the expression $\Delta n(0) \approx \Delta n_{ave}(W/L_{eff})$ is more appropriate for the case of electrically thick samples (where L_{eff} is the effective diffusion length – $L_{eff} = (D\tau_{eff})^{0.5}$)) [188]. In this study, the implied V_{oc} is used often to evaluate the passivation quality. Note that the optical constant has very limited influence on the implied V_{oc}. However, care must be taken when comparing it to values obtained with other devices such as an *I-V* tester, since the spectrum of the flash lamp is not perfectly-matched to the standard AM1.5G spectrum [189-190]. It is important to mention that the calculated implied V_{oc} does not take into account recombination associated with the Si-metal interface; in this sense, it is the upper limit for the V_{oc} of the device.

3.2.3 QSS-PL

QSS photoluminescence (OSS-PL) has been introduced only recently as an effective lifetime measurement system [191-192] and proven an accurate technique for different solar cell applications [193]. The QSS-PL system is used extensively in the course of this study.

The luminescence emission from Si wafer is determined by the bulk radiative recombination rate which, as can be seen from Eq. (3-3), is proportional to the product of the electron and the hole concentrations [194]. The relative PL signal (I_{PL_rel}) is given by [192]:

3-35) $$I_{PL\_rel} = A_i B(T) np = A_i B(T) \Delta n (\Delta n + N_{D/A})$$

where $B(T)$ is the radiative recombination coefficient and A_i is a scaling factor, which takes into account the fact that in most cases the PL signal is measured only in relative units [192]. $B(T)$ is assumed to be constant for injection levels below 1×10^{15} cm^{-3} [191]. Note that the dependence of I_{PL_rel} on Δn is different at different injection levels:

3-36) $$\begin{aligned} I_{PL\_rel\_high} &\cong A_i B(T) \Delta n^2 \\ I_{PL\_rel\_low} &\cong A_i B(T) N_{A/D} \Delta n \end{aligned}$$

The effective lifetime can be calculated by using Eq. (3-32) after extracting Δn from Eq. (3-35):

3-37) $$\Delta n = -\frac{N_{D/A}}{2} \sqrt{\left(\frac{N_{D/A}}{2}\right)^2 + \frac{I_{PL\_rel}}{A_i B(T)}}$$

It is assumed that in the QSS mode, effective lifetime in the order of 1 ns can be detected by the PL system [195]. Since QSS-PL is less prone to intensity artifact effects compared to QSS-PC, accurate results can be obtained even at very low injection levels (see below).

Measurement System

The QSS-PL system employed in this study has been described previously in Ref. [191]. It is based on a modified Sinton bridge (WCT-100) which includes a PL sensor. For the PL sensor a ~10 cm^2 Si *pin*-diode with a low noise preamplifier is used. The sample is placed on the bridge and is illuminated from the top by an LED-array package with an emission wavelength of 810 nm and a rated maximum optical

power of 1.5 W (~ one-sun). A voltage controlled current drives the array according to computer commands. A 900 nm filter is placed between the LED and the sample to block any unwanted emission from the LED [191]. The penetration depth of the LED light in the Si wafer is small compared to a typical sample thickness, so it is assumed that only PL emission from the sample is detected by the sensor. Note that the position of the sensor at the rear of the sample makes this setup more sensitive to the rear surface due to photon re-absorption [196-197]. As part of this thesis, a high intensity capability (up to ~10 suns) was added to the system. This addition is based on a laser illumination and is described in detail in Appendix 7.

A glass plate is used to couple a fraction of the light into a Si photo-detector with a low-gain preamplifier. Both of the signals, from the PL sensor and from the photo-detector are analysed by the software to calculate the effective lifetime (using the generalised analysis) and the implied V_{oc}. Using computer control, it is possible to customise the light pulse profile. Furthermore, improvements in the system's data acquisition abilities allow for the calculation of effective lifetime down to an injection level of 10^8 cm^{-3} [192].

Self Calibration Method

When calculating the effective lifetime using Eq. (3-32), both G and Δn must be measured in *absolute* units. However, as mentioned for the QSS-PC measurements, accurate determination of the generation rate is challenging. Not only the illumination, but also the sample absorptance needs to be measured in order to determine the generation accurately. It is even more difficult if the spectral absorptance of the sample is different from that of the reference cell, such as for textured or thin samples [198]. Recently, Trupke and Bardos introduced a self-consistent method to determine the generation rate from QSS-PC measurements [180]. This method is based on adding a scaling factor f_s, to the generalised expression of the effective lifetime:

3-38)
$$\tau_{eff} = \frac{\Delta n}{f_s G - \frac{d(\Delta n)}{dt}}$$

They demonstrated that only one value of f_s will lead to similar calculated effective lifetime values for the rising and the falling edges of the light pulse. Different values of f_s, create a hysteresis due to different effective lifetime values for the same Δn [180, 198]. The determination of f_s needs to be done in the intermediate frequency regime (between QSS and transient conditions) [180] and by choosing a pulse shape which produces a pronounced hysteresis [198]. However, when using the QSS-PL, two constants need to be found (f_s and A_i). The self-consistent method cannot be used to determine both. One option to overcome this limitation is to use the

self-consistent method to determine f_s, while A_i is found by comparing the QSS-PL and the QSS-PC measurements at high intensity levels [198]. A second option is to determine A_i by using the self-consistent method while f_s is determined by additional means. In this option, f_s is split into its two components. The system component, which includes the photo-detector, the glass plate etc, is determined separately (by an additional calibrated detector) and only once for a system. The second component is the sample absorptance which is measured by other systems, such as a spectrophotometer [199]. However, it was found independently during this study and by Roth *et al*. [200] that care needs to be taken when using the self-consistent method for samples with low lifetime (< 100 μs), due to limitations of the preamplifier [200].

Coping with Trapping and DRM

PL measurement is more robust against artifact effects which limit other measurement techniques, such as QSS-PC, at low injection levels [191, 201]. This is because it is proportional to the *product* of the electron and hole concentrations and not to the *sum* of them.

Trupke *et al*. demonstrated by PC1D simulation that QSS-PL measurements are significantly less affected by the presence of space charge regions, compared to QSS-PC measurements [191]. In contrast, transient PL can be influenced strongly by space charge regions, due to their effects on the recombination and diffusion processes of charge carriers within the bulk [191].

Bardos *et al*. showed that the effect of trapping on the PL measurement is very limited [201]. They calculated a disturbance of only 0.7% in the effective lifetime measurement due to trapping, for a *p*-type 1 Ω.cm substrate. Under similar conditions, the measured effective lifetime using QSS-PC was found to be ~25 times more than the actual one [201]. The superiority of QSS-PL over QSS-PC at low injection level was also demonstrated by other studies [192, 200].

PL is also more stable with temperature variation, compared to QSS-PC [195]. Temperature variation is another source of inaccuracies in PC measurement, especially when measuring poor quality samples where the generated carrier concentration is small. In this case, the small concentration change can be obscured by even a small variation of the temperature between the background conductance and the effective lifetime measurements [195]. In contrast, the value of $B(T)$ changes only by ~3% at room temperature [139], which leads to a relatively marginal variation in the measured PL signal.

Suns-PL

Determining the voltage of a sample from a PL measurement is based on the fact that both are linked to the separation of the quasi Fermi level ($\Delta\eta$) [196]. The relationship between the PL and $\Delta\eta$ is given by [192]:

3-39) $$I_{PL\_rel} = A_i B(T) n_i^2 \exp(\frac{\Delta\eta}{kT})$$

Whereas the voltage (V) of an ideal solar cells is given by $qV = \Delta\eta$ [196]. Using Eq. (3-39), the solar cell voltage can be expressed as:

3-40) $$V = \frac{kT}{q} \ln(I_{PL\_rel}) + C^*$$

where C^* is a calibration factor that needs to be determined. It has been shown that the Suns-PL (PL measurement in combination with the light intensity measurement) is equivalent to the well established Suns-V_{oc} technique [202] for a wide range of injection levels [196]. The main advantage of Suns-PL over Suns-V_{oc} is that it is a contactless method and does not require a complete solar cell [196]. Hence, information regarding the *I-V* behaviour of the solar cell can be obtained in the early stages of its fabrication sequence (excluding series resistance effects).

3.2.4 PL Imaging

Similar to QSS-PL, the PL imaging method has only been introduced recently [203-204]. However, it has already proven to be a very powerful monitoring tool and it is often employed to optimise different fabrication steps and equipment design [205-207]. Its main advantage is the very short measurement time. In a matter of seconds a spatially-resolved measurement of the effective lifetime/implied V_{oc} of a standard sample can be produced. Since this can be repeated quickly at different fabrication stages, these sample parameters can be traced throughout an entire process.

In the PL imaging system, an 815 nm diode laser is used to illuminate the sample, with less than 5% intensity variation across the sample area [203]. The PL signal is detected by a cooled (-30°C) Si Charge-Coupled Device (CCD) camera. In this setup, the illumination and the detection are done from the same side of the sample. To eliminate any possible detection of reflected laser illumination by the CCD camera, a 1000 nm long-pass filter is placed between the camera and the sample. The intensity level (0.001 – 10 Suns) and the integration time are controlled by computer software to optimise the final image [203]. Similar to QSS-PL, PL imaging can be employed at any fabrication stage as it does not require any metal contact or solar cell structure. Based on this system novel methods have been developed for detection of series resistance [208-209] and localised shunts in solar cells [210].

3.3 Chapter Summary

Different recombination mechanisms were reviewed. Special attention was given to surface recombination, as it the main topic of the next chapters. From the flat-band SRH theory, two fundamental methods to reduce the recombination rate were identified: reduction of the density of surface states and reduction of carrier density at the surface. From the extended SRH formalism it was concluded that the inversion condition decreases the recombination rate. Injection level dependence of the surface recombination was identified as resulting from surface charge and the asymmetrical capture cross sections of electrons and holes. The concept of effective lifetime and different effective lifetime measurement techniques and systems were reviewed as they will be referred to often during the course of this thesis.

Chapter 4 : Review - Surface Passivation

In the previous chapter the basic principles of surface recombination were reviewed. It was shown that the recombination rate is dependent on the substrate as well as on the surface states. Two fundamental methods were identified to reduce the surface recombination rate.

The first method aims at reducing the available charge carrier concentration at the surface. Any recombination process requires one minority carrier and one majority carrier, with the former usually contributing most to determining the recombination rate. Decreasing the concentration of the minority carriers provided all else remains unchanged, will reduce the recombination rate. This can be achieved by creating a doping profile, such as back surface field [29] or by an electrostatic field formed by fixed charges at the surface or in the coating film. An electric field can also be formed by the so-called floating junction [211]. This junction is created by diffusing an *n*-type layer (in the case of a *p*-type substrate) into the rear surface. The resulting junction is isolated from the rear metal contacts and therefore "floats". An additional benefit of this *n*-type layer is the fact that holes and not electrons are the minority carriers within this layer. Due to the lower mobility of holes, the recombination rate at the surface reduces significantly.

The second method focuses on reducing the density of surface states. This can be accomplished in several ways, for instance immersing the wafer in solutions such as hydrofluoric acid (HF) [162] or iodine/ethanol [81-82]. Although high quality passivation is obtained by this technique, it is not suitable for solar cell fabrication. Other techniques include hydrogenation (using atomic or molecular hydrogen to saturate dangling bonds) and growing a dielectric film onto the surface. The latter approach is widely used for solar cell application.

Some passivation techniques combine more than one element. For example, silicon nitride film reduces the surface state density and creates an electrostatic field due to high internal positive fixed charge. Its large hydrogen concentration can also be used for hydrogenation during annealing.

This chapter reviews the properties of three passivation layers: silicon dioxide, silicon nitride and a stacked layer of both. These layers will be evaluated in the next chapter as rear surface passivation treatments for low-resistivity *p*-type substrates.

4.1 Silicon Dioxide and Aluminium Annealing

Silicon dioxide (SiO_2) played a crucial role in the development of integrated circuits, especially in the development of field-effect devices such as Metal-Oxide-Semiconductor Field-Effect Transistor (MOSFET) [133]. The dependence of these devices on the properties of the Si-SiO_2 interface has made it the most intensively investigated semiconductor-insulator system [133]. The benefits of using SiO_2 for silicon solar cell applications, especially as a surface passivation were soon recognised by different research groups. One of the early studies in this field was done at the end of the 1970s by Fossum and co-workers. They demonstrated an increase in the open circuit voltage (V_{oc}) and the short circuit current (J_{sc}) of a solar cell when using a thin SiO_2 film as a front surface passivation layer [212]. The improved understanding of the thermal oxidation process over the years has lead to significant enhancement of the passivation qualities of thermal SiO_2. To date, SiO_2 provides the lowest interface state density of all solid-film passivation techniques, mainly due the movement of the Si-SiO_2 interface to a cleaner region within the wafer [133]. As mentioned, numerous studies have been carried out on the Si-SiO_2 interface (for example, see Refs. [133] and [213]). The following section reviews some of these studies in order to highlight the properties of SiO_2 as a passivation layer, as it is used in this work.

4.1.1 Thermal Oxidation Process

Thermal oxidation is typically carried out in a quartz tube furnace at 800 - 1200°C. The oxygen source can be either oxygen gas (O_2) ("dry oxidation") or water vapour ("wet oxidation"). The oxidation reaction for these cases can be described by:

4-1) $$Si + O_2 \leftrightarrow SiO_2$$ (dry oxidation)

4-2) $$Si + 2H_2O \leftrightarrow SiO_2 + 2H_2$$ (wet oxidation)

Typically, the oxidation process includes more than one step. Table 4-1 presents a three-step oxidation process commonly used to achieve high quality passivation: oxidation (either dry or wet), post-oxidation annealing in nitrogen (N_2), or preferably in argon (Ar) ambient, and Forming Gas Annealing (FGA). The last of the three is carried out at lower temperatures in an ambient containing mostly N_2 with a low percentage of hydrogen (H_2).

Since the oxide grows *into* the Si by consuming it, the growth rate changes with time. The growth rate for short oxidation is proportional to the oxidation time (t), while for long processes the growth rate is better described as a function of the square root of the time ($t^{0.5}$) [133]. The growth rate is higher for wet oxidation than dry

oxidation [214]. The growth rate is also influenced by the doping concentration at the surface (doped surfaces oxidise faster) and by the crystal orientation (e.g., oxidation of a (111) surface is faster than a (100) surface) [215].

Table 4-1: A three-step oxidation processes.

Process	Temperature [°C]	Environment
Oxidation	800 - 1200	O_2 or water vapour
Post-oxidation annealing	1000 - 1100	N_2 or Ar
Forming Gas Annealing	350 - 450	N_2 with a few % of H_2

Trichloroethane (TCA, $C_2H_3Cl_3$) can be added to the oxygen gas supply as a chlorine source [87-88]. Chlorine is known to remove metallic impurities from the furnace and from the wafer surface due to the formation of metal chlorides. Although TCA does not change the interface properties, it reduces the contamination level [133]. The reaction of the TCA with O_2 can be described as:

4-3)
$$C_2H_3Cl_3 + 2O_2 \leftrightarrow 3HCl + 2CO_2$$
$$4HCl + O_2 \leftrightarrow 2H_2O + 2Cl_2$$

Due to the formation of water, the TCA can be viewed as wet oxidation and therefore has a faster growth rate than dry oxidation. It is essential to supply enough O_2 to fully feed the TCA reaction, since its absence can lead to the formation of the toxic gas phosgene.

4.1.2 Properties of the Si-SiO$_2$ Interface

Surface State Density

The surface state density (D_{it} or $N_{it} \equiv \int D_{it} dE$) at the Si-SiO$_2$ interface is very low and in some cases can be reduced to 1×10^9 cm^{-2} [216]. For comparison, the atomic density of Si is around 7×10^{14} cm^{-2} and the surface state density of un-passivated Si surface is on the order of 1×10^{13} cm^{-2} [133]. Hence SiO$_2$ reduces the surface states by four orders of magnitude. It was found that lower D_{it} is obtained when the oxidation occurs at high temperatures and that the value of D_{it} of (111) oriented surfaces is 3-4 times higher compared to that of (100) [133]. It was also found that D_{it} is influenced by the doping concentration and by the type of dopant. Donors, such as phosphorus (P), introduce lower D_{it} compared to acceptors such as boron (B). The D_{it} value is constant at concentrations below 10^{17} cm^{-2} for donors and 10^{16} cm^{-2} for acceptors. Above this doping concentration, D_{it} increases linearly with the doping concentration [217]. No difference was found when comparing D_{it} of wet and dry oxides [215].

Interface Charge

Three different kinds of charges exist at the Si-SiO_2 interface [133]:

1. Fixed (immobile) oxide charge density (Q_f). This is a sheet of positive charge which is located very close to the interface (within 2 nm). This charge (5-20×10^{10} q/cm^2) is not influenced by illumination conditions.
2. Mobile charge density (Q_m), mainly due to alkali ions. Improvement of surface cleaning techniques has reduced this charge to negligible levels.
3. Interface state charge density (Q_{it}). This value is strongly influenced by the preparation of the Si-SiO_2 interface. At well-prepared interfaces, Q_{it} is much smaller than Q_f and can be ignored.

The origin of the interface charge is Si dangling bonds, back-bonded with three oxygen atoms ("P_{ox} defects") [133, 218]. The charge density is decreased with high temperature oxidation [154, 215] and especially when dry oxidation is used (at temperatures higher than 1000°C) [215]. The fixed oxide charge (Q_f) does not depend on wafer resistivity [133]. Note that from the viewpoint of interface properties, wet oxidation has advantages over dry oxidation such as higher Q_f and faster growth rate. However, due to the lower purity of de-ionised water when compared to the O_2 gas source and possible corrosion problems in the oxidation system, dry oxidation is preferred.

Kerr and Cuevas studied the injection level dependence on the effective lifetime for different values of substrate resistivity [219]. The effective lifetime was found to increase for increased substrate resistivity. Lifetimes in both *n*- and *p*-type material demonstrate injection level dependence, though the dependence of *p*-type samples is more pronounced at lower injection levels. Similar results were reported by Aberle [133]. The increased effective lifetime with increased resistivity can be explained by the influence of the resistivity on the transition point between depletion and inversion conditions. As mentioned before, the oxide charge is independent of the resistivity; hence the same charge leads to depletion or inversion according to the wafer resistivity.

Not many studies were done on the influence of oxide thickness on the passivation quality, Zhao *et al*. reported lower V_{oc} when using thinner oxide as a passivation layer [32, 34].

4.1.3 Post-oxidation Anneal and FGA

The importance of post-oxidation anneal is well known [220]. It is carried out in an inert ambient (N_2 or preferably Ar) at high temperatures (1000-1100°C). The

quality of the SiO_2 layer to be grown last is extremely important as it forms the Si-SiO_2 interface. As mentioned above, lower D_{it} is obtained when a high temperature is used. Keeping the furnace at high temperatures until all the oxygen in the furnace is consumed ensures a high quality oxide at the interface.

It was found that annealing in hydrogen-containing ambient, such as H_2 or FGA, reduces D_{it} significantly. This reduction is due to the termination of the dangling bonds by hydrogen. More than 20 minutes treatment is needed to ensure stable equilibrium [133]. Note that the weak Si-H bonds can be broken by ultraviolet (UV) light.

4.1.4 Aluminium Anneal - Alneal

Deposition of an Al layer on top of the oxide before annealing it at 350-450°C improves the interface properties dramatically. This process, which is often referred to as *alneal*, provides the best level of surface passivation up to date [221] and has been used to fabricate the world-record highest efficiency PERL solar cell [32]. It seems that Balk was the first to propose that atomic hydrogen is produced at the Al-SiO_2 interface [222]. It is believed that the Al reacts with water vapour [223] or with water in the form of hydroxyl ions within the oxide to produce atomic hydrogen [213, 224]:

4-4) $$Al + OH \rightarrow AlO_x + H$$

The aluminium oxide is denoted as AlO_x (and not as Al_2O_3) because its composition is unknown and probably changes during annealing [224]. The released atomic hydrogen then diffuses from the Al-SiO_2 interface to the Si-SiO_2 interface to passivate dangling bonds. The advantage of atomic hydrogen over molecular hydrogen was explained by Wilkinson and Elliman [225]. According to them, at least two different recombination centres exist at the Si-SiO_2 interface: one that reacts with both atomic and molecular hydrogen and one that can be passivated only by atomic hydrogen.

In their intensive study, Reed and Plummer found no influence of the oxide thickness on D_{it} [224]; this was supported later by Zhao *et al.* [32, 34] and Cuevas *et al.* [223]. An interesting conclusion from this observation is that atomic hydrogen diffusion is not influenced by oxide thickness. As no benefit was found for using a hydrogen-containing ambient for annealing, it is assumed that enough atomic hydrogen is released by the reaction itself [224]. Similar D_{it} was measured for *n*- and *p*-type wafers [224]. However, it was found that crystal orientation has a major influence: (111) shows higher D_{it} than (100) [224]. If possible, thermal evaporation is preferable to sputter or beam evaporation systems, due to less surface damage [133, 224]. Although not widely investigated, it is assumed that the purity level of the Al has an influence on the obtained results. Despite the fact that Reed and Plummer did

not find any advantage for an alneal process longer than 10 minutes, it is commonly performed for a longer time. Table 4-2 presents a summary of the process conditions used by different research groups.

Table 4-2: Summary of alneal process condition used by different research groups.

Temp. [°C]	Duration [min]	Al thickness [µm]	Reference
370	30	N/A	[32]
400	30	0.2	[223]
400	30	0.1	[219]
500	60	0.1	[225]

When using a *p*-type wafer, the presence of the Al on the rear has an additional benefit. Due to the low work function of the Al (~ 4.1 eV), the band bending at the rear puts the surface under inversion, similar to adding more positive charge [133]. Thus, a field effect passivation is achieved. Tang *et al.* reported a loss of 10 mV when striping off the Al layer after alneal process [47].

Table 4-3 summarises some of the surface interface properties measured by Aberle on 1 Ω.cm (100) FZ Si (TCA grown oxide, 20 min alneal at 400°C) [133].

Table 4-3: Summary of measured surface interface properties of alneal samples [133].

	D_{it} (at midgap) [cm^{-2}eV^{-1}]	Q_f [q/cm^2]
Alneal *p*-type	3-4×10^9	6×10^{10}
Alneal *n*-type	4-5×10^9	8×10^{10}

4.1.5 Comparison between Alneal and FGA

Table 4-4 summarises Aberle's fit parameters to experimental data for alneal and for FGA samples [133]. The main conclusion from these fittings is that D_{it} of the alneal samples is lower by more than one order of magnitude than that of FGA.

Table 4-4: Summary of fitted interface parameters for alneal and for FGA [133].

	D_{it} [cm^{-2}eV^{-1}]	Q_f [q/cm^2]
Alneal (fit to experiment)	1.5×10^{10} (at midgap)	5.6×10^{10}
FGA (fit to experiment)	3.9×10^{11} (at E_v+0.4 eV)	8.5×10^{10}

Table 4-5 summarises the effective lifetime values measured by Aberle [133] and by Zhao *et al.* [32] at different oxidation stages. The significant improvement of the effective lifetime after the alneal process illustrates its superiority over the FGA process.

Table 4-5: Summary of the effective lifetime after different oxidation steps.

	As-oxidised	After FGA	After alneal	Reference
FZ (0.7 Ω.cm)	35 µs	62 µs	185 µs	[133]
FZ (1.5 Ω.cm)	14 µs	40 µs	400 µs	[32]

4.1.6 Limitations of Thermal Oxidation

Although using SiO_2 as a passivation layer significantly reduces surface state density at the Si-SiO_2 interface, it has some limitations:

1. The high temperature and the relatively long processing time increase the cost and reduce the throughput.
2. The high temperature process may degrade the bulk lifetime due to contamination in the furnace or an inadequate cleaning sequence.
3. When using CZ or mc-Si wafers, the high temperature process can further reduce the bulk lifetime due to the large concentration of oxygen in CZ wafers [226] and the grain boundaries in the mc-Si wafers.
4. Although providing an excellent passivation for both *n*- and *p*-type substrates of high resistivity, the passivation quality depends on the doping type for low resistivity. While excellent passivation is still obtained for *n*-type substrate, much poorer passivation is obtained for low resistivity *p*-type wafers [158, 160, 227].
5. The S_{eff} at the Si-SiO_2 interface strongly depends on the minority carrier concentration within the wafer or, equivalently, on the injection level. For $\Delta n > 10^{14}$ cm^{-3} the thermal oxide provides good passivation, which leads to a high V_{oc} value, though the S_{eff} at low injection level is much higher. Although this variation of the S_{eff} does not limit the V_{oc}, it limits the fill factor (*FF*) and therefore the obtained efficiency [228].
6. The oxide layer does not contain hydrogen, which could improve both the surface and the bulk passivation via hydrogenation during the subsequent annealing process [229].
7. The low refractive index (n_r) of SiO_2 (1.46) reduces its efficiency as an anti-reflection coating (ARC) when used as a passivation layer on the front surface.
8. The high temperature process limits the possibility of performing the metallisation processes before the passivation, which can limit some cell structures [226].
9. It is well-known that due to the difference in the segregation coefficients of Si and SiO_2, redistribution of dopants during the oxidation process occurs [230]. If *p*-type substrate is used, this redistribution leads to creation of a boron depletion layer below the surface. Robinson *et al*. found that the boron

concentration can be reduced by a factor of two if thick oxide (> 500 nm) is grown [231]. This depletion layer can limit the use of an oxide layer for some applications (such as direct Si-metal contact on the rear surface, without additional diffusion).

These limitations imply the need for developing low temperature, easily-implemented passivation methods. One of the most promising approaches is Si nitride film as a passivation layer, which is reviewed in the next section.

4.2 Silicon Nitride

Plasma enhanced chemical vapour deposition (PECVD) was invented by Sterling and Swann in 1965 [232] and was shortly thereafter adopted by the microelectronics industry [218]. At the beginning of the 1980s it was introduced to the photovoltaic community by Hezel and Schorner [233]. They used the very high interface charge of amorphous hydrogenated silicon nitride film (*a*-SiN_x:H, hereafter referred to as SiN_x) to develop the metal-insulator-semiconductor inversion-layer (MIS/IL) solar cell [234]. Even in these first publications the benefits of SiN_x - such as relatively low interface states, surface passivation abilities and good anti-reflection properties - were recognised [233]. Low SRV values were soon achieved using SiN_x as a surface passivation layer [235]. Kyocera seems to have been the first PV company to use PECVD systems in a production line [218]. The high percentage of hydrogen within the SiN_x film contributed to the improved efficiency of their mc-Si solar cells [229]. PECVD systems were soon incorporated into the production lines of BP Solar, Mobil Solar and others [218]. These days, PECVD systems are used by most solar cell manufacturers. Simultaneously different research groups extensively investigated the properties of the SiN_x film, improved it and extended its application [218, 236-237]. This section reviews some of the work in this area, as SiN_x is employed in this study for rear surface passivation. The section begins with a short review of PECVD systems and continues with SiN_x and Si-SiN_x interface properties.

4.2.1 PECVD Systems

Stoichiometric silicon nitride (Si_3N_4) may be grown in several ways, such as by direct nitration of silicon, nitrogen ion implantation into silicon or sputtering of Si in a nitrogen containing ambient [133]. However due to the fact that some of these methods are limited to a very thin films (< 10 nm) and some create surface damage, chemical vapour deposition (CVD) is commonly used to grow an amorphous silicon nitride film from a gas phase. There are three main types of CVD systems: *atmospheric pressure* CVD (APCVD), which deposits films at 700-1000°C; *low*

pressure CVD (LPCVD), which operates at lower temperature (700-800°C) and reduced pressure (0.01-1 Torr); and *plasma-enhanced* CVD, with processing temperatures below 500°C and reduced pressure (0.01-1 Torr). In general, these systems employ reactants containing hydrogen, resulting in non-stoichiometric, high-concentration hydrogen-containing films [238]. Due to lower deposition temperature, PECVD is the preferred option for PV applications.

The Use of Plasma in PECVD

Plasma is a gas containing charged and neutral species, including some or all the following: electrons, ions, atoms and molecules. On average, plasma is electrically neutral, because any charge imbalance introduces an electric field which will eliminate this imbalance [239]. Although plasma is often referred to as the fourth phase of matter - since it evolves from the gas phase by the addition of energy to the system - there is not a distinct phase change between gas and plasma [239]. To create and sustain plasma requires an energy source. In a PECVD system, this energy source is an electric field produced by either direct current (DC) or alternating current (AC). Typical AC excitation frequencies are 100 kHz, 13.56 MHz (RF) and 2.45 GHz (microwave region) [239]. These plasmas are sometimes referred to as electric discharges or glow discharges.

The extensive use of plasma for deposition (or etching) is due to efficient generation of chemically active species. When an electric field is applied between two electrodes (see for example Figure 4-1), electrons are emitted from the cathode and accelerated by the field. In the presence of reactant gases, collisions occur between the energetic electrons and gas molecules. The outcome of these collisions depends on the kinetic energy of the electron (E_e). For low kinetic energy (< 2eV) elastic collisions occur, conserving the kinetic energy of the colliding particles [240]. Due to the significant velocity and mass difference between the electron and the molecule, the electron energy remains similar after these collisions. If the electrical field is strong enough, the electrons will still continue to gain sufficient energy to cause ionisation. At higher E_e inelastic collisions start to occur, in which E_e is partially converted into internal energy of the target molecule. At high E_e (> 15 eV) the collisions result in ionisation. The excited molecule can then undergo one of the following processes: (a) *electron relaxation*, where the electron falls back to the ground state by emitting a photon which gives the plasma its glow; (b) *ionisation*, which sustains the plasma by supplying it with new free electrons; or (c) *dissociation*, which creates *free radicals* (atom/molecule/ion with unpaired electrons) [240]. There are different types of dissociations; all of them release free radicals (see Table 4-6). The produced radicals are very active chemically, due to their unsatisfied bond and are the primary reactants in the plasma-enhanced film deposition. The type of radicals formed is influenced by

the reactant gases used in the specific system. Analysis of the radicals produced by a silane (SiH_4) - ammonia (NH_3) mixture can be found in Refs. [241-242].

Table 4-6: Summary of the different dissociation processes (AB designates a molecule and the dot indicates a radical).

Process	Reaction
Dissociative ionisation	$AB + e^- \rightarrow A^+ + \bullet B + 2e^-$
Dissociative	$AB + e^- \rightarrow \bullet A + \bullet B + e^-$
Dissociative electron attachment	$AB + e^- \rightarrow \bullet A + B^-$

Reactor Designs

The design of the PECVD reactor has a crucial influence on the SiN_x film properties. Two different PECVD reactor designs exist: the *parallel-plate* or *direct-plasma* reactor and the *remote-plasma* reactor.

In the parallel-plate configuration, all the reactant gases are excited by an electromagnetic field between two parallel plates (see Figure 4-1 (a)). The wafer is placed onto one of the plates, with direct contact to the plasma. Due to this contact, the plasma parameters - especially the plasma excitation frequency - heavily influence the film properties. In a low-frequency direct PECVD system, the excitation frequency is in the 10-100 kHz range, which is below the *plasma frequency* of about 4 MHz. Below this plasma frequency, ions within the plasma can follow the excitation frequency [243], gaining enough energy to create severe surface damage (*ion bombardment*). This problem is solved in high-frequency direct PECVD, where frequencies above the plasma frequency are used to excite the plasma (typically 13.56 MHz). The acceleration periods in this range of frequencies are too short for the ions to gain energy, hence reducing possible damage to the surface. It was shown that the passivation quality achieved in films prepared by high-frequency PECVD is significantly higher than in the low-frequency system [244]. Furthermore, the films deposited by the high-frequency system demonstrate superior UV stability [244].

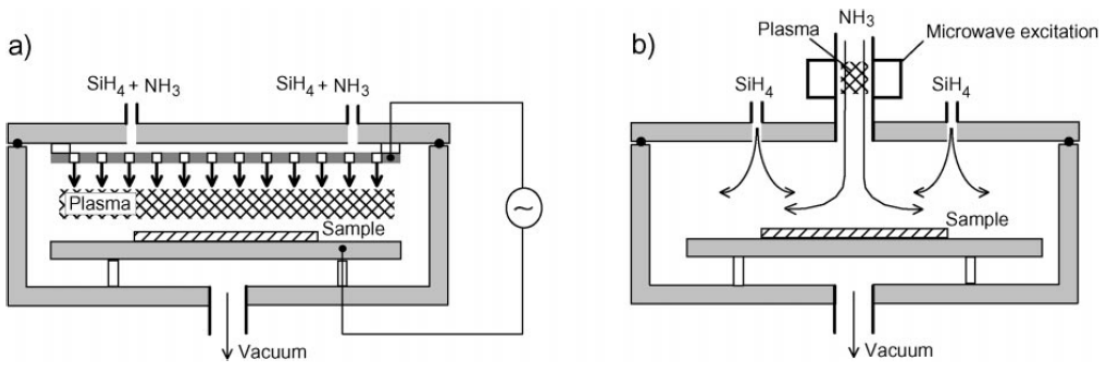

Figure 4-1: Examples for direct-plasma reactor (a) and for remote-plasma reactor (b) [218].

In the remote-plasma reactor, excitation of the plasma is spatially separated from the sample [218]. Several remote-plasma configurations exist, as discussed in Refs. [245] and [246]. Figure 4-1 (b) presents one common remote configuration where ammonia is excited outside the reactor by microwave excitation. Silane is injected into the deposition chamber where it is mixed with the plasma. Since the wafer is not in direct contact with the plasma in this design, no ion bombardment occurs and surface damage is avoided. Other benefits of the remote reactor include higher plasma densities, faster growth rate and the possibility of improving uniformity by using a lower excitation frequency. It was shown that remote-plasma and high frequency direct-plasma films provide similar and very high passivation quality [244], with excellent UV stability [247]. Figure 4-2 summarises some of the key results reported by different research groups relating to the SRV of *p*-type substrates passivated by direct (high frequency) and by remote PECVD systems. The scattering of the presented data can be explained not only by the variety of deposition systems and deposition parameters, but also by different assumptions regarding τ_{bulk} which are used in the calculation of S_{eff}.

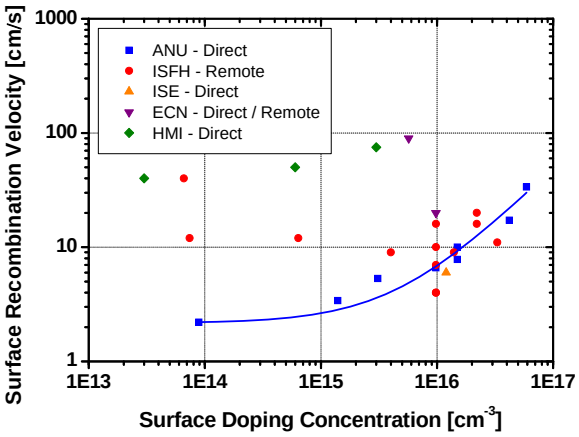

Figure 4-2: SRV as a function of the surface doping concentration, as reported by different research groups: ANU ([159, 248]), ISFH ([158, 160, 238, 249-250]), ISE ([251]), ECN ([252-253]) and HMI ([254]). The solid line is a fit to ANU results.

4.2.2 Si-SiN$_x$ Interface Properties

Interface properties have a significant influence on surface recombination (SRH recombination – Eq. (3-16)). However, it is very difficult to measure Q_f, D_{it} and $\sigma_{n/p}$ at the Si-SiN$_x$ interface due to hysteresis and high leakage current [133]. This section reviews the information regarding these properties, as they play a crucial role in the outcome of surface passivation processes.

Surface State Density

The value of D_{it} at midgap lies in the range of 1×10^{11} - 5×10^{12} cm^{-2}eV^{-1} [161, 235, 255-257], which is one order of magnitude higher than the D_{it} value at the Si-

SiO_2 interface. Hezel *et al*. found that a lower D_{it} value is obtained at higher deposition temperatures; additionally, they found that a post-deposition anneal can reduce this value even further [235, 255, 258]. Elmiger and Kunst found that increasing film thickness reduces the value of D_{it} (up to a saturation value) [256]. Schmidt and Aberle studied the defects at the Si-SiN_x interface for SiN_x films deposited by different PECVD systems. They distinguished three main defect types; one defect, which they designated as defect "C", was found to dominate the quality of interfaces formed by low-frequency direct PECVD [218, 259]. They concluded that this type of defect is created by ion bombardment [259], while the other two defects are Si dangling bond defects like those found at Si-SiO_2 interfaces [218]. The poor passivation of the low-frequency direct system was attributed to the presence of the "C" defect, as all the interfaces studied were found to have similar D_{it} and Q_f values [218].

Interface Charge

Typical reported values of Q_f in the early years of SiN_x investigation fell in the range of 2-7×10^{12} cm^{-2} [234, 255]. This value was found to increase with decreasing deposition temperature [235]. However, recent studies have narrowed the range to 2-3×10^{12} cm^{-2} [237, 254, 256-257, 260].

It was reported that post-annealing of the film reduces the value by almost half [233, 235, 260]. Elimiger and Kunst found that Q_f increases with the film thickness until it reaches a constant value at 20 nm [256-257]. Schmidt and Aberle suggested two components of the charge. The first component - similar to the charge at the Si-SiO_2 interface - is due to dangling bonds (P_{ox} defects) and has a density of ~1×10^{11} cm^{-2}. The second component, which is often referred to as a *K centre*, originates in a Si dangling bond defect back-bonded with three nitrogen atoms. Most interface charge is of this type [218, 259]. The apparent similarity to the Si-SiO_2 interface was explained as resulting from the presence of a very thin (< 2 nm) oxynitride layer that exists in the interface between the bulk Si and the SiN_x film. This thin film is formed in the period between loading the wafers into the deposition chamber and the beginning of the deposition itself [218, 234, 256, 259]. Similar dangling bonds defects exist at the Si-oxynitride interface and the Si-SiO_2 interface. Hence, the positive charge is divided between a thin oxynitride film and a layer of ~20 nm within the SiN_x. Figure 4-3 depicts the charge distribution at the Si-SiN_x interface.

The charge density is usually determined by a capacitor-voltage (CV) measurement in the dark [215]. However, it was found that a good fit can be obtained only by using a lower value of Q_f in the $S_{eff}(\Delta n)$ model (based on the extended SRH formalism [153]). Schmidt and Aberle assumed that the Q_f is influenced by the illumination and proposed a model where Q_f is strongly reduced by electron

neutralisation of the ionised K centres [218, 259]. This assumption allowed for a satisfactory fit between the measurements and the model. Recently Dauwe *et al*. employed corona charging to measure the charge density under illumination for the first time [260]. For comparison the Q_f was measured in the dark as well. Surprisingly the same value (2.3×10^{12} cm^{-2}) was measured under both illumination conditions [135]. By accounting for recombination in the space charge region for the illuminated case [145], a good fit to the $S_{eff}(\Delta n)$ model has been achieved [237, 260].

The influence of the gas ratio on Q_f has not been studied deeply. Mackel and Ludemann found an increased number of K centres in N-rich films [251]. De Wolf *et al*. suggested that the Q_f has two components: Q_{f*}, which is independent on the gas ratio, and Q_t, which increases for decreased n_r [261].

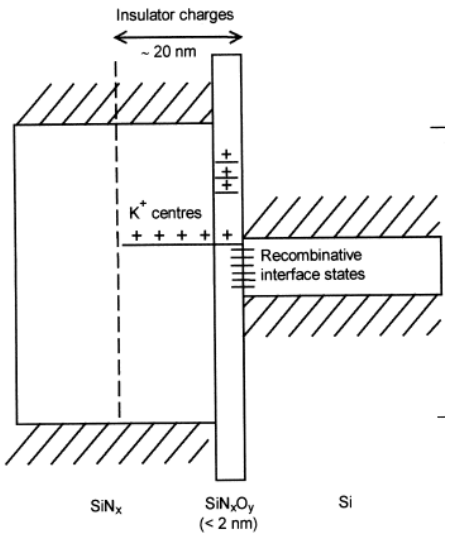

Figure 4-3: Charge distribution at the Si-SiN_x interface [218].

4.2.3 Annealing of SiN_x

As mentioned previously, one of the key advantages of SiN_x is the high concentration of hydrogen within the film ($1\text{-}2.1\times10^{22}$ atoms/cm^3 [238, 262]; this value decreases with increasing deposition temperature [133]). During the annealing process a fraction of this hydrogen diffuses into the wafer, both in atomic and molecular forms [236]. Atomic hydrogen can then saturate dangling bonds within the surface, the bulk or the grain boundaries (in the case of mc-Si wafers) reducing the recombination processes within the solar cell. Improvement of mc-Si solar cells by SiN_x deposition has been studied since the mid-1980s, when enhancement of all cell parameters was reported by Kimura after using SiN_x film as ARC [229]. Since then, SiN_x has been employed by different research groups as bulk and surface passivation for mc-Si solar cells. For example, by changing the ARC from TiO_2 to SiN_x and adjusting the process sequence, Szlufcik *et al*. increased their cells' efficiency from

12.5% to 13.7% [263]. Negel *et al*. employed post-deposition annealing to improve the effective lifetime of their cells from 80 µs to 140 µs [264], while a Georgia Tech group annealed SiN_x together with an Al layer to boost the effective lifetime of different types of silicon ribbons [265].

Although this process clearly improves mc-Si solar cell performance, it seems that the exact mechanism of this improvement is not fully understood.

Influence of the Annealing Process on the Effective Lifetime and S_{eff}

Table 4-7 summarises the influence of the annealing process on the effective lifetime and S_{eff}, as reported by different research groups. Two points that can be concluded from this table are:

1. Although it has been proven that SiN_x annealing improves the performance of mc-Si solar cells, contrary results were achieved using a test structure (as in Figure 3-4). Some of the differences can be explained by variation of the deposition systems and the reactant gases. However, further study is required to fully understand this process.
2. The temperature range of 400 - 800°C has not been studied deeply. Most of the investigations were carried out in the typical ranges for FGA (400°C) and for screen-printed metal contact firing (800°C and above). However the 400 - 800°C range can be used if other metal contacts are employed, such as electroless plating.

Table 4-7: The influence of annealing on the lifetime / S_{eff} as reported by different research groups.

PECVD system	Temp. [°C]	Duration [min]	Conclusions	Reference
Direct	400	30	Improvement of S_{eff}.	[252]
Direct	400 730	30 30 sec	Improvement of S_{eff}. Improvement of S_{eff} (not as good as 400°C annealing).	[266]
Direct	400	25	Improvement of effective lifetime for most of the samples.	[267]
Remote	390, 500, 600, 650 and 700	0-1000	Improvement of the effective lifetime. Peak improvement after shorter annealing time for increased temperature.	[268]
Remote	800	0-60	Steady effective lifetime up to 100 sec of annealing. Degradation for longer time.	[269]
Direct	400 730	15 30 sec	Both degradation and improvement of S_{eff} were observed (depending on the gas mixture).	[270]
Direct	400, 500, 550, 600	0-60	400°C: improvement of effective lifetime up to 30 min and then degradation. Higher temperature: degradation after shorter time.	[271]
Remote	850	10-60 sec	Improvement of S_{eff} only for films in the $2.0 < n_r < 2.2$ range.	[272]
Remote	900	> 10 sec	Improvement of the effective lifetime for $n_r = 2.1$ Degradation of the effective lifetime for $n_r = 2.4$	[237]
Remote	800	1	Improvement only for $n_r = 2.1$ and 2.2	[273]
Remote	800	60	Improvement of the effective lifetime for few samples only (see text).	[274]
Remote	500	40	Degradation of the effective lifetime. Thinner films degrade more.	[238]
Remote	400 730	15 30 sec	Degradation of S_{eff}. Degradation of S_{eff}.	[270]
Remote	800 [a]	1 [a]	Degradation of effective lifetime of most of the samples.	[253]
Remote	N/A	< 1	Reduction of V_{oc}.	[275]
Direct [b]	800 [a]	1 [a]	Degradation of the effective lifetime for Si-rich samples.	[261]

[a] Assumption. The text states – metal firing condition.
[b] Low frequency.

"Blistering" is another mechanism by which the annealing process can influence the quality of the passivation and the effective lifetime. In this phenomenon, hydrogen released from the SiN_x layer creates holes in or otherwise damages the SiN_x film itself [261].

Bonds in SiN_x Film

SiN_x mainly includes three types of chemical bonds: (Si-N), (Si-H) and (N-H). The densities of (N-N) and (H-H) bonds within the film are negligible. It was found

that an increase of the refractive index corresponds to a reduction of the density of (N-H) and (Si-N) bonds and an increase of the density of (Si-H) bonds [238, 251, 273]. Van Erven *et al*. suggested that the transition from low-index to medium-index is due to the replacing of (N-H) bonds with stronger (Si-N) bonds, and that the transition from medium- to high-index is a result of (Si-Si) and (Si-H) bonds replacing (Si-N) bonds [258]. It was found that the density of the (Si-N) bonds is a good indication of the *film mass density*, where higher bond density indicates a denser film [275].

Table 4-8: Absorption spectrum ([262, 267, 276]) and bond energy ([277-278]) in SiN_x film.

Bond	Absorption spectrum [cm^{-1}]	Energy [eV]
Si-H	3300 – 3350	3.10
Si-N	2130 – 2200	3.45
N-H	800 – 840	4.05

Hydrogen Passivation

The variation in the post-annealing passivation quality can be explained by broken hydrogen bonds and diffusion of the free hydrogen atoms. For example, Schmidt *et al*. explained the improvement in the effective lifetime in the first 30 min of annealing by the breaking of weak (N-H) bonds. The free hydrogen atoms then diffuse to passivate dangling bonds within the bulk or at the interface [271]. The reduction in the effective lifetime after 30 min of annealing was attributed to the breaking of (Si-H) bonds, which creates new dangling bonds and therefore degrades the passivation. Other diffusion models with different predictions have been proposed [265, 276, 279-280].

A number of studies have investigated bond density as an indication of the passivation level. Mackel *et al*. concluded that the variation in the hydrogen bond density does not predict the passivation quality, though the density of the total bonds ($[A\text{-}B]_{total}$), can indicate it [267]. Hong *et al*. suggested that the density of the film and not the bond density can be used to predict the passivation quality [281]. They show that the internal quantum efficiency (IQE) at 1020 nm after the annealing process increases with increasing film mass density; the IQE at long wavelengths can be used as an indication of the bulk lifetime. This was supported later by IQE and efficiency measurements by Kessels *et al*. in which they demonstrated that both of the parameters increase with increasing film mass density [282].

Weeber *et al*. then proposed (Si-N) bond density as a fundamental indicator of the passivation quality of the SiN_x film [273-274]. They explained that the (Si-N) bond density (which is related to the film mass density) and not the hydrogen

concentration within the film governs the bulk and surface passivation. They investigated the relationship between the (Si-N) bond density and the passivation quality obtained and found an optimum density of 1.3×10^{23} cm^{-3} [283]. Below this value, the film density is too low, which leads to a film with an "open structure". Under this condition, the released hydrogen is more likely to effuse [274]. However, at higher densities the film becomes too dense, which significantly slows the hydrogen diffusion in the film and limits its ability to passivate dangling bonds [274, 284]. Films with this bond density value were found to provide higher effective lifetime and V_{oc} after the annealing process [274, 283-285]. Dekkers *et al*. pointed later that in a flexible network (open network), a fast release of hydrogen from its bonds to Si or N atoms results in H_2 formation [286]. This molecule is more likely to diffuse out of the film to the ambient than to passivate recombination centres. Despite the mentioned relationship between n_r and (Si-N) bond density, it was shown that variation of bond density for a fixed n_r is possible by adjusting the deposition temperature [285].

4.3 SiO_2/SiN_x Stack Passivation

The passivation quality of a SiO_2/SiN_x stack has been examined on *p*-type substrates and on n^+ emitters by number of research groups. This passivation method was also evaluated during the course of this work. This section includes a short review regarding SiO_2/SiN_x stack passivation.

4.3.1 SiO_2/SiN_x Stack Passivation of *p*-Type Substrate

Rohatgi *et al*. used Rapid Thermal Oxide (RTO) beneath high-frequency direct grown SiN_x to achieve S_{eff} of ~10 cm/s on a 1.3 Ω.cm *p*-type substrate [266]. They found that although each of the layers provides only moderate passivation after annealing at 730°C, the stack layer demonstrates high post-annealing passivation quality. This stack layer also shows a weak injection level dependence in the range $10^{14} < \Delta n < 10^{15}$ cm^{-3}. In a later study, Rohatgi *et al*. compared SiN_x to a SiO_2/SiN_x stack and found that the latter demonstrates superior thermal stability [270]. Better thermal stability of the SiO_2/SiN_x stack was also reported by Schmidt *et al*. [271]. No correlation between the oxide thickness and the passivation quality was reported. To the contrary, Larionova *et al*. found that thin oxide layers (10-40 nm) provide better passivation when applying a SiO_2/SiN_x stack to an *n*-type substrate [287]. They attributed this to the consumption of a large fraction of hydrogen by dangling bonds within the thicker oxide layer, while the hydrogen diffuses toward the Si-SiO_2 interface.

4.3.2 SiO_2/SiN_x Stack Passivation of n^+ Emitters

It seems that Szlufcik *et al*. were the first to report the use of SiO_2/SiN_x as n^+ emitter passivation [263]. Rohatgi *et al*. reported lower J_{0e} values for emitters passivated by a SiO_2/SiN_x stack than by SiN_x, for both planar and textured surfaces [270]. Kerr *et al*. studied a wide range of emitter resistivities and found that emitter passivation using SiO_2/SiN_x stack is of similar quality to that obtained by the alneal process [288-289]. The measured J_{0e} values of a SiN_x-passivated emitter were higher for high-resistivity emitters, although similar values were measured for emitters with resistivity below 100 Ω/□. Similar results were reported by Schmidt *et al*. [271]. Furthermore, similar V_{oc} values were measured for solar cells passivated by SiN_x and by a SiO_2/SiN_x stack layer on both front and rear surfaces [271]. Van Erven *et al*. found that Si-rich SiN_x films (as part of the stack) provide lower J_{0e} values when compared to low-index layers and that all stack layers provide better passivation than SiO_2 alone [258].

4.4 SiN_x Passivated Solar Cells

The proven high passivation quality of SiN_x was employed by different research groups in their fabrication of new solar cell structures. Hubner *et al*. developed a bifacial solar cell structure based on SiN_x passivation of both surfaces [290]. A local BSF was formed on the rear surface using Al evaporation through a shadow mask and sintering. High front and rear efficiencies of 19.5% and 16.5%, respectively, were demonstrated by this structure on a 0.5 Ω.cm FZ *p*-type substrate. Higher efficiencies of 20.1% (front) and 17.2% (rear) were achieved, using the same structure, on a 1.5 Ω.cm substrate with a double-layer ARC of PECVD SiN_x and PECVD SiO_2 [291]. To make this structure affordable, Lenkeit *et al*. replaced the rear evaporated contacts with screen-printed ones and achieved 16.0% (front) and 9.3% (rear) efficiencies on a similar substrate [269]. After an optimisation process these efficiencies were improved to 17.4% and 13.4% for front and rear illumination, respectively [272]. Dauwe *et al*. demonstrated a high efficiency of 20.6% on a 0.5 Ω.cm FZ *p*-type substrate using a MIS structure [292]. A local BSF was formed by Al evaporation and sintering, followed by deposition of a SiN_x layer as rear surface passivation. To improve the internal reflectance, a full area Al film was evaporated onto the rear surface. Mittelstadt *et al*. employed the same structure for a mc-Si cell to achieve 18.1% efficiency on a 1.0 Ω.cm wafer [293-294]. Kerr and Cuevas used a simplified passivated emitter and rear contacts (PERC) solar cell structure [295] to fabricate a 19.7% SiN_x passivated solar cell on a 0.3 Ω.cm FZ *p*-type substrate [296]. Recently, efficiencies of 17.0% (front) and 10.3% (rear) on 2 Ω.cm CZ substrate were reported for a bifacial structure with front and rear screen-printed metal contacts

[297]. However, this structure is still limited by the front side design and the lack of local BSF below the metal contacts.

Despite the high efficiencies, most of these structures are not suitable for mass production due to the expensive fabrication processes involved. One of the aims of this thesis is to develop a high efficiency, SiN_x-passivated structure which is commercially viable.

Table 4-9: Efficiencies of different SiN_x-passivated solar cell structures.

Substrate [Ω.cm]	Front Eff. [%]	Rear Eff. [%]	Rear Passivation	Front Metal	Rear Metal	Ref.
0.3 (FZ)	19.7	----	SiN_x	Evaporation	Evaporation	[296]
0.5 (FZ)	19.5	16.5	SiN_x	Evaporation	Evaporation	[290]
0.5 (FZ)	20.6	----	SiN_x	Evaporation	Evaporation	[292]
0.5 (FZ)	**21.5**	----	SiN_x	N/A	N/A	[298]
1.5 (FZ)	16.0	10.0	SiN_x	Evaporation	Screen-print	[269]
1.5 (FZ)	16.7	----	SiN_x	Evaporation	Evaporation	[299]
1.5 (FZ)	17.4	13.4	SiN_x	Evaporation	Screen-print	[272]
1.5 (FZ)	20.1	17.2	$SiN_x + SiO_2$	Evaporation	Evaporation	[291]
1.0 (mc-Si)	18.1	----	SiN_x	Evaporation	Evaporation	[293]
2.0 (CZ)	17.0	10.3	SiN_x	Screen-print	Screen-print	[297]

4.5 Chapter Summary

The main properties of $Si\text{-}SiO_2$ and $Si\text{-}SiN_x$ interfaces are summarised and compared in Table 4-10. In general, the $Si\text{-}SiN_x$ interface is characterised by one order of magnitude higher surface state density and interface fixed charge than the $Si\text{-}SiO_2$ interface. These values both decrease for increasing deposition temperature; similar behaviour was reported for $Si\text{-}SiO_2$ interfaces. The capture cross section ratio at both of the interfaces varies across a wide range of values, depending on the oxidation/deposition parameters.

Table 4-10: Properties of SiO_2 and SiN_x interfaces.

	D_{it} at midgap [$cm^{-2}eV^{-1}$]	Q_f [cm^{-2}]	σ_n/σ_p at midgap	H concentration [atomic %]
$Si\text{-}SiN_x$	1×10^{11} - 5×10^{12}	2.3×10^{12}	$10\text{-}10^{6}$ [a]	10-40
$Si\text{-}SiO_2$	1×10^{9} - 2×10^{10}	5×10^{10} - 2×10^{11}	50 [b]	----

[a] Defect A: 10^4-10^6, defect B: 10-10^3, defect C: 10^{-2}-1.

[b] After alneal.

Although it provides high-quality passivation in a laboratory environment, SiO_2 has major drawbacks which limit its use in industry. In particular, the relatively low passivation quality of low-resistivity *p*-type substrates, possible lifetime degradation when processing CZ or mc-Si wafers, a high risk of contamination and high cost and reduced throughput are barriers to widespread commercial use of SiO_2 passivation.

SiN_x provides high-quality surface passivation for low-resistivity substrates at low temperature, which makes it suitable for commercial applications. One of the main advantages of SiN_x is the high concentration of hydrogen within it. This high concentration is very beneficial for mc-Si wafers, where the hydrogen released during annealing diffuses into the wafer bulk and passivates grain boundaries. Though several models have been proposed to explain this process, none has managed to fully characterise it. Despite the proven performance enhancement of mc-Si wafers, diverse results have been published regarding the influence of the annealing process on surface passivation. While some studies found that S_{eff} reduced after annealing, some indicate an *increase* in SRV. Furthermore, the temperature range between 400 and 800°C has not been thoroughly studied. The next chapter will shine some light into this range.

Though high efficiency is achievable by SiN_x-passivated solar cells, most of the structures that have been considered are not suitable for commercial applications due to their complexity and high cost. One of the aims of this thesis is to develop a new solar cell structure based on SiN_x passivation and laser doping.

Chapter 5 : Rear Surface Passivation of Solar Cells

Two significant recent developments in solar cell fabrication have contributed to the increased importance of rear surface passivation quality. The first is the reduction of wafer thickness in order to reduce material cost. This reduces the distance between the rear surface and the junction to be less than the diffusion length of a typical commercial wafer. The second is the improvement of front surface designs by a number of commercially-available techniques. These improved designs, mainly based on a selective emitter, leave the rear surface as the main limitation for further improvement of the solar cell efficiency. Wenham identified recombination at the rear surface of buried contact (BC) solar cells as the primary contributor to the total dark saturation current of devices fabricated on substrates with resistivity greater than 0.5 Ω.cm [44]. Stocks *et al*. halved the recombination of their device simply by reducing the rear contact coverage [300].

To date, the most common rear surface passivation technique for commercial solar cells is based on an aluminium (Al) fired BSF. Although it provides moderate passivation, this method is limited by the large Si-metal interface. Figure 5-1 presents the internal quantum efficiency (IQE) and the reflectance curves of an 18.5% efficient, single sided laser-doped (SSLD) solar cell fabricated during this thesis on large area commercial grade CZ *p*-type (2 Ω.cm) substrate (see Chapter 7 for details). It is evident from these curves that the major limitation of this cell's performance is the long-wavelength spectral response. Although the quality of the bulk material plays a role in suppressing the long-wavelength response, this limiting behaviour is mostly due to the relatively poor passivation of the rear. Note that poor internal reflectance cannot explain the reduced response, as the Al rear reflector and textured front surface provide a very good light trapping scheme. Even more importantly, this reduced response indicates a degradation of the device's voltage, due to the high dark saturation current from the rear surface. Similar curves have been obtained for BC and semiconductor finger (SCF) solar cells.

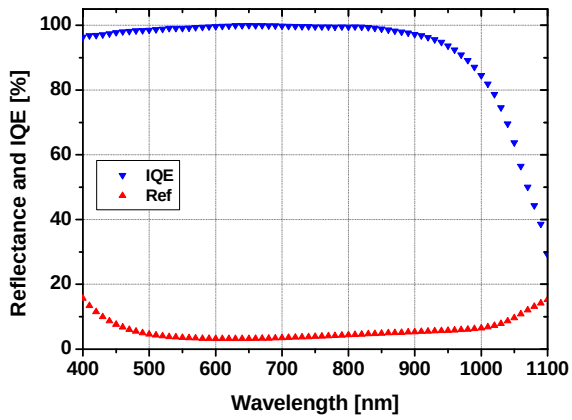

Figure 5-1: IQE and reflectance of 18.5% efficiency SSLD solar cell, made on large area commercial grade CZ *p*-type (2 Ω.cm) substrate.

Figure 5-2 demonstrates the crucial role of the rear surface for achieving high efficiencies. It presents cell efficiency as a function of the rear SRV for different values of front SRV, as obtained from the one-dimensional numerical device simulation program - PC1D [301]. The parameters of this simulation are summarised in Table A11-1. The main conclusion from this simulation is that efficiencies above 20% are possible only for rear SRV below 200 cm/s. It is interesting to compare the influence of the front and rear SRV. While increasing the front SRV by two orders of magnitude (from 10 to 1000 cm/s) reduces the efficiency only by ~0.2% absolute (for rear SRV of 10 cm/s), the same change for the rear SRV will reduce the efficiency by almost 2% absolute (from 20.8% to 19.0% at front SRV equal to 10 cm/s). This difference, which is mainly due to the diffused front surface, highlights the importance of high quality rear surface passivation to enhance solar cell efficiencies.

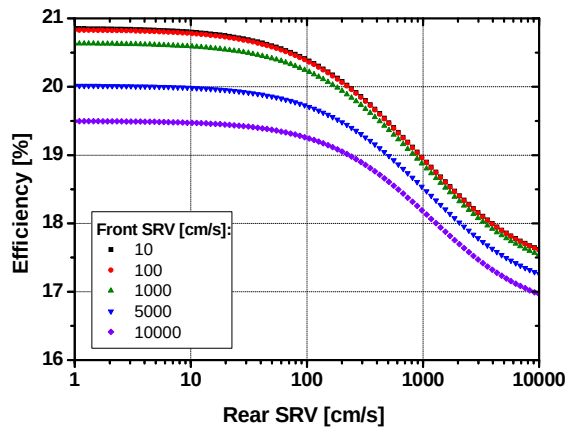

Figure 5-2: Solar cell efficiency as a function of the rear SRV for different values of front SRV. The simulated parameters are summarised in Table A11-1.

This chapter investigates the use of silicon nitride for passivation of the rear surface in low-resistivity *p*-type substrates. This passivation scheme, together with the

laser doping process will be used in the following chapters to develop a novel double sided laser-doped (DSLD) structure. Due to the fact that this structure is not limited by the firing temperature of the rear metal contact, focus is given to optimising the annealing temperature of this film with the aim of reducing recombination throughout the device and particularly at the device surface.

The chapter begins by utilising available equipment to establish baseline processes. Passivation results reported in the literature are verified by comparing silicon dioxide, silicon nitride and a stack layer as rear surface passivation for low-resistivity *p*-type substrates. As silicon nitride is found to provide the highest passivation quality, the influences of refractive index and film thickness on the passivation quality are investigated further. As reviewed in a previous chapter, conflicting results have been reported regarding the influence of annealing on silicon nitride passivation. Furthermore, annealing of SiN_x films in the temperature range of 600-800°C has been rarely studied. This chapter therefore investigates for the first time the dependence of the silicon nitride passivation quality on the annealing temperature in this range, using a variety of films and surfaces. Focus is given to the influence of annealing on the bulk lifetime of the CZ wafer, as this matter has not previously been fully investigated. At the end of the chapter the suitability of the SiN_x passivation to the fabrication sequence of LD solar cell is evaluated.

5.1 Characterisation of the PECVD System

5.1.1 General

A lab-scale PECVD system from Roth & Rau (AK-400) was used in this study. A schematic of this system is given in Figure 5-3. Two microwave antennas (2.45 GHz) in the upper part of the chamber excite the injected ammonia (NH_3) to create plasma. In the lower part, silane (SiH_4) is injected from a metal gas ring, which is located above the substrate holder. The heated substrate holder, which is made of graphite, is connected to an RF (13.56 MHz) source via a matching network. The RF source establishes a bias voltage that draws the plasma down the chamber where it reacts with the SiH_4 to deposit a SiN_x film on the substrate. Since the plasma excitation occurs inside the deposition chamber, it is not a purely remote reactor design; nor is it a direct system, as the wafers are not in a contact with the plasma. Instead, this reactor is classified as a *semi-remote* system.

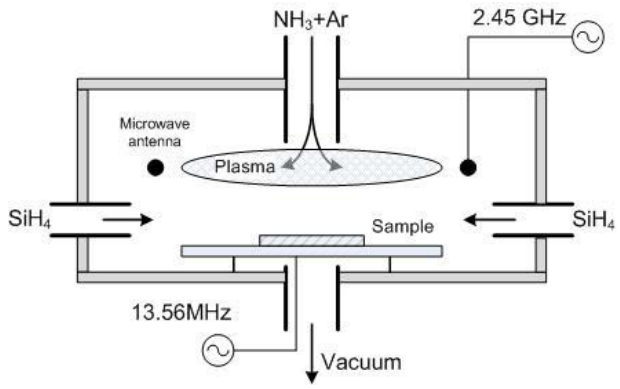

Figure 5-3: AK-400 schematic.

The experiments described in this section were performed in order to characterise the available PECVD system and to establish baselines processes. The results and conclusions from these experiments were used to design subsequent experiments.

The ratio between ammonia and silane flow rates (gas ratio - GR) and the deposition duration were the only parameters which were varied for all the experiments in this chapter. All the other parameters were kept constant and are listed in Table 5-1.

Table 5-1: Deposition parameters which were used in this study.

Parameter	Value
Deposition temperature [°C]	400
Ar flow rate [sccm]	30
Total gas flow rate [sccm]	90
Total pressure [mbar]	0.2
Microwave power [W]	750
RF power [W]	50-65
Bias voltage [V]	150

5.1.2 Index and Growth Rate

The influence of deposition time and GR on the thickness and index of the SiN_x film are investigated in this experiment in order to characterise the PECVD system.

Sample preparation

Nine groups of three single-sided polished wafers were used to investigate the relationship between deposition time and film thickness. The relationship between the deposition time and the refractive index was monitored as well. The wafers were cleaned using RCA solutions [302] and given an HF dip prior to the SiN_x deposition.

Two GRs were used, while the deposition time was in the 65-115 sec range (the rest of the parameters are as shown in Table 5-1). After the deposition, a dual-mode ellipsometer (Gaertner L116A) was employed to measure the film optical parameters at 632.8 nm.

Results and Discussion

Figure 5-4 presents film thickness (a) and film refractive index (b) as a function of the deposition time. Each point in the plots is the average value of 15 measurements (three wafers, five points on each), while the error bars present the standard deviation (STD) of these measurements from the average value. The linear fit is given as a guide to the eye.

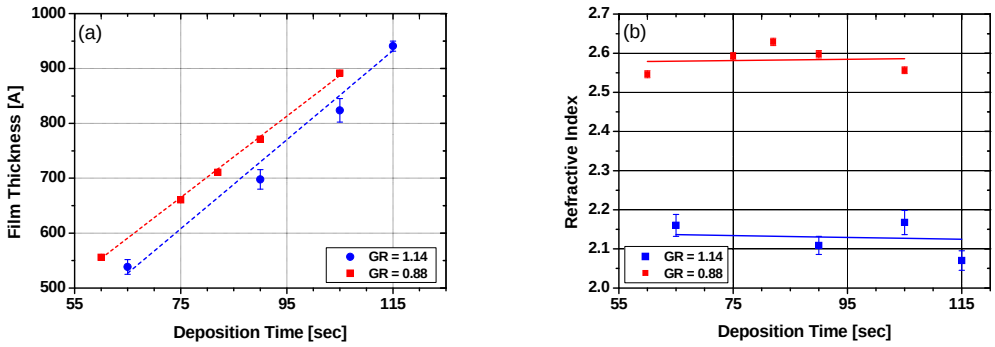

Figure 5-4: Film thickness (a) and film index (b) as a function of the deposition time. The error bars represent the STD of 15 measurements. The linear fit is given as a guide to the eyes.

A linear relationship exists between the film thickness and the deposition time for both gas ratios. The growth rate of Si-rich film (low GR) was found to be faster. Silane is known to be a very reactive gas; it is likely that a high flow rate of silane enhances the deposition rate. No influence of the deposition time (hence, the film thickness) on the refractive index was found. Similar results were also obtained by others; for example, Elmiger and Kunst found that the refractive index reaches a constant value after deposition of 20 nm of film [256]. Note that although a linear fit was obtained, it is possible that parts of the graph, such as the initial deposition period, cannot be described by this relationship.

In the next section, the dependence of film refractive index and thickness on GR is investigated.

Sample preparation

Five groups of three single-sided polished wafers each were used in this part of the study. The pre-deposition preparation was similar to the one described before. However, in this experiment the deposition time was set to 90 sec for all the groups. The GR was the only parameter to be varied.

Results and Discussion

Figure 5-5 presents both the refractive index and the film thickness as a function of GR. A linear relationship was found between the refractive index (n_r) and the GR, which can be empirically described as:

5-1) $$n_r = 3.43 - 1.12 \times GR$$

A linear relationship between the refractive index and GR was also reported by other researchers [238, 253, 292], although the constants depend on the PECVD system and deposition parameters (such as temperature, pressure, etc.). It is interesting to notice the relationship between the film thickness and GR. Low GR (high silane flow rate) leads to a faster average growth rate (9.0 Å/sec and 7.4 Å/sec for GR of 0.77 and 1.07, respectively). This observation is in good agreement with the results shown in Figure 5-4.

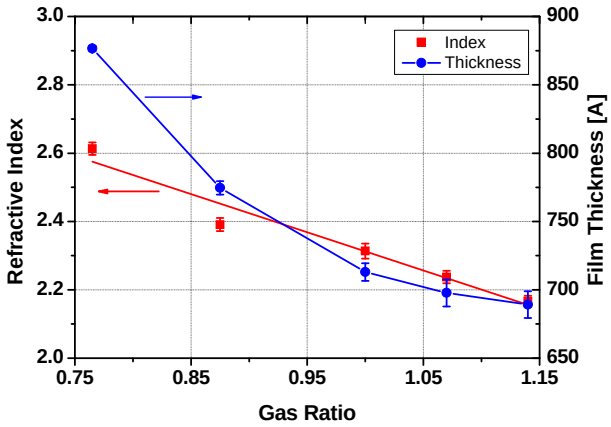

Figure 5-5: Film index and film thickness as a function of the gas ratio. The error bars represent the STD of 15 measurements. The solid line is given as a guide to the eyes.

5.1.3 Uniformity of Deposition

The substrate holder used in this study has eight slots for eight samples, arranged in two rows of four (see Figure 5-6). Evaluation of the deposition uniformity with respect to wafer position in this holder is important for future comparison between different depositions. The next section examines the obtained thickness and index uniformity of different SiN_x films.

Figure 5-6: Top view of the substrate holder.

Sample preparation

Five groups of eight single-sided polished wafers were used to investigate the uniformity. The pre-deposition preparation was similar to the one described before. Both the GR and the deposition time were varied.

Results and Discussion

Figure 5-7 presents film thickness (a) and film index (b) as a function of the position during the deposition. The positions are labelled according to Figure 5-6. Both the thickness and the index were measured at 10 different positions on each sample. The average and the STD values of these measurements are shown in this figure. Figure (a) presents the film thickness for two deposition times (GR = 1.14), while figure (b) shows the film indices of different GRs (deposition time = 90 sec).

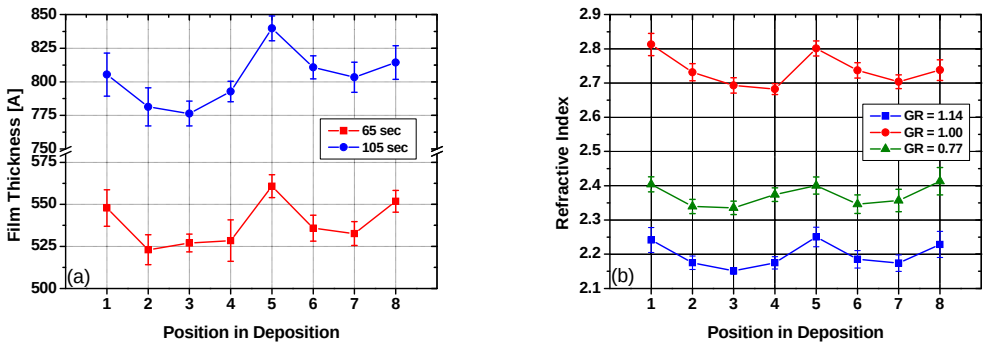

Figure 5-7: Film thickness (a) and film index (b) as a function of the position during the deposition. The error bars represent the STD of 10 measurements on the same sample. The solid lines are given as a guide to the eye.

Figure 5-7 reveals non-uniformity for both of film thickness and index across the samples holder. The average values of samples located in positions 1, 5 and 8 are significantly higher compared to other samples. However, the average values of samples located in other positions are quite uniform. One explanation for this non-uniformity is the SiH_4 gas ring design (see Figure 5-8). It is possible that the SiH_4 is not distributed equally by the ring, hence higher concentration regions are created on the sides.

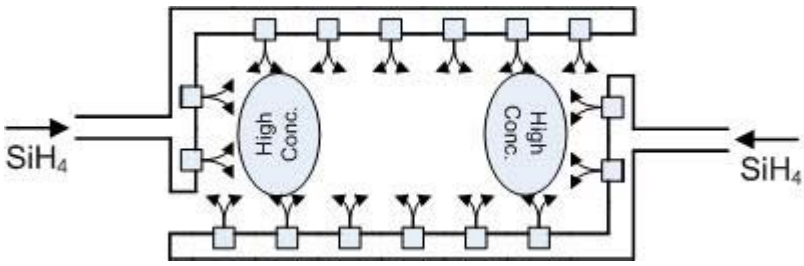

Figure 5-8: Top view of the SiH_4 distribution gas ring.

As a result from this experiment, the position of the samples during subsequent experiments was recorded. Comparison is only done for samples in the same position. When a batch consists of four samples it is preferable to use the middle four positions for a more uniform deposition.

5.1.4 Repeatability

Repeatability of results is a key issue in any research work. In order to monitor the repeatability of the deposition results, the experiment described in Section 5.1.2 was repeated a number of times.

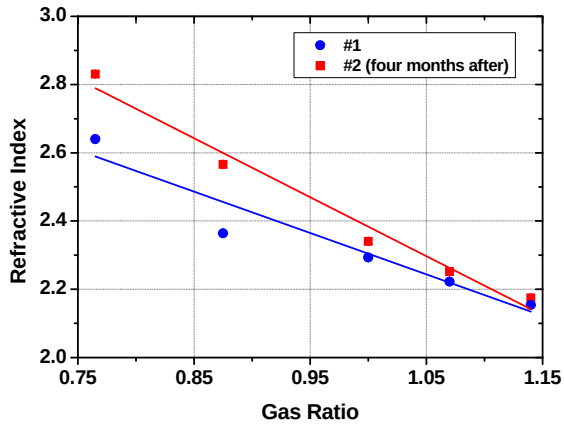

Figure 5-9: Film index as a function of the gas ratio. The solid line is given as a guide to the eyes.

Although only a small change between two successive measurements was found, there is a noticeable drift in the results for measurements taken several months apart. This drift is more pronounced for lower GR values. Figure 5-9 presents the results of two experiments which were done four months apart using identical parameters. The figure reveals a refractive index drift of more than 7% at the lower GR values, despite the fact that similar values were obtained at higher GR values. The origin of this discrepancy is still under investigation, and is possibly due to instability of the RF matching network as well as the instability of the electrical contact between the RF source and the substrate holder.

For subsequent experiments, an effort was made to ensure the samples were deposited with minimal delay between different batches with the aim of avoiding this source of variation in the results. Care must still be taken, however, when results of different experiments are compared.

5.1.5 Conclusions

The available PECVD system was characterised in order to establish baseline processes. The system demonstrates a linear relationship between film thickness and deposition duration. Furthermore, the refractive index is linearly dependent upon the

GR, but is not influenced by the deposition duration within the measured thickness range. Additionally, higher growth rate was observed for Si-rich films.

Non-uniformity across the substrate holder was revealed. It was found that the four positions at the sides produce thicker films (with a higher index) compared to the middle positions. Furthermore, a shift in the refractive index was observed, especially at low GR values.

5.2 Comparison between Different Passivation Methods

Three types of dielectric layers were considered as options for the passivation of un-diffused, low resistivity *p*-type substrates: SiO_2, SiN_x and a SiO_2/SiN_x stack. The aim of this section is to verify published results in the literature and to evaluate the passivation quality of each of these films.

Sample preparation

In this experiment 18 *p*-type (100) wafers were used: nine FZ wafers with resistivity of 1 Ω.cm and nine commercial grade CZ wafers with resistivity of 2.5 Ω.cm. The thickness of the wafers after saw damage etch was 240 μm and 160 μm for the FZ and the CZ, respectively. After a full RCA clean and HF dip, a thick oxide (~270 nm) was grown in a conventional tube furnace, followed by 15 min annealing in nitrogen environment at 1000˚C (see Table 5-2 for details). At the end of the oxidation process, six wafers (three FZ and three CZ) were put aside, while the oxide was removed from the rest of the wafers in an HF dip. Subsequently, a thin dry oxide (~18 nm) was grown on the 12 bare wafers, followed by 15 min annealing. The wafers were then split into two groups, each containing three FZ and three CZ wafers:

1. SiO_2/SiN_x group: SiN_x was deposited onto both surfaces at the end of the oxidation (90 sec deposition, GR = 0.77).
2. SiN_x group: the oxide was removed using an HF dip, before SiN_x deposition onto both surfaces (90 sec deposition, GR = 0.77).

The SiN_x wafers were oxidised twice to eliminate variation in the effective lifetime due to high-temperature processing. Si-rich film was chosen as it is reported to provide the highest quality passivation [237-238, 253, 273]. The complete process sequence is outlined in Figure 5-10.

Table 5-2: Oxidation parameters.

	Duration [min]	Temperature [°C]
Dry oxidation + TCA	30	1030
Wet oxidation	30	980
Dry oxidation + TCA	30	1030
Annealing in N_2	15	1000

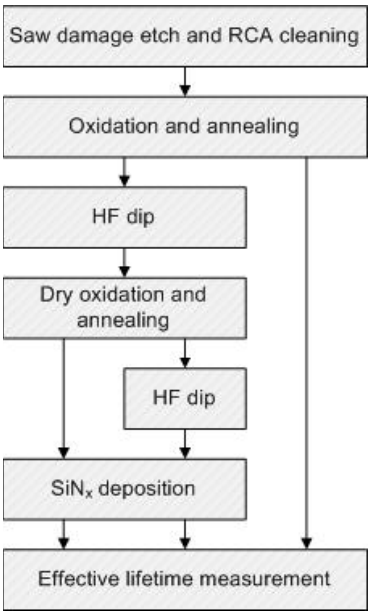

Figure 5-10: Process flowchart diagram.

Results and Discussion

Figure 5-11 presents the effective lifetime as a function of Δn for the FZ (a) and CZ (b) samples. The SiN_x passivated samples demonstrate significantly higher effective lifetime for the entire range. It can be assumed that the bulk lifetime is similar for all the wafers, due to identical substrate and processing sequence. Hence, any variation of the effective lifetime is attributed to difference of the passivation. The SiO_2/SiN_x stack was found to provide a better passivation at most injection levels, compared to SiO_2.

The shape of these graphs is similar to that observed by others [248]. At high injection level ($\Delta n > 10^{16}$ cm^{-3}) the effective lifetime is strongly influenced by Auger recombination, while at low injection level, the injection level dependence of S_{eff} is more pronounced. Note the effective lifetime of the stack passivated samples shows very weak dependence on Δn, similar to reports in the literature [266].

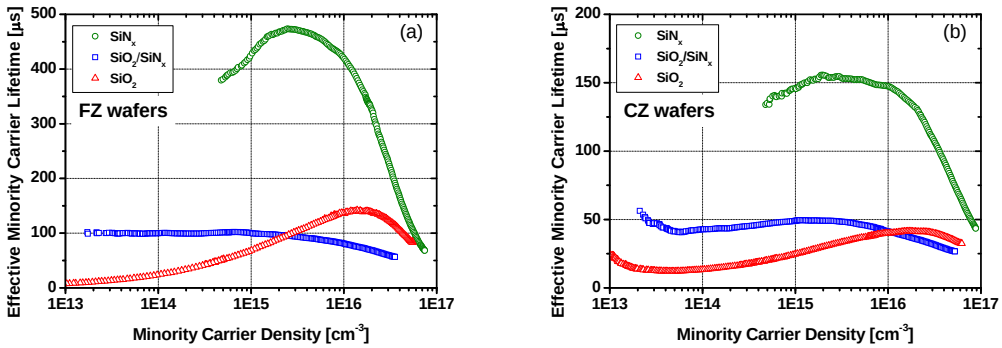

Figure 5-11: Effective minority carrier lifetime as a function of the carrier density for FZ (a) and CZ (b) representative samples passivated by different dielectric layers.

A visual representation of the data from Figure 5-11 is given in Figure 5-12, which presents PL images of one representative sample from each group. All the images were taken under similar condition and are presented in the same scale. Bright regions represent areas with higher PL signal, implying higher lifetime and V_{oc} (see Eq. (3-37) and Eq. (3-40)). As predicted from the effective lifetime measurement, the SiN_x passivated sample image is much brighter than the other two images, while the SiO_2/SiN_x stack image is brighter than that of the SiO_2.

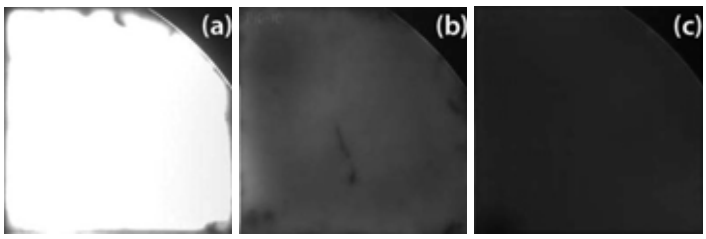

Figure 5-12: PL imaging of representative samples: SiN_x group (a), SiO_2/SiN_x stack group (b) and SiO_2 group (c). All the images were taken under similar conditions and are presented in the same scale.

To further investigate the passivation quality, the S_{eff} values were calculated at an injection level of 1×10^{15} cm^{-3}, using Eq. (3-26) and the measured effective lifetime of the FZ samples. As an intrinsic lifetime, a value of 2.3 ms was chosen (according to Figure 3-1). The *upper* limit of S_{eff} was calculated using an infinite bulk lifetime. Under this assumption the only recombination process within the sample occurs at the surface. Table 5-3 includes both of these values, together with the effective lifetime at 1×10^{15} cm^{-3}. Note that all the calculated values are below 200 cm/s. As expected from the lifetime measurement, the S_{eff} provided by SiN_x is significantly lower compared to the ones obtained by the other two passivations. The superiority of SiN_x to SiO_2 as a passivation layer of low resistivity *p*-type substrate is similar to the findings of others [160, 227]. However, contrary to the obtained results, most studies find that a SiO_2/SiN_x stack provides a lower S_{eff} than SiN_x [266, 270-271]. It is possible that experimental variation arising from the use of different oxidation processes (RTA vs

tube furnace, absence of FGA) and PECVD systems causes this disparity. Similar to the results presented here, Romijn *et al*. measured lower S_{eff} value on SiN_x compared to a stack layer [303].

Table 5-3: Effective minority carrier lifetime and calculated S_{eff} at 1×10^{15} cm^{-3}.

	τ_{eff} [µs]	S_{eff} [cm/s]	S_{eff_max} [cm/s]
SiN_x	433	22.5	27.7
SiO_2/SiN_x	99	115.7	120.9
SiO_2	69	169.5	174.7

The implied V_{oc} values at one-sun were extracted from the effective lifetime measurements and are presented in Table 5-4. The implied V_{oc} of the SiN_x passivated sample is ~40 mV and ~70 mV higher than that of the stack and the SiO_2 passivated samples, respectively. Interestingly, a high implied V_{oc} value above 680 mV was obtained in the SiN_x passivated commercial grade CZ sample.

Table 5-4: Average implied V_{oc} value (one-sun).

	SiN_x [mV]	SiO_2/SiN_x [mV]	SiO_2 [mV]
FZ (as-deposited)	701.9	658.9	632.4
CZ (as-deposited)	683.5	646.2	616.6

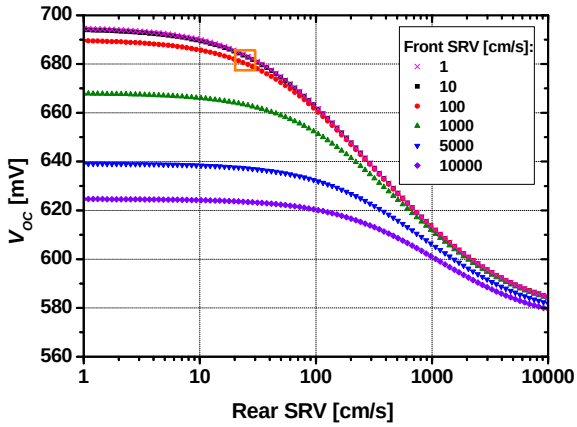

Figure 5-13: V_{oc} as a function of the rear SRV for different values of front SRV. The simulated parameters are summarised in Table A11-2.

To gain a better understanding of the influence of S_{eff} on the V_{oc}, modelling was carried out using PC1D. Figure 5-13 presents the result of this simulation. In order to obtain a good fit between the measurement and the simulation, a bulk lifetime of 160 µs was chosen. The rest of the simulation parameters are as presented in Table

A11-2. According to the simulation, the maximum possible V_{oc} value of sample with this bulk lifetime is 694 mV (for S_{eff} = 1 cm/s for both surfaces).

To investigate the thermal stability of the passivation, all the samples were annealed in an open air belt furnace at peak set temperature of 680°C. The belt speed was set to 4600 mm/m, which leads to less than four sec at the peak temperature. A diagram of the belt furnace used is given in Appendix 12, while a summary of the furnace zones setting can be found in Table A12-1.

Under the assumption that any change in the effective lifetime of FZ samples is due to variation in the passivation quality and not the bulk lifetime, it seems that the annealing process improves the passivation quality of the SiN_x and the SiO_2/SiN_x stack layers, while degradation was observed for the SiO_2 samples. The most striking result is the one-sun implied V_{oc} above 700 mV for SiN_x passivated CZ samples. This value cannot be explained solely by passivation improvement, as the PC1D simulation predicted a *maximum* V_{oc} value of 694 mV (for perfect passivation of both surfaces, see Figure 5-13). An investigation regarding this improvement is presented in following sections.

Table 5-5: Post annealing one-sun implied V_{oc}.

	SiN_x [mV]	**SiO_2/SiN_x [mV]**	**SiO_2 [mV]**
FZ (post annealing)	709.2	691.5	599.6
CZ (post annealing)	706.2	654.8	576.7

Conclusions

It was found that SiN_x provides better passivation when compared to the SiO_2 and SiO_2/SiN_x stack layers. Annealing was found to improve the passivation quality of both SiN_x and SiO_2/SiN_x films, while degradation was observed for SiO_2 passivation. The implied V_{oc} measured for SiN_x passivated samples after annealing exceeded expectations. Further investigation is required to fully understand the reason for this improvement.

5.3 Sample Preparation

Surface preparation prior to deposition was found to significantly influence the passivation quality. Typically the preparation includes a cleaning procedure followed by a diluted/buffered HF dip to remove the chemically-formed oxide. Chen compared the passivation of *n*-type substrates whose surface had been cleaned in RCA [302], in Piranha [304] and as-is (no cleaning) prior to deposition. All samples were dipped in diluted/buffered HF [305]. It was found that RCA-cleaned samples demonstrated

higher effective lifetime, hence better surface passivation. The advantage of using RCA clean is even more pronounced after a firing process. The post-firing passivation quality of these samples improved, while the other samples (Piranha or no clean) showed either no improvement or degradation [305]. The Energy Centre of the Netherlands (ECN) has developed a special pre-deposition cleaning sequence based on wet bench treatment after an HF dip. It was found that this so-called ECN clean improves the blue response to a greater extent than an RCA clean [306]. However, the chemical composition of this sequence is confidential. Schuurmans *et al*. compared the influence of diluted HF and buffered HF (BHF) after an RCA clean on the passivation quality. Choice of solution was found to heavily influence the passivation quality of *p*-type substrates depending on the sample orientation. Diluted HF dip was shown to provide better passivation for (100) and (110) oriented samples, while BHF provides lower S_{eff} for the (111) orientation [307]. Although HF dip is commonly used as a final step prior the deposition, Mackel and Ludemann did not perform it, claiming that the oxide grown chemically during the RCA cleaning improves surface passivation [251]. Based on the results of these studies, all the samples in this thesis were RCA cleaned before the SiN_x deposition. However, due to the ambiguity regarding the HF dip following the RCA clean, this section investigates the impact of omitting the HF dip as the last step of the cleaning sequence prior to deposition.

Sample preparation

Six FZ 1 Ω.cm *p*-type (100) wafers were used in this experiment. After a saw damage etch, the 260 µm-thick wafers were RCA cleaned and split into two groups. While three wafers were HF dipped before the deposition, the other three were not. A Si-rich film (90 sec deposition, GR = 0.77) was deposited onto both of the surfaces prior to effective lifetime measurement. The samples were then annealed in a belt furnace at peak set temperature of 680°C. The belt speed was set to 4600 mm/min; the other furnace settings are listed in Table A12-1.

Results and Discussion

Table 5-6 summarises the average one-sun implied V_{oc} and the STD values of the two groups before and after the annealing process. The HF-dipped samples demonstrated a higher implied V_{oc} (and lower STD values) before and after the annealing process. As the only difference between the samples is the HF dip process, it can be concluded that an HF etch prior to the SiN_x deposition improves the passivation.

Table 5-6: Average one-sun implied V_{oc} and STD of the two groups, before and after annealing.

	Implied V_{oc} [mV]	STD [mV]
No HF dip (as-deposited)	681.3	4.3
HF dip (as-deposited)	727.6	0.8
No HF dip (post-annealing)	726.7	3.4
HF dip (post-annealing)	735.7	0.7

Figure 5-14 presents PL images of two representative samples, one from each group. The brighter image of the HF-dipped sample supports the above conclusion.

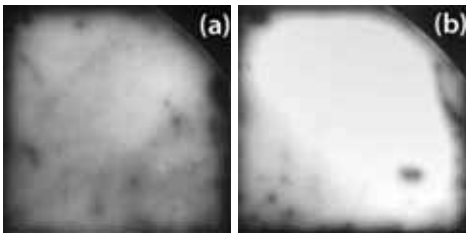

Figure 5-14: PL imaging of representative samples: without HF dip (a) and with HF dip (b). The images were taken under the same conditions and are presented in the same scale.

Conclusions

HF-dipped samples demonstrate higher implied V_{oc} before and after annealing. As a result, the cleaning process for all the samples fabricated during the course of this thesis includes a full RCA clean followed by diluted HF dip. The difference between the results obtained here and those reported by Mackel and Ludemann may be due to the different PECVD systems. It is possible that a thin chemically-grown oxide reduces surface damage caused by the high frequency direct PECVD system which was employed by Mackel and Ludemann, while it degrades the surface passivation when a semi-remote system is used.

5.4 Deposition Parameters and Electrical Performance

As reviewed previously the deposition parameters heavily influence the achieved passivation quality. This section verifies published results and evaluates the passivation obtained by the available PECVD system. In addition to the conventional evaluation by effective lifetime, implied V_{oc} and SRV, the dependence of the *FF* on the passivation quality is investigated in addition by calculating the local ideality factor as a function of the injection level.

5.4.1 Deposition time

Sample preparation

Twenty FZ 1 Ω.cm *p*-type (100) wafers were used in this experiment. The wafer thickness after an alkali saw damage etch was in the 210-220 µm range. After a full RCA clean and HF dip, SiN_x was deposited onto both of the surfaces. Prior to the deposition, the wafers were split into five groups of four wafers each. A GR of 0.88 was used for all depositions. However, the deposition duration was varied in the 60-105 sec range. Single-side-polished wafers were used to measure the film's optical parameters with a dual-mode ellipsometer at single wavelength of 632.8 nm. The electrical parameters of the film were evaluated by effective lifetime measurements, using both QSS-PC and QSS-PL systems, with good agreement between them.

Results and Discussion

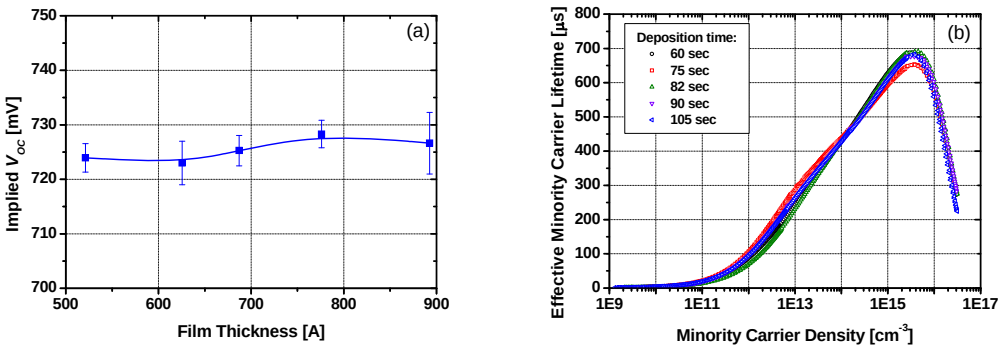

Figure 5-15: Average one-sun implied V_{oc} as a function of the film thickness (a) and the effective lifetime of representative samples measured by the QSS-PL system (b). The solid line is given as a guide to the eye.

Figure 5-15 (a) presents the average one-sun implied V_{oc} as a function of the SiN_x film thickness. The error bars represent the STD of four measurements, while the solid line is given only as a guide for the eye. No influence of the film thickness on the implied V_{oc} was observed in the studied thickness range.

The effective lifetime as a function of the injection level of representative samples from each group is presented in Figure 5-15 (b). The measurements were taken using the QSS-PL system (generalised analysis). For these measurements the illumination range was extended up to ~10 suns using a setup which was specially developed for this thesis (see Appendix 7 for more details). For the first time, QSS-PL measurement was performed at high injection level (up to 5×10^{16} cm^{-3}). The ability of the QSS-PL to accurately measure the effective lifetime down to an injection level of 1×10^{9} cm^{-3} is clearly demonstrated (Figure 5-15 (b)). Similar effective lifetime values were obtained for all samples. The observed dependence of the effective lifetime on Δn accords with the findings of other researchers [236, 248].

At high injection levels the effective lifetime is limited by Auger recombination, while at low levels it is primarily influenced by the injection level dependence of S_{eff}. Similar to the case of SiO_2 passivation, two mechanisms can give rise to this dependence. The first is the asymmetry in the capture cross section of electrons and holes. From the simple flat-band SRH theory this large asymmetry (σ_n/σ_p = 10^1-10^6 at midgap [133]) is predicted to result in strong injection level dependence due to a transition from recombination limited by the capture cross section of electrons to that of holes [308]. A significant decrease in S_{eff} is expected once the injection level exceeds a critical value of $n_s/p_s \approx \sigma_p/\sigma_n$ [309]. The second mechanism is due to a field effect created by the high density of positive fixed charge within the SiN_x film. At low injection levels, this positive charge increases the electron concentration at the surface region relative to the bulk area. Hence, the recombination rate is enhanced. However, at higher injection levels, the fixed charge constitutes an inversion layer in the moderately doped *p*-type substrate. In this layer the holes and not the electrons are the minority carriers. Hence, due to their lower mobility compared to that of electrons, the recombination processes are slowed.

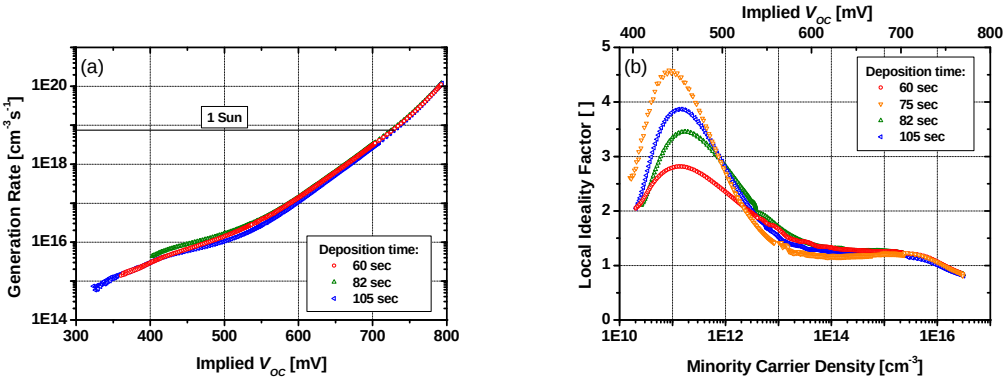

Figure 5-16: Generation rate as a function of the implied V_{oc} (Suns-PL) (a) and the extracted local ideality factor as a function of the injection level and the implied V_{oc} (upper scale) (b). The generation rate equivalent to one-sun illumination is indicated.

This behaviour is also shown in Figure 5-16 (b), which presents the local ideality factor as a function of injection level. The observed transition from high to low local ideality factor indicates a variation of the surface recombination [186]. The high recombination at low injection leads to high local ideality factor, while the decrease of S_{eff} at higher injection leads to a reduction of the ideality factor. The noticeable peaks at an injection level of 1-3×10^{11} cm^{-3} correspond to the aforementioned critical values where $n_s/p_s \approx \sigma_p/\sigma_n$. An important point to examine is the *maximum power point* (MPP); the value of the local ideality factor at this point influences the obtained *FF*. To help identify this point, an upper scale with units of mV was added to the figure. Local ideality factor in the 1.2-1.35 range were extracted at this point (~620 mV), indicating an absolute reduction of 2-3% from the theoretical

limit of the *FF* [310]. Interestingly, a similar value was calculated for the oxide-passivated world record PERL solar cell [308].

Table 5-7 summarises the calculated maximum S_{eff} values of the different films. The calculation employs Eq. (3-26) and assumes infinite bulk lifetime at two injection levels: near open circuit (1×10^{15} cm^{-3}) and near MPP (1×10^{14} cm^{-3}) working condition. As can be seen, similar values were obtained by all the films. Although, S_{eff} increases in the transition from open circuit to MPP working conditions, a good passivation (S_{eff} < 30 cm/s) is obtained at both points.

Table 5-7: Effective minority carrier lifetime and calculated S_{eff} at two injection levels.

Deposition Time	1×10^{15} cm^{-3}		1×10^{14} cm^{-3}	
	τ_{eff} [µs]	S_{eff} [cm/s]	τ_{eff} [µs]	S_{eff} [cm/s]
60 sec	630	19.1	429	28.0
75 sec	596	20.1	440	27.3
82 sec	626	19.2	430	27.9
90 sec	610	19.7	430	27.9
105 sec	610	19.7	430	27.9
Average	**614**	**19.5**	**432**	**27.8**
STD	**14**	**0.4**	**4**	**0.3**

Conclusions

The film thickness (in the studied range) does not influence the passivation quality. Elmiger and Kunst determined a minimum film thickness of 20 nm to achieve maximum passivation; above this thickness no passivation improvement was observed [256]. Similar results were reported later by Kerr [136]. However, it was shown that thicker films provide better UV stability [247]. As a result, in this thesis a film thickness of ~70 nm was set as a minimum thickness.

Good passivation was obtained at open circuit and at MPP working conditions. The Suns-PL measurements were used to extract the local ideality factor. By analysing its value near the MPP, a possible limitation on the *FF* was recognised. However, this limitation is similar to that identified in the world record PERL solar cell.

5.4.2 Gas Ratio

Sample preparation

Twenty FZ 1 Ω.cm *p*-type (100) and five single-sided polished wafers were prepared as described above, excluding the deposition parameters. In this experiment the GR was varied (0.77 ≤ GR ≤ 1.14), while the deposition time was set to 90 sec.

Results and Discussion

Figure 5-17 (a) presents the average one-sun implied V_{oc} as a function of the film refractive index. Si-rich (high index) passivated samples achieve higher implied V_{oc} compared to N-rich passivation. A similar conclusion can be drawn from Figure 5-17 (b), which shows the effective lifetime as measured by the QSS-PL system (generalised analysis). Higher effective lifetime, hence better passivation, was provided by the Si-rich films. The trend in the effective lifetime data is similar to that observed in the previous section. The effective lifetimes for all the different films coincide at low injection (< 2×10^{13} cm^{-3}) and approach the minimum surface lifetime value of $\tau_s = 1/D\times(W/\pi)^2$ [152]. Under this condition, the recombination is limited by the supply of electrons to the rear surface and not by the surface recombination velocity.

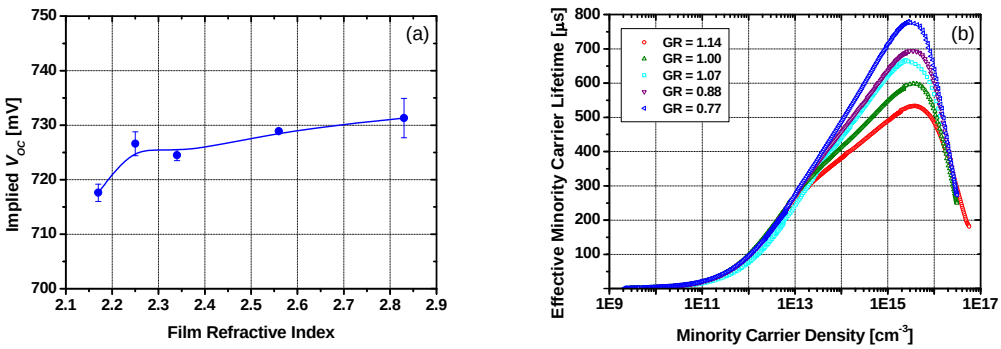

Figure 5-17: Average one-sun implied V_{oc} as a function of the film refractive index (a) and the effective lifetime of representative samples measured by the QSS-PL system (b). The solid line is given as a guide to the eye.

Figure 5-18 corroborates the data presented in Figure 5-17. Comparison of two PL images of representative samples from the GR = 1.14 (a) and the GR = 0.77 (b) group emphasises the superiority of the Si-rich film (image b) over the N-rich film as a passivation layer. Both of the images were taken under identical conditions and are presented in the same scale. Hence, the difference in the brightness can be attributed solely to variation in the effective lifetime/V_{oc} of the samples.

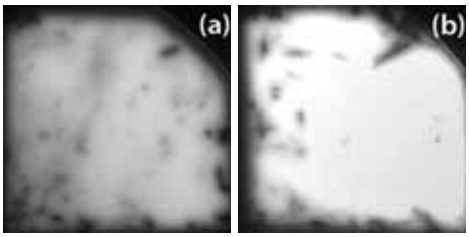

Figure 5-18: PL imaging of representative samples from the GR = 1.14 group (a) and the GR = 0.77 group (b). The images were taken under identical conditions and are presented in the same scale.

Figure 5-19 shows the generation-implied V_{oc} curve (a) and the extracted local ideality factor (b). No clear trend was identified regarding the influence of the film index, excluding the implied V_{oc} value at one-sun conditions, which is similar to the trend presented in Figure 5-17.

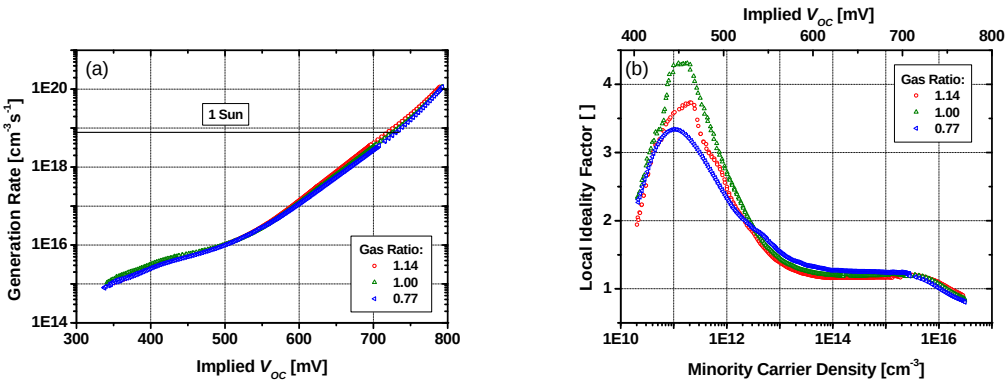

Figure 5-19: Generation rate as a function of the implied V_{oc} (Suns-PL) (a) and the extracted local ideality factor as a function of the injection level and the implied V_{oc} (upper scale) (b). The generation rate equivalent to one-sun illumination is indicated.

Table 5-8 summarises the calculated maximum S_{eff} values of the different films. The calculation was done using Eq. (3-26) and infinite bulk lifetime at two injection levels: near open circuit (1×10^{15} cm^{-3}) and near MPP (1×10^{14} cm^{-3}) operating condition. As predicted by the effective lifetime measurement, Si-rich films provide lower S_{eff}.

Table 5-8: Effective minority carrier lifetime and calculated S_{eff} at two injection levels.

Gas Ratio	1×10^{15} cm^{-3}		1×10^{14} cm^{-3}	
	τ_{eff} [µs]	S_{eff} [cm/s]	τ_{eff} [µs]	S_{eff} [cm/s]
1.14	489	24.5	382	31.4
1.07	622	19.3	441	27.2
1.00	550	21.8	414	29.0
0.88	639	18.8	458	26.2
0.77	717	16.7	491	24.4

Conclusions

Similar to other studies in the literature [237-238, 253, 267], it was found that Si-rich films provide better passivation than N-rich films. Effective lifetime measurements reveal significant variations in injection levels of 5×10^{13}-5×10^{16} cm^{-3}, while comparable values were obtained at other injection levels.

Low S_{eff} values - below 20 cm/s - indicate that the films provide high quality surface passivation that can be employed as a rear surface passivation. The next section will investigate the thermal stability of the obtained passivation under different annealing conditions.

5.5 SiN_x Annealing

As reviewed previously, conflicting results have been reported regarding the influence of annealing on SiN_x passivation (see Table 4-7). Furthermore, the investigations have been focused mainly on annealing within two temperature ranges, the traditional 350-400°C for FGA and the typical screen-printed contact firing range (above 800°C). The middle temperature range has rarely been studied. The aim of this section is to clarify the influence of annealing on the obtained passivation for the temperature range of 600-820°C. This temperature range can be used for solar cell designs that are free from the restrictions of screen-printed contact firing. The passivation quality of different SiN_x films and different surfaces is studied. The second aim of this section is to further investigate the origins of the significant enhancement in post-annealing implied V_{oc} as observed with CZ samples in Section 5.2.

5.5.1 ARC SiN_x Film (Industrial PECVD System)

In this part of the study the passivation performance of an ARC SiN_x layer deposited by an industrial PECVD system is investigated on test structures.

Sample preparation

Two groups of wafers were used in this part of the study. The first group was commercial grade *p*-type CZ 2.5 Ω.cm (100)-oriented wafers while the second was *p*-type FZ wafers with resistivity of 1 Ω.cm and of the same orientation. The CZ wafers were textured using an anisotropic alkaline etch solution, resulting in 1-2 µm-high pyramids and wafer thickness in the 170-180 µm range. The FZ samples received an alkaline saw damage etch and had a final thickness in the 220-230 µm range. All samples were cleaned using a standard RCA sequence and HF dip before SiN_x deposition.

An in-line commercial Roth & Rau remote PECVD system (SINA) was used to deposit a standard ARC SiN_x layer onto both surfaces of the sample. A diagram of the PECVD system and deposition parameters are given in Appendix 13. The film refractive index and thickness were measured using polished wafers and found to be 2.06 and 75 nm, respectively. The samples were then annealed at different temperatures in the range of 600-820°C using an open air belt furnace. The belt furnace zone setting is provided in Table A12-2. The belt speed was set to 4600 mm/min, which leads to less than four seconds in the peak temperature zones. The effective lifetime and the implied V_{oc} were measured before and after this annealing process, using the QSS-PC system (generalised analysis).

Results and Discussion

Figure 5-20 shows the average one-sun implied V_{oc} as a function of the annealing temperature. The solid and the dashed lines represent the average as-deposited implied V_{oc} of the CZ and the FZ samples, respectively, while the error bars represent the STD of four samples annealed at each temperature (from each group).

The very low as-deposited implied V_{oc} values and the similarity between the results for the FZ samples and the CZ samples indicate that the surface passivation, not the bulk lifetime, is the limiting factor for these samples. The small difference between the groups probably arises from the increased surface area of the textured CZ samples, which reduces nearly 14 mV ($kT/q\times\ln(1.73)$) from the V_{oc}, compared to a planar surface. A significant improvement can be observed across the entire temperature range for both types of samples. For the FZ samples, a nearly constant improvement can be observed in the range of 620-680°C. Above 680°C, the implied V_{oc} decreases with increasing temperature. The behaviour of the CZ samples is similar, but with a wider temperature range (620-720°C) where steady improvement can be observed.

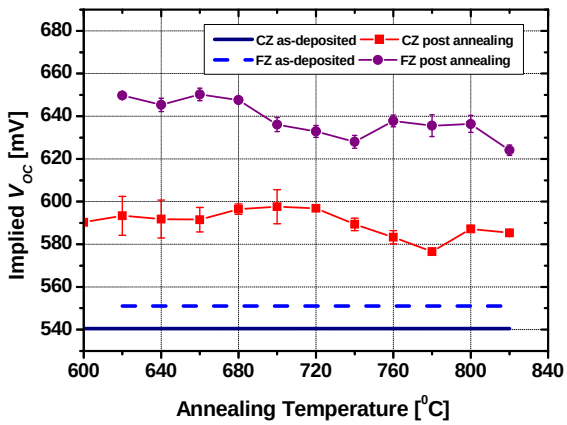

Figure 5-20: Average one-sun implied V_{oc} as a function of the annealing temperature. The error bars represent the STD of four samples annealed at each temperature from each group.

Figure 5-21 presents the effective lifetime as a function of the injection level for representative FZ (a) and CZ (b) samples before and after annealing. As mentioned previously, the very low as-deposited effective lifetime is limited by the surface recombination and not by the bulk lifetime, as indicated by the similar values obtained for both groups. The value (~2 μs) is comparable to the lower limit of surface lifetime ($\tau_s = 1/D\times(W/\pi)^2$), which of course indicates a very poor passivation quality. The post-anneal increase in the effective lifetime indicates an improvement of the surface passivation. As can be seen, the effective lifetime is no longer limited solely by the surface recombination, but also by the bulk lifetime as indicated by the different effective lifetime of the FZ and the CZ samples.

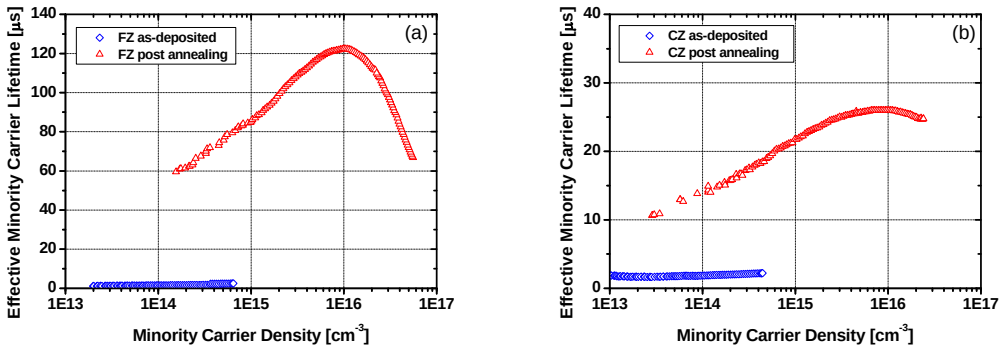

Figure 5-21: Effective lifetime as a function of the injection level of representative FZ (a) and CZ (b) samples before and after annealing at 680°C.

To confirm that the limitation on the implied V_{oc} is due to surface passivation and not degradation of the bulk lifetime, the SiN_x layer was removed from selected FZ samples. After a standard RCA clean, a new SiN_x film was deposited onto both surfaces using the laboratory PECVD system (GR = 0.88, 90 sec). The average one-sun implied V_{oc} value after this deposition was above 725 mV, indicating that the relatively poor passivation achieved with the ARC film and not degradation of the bulk lifetime limits the electrical performance of these samples. Figure 5-22 gives further evidence for this improvement, showing the effective lifetime after the second deposition. For comparison, the effective lifetime of the same sample after the first deposition and after annealing is given as well.

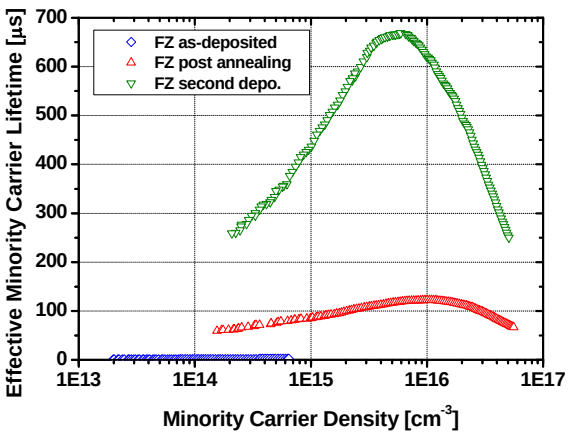

Figure 5-22: Effective lifetime as a function of the injection level of representative FZ sample after second deposition. For comparison the effective lifetime is shown for the first deposition and subsequent anneal.

The variation of the surface recombination is summarised in Table 5-9 by the calculated maximum S_{eff}. Eq. (3-26) and infinite bulk lifetime were used to calculate the post annealing S_{eff} and its value after the second deposition. Note that Eq. (3-26) cannot be employed to calculate the as-deposited S_{eff}, due the poor passivation of this film. The S_{eff} values were calculated under the assumption that the FZ bulk lifetime

does not change during the annealing process; this assumption will be confirmed in the following section.

Table 5-9: Effective minority carrier lifetime and calculated S_{eff} at injection level of 1×10^{15} cm^{-3}.

	τ_{eff} [µs]	S_{eff_max} [cm/s]
As-deposited	2	> 10^4
Post annealing	86	134
After second deposition	457	25

Conclusions

It was found that annealing improves the passivation quality of the ARC SiN_x film. Although improvement was observed for the entire range, greater improvement was observed for annealing temperatures in the range of 620-720°C. However, the obtained passivation is relatively poor.

5.5.2 Si-rich Film

To fully explore the potential of annealing to enhance the passivation quality, Si-rich films deposited using the laboratory PECVD system were examined in the following section.

Sample preparation

For this study *p*-type CZ and FZ 1 Ω.cm (100)-oriented wafers were used. Wafer thickness after an alkaline saw damage etch was found to be in the range of 210-220 µm and 220-230 µm for the CZ and the FZ wafers, respectively. All samples were cleaned using a standard RCA sequence and HF dip before SiN_x deposition. The laboratory semi-remote PECVD system was used to deposit a Si-rich film (GR = 0.88, 90 sec) onto both surfaces of the sample. The samples were then annealed at different temperatures in the range of 600-820°C using the same belt furnace as employed above with similar settings (Table A12-2). The effective lifetime and the implied V_{oc} were measured before and after this annealing process using the QSS-PC system (generalised analysis).

Results and Discussion

Figure 5-23 presents the average one-sun implied V_{oc} as a function of the annealing temperature. The as-deposited averages are given by solid and dashed lines for the CZ and for the FZ samples, respectively. Also given are the STD of four samples annealed at each temperature. A significant improvement can be seen for the entire range of the temperatures: implied V_{oc} values above 700 mV were achieved for all samples. For most of the range the improvement is constant, with an indistinct

peak in the range 680-700°C. In this range, the obtained average one-sun implied V_{oc} is comparable to that obtained for the FZ samples.

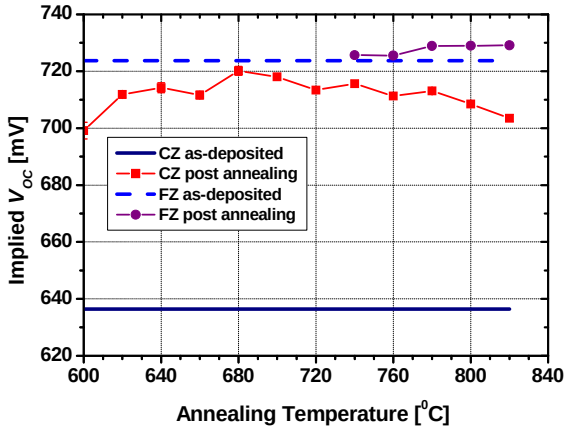

Figure 5-23: Average one-sun implied V_{oc} as a function of the annealing temperature. The error bars represent the STD of four samples, which were annealed at each temperature, from each group.

The improvement is clearly shown in Figure 5-24, where the effective lifetime of representative CZ and FZ samples annealed at 680°C is given as a function of the injection level. A significant enhancement of the effective lifetime is seen. Similar improvement was observed for the other samples. The observed enhancement of the FZ samples is attributed to surface passivation improvement, while further investigation is needed to explain the enhancement seen for the CZ samples.

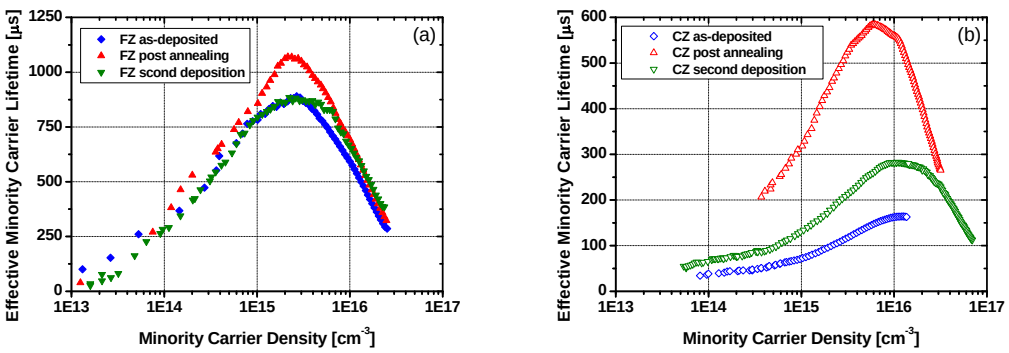

Figure 5-24: Effective lifetime as a function of the injection level of representative FZ (a) and CZ (b) samples before and after annealing at 680°C and after second deposition (see text).

For a better understanding of the source of this enhancement, the SiN_x was removed from selected samples (both CZ and FZ samples) and an identical film was redeposited onto both surfaces for each sample. Figure 5-24 includes the effective lifetime after this second deposition. As can be seen, the effective lifetime of the FZ samples after the second deposition is almost identical to the as-deposited value. This indicates that the post-annealing effective lifetime enhancement is due to improvement of surface passivation. It also implies that the annealing process produces no alteration of the FZ bulk lifetime. In contrast, for the CZ samples an

enhancement of the effective lifetime is observed when comparing the effective lifetime after the second and first depositions. Under the assumption that a similar film was deposited by using identical deposition parameters in the same PECVD system, the most likely explanation for the higher as-deposited lifetimes (after the second deposition) is due to improvement of the *bulk* lifetime during the previous annealing process. It is well-known that CZ wafers contain a high level of oxygen [311-312], metastable defects [313-316], iron [317-318] and in the case of low commercial grade substrates a high level of contamination [319] and even crystal dislocation [320-322]. It is assumed that hydrogen released during annealing diffuses into the bulk and passivates these defects [323], much like the process of hydrogenation in mc-Si wafers. Hence, reduction of the bulk recombination and improvement of the substrate quality occur. The fact that the values after the second deposition are lower than the post-annealing ones indicates that the annealing process improves the surface passivation as well. Similar conclusions can be obtained from Table 5-10 which summarises the one-sun implied V_{oc} of representative samples after different stages of the process.

Table 5-10: One-sun implied V_{oc} of representative samples after different processing stages (the samples were annealed at different temperatures).

Sample ID	After first deposition [mV]	Post annealing [mV]	After second deposition [mV]
W23	644.6	713.0	667.8
W24	639.9	715.6	669.3
W12	642.0	713.4	672.7

The maximum S_{eff} values were extracted from the FZ samples' effective lifetime measurement at an injection level of 1×10^{15} cm^{-3} using Eq. (3-26) and infinite bulk lifetime.

Table 5-11: Effective minority carrier lifetime and calculated S_{eff} at injection level of 1×10^{15} cm^{-3}.

	τ_{eff} [µs]	S_{eff_max} [cm/s]
As-deposited	788	14.6
Post annealing	890	12.9

To confirm the conclusions, the experiment was repeated, this time using commercial grade *p*-type CZ 2.5 Ω.cm (100)-oriented wafers together with FZ 1 Ω.cm samples with the same orientation.

Sample preparation

The CZ wafers were textured using an anisotropic alkaline etch solution, resulting in 1-2 µm-high pyramids and wafer thickness in the 170-180 µm range. The FZ samples received an alkaline saw damage etch, resulting in a final thickness in the 220-230 µm range. The rest of the preparation was similar to that described above. Here, however, the deposition time was increased for the textured wafer to 105 sec. Due to the larger surface area, the deposition rate on textured surfaces is slower; hence a longer deposition time is needed on textured surfaces to produce film thicknesses similar to those on planar surfaces.

Results and Discussion

Figure 5-25 shows the average one-sun implied V_{oc} as a function of the deposition temperature. As before, the solid and the dashed lines represent the as-deposited average of the CZ and the FZ samples, respectively. These values are similar to the ones presented in Figure 5-23. The slightly lower as-deposited values of the CZ samples can be explained by the larger surface area and higher resistivity. As before, an improvement can be observed for the entire temperature range for both the CZ and the FZ samples. While the improvement of the FZ samples is quite constant across this temperature range (~17 mV), the improvement seen in the CZ samples shows a peak in the 660-680°C range. In this range, the implied V_{oc} is significantly increased to above 680 mV. The difference between these values and the values obtained before (Figure 5-23) are explained by the larger surface area, higher resistivity and lower quality commercial grade CZ wafers. The very high implied V_{oc} of the post annealed FZ samples, approximately 740 mV, indicates a very high surface passivation quality.

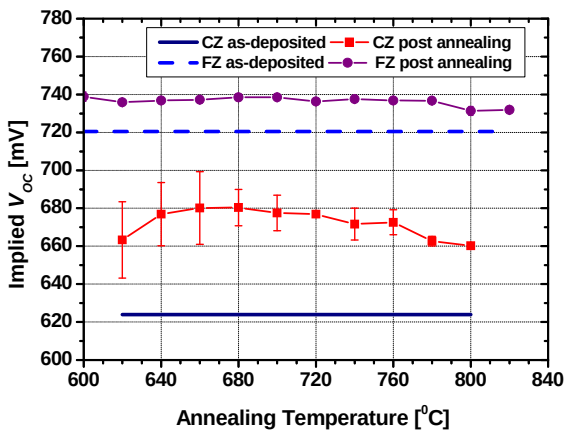

Figure 5-25: Average one-sun implied V_{oc} as a function of the annealing temperature. The error bars represent the STD of four samples annealed at each temperature from each group.

Figure 5-26 demonstrates the same improvement by comparing two PL images of the same CZ sample before and after the annealing process. It is important to note

that although the same scale was used for both images, they were taken using different laser exposure times (0.8 sec for the as-deposited (a) and only 0.1 sec for the post annealing one (b)). Although it is challenging to extract a quantitative conclusion from these images, a qualitative observation can be made: despite the shorter exposure time, the image on the right (b) is much brighter. Hence this sample has higher effective lifetime and V_{oc}.

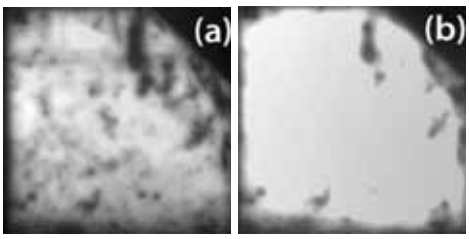

Figure 5-26: PL imaging of CZ sample, before (a) and after annealing at 680°C (b).

Figure 5-27 presents the effective lifetime of representative CZ and FZ samples before and after annealing as a function of the injection level. Significant enhancement is clearly observed for both cases. Effective lifetime approaching 1.75 ms was measured by both QSS-PL and QSS-PC (generalised and transient analysis) with good agreement between them. Effective lifetime above 350 µs was measured for the post annealed CZ sample, which is well above the expected value for this quality of wafers. To confirm the source of this enhancement, the SiN_x layer was removed from selected samples. A new film was deposited onto both of the surfaces, using the same PECVD system with identical parameters. Figure 5-27 (b) includes the effective lifetime after this process. As before, the measured effective lifetime after the second deposition is higher than after the first deposition, which supports the conclusion that annealing improves not only the surface passivation but also the CZ bulk lifetime. Table 5-12 adds more information by presenting the one-sun implied V_{oc} of representative samples after different processing stages.

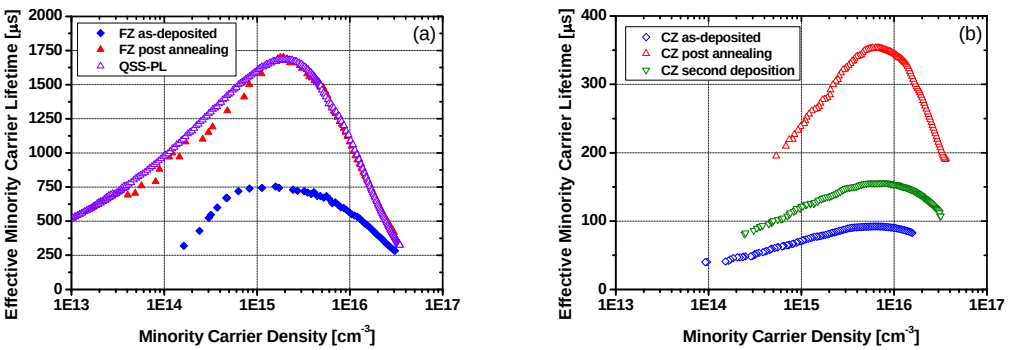

Figure 5-27: Effective lifetime as a function of the injection level of representative FZ (a) and CZ (b) samples before and after annealing at 680°C and after second deposition (see text).

Table 5-12: One-sun implied V_{oc} of representative samples after different stages (the samples were annealed at different temperatures).

Sample ID	After first deposition [mV]	Post annealing [mV]	After second deposition [mV]
W1	629.4	675.9	659.2
W7	631.9	665.2	655.6
W8	626.1	666.0	653.2

The S_{eff} values were extracted from the effective lifetime measurement at an injection level of 1×10^{15} cm^{-3}, using Eq. (3-26). Two bulk lifetimes were used: as an upper bound, an infinite bulk lifetime was used (S_{eff_max}), while the intrinsic limit on the effective lifetime (τ_{bulk} = 2.3 ms) was used to compare the obtained passivation to that reported by Kerr [136]. The as-deposited S_{eff} value of 10.5 cm/s is comparable to that achieved by others for this kind of wafer (see Figure 4-2 and [136]). However, the post-annealing value of 2.1 cm/s is the lowest value reported to date for SiN_x passivated 1 Ω.cm *p*-type substrate, according to the author's knowledge.

Table 5-13: Effective minority carrier lifetime and calculated S_{eff} at injection level of 1×10^{15} cm^{-3}.

	τ_{eff} [µs]	S_{eff} [cm/s]	S_{eff_max} [cm/s]
As-deposited	744	10.5	15.5
Post annealing	1611	**2.1**	7.1

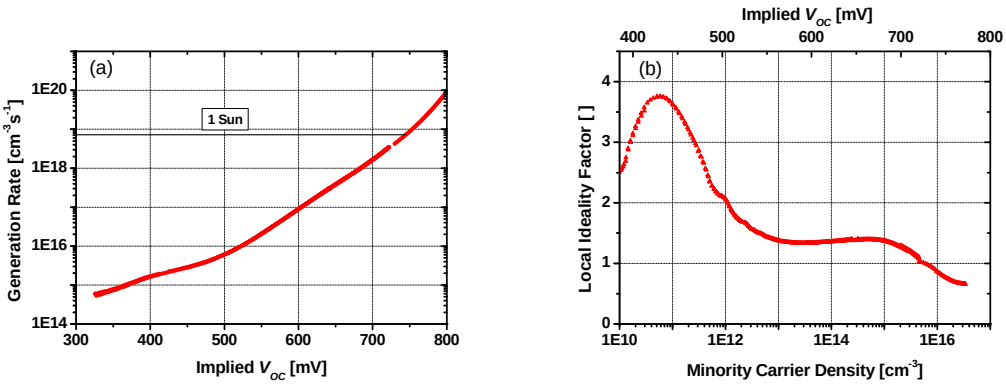

Figure 5-28: Generation rate as a function of the implied V_{oc} (Suns-PL) (a) and the extracted local ideality factor as a function of the injection level and the implied V_{oc} (upper scale) (b). The generation rate equivalent to one-sun illumination is indicated.

The ideality factor was extracted from the generation-rate-implied V_{oc} curve and is presented in Figure 5-28. The ideality factor value at MPP is in the 1.3-1.35 range. As mentioned above, this value, which exceeds unity, can reduce the *FF* by 2-3%. At high injection the ideality factor approaches the Auger ideality factor (for high injection) limit of 0.66 [31].

5.5.3 Influence of Film Parameters

In the previous section it was found that the optimum annealing temperature range for passivation by SiN_x films is 660-700°C for both ARC and Si-rich films and for different surfaces. This section extends the investigated range of SiN_x films and studies the influence of the film parameters on the obtained implied V_{oc} after annealing at the optimum temperature.

Sample preparation

P-type CZ 1 Ω.cm (100) oriented wafers were alkaline saw damage etched to a thickness in the 220-230 µm range. Following a standard RCA clean and HF dip, the samples were divided into groups of four wafers. SiN_x layers with different indices and thicknesses were deposited onto both surfaces using the laboratory semi-remote system. The film parameters were measured using single-sided polished wafers and a dual-mode ellipsometer. The samples were then annealed at the optimal temperature of 680°C, using a belt furnace as described previously. Table A12-1 summarises the furnace zones setting, while the temperature profile of the used setting is given in Figure 5-29. The effective lifetime of each sample was measured before and after this annealing process, using both QSS-PC and QSS-PL systems.

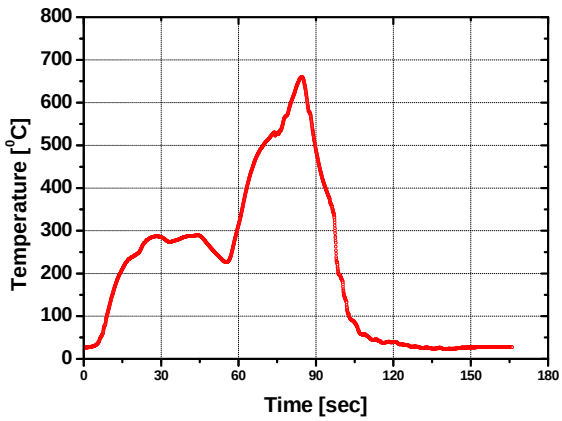

Figure 5-29: Temperature profile of the belt furnace (for zones setting see Table A12-1).

Results and Discussion

Figure 5-30 (a) shows the average one-sun implied V_{oc} as a function of the film index where all samples are of a thickness in the range 74-76 nm. Figure 5-30 (b) presents the implied V_{oc} as a function of the film thickness, where the refractive index of all the samples falls between 2.42 and 2.44. The as-deposited trends for both of the graphs are similar to those observed previously (see Figure 5-15 (a) and Figure 5-17 (a)). As before, all the samples demonstrate a post-annealing improvement. The post-annealing influence of the refractive index on the one-sun implied V_{oc} is more pronounced, that is, a Si-rich film provides better passivation. The behaviour of the

n_r = 2.24 samples (after annealing) does not appear consistent with that of the other samples; however, the experiment was repeated a number of times with a similar result. The post-annealing influence of the film thickness on the one-sun implied V_{oc} is interesting: while no as-deposited influence was observed, a strong correlation between the post-annealing implied V_{oc} and the film thickness was found. Thicker samples demonstrate greater improvement.

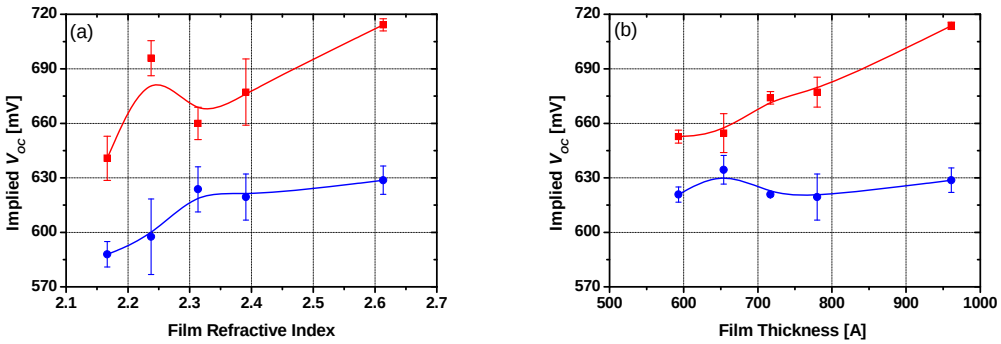

Figure 5-30: Average one-sun implied V_{oc} as a function of the film index (a) and the film thickness (b). The solid lines are given as a guide to the eye. The error bars represent the STD of four samples.

The as-deposited relationship between the film thickness and the obtained passivation is similar to the results reported by Elmiger and Kunst [256] and by Lauinger *et al.*[238]. Neither study found a dependence of the as-deposited passivation on the film thickness. However, the post-annealing result is different. In the study presented here, improvement was observed for all thicknesses, while degradation was observed for most of the thicknesses in Ref. [238]. Despite this difference, the same trend was found in both of the studies: thicker films respond better to annealing. A possible explanation can be the large reservoir of hydrogen provided by a thick SiN_x film. As mentioned, hydrogen released during annealing - especially in the form of atomic hydrogen - can passivate dangling bonds in the bulk of the SiN_x, at the Si-SiN_x interface and in the bulk of the silicon wafer.

5.5.4 Investigation of Surface Passivation Enhancement

The effective post-annealing lifetime enhancement of the FZ samples indicates improved surface passivation, as improvement of the bulk lifetime is unlikely to occur in this high quality substrate. It is expected that the thermal treatment changes some or all of the Si-SiN_x interface properties: the surface state density, the surface charge density and the capture cross section of electrons and holes. As the $S_{eff}(\Delta n)$ depends on these parameters in different ways for *n*- and *p*-type substrates, comparison between the two may reveal more information regarding the origin of the enhancement. In this section, a preliminary investigation is performed by comparing the post-annealing behaviour of *n*-type and *p*-type substrates. However, a more comprehensive study must be done in order to fully understand this process.

Sample preparation

For these experiments, *n*-type CZ 1.7 Ω.cm (100)-oriented samples were used. The thickness of the samples after saw damage etch was in the range of 220-230 μm. The sample preparation, the SiN_x deposition and the annealing process were identical to that described above in Section 5.5.2.

Results and Discussion

The influence of the four parameters - the surface state density (D_{it}), the positive surface charge density (Q_f) and the electron and hole capture cross sections on the effective lifetime of low resistivity *n*- and *p*-type substrates – is summarised in Table 5-14. D_{it} and Q_f have similar influence on the effective lifetime of *n*- and *p*-type substrates. The influence of the capture cross sections is more complicated, but in general they have opposite effects for substrates of different polarities. Like in any other investigation of recombination processes, it is assumed here that some or all of the mentioned parameters change simultaneously, so that any variation of the effective lifetime is due to a combination of several effects. Improvement of the effective lifetime for both *n*- and *p*-type substrates is expected for decreases in the surface state density and/or increase of the positive surface charge.

Table 5-14: Influences of variation of surface state density, surface charge and capture cross section ratio on the effective lifetime of low resistivity *n*- and *p*-type substrates (↓ = decrease, ↑ = increase).

	D_{it} ↓	Q_f ↓	σ_p ↓	σ_n ↓
p-type (effective lifetime)	Increases	Decreases	See Appendix 10	
n-type (effective lifetime)	Increases	Decreases	Increases	No change

Figure 5-31 presents the effective lifetime as a function of the injection level, before and after annealing. Significant post-annealing effective lifetime improvement can be observed for both *n*- and *p*-type substrates; see Figure 5-27. Published studies report a reduction of the surface charge density after annealing. Hezel and Schorner found that the surface charge density reduced by almost a half after 5 min annealing at 300°C [233]. Dauwe *et al*. reported similar results for a short anneal (20 sec) at 850°C [260]. Therefore, reduction of the surface state density is most likely the dominant mechanism for this improvement. It is assumed that hydrogen passivation of dangling bonds at the Si-SiN_x interface reduces the surface state density. A study by Hezel *et al.* supports this conclusion; in their study a post-annealing reduction of the D_{it} was observed [255]. Reduction of D_{it} was also reported by Duerinckx and Szlufcik [324]. Note that variation in the surface charge density can still occur, but the reduction of the surface state density screens any deleterious effects.

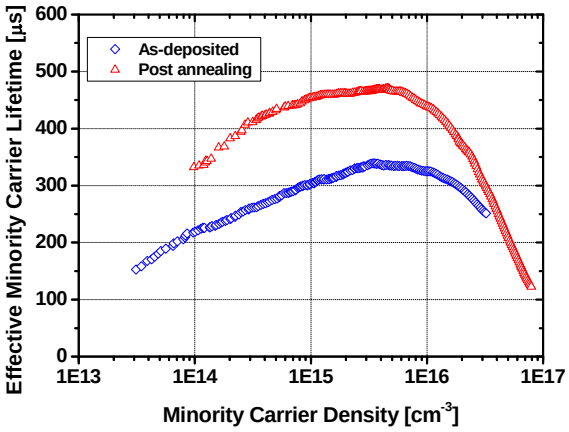

Figure 5-31: Effective lifetime as a function of the injection level of representative *n*-type sample before and after annealing at 680°C.

Interestingly Figure 5-32 reveals a possible change within the capture cross section ratio as well. The figure presents the extracted local ideality factor of *p*-type substrates before and after annealing. The shift in the ideality factor peak to a lower injection level indicates a possible variation of the capture cross section ratio and/or change of charge. Increase of one or both will shift the peak to lower injection levels.

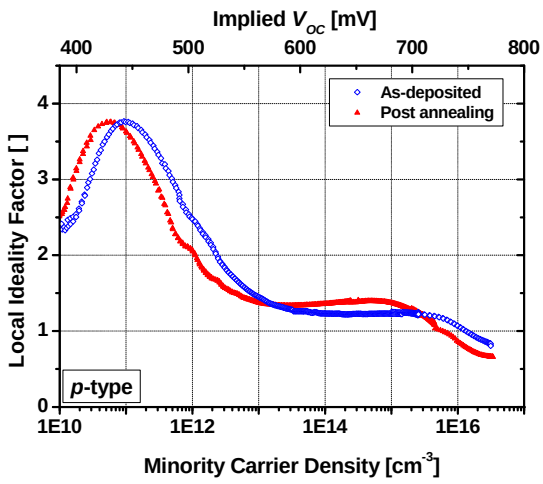

Figure 5-32: The extracted local ideality factor as a function of the injection level and the implied V_{oc} (upper scale) of *p*-type sample before and after annealing.

Despite the interest in understanding the origin of this process, due to different focus of this thesis and limited time, no further investigations have been done. However it is recommended to perform a future study using different methods, such as C-V measurements, to fully understand the origin of the observed enhancement.

Examination of the local ideality factor of the *n*-type substrate is very interesting. As mentioned before, the "hump" in the ideality factor curve is due to the transition from electron-limited to hole-limited surface recombination. However,

when using an *n*-type substrate, no inversion layer is formed by the positive interface charge. Hence, no "hump" can be seen in low/medium injection levels.

The observed hump at high injection levels is due to high injection effects. Under this condition, the concentrations of the minority and the majority carriers are similar across the entire device. The increase of the depletion region width pushes the ideality factor value toward 2 (which characterises depletion region recombination). At a higher injection level this process is balanced by Auger recombination which pulls the ideality factor value down toward 0.66 (which characterises Auger recombination). Due to the relatively low background doping of the *n*-type 1.7 Ω.cm substrate ($N_D = 2.8\times10^{15}$ cm^{-3}), this effect starts to dominate at a lower injection level than in the *p*-type 1 Ω.cm substrate.

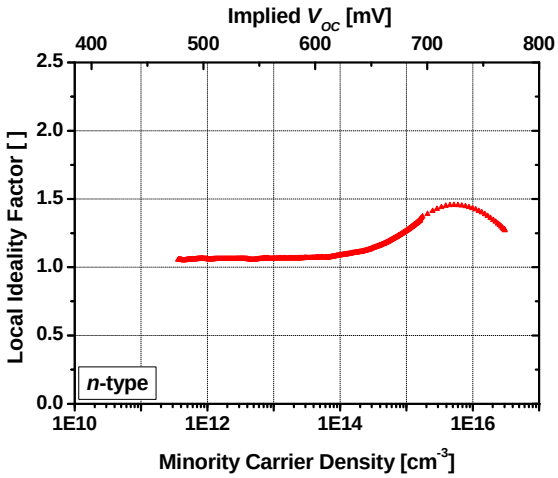

Figure 5-33: The extracted local ideality factor as a function of the injection level and the implied V_{oc} (upper scale) of a representative *n*-type sample.

5.5.5 Conclusions

For the first time, a comprehensive study regarding the influence of annealing in the range 600-820°C on the passivation quality was carried out, using different SiN_x films and different surfaces. Passivation enhancement was observed across the entire temperature range for all the samples. It seems that maximum improvement is obtained in the range 660-700°C. Similar to the findings of this study, Rohatgi *et al.* found an optimum SiN_x anneal temperature of 700°C for passivation of defects in edge-defined film-fed grown (EFG) Si [265]. Szlufcik *et al.* recognised an optimum in the range 650-700°C when annealing their passivation layer [263]. It is believed that hydrogen in atomic form diffuses to saturate dangling bonds at the Si-SiN_x interface, improving the surface passivation [236, 271]. It is possible that the poorer enhancement at lower annealing temperatures is raised from the limited amount of hydrogen released from the film due to lower thermal energy. The lower improvement at a higher temperature range can be due to a decrease in hydrogen retention at defect sites in the Si and at the Si-SiN_x interface [265] or by formation of molecular hydrogen which tends to effuse instead of diffusing toward the interface. This study

completes the gap in the literature regarding the influence of annealing temperature on the passivation.

It was shown that the bulk lifetime of CZ samples and not only the surface passivation improves during annealing. Effective lifetime above 350 μs exceeds the expected lifetime from a commercial grade CZ substrate. It is well known that hydrogenation that occurs during annealing enhances the electrical performance of mc-Si [229, 263-264]. However, the influence of this process on the electrical parameters of CZ substrates has not been reported up to date.

It was shown that Si-rich films provide better passivation before and after annealing. No correlation was observed between film thickness and as-deposited passivation quality. However, a clear correlation was found post-annealing, where thicker films demonstrate higher implied V_{oc}.

High quality as-deposited and post-annealing passivation was achieved, as indicated by the low values of S_{eff}. These values are comparable to the record low SRV on a 1 Ω.cm *p*-type substrate [248].

5.6 The Influence of Second Annealing (at 400°C)

Metal contacts must be formed in order to extract power from the solar cell. Electroless and photo-plating metallisation are the preferred methods to create metal contacts in double sided solar cells. Both techniques require nickel sintering, typically performed at 350-400°C. In order to evaluate the suitability of the SiN_x passivation to future fabrication processes, this section investigates the influence of the second anneal at 400°C on the obtained passivation.

Sample preparation

Representative CZ samples from previous experiments that had already undergone annealing at a range of temperatures (Figure 5-20) were re-annealed at 400°C using the belt furnace. All the furnace zones were set to 400°C while the belt speed was set to 4600 mm/s, leading to ~70 sec at peak temperature. The effective lifetime and the implied V_{oc} were measured before and after this process.

Results and Discussion

Table 5-15 presents the one-sun implied V_{oc} of representative samples before and after the second anneal. All of the samples demonstrate high thermal stability; most show a small improvement in implied V_{oc}. Subsequent anneals (at 400°C) show similar results.

Table 5-15: One-sun implied V_{oc} of representative samples after first and second annealing. The first anneal was done at different temperatures, while the second was done at 400°C.

	W6	W9	W10	W15	Average
After first anneal [mV]	660.5	668.2	681.0	668.5	662.0
After annealing at 400°C [mV]	668.1	672.4	683.6	667.1	665.3
Change [mV]	+ 7.6	+ 4.2	+ 2.6	- 1.3	+ 3.3

Similar conclusions can be obtained from Figure 5-34, which presents the effective lifetime as a function of the injection level of a sample annealed first at 700°C and then re-annealed at 400°C. As can be seen, the sample demonstrates good thermal stability under the given test conditions.

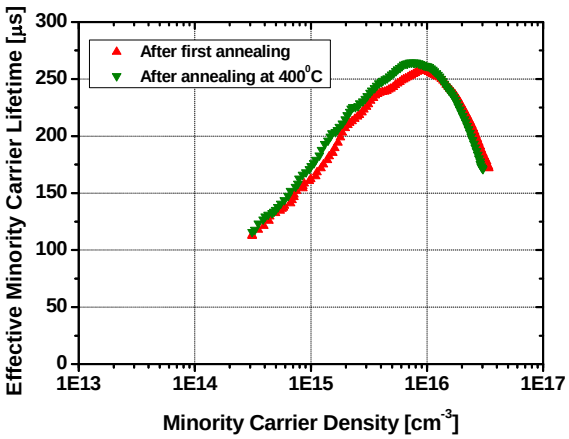

Figure 5-34: Effective lifetime as a function of injection level after first annealing and after annealing at 400°C.

Conclusions

All the tested SiN_x films demonstrate high thermal stability under a second anneal at 400°C. Thus it is concluded that these films will retain their passivation quality under similar nickel sintering conditions during the metallisation process.

5.7 Optical Properties

Up to this point the focus was given to the electrical parameters of various SiN_x films, however the optical parameters of the film have important influence on the solar cell performance as well. Furthermore, these parameters influence some of the fabrication processes, such as laser doping. In this section the optical parameters of the different layers are investigated.

5.7.1 Influence of Annealing on the Optical Properties

In previous sections the dependence of the passivation quality on the annealing conditions was studied. However, the annealing process can influence the optical parameters of the dielectric layer as well. Variation of the SiN_x ARC properties is a main concern, as it can degrade the solar cell current. In this section the post anneal optical parameters are measured and compared to the as-deposited ones.

Sample preparation

Single-sided polished wafers were employed in this part of the study. After a full cleaning procedure, SiN_x layer was deposited onto the front surface, using the laboratory PECVD system. Both the deposition time and the GR were varied in order to investigate a wide range of films. The optical parameters were measured using a dual-mode ellipsometer (at 632.8 nm) and spectrophotometer (Cary 500), before and after annealing at optimum temperature (680°C) using an open air belt furnace (see Table A12-1 for the zones setting).

Results and Discussion

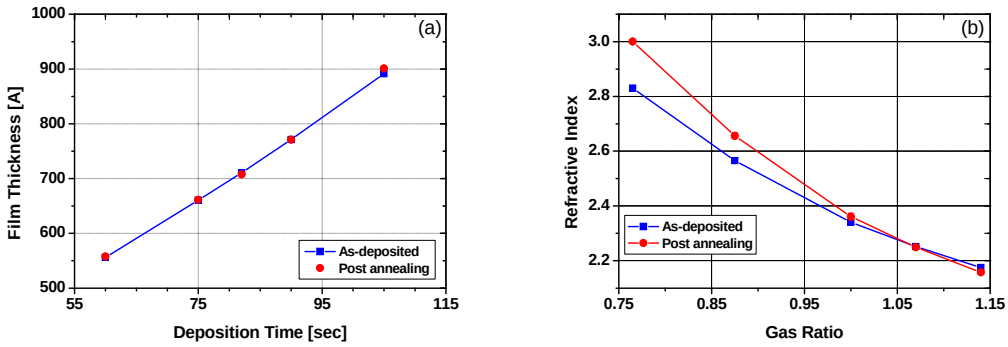

Figure 5-35: Film thickness as a function of the deposition time (a) and refractive index as a function of GR (b), before and after the annealing process. The solid lines are given as a guide to the eye.

The film thickness as a function of the deposition time, before and after the annealing process, is shown in Figure 5-35 (a). All the presented films were deposited using GR = 0.86, while the deposition time was varied. As previously, a linear dependence of the film thickness on the deposition time was found. Only negligible changes were observed when comparing the post annealed measurements to the as-deposited ones. Unchanged film thickness after deposition was also reported by Winderbaum *et al*. [325]. The GR dependence of the refractive index before and after annealing is presented in Figure 5-35 (b). The deposition duration of all the films was set to 90 sec, while the GR was varied. These results show a clear difference between Si-rich and N-rich films. While the refractive indices of the N-rich films stayed steady, the refractive indices of the Si-rich samples increased significantly. It was also

found that this increase is independent of the film thickness. A similar trend was observed by others [268, 272, 275]. Wright *et al*. noted this type of behaviour only for an annealing temperature above 750°C [326].

Figure 5-36 corroborates the variations in the refractive index observed above, presenting the reflection of representative films before and after annealing. While the post-annealing reflectance of the GR = 1.14 film is identical to the as-deposited one, a significant variation can be seen for the lower-GR films. It is assumed that densification of the Si-rich SiN_x film during annealing is the cause of this change [327]. During this process, Si-Si bonds replace Si-H and N-H bonds, increasing the film refractive index.

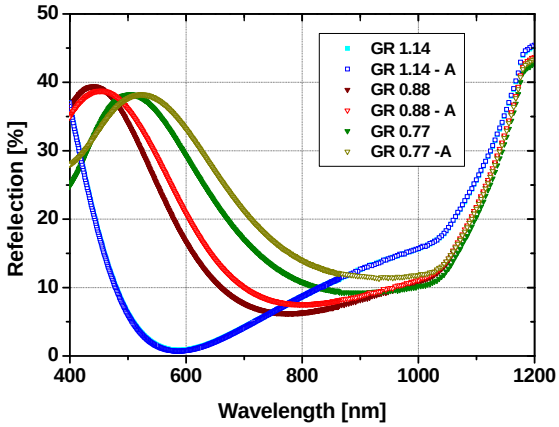

Figure 5-36: The wavelength-dependent reflectance of different GR films, before and after the annealing. Note that the measurements of GR = 1.14 are identical.

5.7.2 Transmission, Reflectance and Absorption

In order to analyse the optical losses of the film, the absorption coefficient needs to be calculated. In this section an optical model of the film, based on reflectance and transmission measurements, is developed in order to extract the extinction coefficient. The extinction coefficient is then used to calculate the absorption coefficient as a function of the wavelength.

Sample preparation

Two quartz pieces were Piranha and RCA cleaned before SiN_x deposition. Two GRs (GR = 1.14 and 0.77) were used to form N-rich and Si-rich films with layer thickness in the 95-100 nm range. A Cary 500 spectrophotometer was used for reflectance and transmission measurements. The WVASE32 software package from Woollam & Co. was employed to fit the measurements using the Tauc-Lorentz oscillator parameterisation, developed by Jellison and Modine [328]. From the fit, the wavelength dependence of the refractive index ($n_r(\lambda)$) and the extinction coefficient ($k(\lambda)$) were extracted to calculate the absorption coefficient.

The Tauc-Lorentz formalism combines Tauc's expression for the joint density of states with the Lorentz oscillator to determine the imaginary part (ε_2) of the dielectric function [328]:

5-2)
$$\varepsilon_2(E) = \begin{cases} \left[\dfrac{AE_0C(E-E_g)^2}{(E^2-E_0{}^2)^2 + C^2E^2} \dfrac{1}{E} \right] & E > E_g \\ 0 & E \le E_g \end{cases}$$

where A is the amplitude, E_0 is the peak transition energy, C is a broadening term and E_g is the optical band-gap. All or some of these parameters are used to fit the measured data. The real part (ε_1) of the dielectric function is calculated using Kramers-Kronig integration (for more details see Ref. [328]). Using these two parts, the wavelength dependence $n_r(\lambda)$ and $k(\lambda)$ can be calculated [329]:

5-3)
$$n_r = \left\{ \frac{1}{2} \left[(\varepsilon_1{}^2 + \varepsilon_2{}^2)^{1/2} + \varepsilon_1 \right] \right\}^{1/2}$$
$$k = \left\{ \frac{1}{2} \left[(\varepsilon_1{}^2 + \varepsilon_2{}^2)^{1/2} - \varepsilon_1 \right] \right\}^{1/2}$$

Table 5-16 summarises the Tauc-Lorentz parameters which were found to provide the best fit for the measured reflectance and transmission.

Table 5-16: Tauc-Lorentz parameters, which were found to provide the best fit for the measured data.

Parameter	GR = 1.14 [eV]	GR = 0.77 [eV]
A	134.05	162.31
E_0	7.37	5.56
C	18.83	16.98
E_g	**2.32**	**1.95**

Results and Discussion

Figure 5-37 presents the measured and the fitted reflectance and transmission of the two films. Good fit was obtained for the N-rich film; however, it was challenging to fit the measurements of the Si-rich film at long wavelength, possibly due to accuracy of the measurements in this range (limitation of the IR sensor).

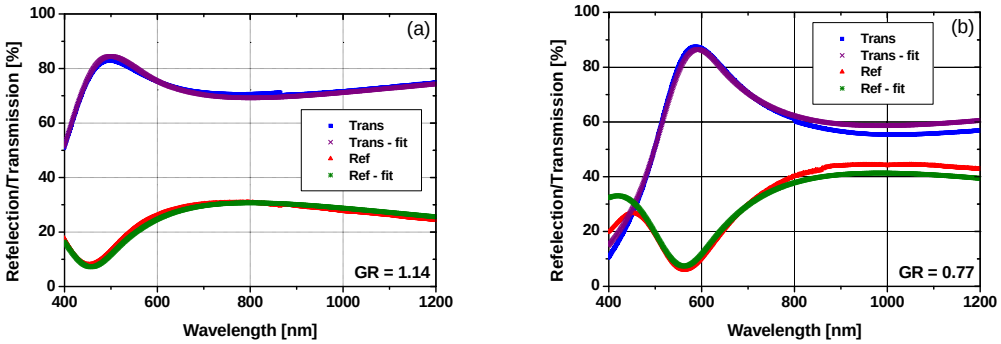

Figure 5-37: The measured and fitted reflection and transmission of films deposited with GR = 1.14 (a) and GR = 0.77 (b).

From the obtained fitting, the wavelength dependence of the refractive index and the extinction coefficient were extracted and are presented in Figure 5-38 (a). As expected from the lower optical band-gap (see Table 5-16), the extinction values of the Si-rich film, at short wavelengths are higher than the ones of the N-rich film. Higher k values for Si-rich films have been reported widely and are attributed to the increased number of Si-Si bonds [242, 253, 282, 326]. The absorption coefficient (α) was then calculated using the extracted $k(\lambda)$ and the well known expression [329]:

5-4)
$$\alpha = \frac{4\pi k(\lambda)}{\lambda}$$

where λ is the wavelength. The calculated values as a function of the wavelength are given in Figure 5-38 (b). The high absorption of the Si-rich film in the short wavelength range limits its use as a front surface passivation; however, it still can be employed as a rear surface passivation in non-bifacial solar cell structures.

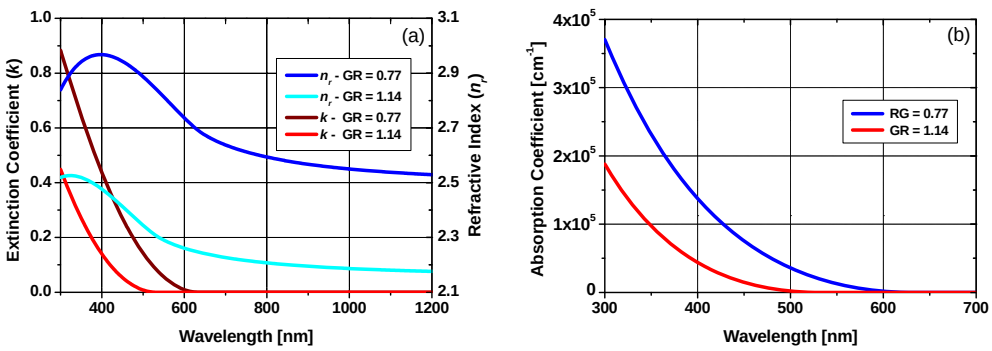

Figure 5-38: The calculated wavelength dependence extinction coefficient (k) and refractive index (n_r) of GR = 0.77 and GR = 1.14 films (a) and the calculated absorption coefficient of both the films as a function of the wavelength (b).

5.7.3 Conclusions

The influence of the annealing process on the optical parameters was investigated. Only negligible variation was observed in the refractive indices of N-rich films, while the variation in Si-rich films was significant. Therefore, it can be assumed that the optimum annealing condition will not degrade the optical parameters of the SiN_x ARC layer.

Optical models were developed for the two films and were used to calculate the absorption coefficient as a function of the wavelength. The obtained information will be used in following chapters to evaluate the optical losses of the SiN_x layers.

5.8 Etching Rate of SiN_x

In order to be suitable for the fabrication sequence of solar cells, the SiN_x passivation layer needs to withstand different types of wet chemical processes. This section investigates the etching rate of the SiN_x layers in different solutions commonly used during solar cell fabrication. Focus is given to aqueous HF solutions, as they are typically employed for surface preparation prior to the metallisation process (deglazing).

Sample preparation

Single-sided polished wafers were used to evaluate the etching rate. Following a full RCA clean and HF dip, different SiN_x layers were deposited onto the wafers. Four different etching solutions were used (see Table 5-17 for details). The etching time was varied in the range of 5-60 sec (at room temperature) and 5-10 min (at 55°C) for the HF and the NaOH solutions, respectively. The film index and thickness were measured by a dual-mode ellipsometer at 632.8 nm at 10 different locations, before and after the etching process. The etching rate was extracted from the linear fit to the etching graph (change of thickness vs etching time).

Table 5-17: Etching solutions mixture (DI H_2O = distilled water, RT = room temperature).

	DI H_2O	**HF (49%)**	
HF 1%	98 ml	2 ml	RT
HF 2.5%	95 ml	5 ml	RT
HF 5%	90 ml	10 ml	RT

	DI H_2O	**NaOH (50%)**	
NaOH 12.5%	75 ml	25 ml	55°C

Results and discussion

Figure 5-39 presents the measured thickness change as a function of the etching time of a representative sample (n_r = 2.1). The solid lines are a linear fit to the measured data. The etching rate was found to be relatively constant throughout the whole etching time. No change of the refractive index was observed. Similar graphs were found to describe the behaviour of the other films, although with different etching rate Table 5-18 summarises the calculated etching rate of different films in different solutions.

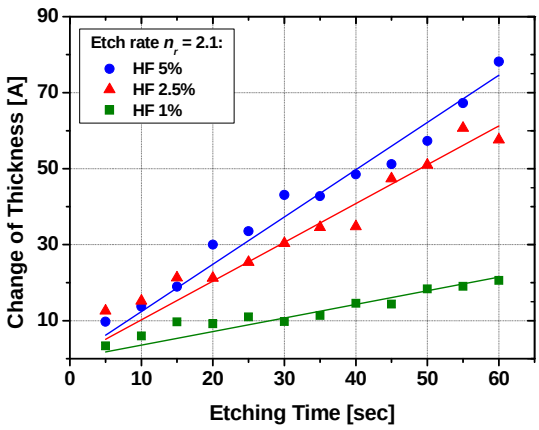

Figure 5-39: Change of film thickness as a function of the etching time. The solid lines are linear fits to the measured data.

As can be seen, Si-rich films demonstrate a slower etching rate in aqueous HF solutions, compared to N-rich films. This finding agrees well with published data [159, 238, 330]. Due to variation between PECVD systems, the deposition parameters and the etching solution concentration, a direct comparison between the etching rates calculated here and by others is not straightforward. However, it seems that the extracted values are comparable to the ones measured by Schmidt *et al*. [159] and by Lauinger *et al*. [238], one order of magnitude faster than those reported by Williams *et al*. [203, 330] and slower than those in Ref. [326].

The most striking result is the fast etching rate of Si-rich film in NaOH solution. In contrast to the etch rate in HF solutions, Si-rich film is etched more than one order of magnitude faster in NaOH solution than N-rich film. This measurement was repeated a number of times with similar results. No comparable data was found in the literature; the most related one examines the etching rate of SiN_x in KOH solution (30-33% by weight) at 80°C, published by Williams *et al*. [330-331]. However, they measured significantly slower etching rates.

Table 5-18: Etching rate of different solutions.

Gas Ratio	n_r	1% HF [Å/sec]	2.5% HF [Å/sec]	5% HF [Å/sec]	BHF [a] [Å/sec]	NaOH [Å/sec]
1.14	2.12	0.4	1.0	1.2	1.2	0.02
1.00	2.37	0.3	----	0.9	----	0.06
0.77	2.74	0.2	----	0.6	----	0.82

[a] 100% BOE (1:7) of J.T. Baker at room temperature (NH_4F: ~35%, HF: ~6.3%).

Conclusions

Etching rates of different films in a number of solutions were measured. It was shown that the etching rate of Si-rich film in HF solutions is very slow. This can produce a problem if the subsequent fabrication sequence is based on wet chemistry etching. However, it does not limit solar cell structures which are based on laser opening of the dielectric film. Surprisingly, it was found that the etching rate of Si-rich film in NaOH solution is very fast, more than one order of magnitude faster than the etching rate in HF solutions.

5.9 Chapter Summary

The use of SiN_x as rear passivation of a low resistivity *p*-type substrate was investigated in this chapter. By comparing SiN_x, SiO_2 and SiO_2/SiN_x stack layers it was shown that SiN_x provides superior passivation before and after annealing.

The dependence of the obtained passivation on the SiN_x film parameters was studied using a variety of films. It was found that Si-rich layers provide lower S_{eff} values than N-rich films before and after annealing. In as-deposited samples, no influence of the film thickness on the one-sun implied V_{oc} was observed, but a strong correlation was found post-annealing.

A comprehensive study regarding the influence of the annealing temperature on the obtained passivation was carried out. This study completes an existing gap in the published literature. Significant improvement was observed across the entire temperature range for different films and surfaces. Interestingly, an optimum annealing temperature was identified in the 680-700°C range, which falls within the range not previously studied. The enhancement of the effective lifetime is attributed to improvement of the surface passivation, probably due to reduction of the surface state density by hydrogen passivation. However, it is assumed that variation of the surface charge density and electron/hole capture cross section occurs simultaneously. It was shown that when CZ substrates are annealed, a significant bulk lifetime enhancement occurs as well. Using an optimum annealing condition the implied V_{oc} of CZ substrates increased remarkably to a value comparable to that of FZ wafers.

A very low S_{eff} values were calculated both in one-sun and MPP operating conditions. The local ideality factor was extracted and was used to predict the influence of this dependence on the solar cell *FF*. It was shown that the injection level dependence of the S_{eff} can reduce the theoretical optimum *FF* by 3%. This value is similar to the one calculated for PERL solar cells. Hence, the investigated passivation scheme is suitable for high efficiency solar cell structures.

The suitability of the SiN_x passivation layers for laser-doped solar cell fabrication sequences was examined and was found to be highly suitable. In addition to having good passivation properties SiN_x films also demonstrated excellent tolerance to all processing conditions. Good thermal stability was shown under nickel sintering conditions. No influence of annealing on the optical parameters of the ARC layer was observed. Slow etch rates in aqueous HF solutions ensure no degradation during the deglazing process, prior to the metallisation. However, care needs to be taken when a NaOH-based solution is used.

Chapter 6 : Laser-Induced Defects in Laser Doped Solar Cells

Laser doping offers a promising method to define selective emitters for solar cells. Its main advantage is the localised nature of the laser beam, which allows melting of the surface area without heating the bulk. The ability to perform this process with a dielectric film on the surface offers further benefits, such as the possibility of creating self-aligned metallisation patterns simultaneously with the selective emitter formation. In this method, which has been developed at UNSW by Wenham and Green [127], the dopant source is applied onto the dielectric film. A laser beam scans over the areas where metallisation will be applied locally melts the silicon, removes the dielectric film and induces diffusion of dopants in the liquid phase. In this way, a selective emitter and self-aligned metallisation pattern are formed simultaneously. This method was employed in this thesis to fabricate a laser-doped (LD) solar cell. However, laser-induced defects, contaminations and discontinuities in the LD junctions degrade the solar cell performance. The study presented in this chapter investigates laser-induced defects associated with this laser doping approach. Focus is given to the influence of different dielectric films on defect formation.

As a starting point, the implied V_{oc} values achieved with different dielectric films are compared. A variety of characterisation methods are then employed to obtain insights into the nature of these defects. Crystal orientation is studied using electron backscattering diffraction (EBSD) [332], while the formation of defects is investigated using Yang defect etch [333] and transmission electron microscopy (TEM). The quality of the formed junction is examined using electron beam induced current (EBIC) [334]. Contaminants such as oxygen and nitrogen in the molten areas are determined using secondary ion mass spectrometry (SIMS). Following these investigations, laser-doped solar cells with standard SiN_x and a double SiO_2/SiN_x stack layer ARC are fabricated on commercial grade *p*-type CZ substrates. Their electrical parameters are compared and analysed. At the end of the chapter a novel method is introduced to minimise laser-induced defects by modification of the laser pulse in order to reduce the cooling rate of the Si post melting.

6.1 Literature Review

In order to form a theoretical base, the chapter begins with a short literature review of laser operational principles, interaction between laser light and Si, defects in Si and laser-induced defects.

6.1.1 Laser Operational Principles

A laser (light amplification by stimulated emission of radiation) oscillator is a combination of two basic components: an optical amplifier and an optical resonator (see Figure 6-1). The optical amplifier includes a light source, such as lamp or diode, and a laser crystal made of a semiconductor material (laser rod). The optical resonator (laser cavity), consisting of two opposing parallel mirrors perpendicular to the axis of the crystal, acts as a selective feedback element by coupling some of the photons emitted from the amplifying medium back into the medium in phase with the amplified light [335].

Illumination of the crystal by the light source leads to a large number of electrons being excited to higher energy levels (inversion). Continued illumination increases the number of excited electrons until the number of generated electrons is balanced by their elimination via spontaneous recombination, predominantly by radiative recombination (emission of photons). If the spontaneously-emitted photon travels in line with the crystal axis, it will be reflected back into the crystal by the optical resonator. By passing through the crystal this photon can trigger the recombination of excited electrons, i.e., it can induce *stimulated* emission. The newly-emitted photon is identical to the incident photon in terms of wavelength, direction, phase and polarisation. This process is the basis of lasing action, which can be initiated if the feedback is sufficiently large to compensate for the internal losses of the system [335]. The amount of feedback is mainly determined by the reflectivity of the aperture-end mirror, which must be partially transparent in order to allow the laser beam to escape. The laser oscillator continues to increase the photon flux as long as the gain remains above unity, where the gain is determined primarily by the number of excited electrons and the rate of stimulated emission. In steady state, the emission rate of new photons from the crystal is balanced by the optical losses within the oscillator; in this case the gain is unity. This mode of laser operation is known as continuous wave (CW).

The density of electrons in the excited level at steady state is often called the *threshold* density, which is determined by the power of the light source, the losses in the optical resonator and the properties of the laser crystal. Change in one of these parameters leads to the oscillation of the system until a new steady state is achieved with a new threshold density. For example, increasing the light source power increases the number of excited electrons (gain > 1), however this leads to

enhancement of the stimulated recombination which reduces the number of the excited electrons. Reducing the number of excited electrons decreases the recombination rate; hence the density of electrons in higher energy levels increases again. This process continues until a new steady state is reached (with unity gain).

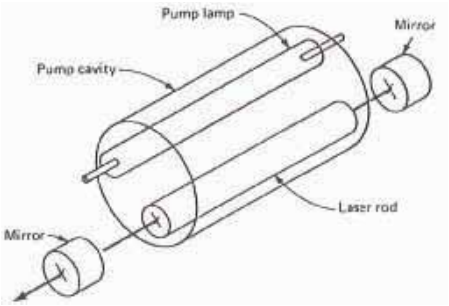

Figure 6-1: Major components of an optically pumped solid-state laser [335].

Q-switching is a mode of laser operation often used to generate high laser pulse power. The quality factor - Q - is defined as the ratio of the energy stored in the cavity to the energy losses per cycle. In this mode, the Q-factor of the optical resonator is altered in order to generate a light pulse: energy is stored in the laser crystal by optical pumping while the Q-factor is lowered to prevent laser emission. Under this condition the density of excited electrons in higher energy states reaches a level far above the threshold density of CW operation. This level is known as *population inversion*. The excited electron density is now limited by the excited electron lifetime, which is a specific property of the laser crystal. When a high Q-factor is restored, the stored energy is released rapidly in the form of a very short light pulse, due to the high gain created by this energy. The pulse peak power is several orders of magnitude higher than the power under CW condition [335]. Figure 6-2 provides a schematic of the Q-switched laser oscillator.

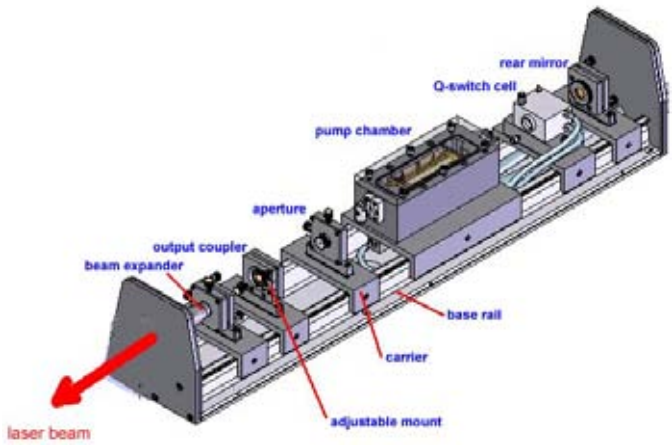

Figure 6-2: Q-switched laser oscillator [336].

Figure 6-3 presents the resonator losses, population inversion and the photon flux as a function of time. When the resonator losses are high, due to low a Q-factor,

the lasing action is disabled. Under this condition, the density of excited electrons increases until population inversion is achieved. Lowering the resonator losses at this point (switching to high Q-factor), enables stimulated emission to occur. The photon flux grows exponentially and a Q-switched laser pulse is emitted. Note that the pulse is emitted after appreciable delay due to the required time for the stimulated emission to build up from spontaneous recombination. Note also that the excited electron density at the end of the pulse is well below the threshold level. Hence, a successive pulse can be emitted only after a significant time, in which the excited electron density returns to a value well above the threshold level. This can be a severe limitation for the laser doping process due to the short melting period of the Si, as will be discussed in the following sections.

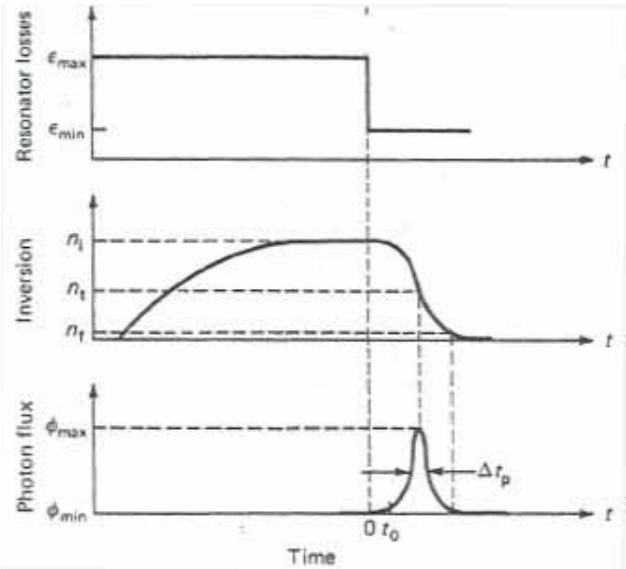

Figure 6-3: Resonator losses, population inversion and photon flux as a function of time [335].

6.1.2 Interaction between Laser Light and Silicon

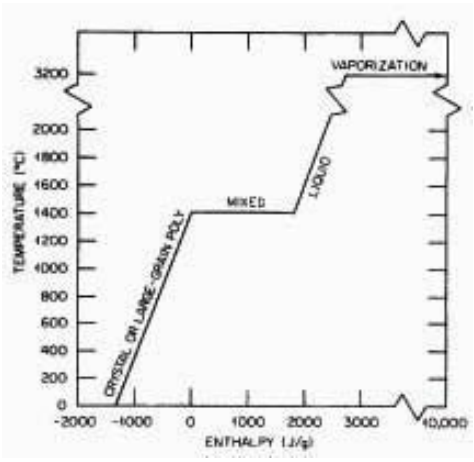

Figure 6-4: The state diagram of Si. The zero enthalpy point is taken to be the melting point [337]

For photons with energy above that of the silicon band gap, laser radiation incident on the surface of a Si wafer is absorbed by the excitation of electrons within

the crystalline lattice. As these electrons interact with the lattice, the temperature near the excitation region rises rapidly up to the Si melting point (1414°C). Further heating increases the enthalpy until the latent heat of fusion is reached and the Si undergoes a phase change from solid to liquid [338]. The temperature continues to rise, though not as rapidly as in the solid phase, until the boiling point is reached. Once the latent heat of vaporisation is exceeded, Si starts to be removed. Figure 6-4 displays a temperature-enthalpy diagram of this process. The post-melting slower heating rate is explained by the enhanced surface reflectance and the large absorption coefficient of liquid Si. The latter results in an absorption depth of only ~0.01 μm (see Table 6-2). The deeper regions are therefore no longer directly heated by absorbing incident radiation, but instead by thermal conduction from areas near the surface. This and the high thermal conductivity of liquid Si slows down the temperature increase [339]. When the thermal loss by conduction exceeds the energy gained by the laser irradiation, the temperature falls until the freezing point is reached, when the latent heat needs to be removed prior to solidification. While the *front melt* (the position of the liquid-solid interface) sweeps back, the Si epitaxially recrystallises [340]. The quality of the recrystallised area is strongly influenced by the front melt velocity, as will be discussed in the next sections.

Figure 6-5 presents the front melt position as a function of time for a variety of laser energies. Higher laser energy increases the melting duration and the melting depth, although it takes a similar time to reach this depth. Hence, the front melt penetration speed *into* the wafer increases with increasing laser energy. On the contrary, due to the much longer melting duration, the front melt velocity *outside* the wafer is slower for increased laser energies.

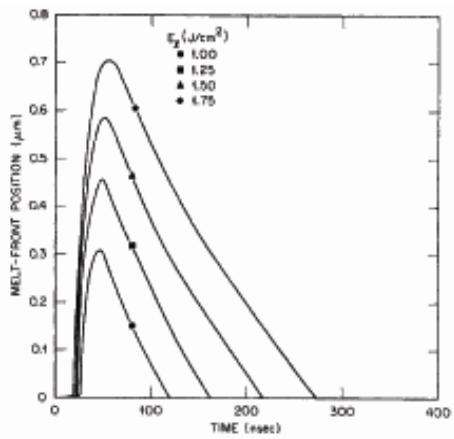

Figure 6-5: Front melt position as a function of the time for variety of laser energies [341].

If a dopant source is available during the melting duration, a diffusion of dopants in the liquid phase occurs. The shape of the resulting doping profile depends on the dopant parameters (mainly diffusion and segregation coefficients) and the melting duration. This will be discussed in detail in the next chapter.

The presence of dielectric films (SiO_2 or SiN_x) on the surface modifies some aspects of the process. Firstly, the amount of laser energy absorbed by the Si increases due to reduced surface reflection (see Figure 6-6), which exceeds the relatively low absorption loss within the film (maximum 14% for 75 nm Si-rich SiN_x layer; see Table 6-2). Secondly, although the film is heated by thermal conduction, a temperature gradient is still expected, which results from the low thermal conductivity of Si at higher temperature. Due to the lower melting point of Si compared to both types of dielectric films (see Table 6-1), it is expected that parts of the film will be mechanically lifted off by pressure from the substrate. This process, together with the stress resulting from different thermal expansion coefficients, creates crystallographic defects. These laser-induced defects are the focus of this chapter.

Table 6-1: Silicon, SiO_2 and SiN_x properties.

	Silicon	**Ref.**	**SiO_2**	**Ref.**	**Si_3N_4**	**Ref.**
Melting Point [K]	1687	[342]	~1970	[154]	~2150	[343]
Boiling Point [K]	3540	[344]	----	----	----	----

	Silicon Solid	**Ref.**	**Silicon Liquid**	**Ref.**	**SiO_2 Solid**	**Ref.**	**Si_3N_4 Solid**	**Ref.**
Density [g cm^{-3}]	2.33	[154]	2.56	[342]	2.27	[154]	3.1	[154]
Thermal Conductivity [W cm^{-1} K^{-1}]	1.56 0.22 [a]	[342]	1.10	[344]	0.014	[154]	0.3	[345]
Specific Heat [J g^{-1} K^{-1}]	0.713 1.032 [a]	[342]	0.89	[342]	1.0	[154]	----	----
Thermal Expansion Coefficient [$\times 10^6$ K^{-1}]	2.616 4.661 [a]	[342]	----	----	0.5	[154]	3.9 6.8 [b]	[346]

Properties are at room temperature if not stated differently.

[a] At melting point.

[b] At 1000K.

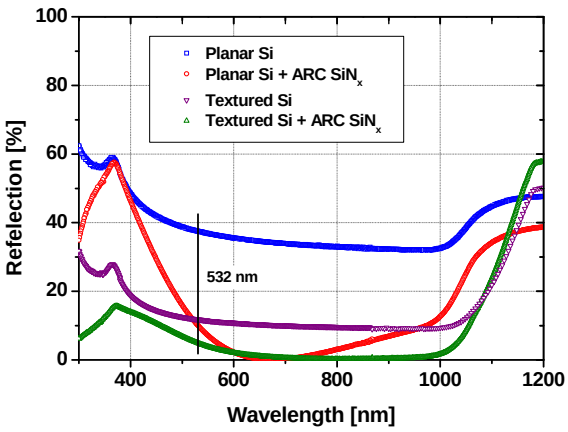

Figure 6-6: Measured reflection as a function of the wavelength of Si with different surface treatments. SiN_x properties: n_r = ~2.05, d = ~82 nm.

The melting depth is strongly related to the absorption depth of the laser energy. Figure 6-7 (b) presents the absorption depth and absorption coefficient of Si as a function of the wavelength. Short wavelength lasers create shallow melting, while longer wavelengths penetrate farther into the Si and so create deeper melts. Furthermore, it was shown that for incident photon energy close to the Si band-gap, smalls variations in the laser illumination lead to significant differences in the surface temperature, due to the temperature dependence of the absorption coefficient (see below). Modelling of this so-called thermal runaway behaviour using 10% variation in the laser energy predicts a difference of almost 2000°C in the surface temperature for long wavelengths, while only 100°C is predicted for short wavelengths [347].

Two laser wavelengths were available for this work: 1064 nm and 532 nm. The 532 nm was preferred due to the shallow absorption depth (1-2 µm at 532 nm) and the lack of thermal runaway effect.

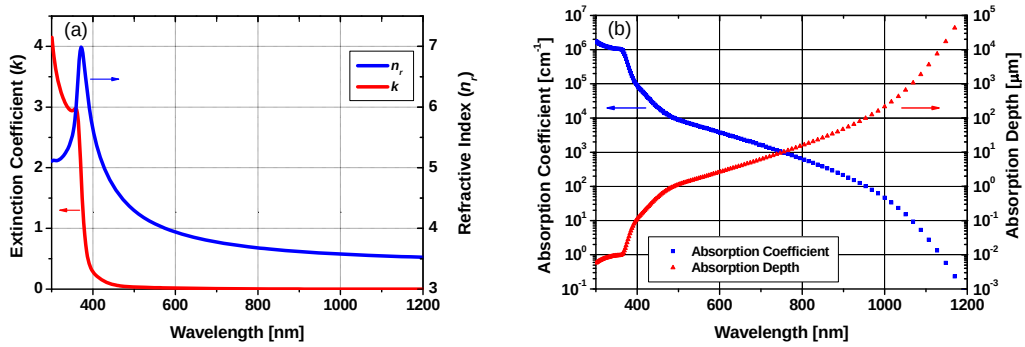

Figure 6-7: Optical parameters of Si as a function of the wavelength (obtained from Ref. [342]).

As mentioned before, the optical properties depend not only on the wavelength but also on the temperature. Both the reflectance and the absorption coefficient increase with increasing temperatures. The temperature dependence (at 532 nm) of the absorption coefficient can be expressed by [348]:

6-1) $$\alpha(T) = 5.02 \times 10^3 \exp(\frac{T(K)}{430})$$

The dependence of the reflection (R) on the temperature, at the same wavelength, was found to be [349]:

6-2) $$R(T) = 0.356 + 5 \times 10^{-5} T(K)$$

In the transition from solid to liquid, the values of these parameters are further increased. Table 6-2 summarises key optical parameters of Si and SiN_x at room temperature (RT) and in liquid phase (both at 532 nm). The SiN_x data was obtained from Figure 5-38.

Table 6-2: Optical properties of Si and SiN_x at 532 nm. The properties of Si are given at room temperature (RT) and in liquid phase. The properties of SiN_x were obtained from Figure 5-38.

	Silicon RT	**Ref.**	**Silicon Liquid**	**Ref.**	**SiN_x GR 1.14**	**SiN_x GR 0.77**
Refractive Index	4.13	[342]	3.11	[342]	2.31	2.84
Absorption coefficient [cm^{-1}]	6550 10085	[342] [348]	1.19×10^6	[342]	5.1	1.95×10^4
Reflectance [%]	37	[350]	70	[349]	----	----

6.1.3 Defects in Silicon

Defects in Si can be classified into four main categories: point, line, area and volume defects [351-352]. Although the classification is based on the spatial dimension of the defect, it is also related to their electrical activity due to the strong correlation between physical imperfections and recombination activity of the defect [353]. This section provides a brief review regarding defects in Si. More information can be found in Ref. [352-353].

The point defect category includes a wide range of defects, including dopant impurity atoms and vacancies. Such defects introduce lattice strain among the neighbouring lattice sites. The amount of strain is determined by the size and the concentration of the defects [353]. Line defects are introduced in the form of dislocations. The two main types of line defects in the Si lattice - *edge* and *screw* dislocations - are illustrated in Figure 6-8. Edge dislocation results from inserting or removing partial planes of the lattice, while screw dislocation results from a fault in the atom stacking, which joins the upper plane with a lower one [353]. *Misfit* dislocations are generated by growing a material with lattice constant '*a*' on top of a substrate with lattice constant '*b*'. Area defects include mainly defects at the crystal surface and grain boundaries. The latter type of defect is classified according to the level of misorentation and size. If the lattice atoms on one side of the grain boundary create a mirror image of the ones on the other side, a twin boundary is formed. The simplest form of twin boundary is a *stacking fault*, where no dangling bonds are formed along the boundary. Volume defects comprise *precipitates* and *inclusions*, which are clusters of defects or impurities in the Si lattice. These defects act as nucleation sites for other defects, such as point defects [353].

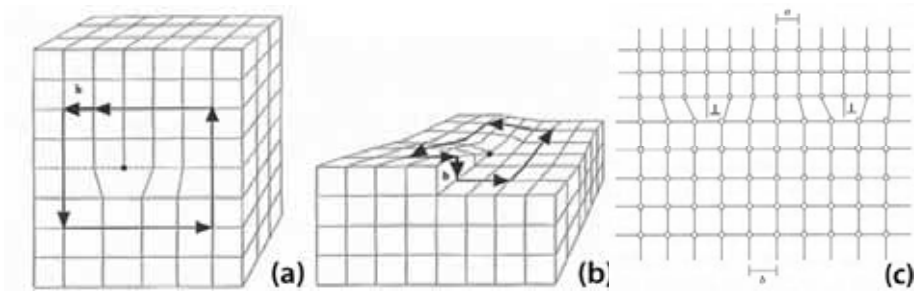

Figure 6-8: Edge dislocation (a), screw dislocation (b) and misfit (c) [353].

Both crystal growth and device fabrication generate defects. For example, incorporation of interstitial oxygen (O_i) into the wafer during its growth (mainly when the CZ growth method is employed) generates bulk defects, which degrade the solar cell performance [353]. High temperature processes are the main source of defects during solar cell fabrication. In addition to possible contamination, high temperature processes introduce thermo-mechanical stresses within the wafer. When the stress exceeds the elastic limit of the wafer, plastic deformation takes place via dislocation generation [353]. Although only a very localised region of the wafer is heated by laser irradiation, the large thermal gradient between the irradiated area and its surroundings generates stress that results in the formation of defects [354]. Furthermore, as mentioned before, the laser doping process involves recrystallisation of the molten Si; similar to crystal growth, this process can generate defects. The next section reviews laser-induced defects as the basis for the study presented in this chapter.

6.1.4 Classification of Laser-Induced Defects

Laser-induced defects were identified as a performance-limiting factor when the laser was used for the first time to form a semiconductor *p-n* junction more than 40 years ago. In their pioneering work, Fairfield and Schwuttke focused laser radiation onto a polished silicon surface which was coated with phosphorus to create a junction [87]. Although the junction performance was comparable to that of a conventional diode, they identified laser-induced defects as a possible degradation source. Attention was then turned to the use of laser annealing, especially for ion-implanted silicon. In this process the laser removes crystallographic defects by melting the surface layer and allowing it to epitaxially resolidify. The quality of the recrystallised layer and the influence of crystal defects on the electrical characteristics of the semiconductor were widely investigated by several research groups [88, 97, 355-356].

In their research, Mooney *et al*. used deep level transient spectroscopy (DLTS) and found defects up to 10 μm into the material, with high defect concentration near the surface when using a Q-switched ruby laser [355]. They indicated that defect formation occurs up to the photon absorption depth and concluded that heat conduction is not an important damage mechanism. However, these defects were not observed by TEM. Narayan *et al*. used the same type of laser and did not observe any defects (neither precipitates nor dislocations) in the recrystallised zone [97]. Similar results were also reported by Young *et al*. [88, 356]: no defects either in the form of clusters, dislocations or stacking faults were observed in the TEM images. Young *et al*. concluded that a defect-free epitaxial layer was grown from the melt, with the same crystallographic orientation as the bulk wafer. They later found that while a defect-free recrystallised layer could be grown on a (100) substrate, a high density of stacking faults was observed on a (111) substrate. They speculated that the formation

of stacking faults results from a single mistake in the stacking of atoms during the crystal growth [357]. Defect-free recrystallised zones were also achieved using different types of lasers [103, 105]. Recently, Hopman *et al*. observed near-surface dislocation when using high laser power [131]. These dislocations were not found when low laser power was employed.

Despite the fact that no defects were found in TEM images, some researchers observed degradation of the electrical performance of the molten areas [89-90, 358]. It is widely believed that electrically-active point defects are the source of the degradation. This assumption is also supported by depth profile measurements utilising DLTS [355, 358-359] and by Hall mobility measurements [35].

It has been shown that the recrystallisation velocity is a critical parameter in the formation of electrically-active point defects [360]. Rapid cooling was found to create such defects, which severely limit the carrier lifetime in the recrystallised area [31-32]. In solar cells these point defects lower the minority carrier lifetime and hence the open circuit voltage [90, 361-362]. The critical recrystallisation velocity was determined to be 1-1.5 m/sec; velocities above this value produce high levels of defects [98, 363]. The importance of the regrowth velocity was demonstrated by Young *et al*., who suggested substrate heating during the annealing as a method to slow the regrowth velocity and thereby improve the quality of the regrowth layer. They attributed the improvement to a reduction in the point defect density [89-90]. Tong *et al*. used double crystal X-ray diffractometry (DCD) to demonstrate the same effects [364]. An interesting finding was that the bulk lifetime decreases at laser power levels below those which produce any visible surface damage [361, 365]. It was concluded that there are two critical laser power thresholds for Q-switched lasers: one for production of bulk defects and a higher one corresponding to visible changes in the surface morphology [366].

The role of contaminants in the recrystallised area was also investigated. These contaminants are more likely to penetrate into the material during the melting period and are influenced by the process environment and the doping source. High levels of oxygen in the melt area were measured by some research groups [367-369]. Hoh *et al*. measured oxygen levels of 10^{18}-10^{21} cm^{-3} [368]. Such high concentrations can create micro-defects and influence the electrical performance of the device [370]. If a spin-on dopant (SOD) is used as the dopant source, its purity level also has an impact on the device performance [367, 371].

As mentioned above, another source of degradation is thermally-induced stress. Arora and Dawar concluded that thermally-induced stress and the generation of long-lived traps are the most probable causes for laser damage in silicon. They formulated an equation to calculate the surface damage threshold energy and they found that this energy is influenced mainly by the pulse duration and the number of laser pulses that are incident on an area [372]. Thermally-induced stress was also

found to create cracks at the surface [68] and to generate defects in the surrounding regions [354]. It has also been shown that the presence of a dielectric film on the surface of silicon solar cells can reduce their V_{oc} and FF [128, 373]. In this case, thermally-induced stress is enhanced due to the different thermal expansion coefficients of the film and the silicon.

6.1.5 Conclusions

The basics of laser operation were reviewed. The fast decay time of the Q-switched pulse was identified as a possible limitation when this laser is employed for laser doping due to the fast cooling rate of the Si after melting. A laser wavelength of 532 nm was found to be more suitable for laser doping applications than 1064 nm, due to shallower absorption depth and the avoidance of thermal runaway effect.

Defects in the Si lattice in general and laser-induced defects in particular were reviewed. Most studies indicate that following the melting, the Si is recrystallised by epitaxial regrowth without noticeable crystal defects, although some studies indicated near-surface defects. However, electrical post-treatment degradation was observed by a large number of researchers. This degradation is explained by contamination - primarily high oxygen content - and by the formation of electrically-active point defects. The recrystallisation velocity was recognised to have a significant influence on these defects. A critical velocity value of 1-1.5 m/s was identified, above which the formation of point defects is enhanced. Thermal stresses are another source of defects, especially when the surface is covered with a dielectric film.

In the following section the recrystallisation velocity under typical conditions is estimated using a heat transfer simulation. A comprehensive study is then presented regarding laser-induced defects in the presence of a dielectric film.

6.2 Laser System and Front Melt Velocity

As mentioned before the recrystallisation velocity significantly influences the quality of the regrown Si. After reviewing the laser system which employed for this study, a heat transfer simulation is performed in order to estimate this velocity.

6.2.1 Laser System

A diode-pumped, Q-switched, frequency-doubled Nd:YVO_4 laser (λ=532 nm) with a Gaussian beam was used in this work.

Figure 6-9 displays oscilloscope images of a variety of laser pulses produced by this system. Identical scales were used for both of the images, where the x-axis has unit of time (ns) and the y-axis has an arbitrary unit of laser power. Image (a) presents the influence of the laser diode current on the pulse energy (constant Q-switch

frequency), while image (b) shows the dependence of the laser power on the Q-switch frequency (constant laser diode current). Increasing laser diode current and decreasing Q-switch frequency both result in increased pulse power. However, increasing laser diode current also increases the duration of the pulse, while varying the Q-switch frequency has no effect on pulse duration. During the pulse, the laser crystal is still illuminated by the diode, therefore electrons are still excited to higher energy levels. Hence, variation in the diode current influences not only the energy stored in the laser crystal prior the pulse, but also the crystal energy during the pulse. Due to the change in the density of excited electrons during the pulse, the pulse decay time is modified. In contrast, variation of the Q-switch frequency influences only the initial laser crystal energy. Since the diode current is constant, the density of excited electrons does not vary during the pulse.

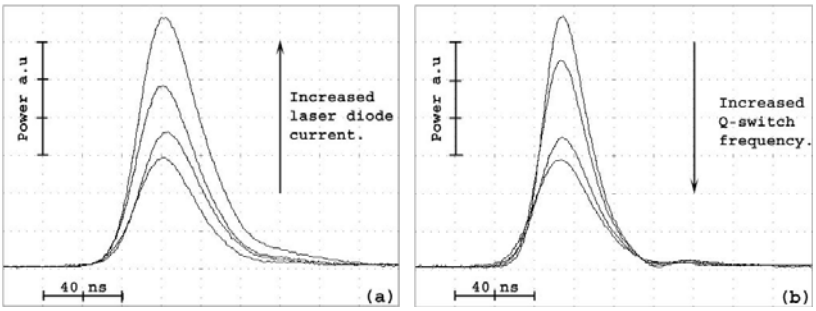

Figure 6-9: Oscilloscope images of laser pulses using different diode current at 100 kHz (a) and using different Q-switch frequency at diode current of 28.0 A (b).

As both have a similar influence, if the scan speed is adjusted to form a similar overlap between pulses, in this work the Q-switch frequency was set to 100 kHz and the pulse energy was varied by adjusting the laser diode current. The pulse full width at half maximum (FWHM) was measured and found to be in the 35-45 ns range (see Figure 6-9 (a)).

Table 6-3 provides the laser parameters used in this thesis. If not stated otherwise, the laser diode current is the only parameter to be varied. Note that due to system limitations the laser diode current - not the pulse energy density - is used to indicate laser energy (see more in Appendix 8).

Table 6-3: Laser setting used in this thesis.

Parameter	Value
Wavelength [nm]	532
Q-switch frequency [kHz]	100
Scanning Speed [mm/s]	10

6.2.2 Front Melt Speed

The recrystallisation velocity is a critical parameter in the formation of electrically-active point defects. In order to estimate the front melt speed in this laser system, a transient 3D simulation of laser-induced melting was performed. This simulation, which has been developed by Fell, is based on a mathematical model which solves the heat transfer equation using MATLAB [338, 374-375]. The simulated parameters are provided in Table A14-1.

Figure 6-10 presents the simulation results. Image (a) shows the spatial temperature distribution on the (*X*-*Z*) plane, while image (b) provides the phase diagram of the same plane. Both images were taken at time corresponding to maximum melting penetration. The point x = 100 μm represents the centre of the pulse. A maximum melting depth of 1.2 μm and line width of 15 μm is predicted by the simulation under this laser condition. This is in good agreement with SIMS measurements presented in the following sections. Note the large temperature gradient on the surface, where the temperature drops from ~1500°C to ~200°C within a distance of less than 5 μm. As mentioned before, such large temperature gradients are believed likely to generate defects within the Si.

Image (c) displays the melt front position as a function of the time, together with the normalised laser intensity. The shown "staircase" profile is not physical; it is due to the spatial discretisation and the special time integration method used in the simulation. The shape of this graph is similar to those published previously [340-341] and to the one presented in Figure 6-5.

Using this image, the recrystallisation velocity was calculated and found to be ~2.4 m/s [376]. By changing the pulse power, this value was found to vary in the 2.1-2.6 m/s range. This range of values is above the limit velocity of 1.5 m/s. Hence, it can be assumed that point defects are generated during the recrystallisation of the Si. Image (d) presents the surface temperature in the centre of the pulse as a function of time. A peak temperature exceeding 3000°C is predicted under this condition. Note that the maximum melting time is approximately 0.6 μs.

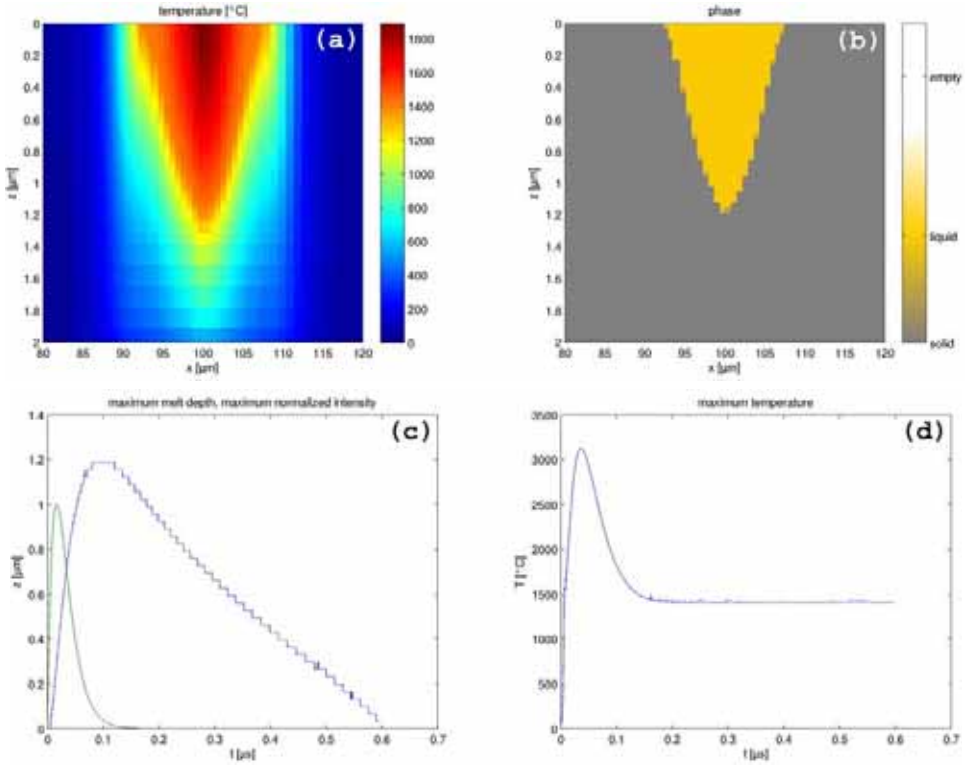

Figure 6-10: Heat transfer simulation of representative pulse: (a) spatial temperature distribution (at maximum melting depth), (b) spatial phase diagram, (c) front melt position as a function of the pulse duration and (d) surface temperature as a function of pulse duration.

Figure 6-11 shows the maximum temperature as a function of time for a full pulse cycle (10 µs). Although the cooling rate of the sample varies according to the method by which the wafer is mounted to the stage and to the stage material, it can be assumed that the wafer surface returns to room temperature before the beginning of the next pulse.

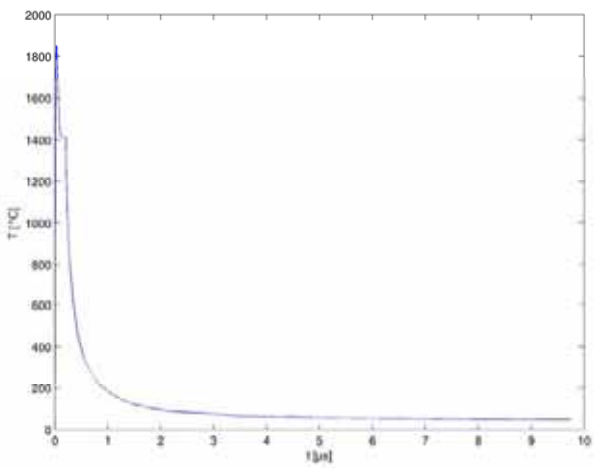

Figure 6-11: Surface temperature as a function of time (beginning of the pulse at $t = 0$ sec).

6.2.3 Conclusions

Using the heat transfer simulation, it was found that the recrystallisation velocity is above the limit value of 1.5 m/s. Hence, the formation of point defects is assumed to occur during the laser doping process. At the end of this chapter, a novel method is presented to reduce this velocity.

6.3 Laser-Induced Defects

As reviewed in previous sections it was found that laser-induced defects and contaminations degrade the solar cell electrical parameters. This section investigates the formation of laser-induced defects and the impact of different dielectric films on it. A variety of characterisation methods are employed to obtain insights into the nature of these defects.

6.3.1 Implied V_{oc} and Effective Lifetime

As a starting point, the implied V_{oc} values are compared for different dielectric films, after laser treatment.

Sample preparation

For the first experiment, 18 *p*-type FZ wafers with resistivity of 1 Ω.cm were used. The thickness of the wafers after saw damage etch was 240-250 μm. After a full RCA clean and HF dip, a thin dry oxide (~18 nm) was grown in a conventional tube furnace, followed by 15 min annealing in nitrogen environment at 1000˚C. The wafers were then split into three groups:

1) SiO_2/SiN_x group (SON): an ARC SiN_x layer (n_r = 2.1, thickness (d) = 75 nm) was deposited onto the front surface immediately after the oxidation (using the laboratory PECVD system, see Table 5-1 for deposition parameters).
2) SiN_x group (SiN): the oxide was removed using an HF dip before depositing a SiN_x layer.
3) Bare wafers: the oxide was removed using an HF dip.

All wafers were oxidised at the same time to eliminate the possibility of variations in the effective lifetime due to degradation associated with the high temperature process.

The same laser doping process was applied for all the groups. Phosphorous SOD (P512 from Filmtronics) was spun onto the front surface, followed by baking in an oven at 120˚C in an air ambient to dry out the solvents and any moisture in the film. Five different laser powers covering a wide range of melting profiles, from a

very shallow melt zone to ablation (see Figure 6-12), were used to form the laser-doped (LD) pattern. The pattern consisted of 28 mm-long LD lines; the spacing between the lines was chosen to be identical to the width of the LD line. It is important to note that the width of the LD line is influenced by the laser energy and by the surface coating. For each wafer, the width of the LD lines was measured using a microscope and their spacing was determined accordingly. At the end of the process, the LD area on each wafer was 28 mm × 28 mm, with 50% of the area covered by LD lines. We chose to separate the lines to avoid any possible influence of one LD line on the other. After any change in the settings of the laser, the system was allowed to stabilise for 20 min before processing the wafers. One sample from each wafer group was processed sequentially at each laser energy.

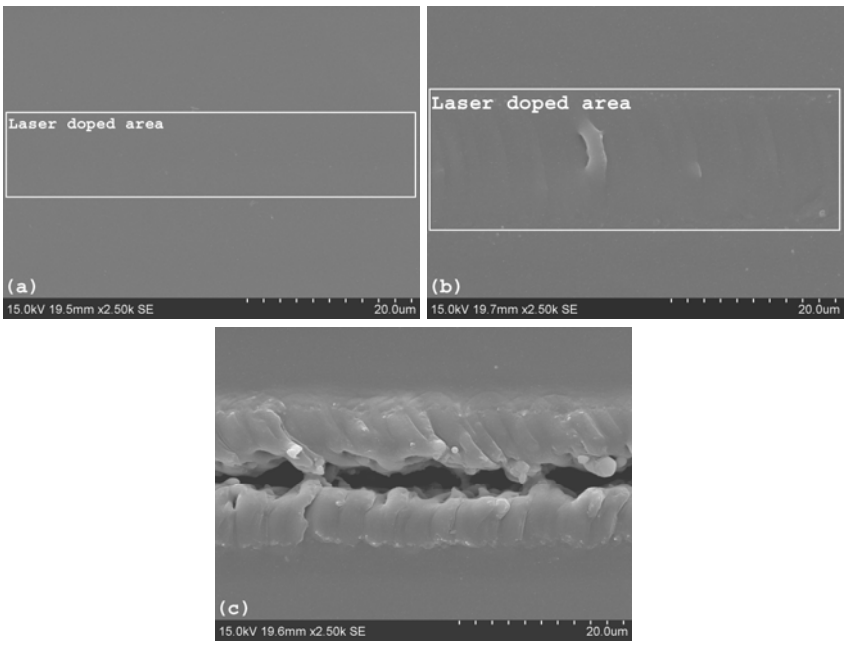

Figure 6-12: SEM images of laser-doped lines from the bare wafer group processed at different laser diode currents (a) 28.0 A - virtually no melting observed, (b) 28.6 A and (c) 29.4 A – ablation.

At the end of the laser doping process, the dielectric films were removed from the surfaces using hot phosphoric acid. The wafers were then RCA cleaned and after a short dip in an HF solution, SiN_x was deposited onto both sides of all the wafers. The SiN_x deposition parameters were chosen so as to provide a high surface passivation quality (GR = 0.77, see Chapter 5). One wafer from each group did not undergo the laser doping process and was used as a reference. The complete process is outlined in Figure 6-13.

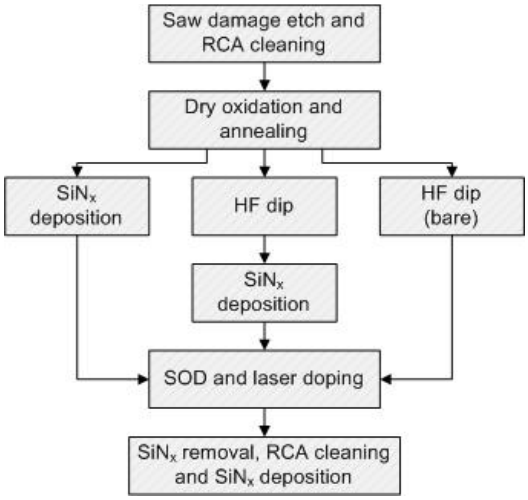

Figure 6-13: Process flowchart diagram.

Results

Photoconductance in the generalised mode using a Sinton Consulting bridge (model WCT-100) was employed to obtain the effective minority carrier lifetime (τ_{eff}) and the implied V_{oc}. Note that the reported implied V_{oc} values were recorded at an intensity equivalent to one sun. Both PL imaging and a Semilab system (WD-2000) were used for effective lifetime mapping. To minimise any possible influences due to the different optical properties of the surface resulting from different laser energies, such as the reflection and absorption of incident light on the LD areas, all the measurements were carried out using rear surface illumination.

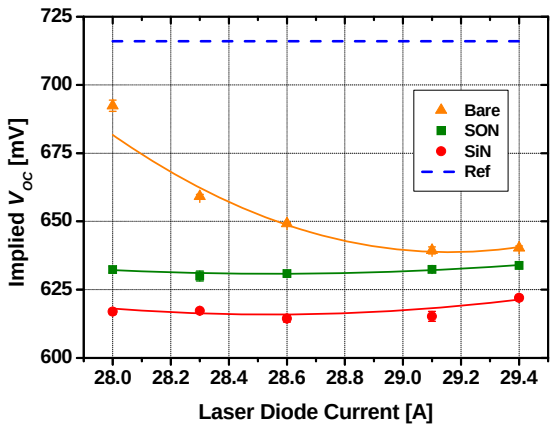

Figure 6-14: One-sun implied V_{oc} as a function of the laser diode current. The average implied V_{oc} of the reference group is presented (dashed line). The error bars represent the standard deviation of five samples. Solid lines are given only as guide to the eyes.

Figure 6-14 presents the one-sun implied V_{oc} as a function of the laser diode current for the three groups of samples and the average value of the reference group. Significant drops in implied V_{oc} can be observed for all groups, although the groups that had dielectric layers demonstrate a much more pronounced degradation in

comparison to the reference samples. Two points are worth noting. First, the implied V_{oc} of the SON group is higher than those of the SiN group for all laser diode currents. Second, the implied V_{oc} of these two groups remains reasonably constant for the entire range of diode currents, while it decreases with increasing diode current for the bare wafers.

The observed difference in behaviour between the groups can clearly be seen in the effective lifetime mapping. Figure 6-15 shows PL imaging and Semilab effective lifetime scans of two wafers from the bare and the SON groups, displaying the effects of the two laser diode current extremes. The acquisition time for PL imaging was increased to obtain better resolution of the LD zones. For that reason, the surrounding areas appear saturated. The corresponding Semilab image of each wafer is presented below the PL image of the same wafer.

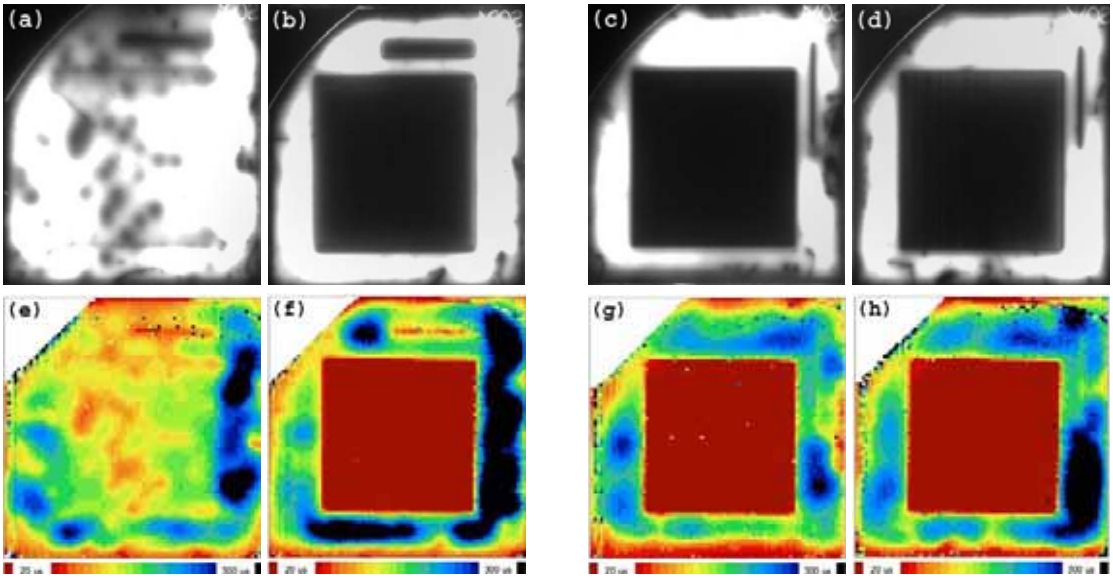

Figure 6-15: PL imaging (a-d) and Semilab effective lifetime scans (e-h) of wafers from the bare wafers group (left) and from the SON group (right). The lowest laser diode current was used for images (a, e) and (c, g), while the highest diode current was used in images (b, f) and (d, h).

As mentioned before, the bright areas in the PL images indicate high PL signal, which corresponds to high excess minority carrier concentration and, thus, high minority carrier effective lifetime [192]. As evident by the trends in implied V_{oc} in Figure 6-14, Figure 6-15 (a) and (b) visually show significant degradation in the effective lifetime with increasing laser diode current for the bare wafer group. On the contrary, virtually no change in the PL signal was observed for the SON group, indicating no or little change in the effective lifetime of this wafer group as a result of the LD process. The Semilab images gave similar results leading to the same conclusion.

6.3.2 Electron Backscattering Diffraction

Electron backscattering diffraction (EBSD) – also known as electron backscatter Kikuchi diffraction (BKD) – is used in this section to analyse the crystal orientation of the recrystallised areas.

The Kikuchi pattern is a characteristic of the local crystal structure and orientation (on the scale of the electron probe size). When the electron probe scans the sample, a Kikuchi pattern of each scanned point is formed and indicates the local orientation of the grown region. In the EBSD system, these Kikuchi patterns are formed on a phosphor screen mounted in the SEM when a stationary parallel beam of electrons is focused on the bulk sample whose surface is tilted at about 70˚ with respect to the primary electron beam. This results in an enhanced backscattering signal from a submicron area of the sample [332].

An EBSD system (EDAX-TSL5.2) installed on a JEOL 7001F SEM was employed for this study. A 15 keV electron beam was used to scan all the samples at working distance (WD) of 15 mm.

Sample preparation

A *p*-type, FZ (100) wafer with resistivity of 1 Ω.cm was used for this part of the study. After a saw damage etch and full RCA clean, a thin (~18 nm) dry oxide was thermally grown in a conventional open tube furnace, followed by 15 min annealing at 1000˚C in nitrogen. An ARC SiN_x (n_r = 2.1, d = 75 nm) was then deposited onto the front surface. After applying SOD onto the SiN_x film, laser doping was performed using seven different laser diode currents. Three closely-spaced LD lines were formed at each laser condition on the same wafer. Subsequently, the SOD was removed by a short dip in HF solution prior to a clean in Piranha etch [304]. A rear contact was formed by evaporating Al on the back surface and sintering it for 30 min at 850˚C in nitrogen. Cross-sections of the LD line received mechanical polishing to obtain the smooth surface required for EBSD scans. Initially, an EBIC scan was performed for the cross-sections of each line to determine the junction position since the junction depth represents the melt depth under this laser processing condition. EBSD measurements were subsequently taken to resolve the crystal orientations.

Results

Figure 6-16 presents the cross-sectional scans of a representative laser-doped line produced by a high laser diode current. The intention was to increase the melting depth so that the recrystallised area became more noticeable. However, such a high current also resulted in undesirable ablation of the silicon. Figure 6-16 (a) depicts a secondary electron (SE) micrograph superimposed with an EBIC image. The prominent white Gaussian-shaped line is the EBIC signal which indicates the location of the *p-n* junction. In the later section on EBIC more details are presented. One side

of the junction, above the EBIC line, is the unmelted *p*-type silicon substrate; the other side of the line is the melted and recrystallised area. Diffusion of dopants in the liquid phase is known to take place during the melting period in which phosphorous atoms from the SOD diffuse into the molten region, creating *n*-type silicon [377] (see next chapter as well). Figure 6-16 (b) displays the SEM image obtained by the EBSD system. Due to different sample orientation in the different SEM systems, Figure 6-16 (a) and (b) show the same area but at different angles. As a result, comparison between the images is not always straightforward. The equivalent area in (b) is approximately indicated by the red rectangular box in (a). Image (c) shows the result of an EBSD scan, analysed using the zone axis orientation mode, where each colour represents a different orientation. The green colour represents, in this case, the (011) plane (see the attached angular scale). A scanning step of 50 nm was used. It is clear that the melted silicon re-grows epitaxially during cooling according to the orientation of the substrate. No change of orientation can be detected between the two sides of the junction. The different colours at the edges of image (c) correspond to the laser groove and the edge of the wafer. A high level of noise due to shading of the detector by the topography of the specimen dominates the signal. Figure 6-16 (d) is a combination of images (b) and (c), while image (e) is the pole diagram of the scanned area. The perfect orientation of the scanned area can also be seen in this diagram. Only the six {110} planes can be observed; other planes were not detected. Similar results were obtained for the other samples.

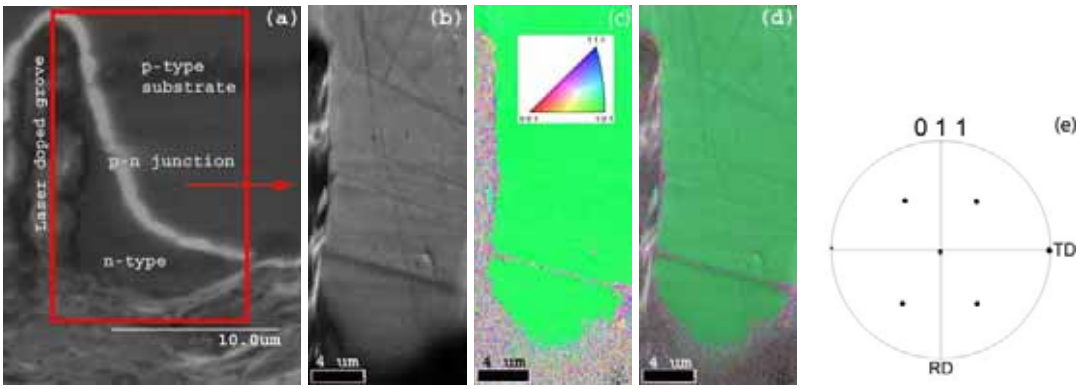

Figure 6-16: Cross sectional EBSD scans for diode current of 29.1A. (a) SE superimposed with EBIC image; (b) SEM image using the EBSD system; (c) EBSD scan; (d) SEM superimposed with EBSD scan; and (e) poles diagram of the EBSD scan. Note the different angles at which the images were taken.

6.3.3 Transmission Electron Microscopy

In this section, TEM analysis of laser-doped samples is presented, which was undertaken in order to achieve high-resolution examination of defect formation.

Sample preparation

Certain samples were selected from the SON and bare wafer groups (see above) for TEM observation. Cross-sectional specimens were fabricated using focused ion beam (FIB) milling and an ex-situ liftout procedure [378]. In order to protect the top surface from possible damage during the milling process, all samples were coated with platinum (Pt) using the gas chemistry system interfaced with the FIB instrument. Electron diffraction patterns were obtained from an electron beam parallel to the <110> zone axis (of the cubic silicon crystal), {200} planes and {111} planes (see Figure 6-17 (a) and (b)). Under each diffraction condition, bright and dark field images were taken.

Results

Figure 6-17 (b) presents the diffraction pattern of an electron beam parallel to the {111} planes. This diffraction condition was found to give the best contrast between the bright and the dark field images, hence the best identification of defects. In this image the label "BF" indicates the principal beam used for the bright field image, while "DF" labels the reflection used for the dark field one. Figure 6-17 (c) and (d) provides the bright and dark field images, taken under this diffraction condition. Comparison between the images reveals no defects either in the form of dislocations or stacking faults in most of the molten area, though some defects can be observed in the vicinity of the surface, up to a depth of ~60 nm. No significant difference was observed between the samples.

Figure 6-17: Electron diffraction of the <110> zone axis (a) and the {111} planes (b). Bright field (c) and dark field (d) images which were taken under {111} planes diffraction condition.

Figure 6-18 shows a low-magnification bright field image of laser-doped area taken under {111} planes diffraction condition. Similar to Figure 6-17, it is clear that most of the recrystallised region is defect-free.

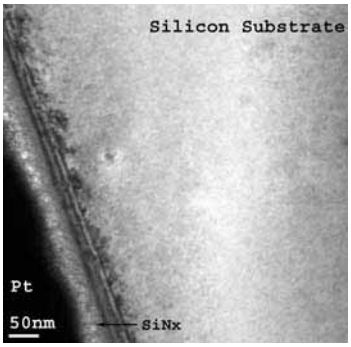

Figure 6-18: Bright field image taken under {111} planes diffraction condition.

6.3.4 Defect Etch

In this part of the work, a Yang etch was used to delineate the defects. This etch, which is based on a mixture of CrO_3, H_2O and HF, can delineate a wide variety of crystal defects on different surface orientations [333].

Sample preparation

Both planar and textured wafers with different coatings were used. The influence of the SOD was tested for several cases as well. Table 6-4 summarises the difference between the samples. Seven different laser diode currents were again used to form different melt profiles. At each current, three lines were scribed on each wafer. After removing the coating films using an HF dip, the wafers were cut in half. One half from each wafer received the Yang etch, while the other half was not etched for comparison purposes.

Table 6-4: Summary of different samples which were defect etched.

Wafer ID	Surface	Coating Film	Using SOD
BP	Planar	Bare	No
SP	Planar	Bare	Yes
SNP	Planar	SiN_x	No
SOP	Planar	SiO_2/SiN_x	No
BT	Textured	Bare	No
ST	Textured	Bare	Yes
SNT	Textured	SiN_x	No
SOT	Textured	SiO_2/SiN_x	No
SSOT	Textured	SiO_2/SiN_x	Yes

Results

As seen in Figure 6-19, direct comparison can be made for selected planar samples with and without Yang etching. The SEM images on the left show the edge of the lines after laser doping, while those on the right depict the same lines but after Yang etch. The etch delineated some crystal defects, especially in the interface

between the melted and unmelted areas. Evidently, crystal defects were exposed in all planar samples for the entire range of diode currents. Figure 6-19 (a) and (b) shows a LD line of sample BP formed by the highest diode current. Similar behaviour can be seen in Figure 6-19 (c) and (d) for the lowest diode current, on the same sample. While it is hard to even notice the laser melted regions prior to etching in image (c), they became very clear after etching (image (d)). This change indicates that some crystal defects were created, even at the lowest diode current. The influence of the dielectric film on the defect density was found to be critical. Figure 6-19 (e) shows the case where SiN_x was present when the laser process was performed (sample SNP). In this case defects can be observed even without any etch. The etch exposes defects of significantly higher density compared to sample BT, which had no dielectric film.

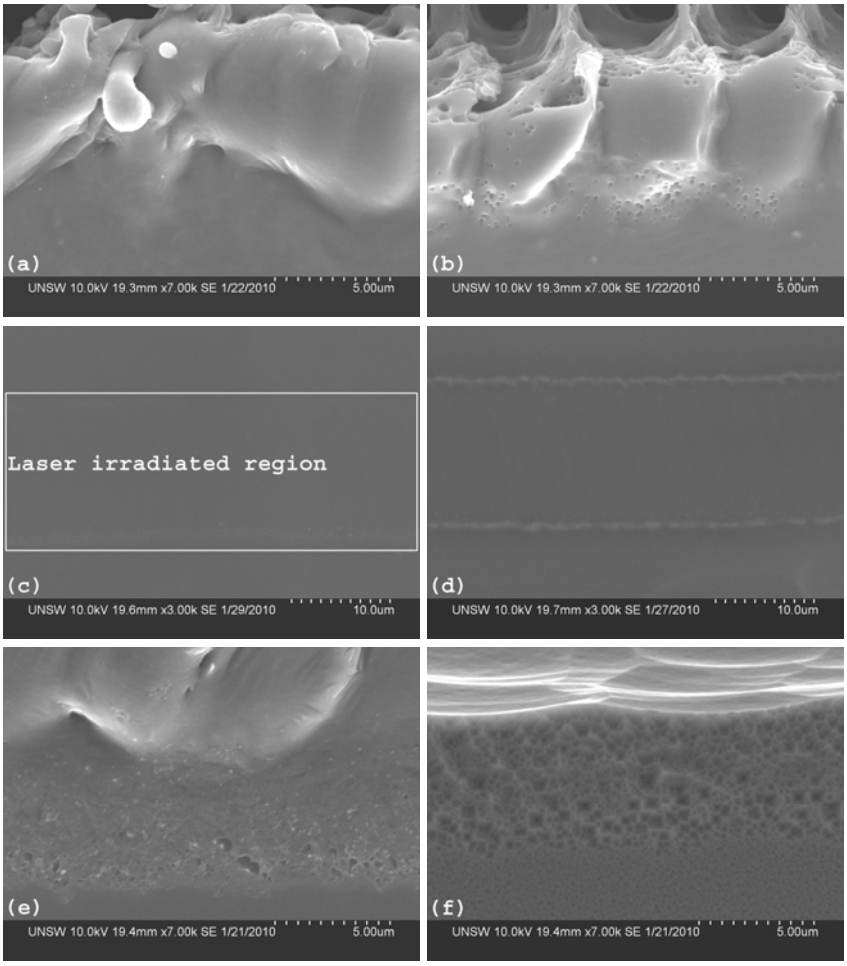

Figure 6-19: Planar view of laser lines on sample BP (a-d) and sample SNP (e-f). High laser diode current was used to create the lines of the top and bottom images, while low current was used for the middle ones.

Figure 6-20 presents SEM images of different textured samples after Yang etching. The higher laser diode current was used to form the LD lines of these images. Figure 6-20 (a) shows a bare textured wafer (sample BT) in which no crystal defects can be seen. Yet when a dielectric layer was deposited on the surface, defects are obvious as shown in images (b) and (c). The density of these defects seems dependent

on the type of dielectric film. It is lower for SiO_2/SiN_x (image (b)) than for SiN_x alone (image (c)).

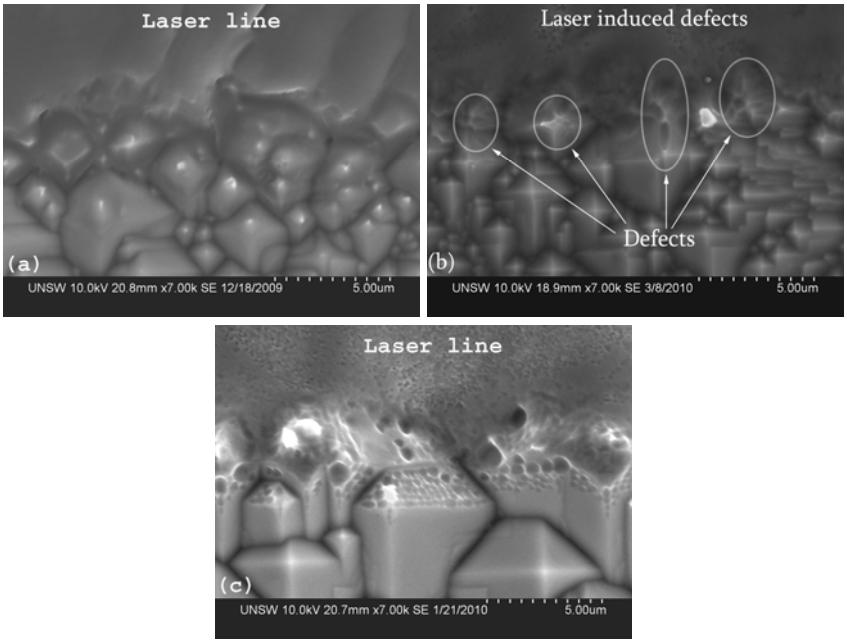

Figure 6-20: Planar view of laser lines on textured samples: (a) BT, (b) SOT and (c) SNT. For all the images the higher laser diode current was used to create the lines.

Figure 6-21 shows SEM images of the SNT and SNP samples after Yang etch. Different laser diode currents were employed to from the LD lines. It can be seen that the laser diode current does not have a significant influence on the defect density.

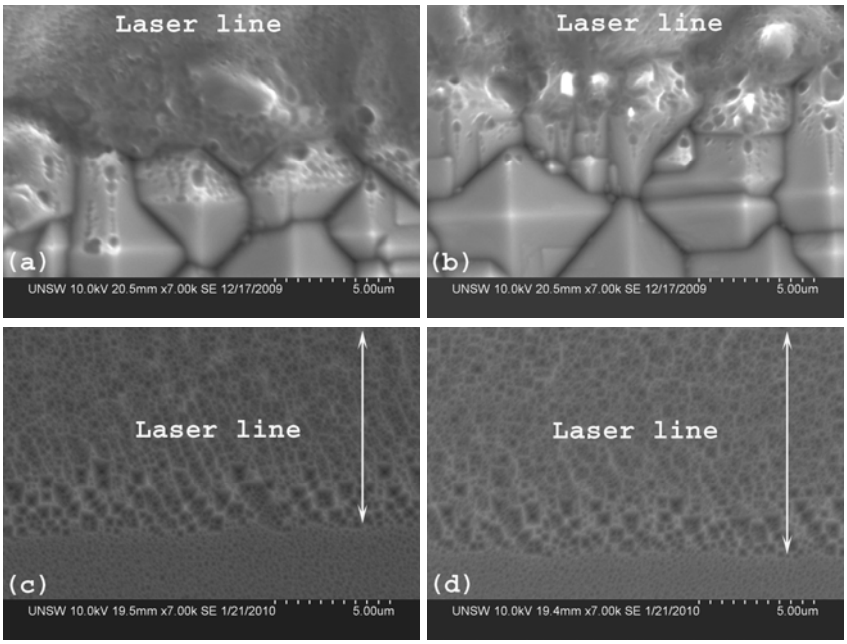

Figure 6-21: Planar view of laser-doped line: (a) SNT (29.1 A), (b) SNT (28.3 A), (c) SNP (29.1 A) and (d) SNP (28.3 A).

It was also found that the presence of SOD does not influence defect formation. Samples with and without SOD have a similar appearance.

6.3.5 Secondary Ion Mass Spectrometry

Secondary ion mass spectrometry (SIMS) [379] was used to detect the level of oxygen and nitrogen in the laser-doped areas. A SIMS system with resolution capability of 10 µm was employed to perform the measurements and therefore was able to detect the atomic concentration in a single LD line.

Sample preparation

Laser-doped samples were prepared in the same manner as previously described in the EBSD section, excluding the deposition and sintering of the rear aluminium contact. The SOD was removed by a short dip in HF solution prior to SIMS measurement.

Results

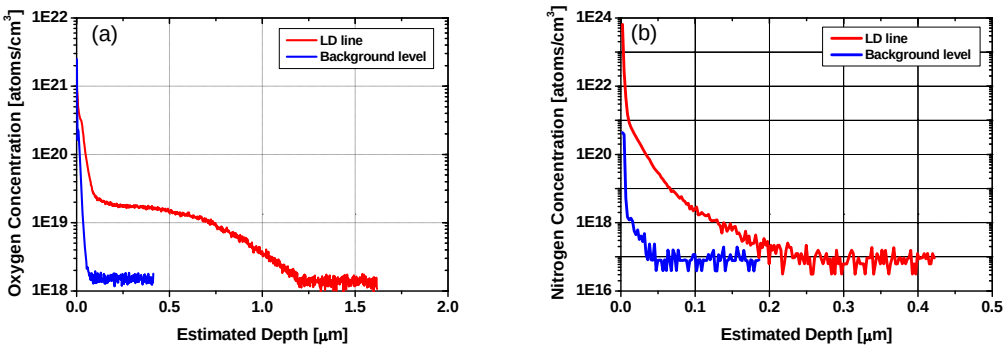

Figure 6-22: Oxygen (a) and nitrogen (b) concentration levels in LD lines as detected by SIMS. The blue line represents the background levels in the wafer while the red line shows significantly higher oxygen/nitrogen level in the LD lines.

Figure 6-22 shows SIMS measurements for the LD line with medium laser diode current. The detected oxygen level in the LD line (Figure 6-22 – (a)) is one order of magnitude higher than the background level. It is assumed that the concentration level of 2×10^{19} atoms/cm^3 is fairly constant up to the junction location (~1.25 µm, with good agreement to the heat transfer simulation - Figure 6-10). The observed decrease in concentration for depths greater than 0.5 µm is due to the Gaussian shape of the laser beam and the resolution limitation of the SIMS measurement system. At depths greater than 0.5 µm below the surface, the width of the LD lines is smaller than 10 µm (see Figure 6-10 (b)); therefore, the SIMS system begins detecting signal from the adjacent silicon substrate that was not melted, thereby reducing the average detected concentration.

High nitrogen concentration was detected up to a depth of 0.2 µm, with extremely high levels in the first 0.1 µm (Figure 6-22 – (b)). This high surface concentration is probably due to the very low segregation coefficient of nitrogen in silicon [342], although it could partly arise from remnants of the SiN_x film. Such a

high concentration of nitrogen has the potential to modify the silicon properties at the surface, for instance the silicon conductivity. This could degrade subsequent metal plating onto this region and prevent formation of an ohmic contact.

6.3.6 Depth of the Defected Area

It was found in the past that laser-induced defects can be significantly deeper than the melting depth. This formation of defects was often explained by thermal stress [353]. In this section the depth of the laser-degraded region is studied.

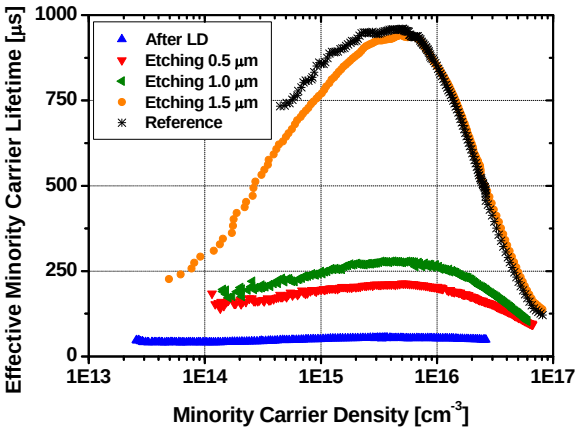

Figure 6-23: Effective lifetime as a function of injection level for a single laser-doped sample after the laser doping process and after etching 0.5, 1 and 1.5 µm from both surfaces.

In order to investigate the depth of laser-degraded regions, the SiN_x was removed from one sample from the bare wafer group (Section 6.3.1). Approximately 0.5 µm of Si was then etched away using NaOH solution (12.5%, 55°C). After a full RCA clean, both surfaces were re-passivated using Si-rich SiN_x (GR = 0.77). A separate FZ *p*-type wafer was used to evaluate the passivation quality. At the end of the process, the effective lifetime and implied V_{oc} were measured using the QSS-PC system (generalised analysis). The etching process was repeated twice, each time removing 0.5 µm, so a total of 1.5 µm was removed from both surfaces.

Figure 6-23 presents the effective lifetime as a function of the injection level after the laser doping process and after etching 0.5, 1 and 1.5 µm from each surface. Also shown is the effective lifetime of the reference sample. It seems that etching 1.5 µm from the surface completely removes the defected region, as indicated by the similarity of the effective lifetime in this case to that of the reference sample. This depth is similar to the melting depth found by SIMS measurements (see Figure 6-22).

Figure 6-24 provides visual evidence of the findings of Figure 6-23. The figure presents PL images of the wafer after each etching step. No evidence of the laser defects can be observed after etching 1.5 µm (see Figure 6-24 (d)). It seems that the laser-induced defects in the case of laser doping are limited to the melting depth.

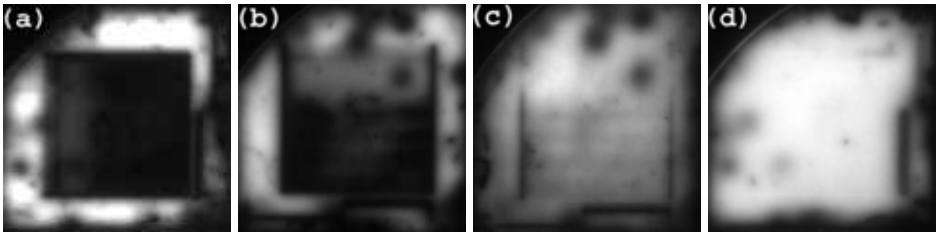

Figure 6-24: PL imaging of the same sample after the laser doping process (a) and after etching 0.5, 1 and 1.5 μm ((b) to (d)). The same exposure time and scale were used for all images.

6.3.7 Electron Beam Induced Current

Electron beam induced current (EBIC) has been used extensively to investigate a wide range of semiconductor materials and their properties [380]. The main advantage of the EBIC method is its high sensitivity in the junction regions, which makes it a powerful investigation tool for imaging the junction and for measuring different minority carrier parameters and semiconductor surface properties [381-382]. In this technique, the material is bombarded with an electron beam. The beam electrons ("primary" electrons) enter the sample and collide with atoms. Two types of collisions occur: elastic and inelastic. In elastic collisions, the primary electrons do not lose energy and are only scattered to different directions. In the second type of collision, the primary electrons give up some energy which can generate electron-hole pairs. The volume in which these electron-hole pairs are generated is often called the *interaction volume* or *generation volume* and is a function of the beam energy. These electron-hole pairs usually diffuse in the sample to areas of low carrier concentration. However, if an electric field exists in the sample, such as that of a *p-n* junction, the minority carriers generated within the junction region will drift across it and be collected. By connecting this junction to an external circuit these collected carriers flow as an electrical current which can be measured as the EBIC signal [383]. More information regarding EBIC can be found in Ref. [334].

In this part of the study, EBIC based on an SEM system was used. A 4 keV electron beam was employed to scan the cross section of the junction region.

Sample preparation

The preparation of the samples for this part of the work is similar to the preparation of the EBSD samples as detailed above. The only difference is that no mechanical polishing was required for the EBIC samples.

Results

The right column of Figure 6-25 demonstrates EBIC scans of the cross-sections of selected LD lines, superimposed on the corresponding SE images shown on the left. Regions of strong EBIC signal appear brighter than others, thus providing a visual method for locating the *p-n* junction. It is important to emphasise the fact that

since no conventional diffusion was carried out, any detected junction is one that was created solely by the laser doping process. Interesting observations were obtained for the high current LD lines. Despite considerable ablation of the silicon, a continuous and uniform junction may still form as shown in Figure 6-25 (b). However, it is obvious from (d) that discontinuities in the junction exist at some locations. It is possible that micro-cracks, most likely formed during the cooling process, electrically isolate some of the junction region, making it impossible to collect any EBIC signal when such regions are exposed to the electron beam. A large number of cross-sections were investigated and it was found that these discontinuities occur more frequently with high diode current. Figure 6-25 (f) shows the case of medium diode current and, similar to image (b), a continuous and uniform junction can be seen. The investigation of the influence of laser diode current on the junction parameters using EBIC will be discussed in greater detail in the next chapter.

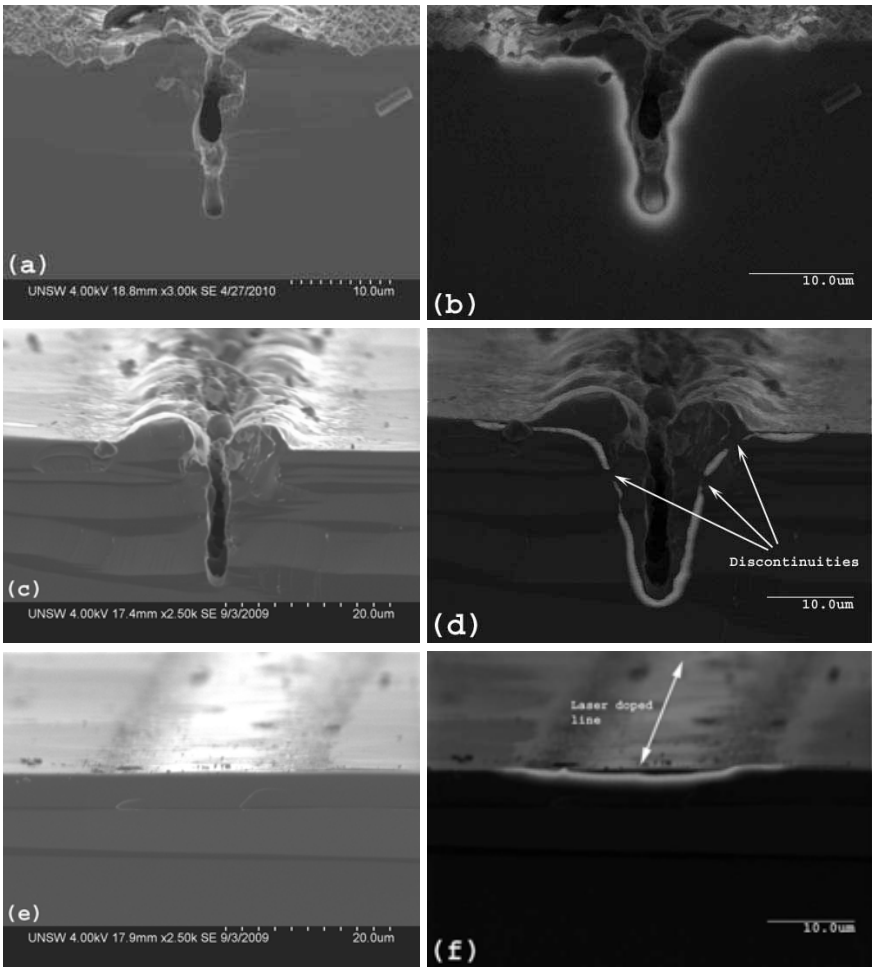

Figure 6-25: SEM (left) and SE+EBIC (right) images of *p-n* junction regions created by different laser diode currents – (a-b) continuous junction at high diode current, (c-d) discontinuous junction at high diode current and (e-f) continuous junction at medium diode current.

6.3.8 Discussion of Junction Characteristics

The significant decline in the implied V_{oc} in comparison to the reference samples for all the tested groups (see Figure 6-14) indicates that additional recombination sites are created or introduced through the laser doping process, leading to degradation of the electrical parameters of the material. The combination of EBSD and EBIC was used for the first time as an investigation tool and proves to be a very powerful one (Figure 6-16). The scans confirm that melting of silicon followed by an epitaxial recrystallisation process occurs during the laser doping procedure. Within the resolution limitation of the scan, no disorientation in the regrown layer was found; this finding is consistent with reports by others [88, 356]. Transmission electron microscopy was employed to investigate the material for defects at higher resolution. No defects in the form of dislocation or stacking faults were found in deep areas, although some defects were found near the surface (Figure 6-17). These defects were also delineated by Yang etch. A high concentration of defects near the surface has been reported in other studies [355]. It is assumed that these defects contribute to the noticeable decrease in the implied V_{oc} and the effective lifetime. Another source of recombination sites is likely to be associated with the high concentration of oxygen in the molten area (Figure 6-22). The high oxygen concentration of more than 1×10^{19} cm^{-3} is known to reduce the effective lifetime in the material, especially in the presence of nitrogen [384]. Due to the relatively high recrystallisation velocity, the existence of electrically-activated point defects is believed to be another cause of this degradation [358-360].

Figure 6-14 reveals the dependence of laser doping on the surface type and conditions of the substrate. In particular, it compares bare silicon to a wafer coated with a dielectric film. Although demonstrating higher implied V_{oc} values, the bare wafer is not the preferred option due to the lack of a plating mask for the subsequent metallisation step. It seems that generated defects, especially at the interface between the melted and unmelted areas, are the source for this dissimilarity. The SEM images of LD lines after Yang etching show significant variation in defect density between the groups (Figure 6-19). Only a small number of defects were revealed by the etching when the laser process was performed on bare wafers. In comparison, a high density of defects was observed when the laser scans a wafer coated with a SiN_x layer. Importantly, the defect density reduces when a double layer of SiO_2/SiN is applied. According to results reported by others, this double layer eliminates the formation of any defects [373]. However, it was found in this work that some defects are still formed, but with a lower density compared to the single SiN_x layer. It has been suggested that induced stress due to thermal expansion mismatch between the different materials is the source of these defects [373]. The stress induced by the difference in thermal expansion of the film and of the substrate is given by [385]:

6-3) $$\sigma_s = \Delta\alpha_t \Delta T E/(1-\nu)$$

where σ_s is the stress, $\Delta\alpha_t$ is the difference in thermal expansion coefficients, ΔT is the change of temperature, E is Young's modulus of elasticity and ν is Poisson's ratio. The thermal expansion coefficient of SiO_2 is one order of magnitude lower than that of silicon (5×10^{-7} K^{-1} and 2.6-4.6$\times10^{-6}$ K^{-1} for SiO_2 [386] and for silicon [342], respectively; see also Table 6-1). During heating, this difference in the expansion coefficient puts the SiO_2 under a tensile stress and hence the underlying silicon surface is placed under compression. The thermal expansion coefficient of SiN_x depends on the film's composition and the deposition method. Jiang *et al*. measured values in the range of 4-7$\times10^{-6}$ K^{-1} for Si_3N_4 [346], which places the silicon beneath it under tensile stress. Silicon is known to be weak and therefore easily defected under tension, but particularly strong under compression [387], so the presence of a thin SiO_2 interface layer is believed to be responsible for reducing the generation of defects at the surface of the crystalline silicon.

Furthermore, the presence of the oxide beneath the SiN_x film is known to provide a greater relaxation of the SiN_x stress, especially by undergoing viscoelastic deformation [385]. This relaxation ability probably also contributes to the reduction of laser-induced defects observed for those samples with a thin oxide. It is important to note that some form of thermal stress exists also in the absence of a dielectric film, as shown by Amer *et al*. [388] and by Hayafuji *et al*. [354].

Interestingly, no defects were discovered in the interface between the melted and unmelted areas when the laser doping process was applied to bare textured surfaces (Figure 6-20 (a)). During the heating and cooling durations this interface is subjected to extremely large temperature gradients that may generate defects. It is possible that the (111) plane has higher stress strength compared to the (100) plane.

Another interesting conclusion from Figure 6-14 is that the influence of the laser diode current on the implied V_{oc} is minimal when a dielectric film is present during the laser doping process, in contrast to the case without the dielectric film. Examination of the defect density after Yang etching has not shown a significant influence of the laser diode current on defect density (Figure 6-21), which can help explain the independence of the implied V_{oc} of the dielectric-coated wafers as the laser diode current was varied. The amount of oxygen incorporated in the molten region during the laser doping process rises with increasing laser energy [367]. It was also found that the formation of point defects in the recrystallised regions is accelerated by high regrowth velocity [89-90, 98, 363]. As the volume of the regions that were melted and subsequently recrystallised increases with increasing pulse energy, their influence on the electrical performance of the device is assumed to increase as well. The combination of these two effects explains the reduction in the implied V_{oc} of the bare wafer group when the laser power is increased. However, this reasoning does not

explain the observed behaviour of the implied V_{oc} results obtained for the other two sets of data for the wafers with dielectric layers. One explanation is that defect formation and density is the dominant degradation mechanism in these samples, while the negative contribution from other sources - contamination and point defects, for example - is negligible. However, in the absence of the dielectric film, laser-induced defects no longer dominate due to their low density. Instead, the increase of the point defect density and the contamination level reduces the effective lifetime and hence the implied V_{oc}.

EBIC was used to image the cross-section of LD lines. It was found that a *p-n* junction is formed even when ablation occurs, although discontinuities in the junction are more frequently observed at the high end of the laser current range. These discontinuities, which are attributed to micro-cracks, do not seem to have an impact on the implied V_{oc}, but have the potential to induce shunts when metal is plated in these regions, therefore reducing the device performance. This will be examined in next chapter.

6.4 The Influence of Spin-on-Dopants

To further investigate the influence of the SOD on the implied V_{oc}, two groups of six bare wafers were fabricated using a similar process to that described in Section 6.3.1. Prior to the LD processing, SOD was spun onto the front surface of only one group. As before, the spacing between the LD lines was adjusted according the width of the line, so the LD area covers 50% of the total area. Note that due to reduced reflection when SOD is applied (see Figure 6-26 (b)), different line widths were obtained by the two wafer groups. Figure 6-26 (a) presents the one-sun implied V_{oc} as a function of the laser diode current of the two groups. The SOD group demonstrates higher implied V_{oc} values for the entire diode current range. As mentioned, no difference in the defect density was observed between samples with and without SOD. Therefore, it is assumed that the heavily-doped regions created by the laser doping process isolate the bulk of the wafer from the defected region formed by the laser. Due to the heavy doping, these defected regions are more than one diffusion length from the active area of the device, so their influence on the implied V_{oc} is reduced.

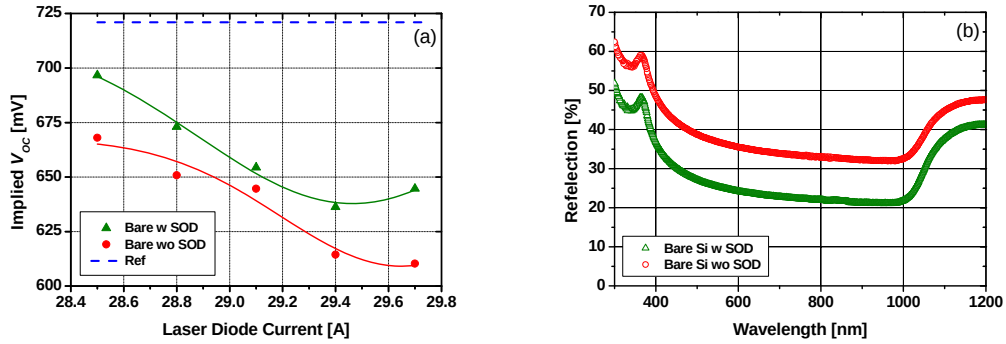

Figure 6-26: One-sun implied V_{oc} as a function of the laser diode current (a) and the reflectance as a function of the wavelength (b) for bare Si wafer and for bare Si wafer with SOD. The solid lines are given as a guide to the eye.

6.5 Solar Cell Fabrication

To investigate the influence of laser-induced defects on solar cell performance, two batches of five single sided laser-doped (SSLD) solar cells on a large area (154 cm^2) *p*-type CZ substrate (1-3 Ω.cm) were fabricated.

Sample preparation

The fabrication process was similar to that developed by Tjahjono *et al*. [128] with some modifications. After alkaline texturing and cleaning, a 40 Ω/□ emitter was formed in a conventional diffusion tube furnace. Phosphosilicate glass (PSG) removal and edge isolation increased the emitter sheet resistivity to the value of 80 Ω/□. After a short dry oxidation the wafers were split into two groups:

1) SON group: SiN_x was deposited after oxidation.
2) SiN group: SiN_x was deposited after the removal of the oxide layer by an HF dip.

An industrial remote PECVD system from Roth & Rau (SINA) was used for the SiN_x depositions; the film thickness was adjusted to achieve similar reflectance for the two groups (see Figure 6-27), while the rest of the parameters were kept the same (Table A13-1). The rear contact was formed by firing screen-printed Al paste prior to the laser doping process. The optimum laser setting was chosen according to the EBIC investigation conclusions. Nickel and copper photo-plating [389-390] were used to form the front grid and contact pads.

Results and discussion

The electrical parameters of the solar cells were measured using a class A solar simulator according to the international standard IEC 904-9 (QuickSun 120CA

from Endeas). All the measurements were carried out under standard test conditions using the AM 1.5G spectrum according to IEC 904-3 edition 2 (100 mW/cm^2, 25°C). Prior to each set of measurement the simulator was calibrated against a reference solar cell of the same type and spectral response, calibrated by the Fraunhofer Institute for Solar Energy Systems (ISE). Table 6-5 summarises the average and the standard deviation values for the electrical parameters of the batches. It is clear from this table that the main differences are the V_{oc} and the *FF*, which account for the difference in cell efficiency between the two groups. From reflectance measurements (see Figure 6-27), it seems that the ARC properties of the two groups are close to being identical and, indeed, similar J_{sc} values were obtained.

Table 6-5: Average and standard deviation values (STD) of the electrical parameters (AM 1.5G, 100 mW/cm^2, 25°C).

	SiN Group		SON Group	
	Average	**STD**	**Average**	**STD**
J_{sc} **[mA/cm^2]**	37.2	0.2	37.5	0.1
V_{oc} **[mV]**	618.9	6.6	631.2	2.8
***FF* [%]**	75.7	1.2	76.8	0.6
Pseudo *FF*[%]	80.9	0.8	82.0	0.8
Efficiency [%]	17.4	0.4	18.2	0.2

The difference of more than 12 mV in V_{oc} was predicted by the implied V_{oc} values (refer to Figure 6-14). The identical short and long wavelength spectral response indicates that the V_{oc} variation is not due to any significant difference in the front surface passivation quality, or the minority carrier lifetimes in the bulk. Hence it is concluded that the difference in V_{oc} is due to the different defect densities adjacent to the LD lines in the vicinity of the *p-n* junction as observed in previous sections. Increased junction recombination and possible junction shunting are also responsible for the lower *FF* values of the SiN group. To investigate this further, Suns-V_{oc} measurements were taken [202]. In this technique, the solar cell is put under open circuit conditions and the V_{oc} is measured under different illumination intensities. Under these conditions no current flows through the contacts, hence any impact of series resistance is eliminated. The calculated *FF,* often called the pseudo *FF* (*p-FF*), is mostly influenced by the shunt resistance and junction recombination. Table 6-5 also includes the average pseudo *FF*'s. The value for the SiN group is low compared to that for the other group, indicating that the lower *FF* is indeed due to either junction recombination or shunting. To gain further insight, the shunt resistance value (R_{sh}) was extracted from the *I-V* curve, while the junction recombination saturation current (J_{02}) was obtained from the fit to the Suns-V_{oc} measurement. Table 6-6 summarises the average R_{sh} and J_{02} values of the two groups. Both of the parameters explain the

lower *FF* of the SiN group, while the higher J_{02} value also explains the accompanying loss in V_{oc}.

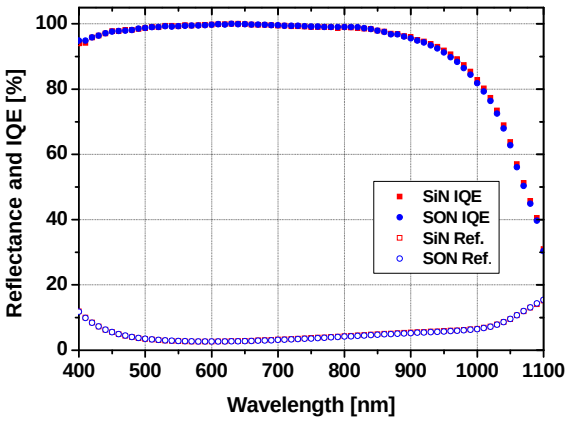

Figure 6-27: Reflectance and internal quantum efficiency of the two groups.

Table 6-6: Average R_{sh} and J_{02} values of the two groups.

	R_{sh} [Ω.cm^2]		J_{02} [nA]	
	Average	**STD**	**Average**	**STD**
SiN Group	938.2	85.2	35.6	7.1
SON Group	1649.2	421.8	18.1	3.9

Figure 6-28 presents the *I-V* curves of the best solar cells from each group, clearly illustrating the variation of V_{oc} and *FF* between the cell types. An efficiency of 18.4% was achieved on the large area commercial grade *p*-type CZ substrate.

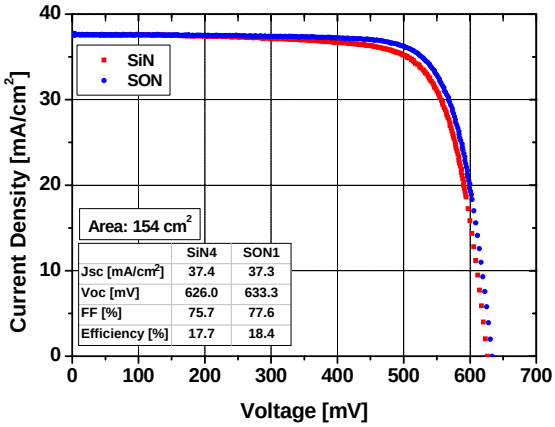

Figure 6-28: The current-voltage characteristics of the best solar cells from each group (AM 1.5G, 100 mW/cm^2, 25°C).

Conclusions

SSLD solar cells with SiO_2/SiN_x and with SiN_x were compared. The cells with the stack layer demonstrate higher V_{oc} and higher *FF*, similar to the findings of

Tjahjono *et al*. [128]. It was shown by a spectral response measurement that the observed change of the V_{oc} is not due to differences in the front surface passivation, but is more likely due to formation of defects adjacent to the LD lines. Suns-V_{oc} measurements confirmed that the reduced *FF* is due to junction recombination and shunt and not series resistance. An efficiency of 18.4% on commercial grade CZ substrates demonstrates that high efficiencies are achievable despite the laser-induced defects, if the dielectric layer and laser power are optimised.

6.6 Pulse Shaping System

It has been shown in previous sections that laser-induced defects degrade solar cell performance. The majority of these defects are generated in areas adjacent to the laser-doped regions. The large mechanical stress that results from the significant temperature gradient established during laser exposure creates fractures or plastic deformations in the Si lattice. This stress is further enhanced if a dielectric film covers the Si surface, due the difference in the thermal expansion coefficients. As can be concluded from Eq. (6-3), decreasing the temperature gradient leads to reduction in the thermal stress. This can be achieved by modifying the Q-switched pulse shape such that reduction in the recrystallisation velocity is obtained. This section presents a new approach to controlling the pulse shape in order to reduce laser-induced defect formation.

6.6.1 Motivation

As reviewed at the beginning of this chapter, a laser operating in Q-switched mode releases very short and powerful light pulses. Measurements of the laser system used here revealed pulses with FWHM of 40 ns and total width of 120-130 ns (see Figure 6-9). Despite the short duration, this energy pulse is still capable of raising the surface temperature to above 3000°C and melting the Si up to a depth of 1.2 µm (see Figure 6-10). However, the rapid change in temperature, as indicated by the high front melt velocity, generates defects within the solidified Si. Additionally, the fast heating process combined with the limited thermal conductivity of Si creates a spatial temperature gradient, especially at the surface but also in deeper regions. This temperature gradient enhances the formation of mechanical stress in the Si.

The short pulse duration results in a very short melting duration of only 0.6 µs, as indicated by the heat transfer simulation. This short melting duration imposes additional degradation effects apart from defect formation. The short melting time limits the depth of the formed junction to a very shallow one. Although the diffusion coefficient of dopants in liquid phase Si is quite high, their diffusion speed is still slow compared to the front melt velocity, as will be discussed in detail in the next

chapter. Hence, most of the melted regions will not be doped. Furthermore, this short time is not sufficient to allow proper mixing of the diffused dopants. Sugianto indicated that due to the short melting duration, non-uniform dopant distribution following the recrystallisation process occurs [391]. This process forms isolated *n*- and *p*-type areas and results in increasing sheet resistivity.

As has been shown before, the dependence of the FWHM on the laser diode current or the Q-switch frequency is very weak. One way to increase the melting duration, in order to deepen the formed junction and improve the dopant mixing, is to melt each spot a number of times. This can be done by adjusting the scanning speed or/and the Q-switch frequency. However, due to the low excited electron density in the higher energy level of the laser at the end of each pulse (much below the threshold level – see Figure 6-3), the successive pulse is only generated after the Si has already recrystallised. This implies that defects are generated with each pulse; thus re-melting each point a number of times may cause an unacceptable accumulation of defects.

Therefore, a method has been developed which increases the melting time without increasing the number of melting-resolidification cycles. This method is described in the next section.

6.6.2 Pulse Shaping Principles

Increasing the melting duration without vaporising a significant amount of Si requires improved control of the laser power. Efficient melting requires a range of laser powers: at the beginning of the process, high power is needed in order to heat the Si to the melting point and to supply the required latent heat of fusion in order to allow the phase change to take place. However, after achieving melting, lower laser power is needed to sustain the molten state without inducing vaporisation.

Typical laser systems are not designed with the option to modify the pulse shape. In most laser systems, the Q-switch is controlled by a square (i.e., binary) trigger signal, whereby one logic level reduces the cavity Q-factor, while the other increases it. Usually, only the frequency of this signal is variable. The duty cycle (the ratio between the high level duration and the total pulse duration) is typically fixed.

One approach to increase the melting duration is by incorporating a programmable control signal into the system. The duty cycle of each signal and the spacing between following signals would then be adjustable according to the user's requirements. In this approach, when a Q-switched pulse is generated, the cavity losses are removed by increasing the Q-factor (using the control signal). Under these conditions, stimulated emission is allowed and a laser pulse is generated. As the pulse rises, the cavity losses are re-applied quickly enough before the excited electron density drops below the threshold level. This preserves a relatively large number of excited electrons, allowing for the generation of a successive pulse almost immediately. In this way, a series of shorter and smaller pulses over a long period of

time can be generated, instead of one long pulse. Providing that the spacing between the pulses is sufficiently short so that no Si solidification occurs, this pulse sequence is proposed as a way to increase the melting period and reduce the cooling rate of the Si significantly. Although the total output energy of the series of pulses and the high-power pulse is similar, a longer melting time is achieved with the series of pulses due to its better power distribution. This reduces the density of generated defects and decreases the required number of melting cycles. Note that due to the negligible level of excited electrons at the end of the high energy pulse, this approach cannot be applied to a conventional laser system. Figure 6-29 presents the control signal, the density of electrons in excited states and the laser emission as a function of time. In this diagram, the high logic level of the control signal lowers the cavity losses (high Q-factor) and allows stimulated emission to occur.

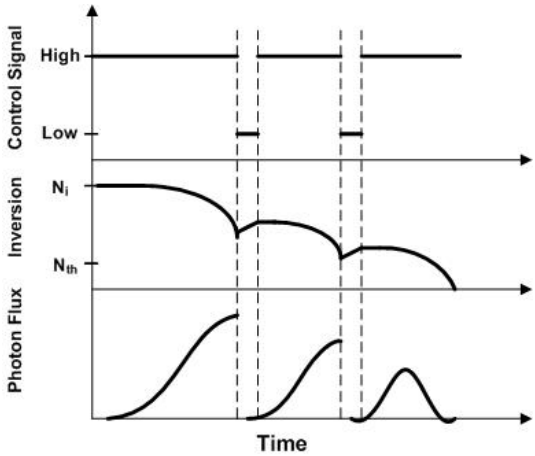

Figure 6-29: Control signal, population inversion and photon flux as a function of time for a laser system with a programmable Q-switch control signal.

For better control, a feed-back mechanism can be integrated into the system. In this case a photosensitive device, such as a photodiode, can be employed to measure the photon flux. When the photon flux reaches a programmed level, a trigger signal is used to increase the cavity losses, hence eliminating further stimulated emission [392].

A system based on similar principles was developed by Windsor, however the focus of his work was scribing and diffusing BC solar cell grooves simultaneously, not reducing the density of laser-induced defects [393]. Most other pulse-shaping systems found in the literature are based on a modification of a Gaussian laser beam into a “Top Hat” profile using a splitting element such as a mirror [394] or diffractive optical device [395].

6.6.3 Mathematical Model of Q-Switched Laser

In order to evaluate the feasibility of the proposed approach, a mathematical model was employed. The differential equations describing the operation of the Q-switched laser were first derived almost four decades ago [396-397]. A full description of the theory behind these equations can be found in Ref. [335]. It has been shown that two coupled differential equations for the photon density (Φ) and the excited electron density (n) can be employed to solve the Q-switched laser problem [335, 398]:

6-4) $$\frac{d\Phi}{dt} = \frac{\sigma_{em} l C}{l^*} n\Phi - \frac{C}{2l^*}\left(\ln(\frac{1}{R}) + \zeta(t)\right)\Phi + \frac{n}{\tau_{sp}}$$

6-5) $$\frac{dn}{dt} = L(t) - (\gamma\sigma_{em} C) n\Phi$$

where C is the speed of light, $L(t)$ describes the optical pumping and $\zeta(t)$ represents the cavity loss introduced by the Q-switch. The remaining symbols are summarised in Table 6-7. Note that due to the short pulse duration, the terms for spontaneous emission and for optical pumping are usually neglected [335]. However, in this study only the optical pumping term was ignored.

A MATLAB code was written to solve the equations. The modelled values are summarised in Table 6-7 ("Model" column). Note that the output mirror reflectivity and the length of the laser rod and laser resonator were not provided by the laser supplier due to confidentiality. Direct measurement cannot be done as the laser head is sealed. These values were estimated by comparison to a similar laser system.

Table 6-7: Eq. (6-4) and (6-5) list of parameters, their meaning and their values (for Nd:YVO_4 laser).

Parameter	Meaning	Value	Ref.	Model
σ_{em}	Stimulated emission cross section [cm^2]	1.2×10^{-18} 1.6×10^{-18}	[399] [400]	1.5×10^{-18}
γ	Inversion reduction factor	0.9 - 1	[401]	1
τ_{sp}	Spontaneous emission decay time constant [μs]	84 100	[402] [335]	84
R	Output mirror reflectivity [%]			80
l	Length of the laser rod [cm]			10
l^*	Length of the laser resonator [cm]			50

Figure 6-30 presents the solution of the laser equations. The shape of this graph is similar to the pulse shape obtained by the oscilloscope (see Figure 6-9). Note that presenting photon density is equivalent to presentation of laser power $P(t)$, due to the linear relationship between the two parameters [398]:

6-6) $$P(t) = (0.5C \times h\upsilon \times A\ln(\frac{1}{R}))\Phi(t)$$

where A is the resonator cross sectional area and $h\upsilon$ is the photon energy (3.73×10^{-19} J for 532 nm laser emission).

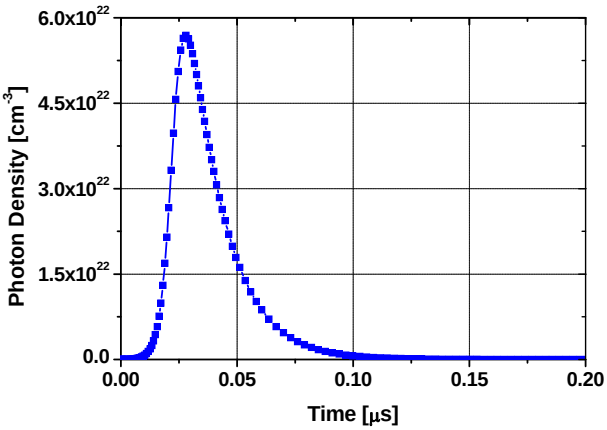

Figure 6-30: Solution for the laser equations for the parameters given in Table 6-7.

Three regions can be distinguished in Figure 6-30. The first region is the slow rise at the beginning of the pulse. This region is dominated by spontaneous emission only (the third term in the right side of Eq. (6-4)); in this period of time the stimulated emission has not begun. Figure 6-31 (a) demonstrates the influence of the spontaneous emission decay constant on the rise time of the pulse. A longer decay time slows the rise of the laser pulse due to the longer time needed to reach an adequate photon density in the resonator to trigger stimulated emission. The second region in Figure 6-30 is the rapid rise of the pulse, in which the stimulated emission rate increases through the feedback mechanism. Due to the fast emission, the density of excited electrons decreases until it reaches the threshold level, corresponding to the pulse peak. The height of the peak is proportional to the initial population inversion density and to the ratio l/l^*. Figure 6-31 (b) and (c) show the influence of these two parameters (l and l^*) on the peak value. The third region in Figure 6-30 is the decay of the pulse. In this region the stimulated emission ceases and the photon flux decays exponentially with a time constant that is related to the reflectivity of the output mirror and the length of the resonator – $2l^*/(C\times\ln(1/R))$. Figure 6-31 (c) and (d) present the influence of both the resonator length and the output mirror reflectivity on the decay time of the pulse.

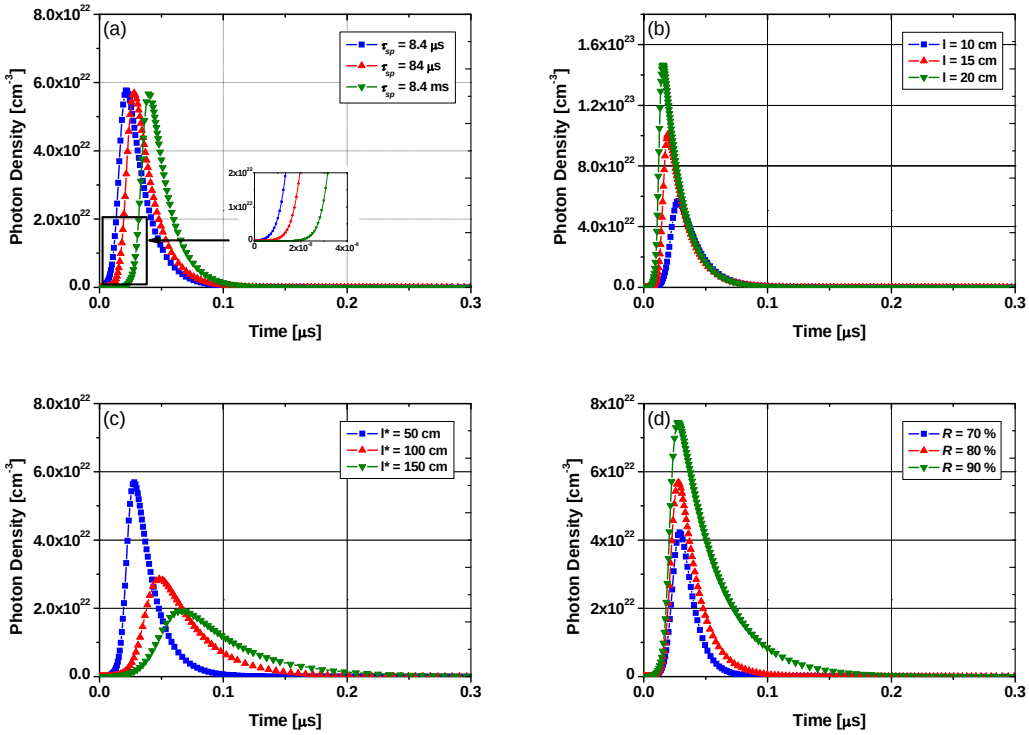

Figure 6-31: The influence of different parameters on the Q-switched pulse shape: spontaneous emission decay constant (a), length of the laser rod (b), length of the laser resonator (c) and the reflectivity of the output mirror (d).

A similar code was employed to model the proposed pulse shaping approach. Figure 6-32 compares the conventional pulse to the shaped pulse, demonstrating the shift of energy from the first pulse to create a successive one. Note that in contrast to the conventional operation, a closely-spaced second pulse can be generated using the new approach (10 ns in this case). The redistribution of the laser power can be seen clearly; the power was shifted from the initial part of the pulse (the peak of the first pulse) to its tail, in order to reduce the cooling rate. Although Figure 6-32 presents only two successive pulses, a larger number of pulses can be generated using the same approach.

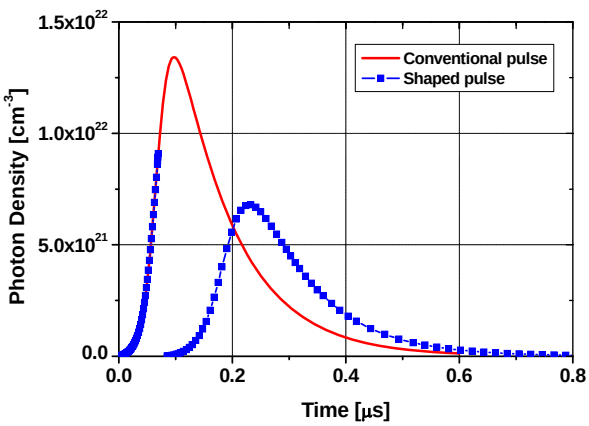

Figure 6-32: Comparison between conventional pulse (solid line) and shaped pulse (filled symbols).

By adjusting the laser diode current, it is possible to achieve a shape with a similar peak pulse power but with a modified tail. Figure 6-33 compares two pulses with similar peak power; however, one was created by the conventional Q-switched operation while the second was created by the new approach. The benefit of the shaped pulse in regard of the laser power distribution is obvious.

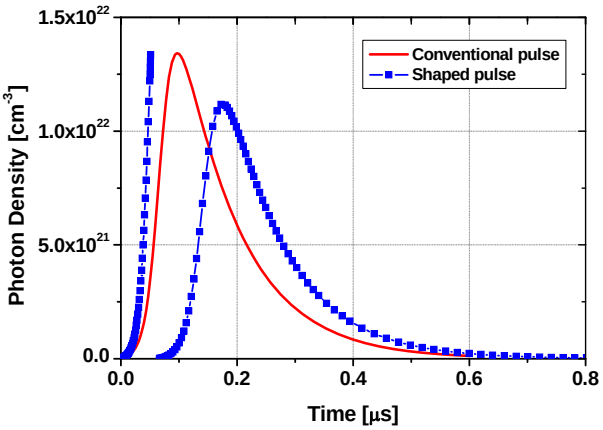

Figure 6-33: Comparison between conventional pulse (solid line) and shaped pulse (filled symbols) showing similar peak power. Different laser diode currents were used to model the two pulses.

Choosing the right point to reapply the cavity losses during the rise of the first pulse is crucial. Figure 6-34 demonstrates this by presenting two shaped pulses generated using identical parameters except for the point when the cavity losses were reapplied to the system. In the first case (filled squares), the cavity losses were reapplied too late, so that an insufficient amount of excited electrons were preserved for the second pulse. This situation is very similar to the conventional operation of a Q-switched laser, where a successive pulse can be generated only after a relatively long time. In the second case (filled triangles), the cavity losses were reapplied too early; in this case the first pulse does not have sufficient energy to melt the Si, so no significant benefit was obtained from the modification. However, there is a large time window in which the losses can be reapplied, allowing the user to modify the pulse shape according to specific requirements.

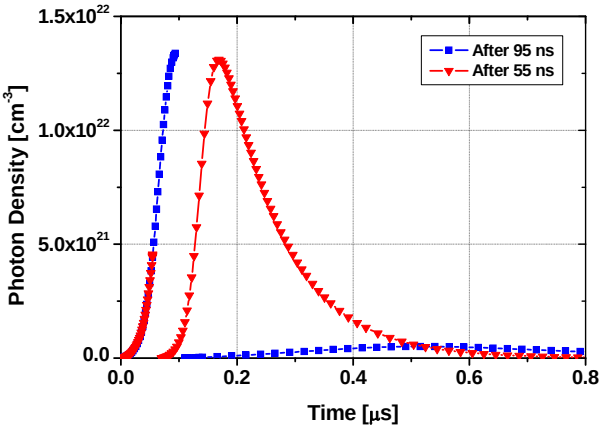

Figure 6-34: Shaped pulses generated by reapplying the cavity losses at two different points in the rising of the first pulse.

6.6.4 System Design

This section presents a preliminary design of the pulse shaping system. The system design is based on a programmable-voltage digital waveform generator from National Instruments (NI 6552). This high-speed device (100 MHz) is capable of defining digital waveforms with a resolution of 10 ns. The generated waveform is connected to the Q-switch driver and is used as a control signal.

A photo-detector and a beam splitter are employed to obtain a real-time measurement of the photon flux. The photo-detector signal is employed as a feedback signal to the waveform generator. When a pre-programmed photon flux value is reached, a control signal is sent to the Q-switch driver, commanding it to increase the cavity losses in the laser resonator. As a result, the stimulated emission of the laser is halted. After a set period of time, the optical losses are removed, allowing a new pulse to be generated. Figure 6-35 presents a schematic of this system.

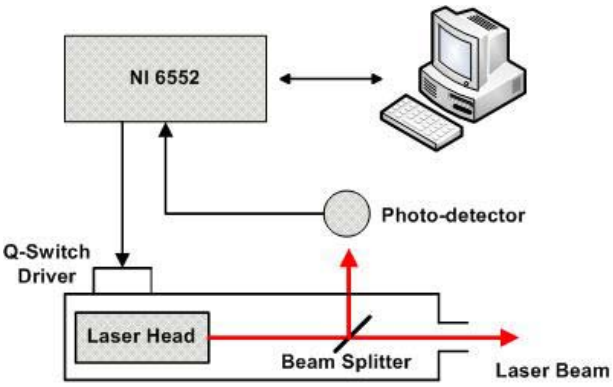

Figure 6-35: Pulse shaping system schematic.

6.6.5 Conclusions

In this section, a new method to increase the melting duration and decrease the recrystallisation velocity was presented. The method is based on redistribution of the Q-switched pulse power, using an improved Q-switch control.

By introducing cavity losses during the rise time of a laser pulse, before the excited electron density drops below the threshold level, energy is reserved for a closely-separated second pulse. A mathematical model of the Q-switched pulse validates the feasibility of this approach. The resulting shaped pulse has a longer tail, so a longer melting time can be obtained. An increased melting duration can improve several aspects of the laser doping process. First, it decreases the laser-induced defect density by reducing thermal stress and by slowing the front melt velocity. Second, it allows more thorough dopant mixing to occur.

A preliminary design for the pulse shaping system was introduced. However, the available laser system was limited by the slow response of the Q-switch driver. It was not possible to properly evaluate and optimise the proposed design. The originality and importance of the proposed approach however has been captured with a patent application filed by UNSW, with the author of this thesis an inventor along with an undergraduate thesis student working on the project under his supervision (see Appendix 1).

6.7 Chapter Summary

Laser-induced defects were investigated using a wide variety of methods. As a starting point the implied V_{oc} of different samples was measured before and after the laser doping process. A significant degradation was observed after laser treatment. This degradation is more pronounced when a dielectric layer is present during the laser process, possibly due to the thermal expansion mismatch between the silicon and the overlying dielectric layer. Observations from a combination of EBIC and EBSD microscopy show that no crystalline disorientation resulted from the epitaxial regrowth process. It appears that laser-induced defects near the surface and a high level of oxygen in the molten area are the source of the electrical parameter degradation. Although not directly observed, a high point defect density may contribute to this degradation, which is in agreement with conclusions of other research groups.

Near-surface defects caused by the laser doping process were observed both in TEM images and after Yang etching. A higher density of defects was revealed by the etch when a dielectric film was deposited on the surface. It was found that the SiO_2/SiN_x stack is able to reduce the defect density. It seems that the well-known ability of the oxide to relieve stress in the SiN_x together with its low thermal

expansion coefficient are the reasons for the reduced defect density. The influence of the laser power density was investigated by varying the laser diode current for samples with a bare surface and a dielectric coated surface. It appears that the dominant mechanism for the observed electrical performance degradation is the formation of defects when a dielectric layer is used, whereas contaminations and point defects are the predominant defects in the case of bare wafers. Interestingly, no defects were observed on bare textured wafers when applying the same diode current that is shown to cause defects on a bare planar surface. It is possible that the (111) plane has higher stress strength compared to (100) plane.

A cross-sectional EBIC investigation of LD lines was performed. It was found that a continuous and uniform *p-n* junction is formed even when ablation occurs, although discontinuities in the junction are more frequently observed in extreme conditions.

SSLD solar cells with SiO_2/SiN_x and with SiN_x were compared. The cells with the stack layer demonstrated higher V_{oc} and higher *FF*. It was shown by a spectral response measurement that the observed change of the V_{oc} is not due to differences in the front surface passivation, but is more likely due to formation of defects adjacent to the LD lines. Efficiency of 18.4% on commercial grade CZ substrates demonstrates that high efficiencies are achievable despite the laser-induced defects, if an optimum dielectric layer and laser power are chosen.

At the end of the chapter, a new laser pulse shaping method to increase the melting duration and to slow the recrystallisation velocity was proposed and a patent application filed. It is believed that by using this approach a reduction of the laser-induced defect density and improvement of dopant mixing can be achieved. However, further work is needed to evaluate this method.

In the next chapter the influence of the laser diode system on the SSLD solar cells will be investigated and analysed based on the conclusions obtained from the study presented in this chapter.

Chapter 7 : Influence of Laser Power

In the previous chapter the influence of laser power on laser-induced defects was studied. This chapter investigates the influence of laser power on solar cell electrical parameters.

The chapter begins with a short literature review regarding doping profile. Following this presentation of the basic theory, the main discussion is divided into three major parts. The first part investigates the influence of laser power on the electrical parameters of the laser-doped junction. Heat transfer simulations are employed to calculate the influence of laser power on the melting depth and duration. The four-point probe method is used to study the dependence of the sheet resistivity on the laser power, scanning speed and surface topology. Variation in the surface concentration and the junction depth is measured by SIMS. Finally, an EBIC system is used to study a wide variety of melting profiles.

Concerns have been raised regarding the adhesion of the metal to the shallow laser-doped areas [66]. This problem may be alleviated by increasing the roughness of the surface or even more so by creating holes or grooves in the laser-doped areas. One way of achieving this is by carrying out the laser doping at higher laser powers to deliberately induce some ablation. The second part of this chapter examines these issues by studying the influence of the laser power on the electrical parameters of the completed solar cell. In this way the relationship and the tradeoff between surface roughness and electrical performance are ascertained. SSLD solar cells were fabricated using a range of laser powers. Different methods such as PL imaging, lock-in thermography (LIT) and EBIC were employed to obtain a better understanding of the influence of laser parameters.

The third part of this chapter investigates the influence of laser power and plating techniques on shunt resistance, using techniques such as Suns-V_{oc} and LIT. The formation of resistance-limited enhanced recombination regions is investigated using the local ideality factor.

7.1 Review – Doping Profile

Different parameters influence the doping profile of laser-doped junctions. Some of these parameters, such as melting duration and melting depth, depend on the laser system and the operating condition. Others relate to the behaviour of the dopant atoms in the Si melt. These parameters, especially the diffusion and segregation coefficients and the solubility of dopants in Si, are summarised in this section.

As reviewed in the previous chapter, when the laser scans the surface its energy is absorbed by the Si, leading to melting of the Si if the power is sufficiently high. In the presence of a dopant source, diffusion in liquid phase occurs. This diffusion is characterised by a large diffusion coefficient in the order of 1×10^{-4} cm^2/s (see Table 7-1), which is independent of the melt temperature [375]. Due to the large difference between the diffusion coefficients in liquid and solid phases ($\sim1\times10^{-10}$ cm^2/s in solid Si) and the very short time involved, diffusion in the solid phase can be neglected [340]. Although the diffusion velocity of the dopants is very high in the liquid phase, in most cases the melt front progresses more quickly into the bulk. Figure 7-1 (a) compares the maximum melt penetration and the junction depth as a function of excimer laser energy. At low laser energy the melt front velocity is low; hence the melt front is at approximately the same depth as the junction. However, at higher laser energies the melt front penetrates faster than the dopants diffuse. Under this condition the junction depth is determined by the position of the dopants when the melt front sweeps back. Figure 7-1 (b) illustrates this process for an excimer laser.

During epitaxial growth, the dopants and the Si atoms are rearranged in the lattice to create doped Si. Importantly, it was found that during recrystallisation the dopant atoms substitute the host atoms at the lattice [90, 101]. Therefore, complete electrical activation of the dopants is achieved [95].

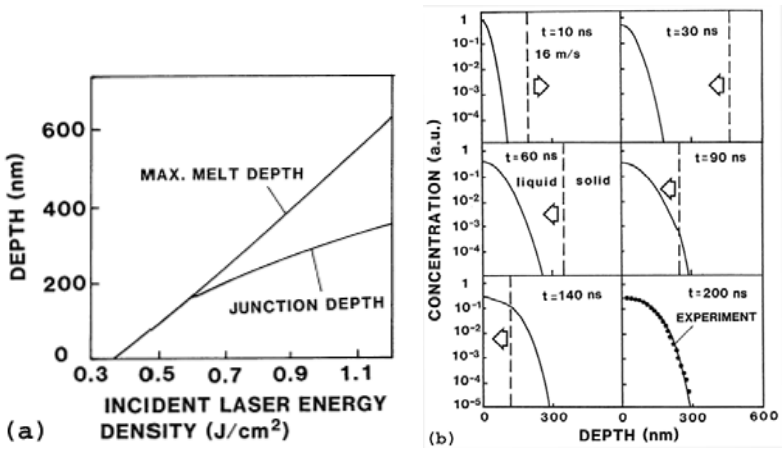

Figure 7-1: Calculated maximum melt and junction depth as a function of the laser energy (a) and calculated dopant profile at various of times [403].

The dopant concentration is determined by the *solubility* of the dopant atoms in Si. If the dopant concentration in the solid is higher than the effective solubility limit, the dopants will not be incorporated substitutionally in the Si lattice [377]. Table 7-1 includes the maximum solubility of phosphorus and boron in Si under equilibrium conditions. However, it was found that the maximum solubility after laser treatment is well above the equilibrium limit [90, 404]. This enhanced solubility limit, which was found to be nearly independent of the laser power, is explained by the fast movement of the melt front towards the surface. Due to the fast re-solidification, there

is not sufficient time for the excess dopants to diffuse into the liquid in order to establish the equilibrium concentration in the solid, so their concentration in the solid increases [404].

Table 7-1: Diffusion coefficient (in Si melt), maximum solubility and segregation coefficient of phosphorus and boron in Si.

	Diffusion Coefficient [cm^2/s]	Ref.	Max. Solubility [a] [cm^{-3}]	Ref.	Segregation Coefficient [a]	Ref.
Phosphorus	$(5.1\pm1.7)\times10^{-4}$	[405]	1.3×10^{21}	[342]	0.35	[405]
	$(2.3\pm1.3)\times10^{-4}$	[406]				
Boron	$(2.4\pm0.7)\times10^{-4}$	[405]	6×10^{20}	[342]	0.8	[405]
	$(1.2\pm0.4)\times10^{-4}$	[406]				

[a] Equilibrium conditions.

Another parameter which influences the doping profile is the *segregation coefficient*, which is defined as the ratio between solubilities in the solid and liquid (melt) phases. Similar to the solubility limit, the value of this coefficient is higher after laser irradiation than at equilibrium, due to the fast cooling rate. It was shown that, for both phosphorus and boron, the segregation coefficient during laser-induced diffusion approaches unity [407-408]. The influence of the segregation coefficient on the doping profile is shown in Figure 7-2. When the segregation coefficient is below one, the dopants are segregated from the resolidified regions towards the melt. When the melt approaches the surface, the effective segregation coefficient rises to the limiting value of unity in order to satisfy the requirement that all dopant atoms are confined to the sample and do not "escape" [377]. This constraint results in an accumulation of dopant atoms at the surface of the sample. Conversely, if the segregation coefficient is unity, a uniform profile is obtained (see Figure 7-2 (a)).

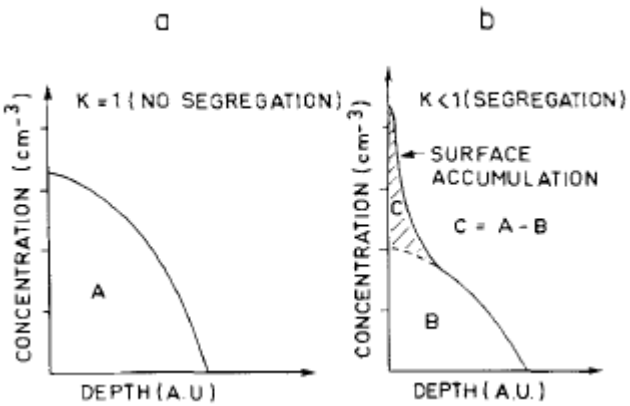

Figure 7-2: Schematic representation of dopants distribution for (a) segregation coefficient = 1 and for (b) segregation coefficient < 1 [377].

The large diffusion coefficient together with the enhanced solubility values and the segregation coefficients explain the relatively deep and uniform doping profiles produced by the laser doping process (for example, see Figure 7-3).

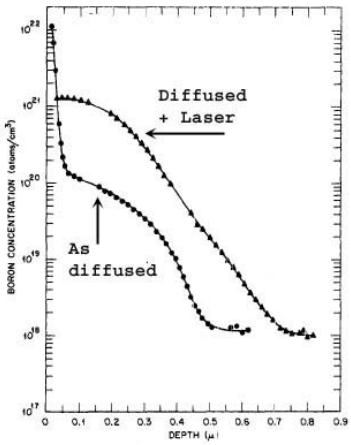

Figure 7-3: SIMS profile for boron diffused Si before and after laser treatment [88].

The depth of the junction depends on the laser wavelength and power, but also on the number of melting cycles. If the melt depth is deeper than the junction depth, increasing the number of melting cycles allows the dopant to diffuse deeper. As reviewed in the previous chapter, an increased number of melting cycles also improves the dopant redistribution [391]. Note the melt depth itself is not influenced by the number of melting cycles, because prior to each subsequent pulse the surface temperature returns to room temperature (see Figure 6-11). Full dopant activation, together with the increased segregation value, was employed by several research groups to redistribute and to activate dopants after a conventional furnace diffusion [88] or after implantation [69] (see Figure 7-3). In some applications it is used to form a selective emitter [110].

7.2 Visual Inspection

This section includes a visual inspection of the influence of laser power on the laser-doped regions.

Figure 7-4 presents series of planar views of LD lines fabricated using different laser powers on a bare textured surface. Increasing laser power improves the uniformity of the melting. At low laser power, un-melted regions can be observed (image (a)), while a very uniform melting is achieved when higher power is employed (image (c)). Note that due to the Gaussian shape of the laser beam, the width of the line increases with increasing laser power.

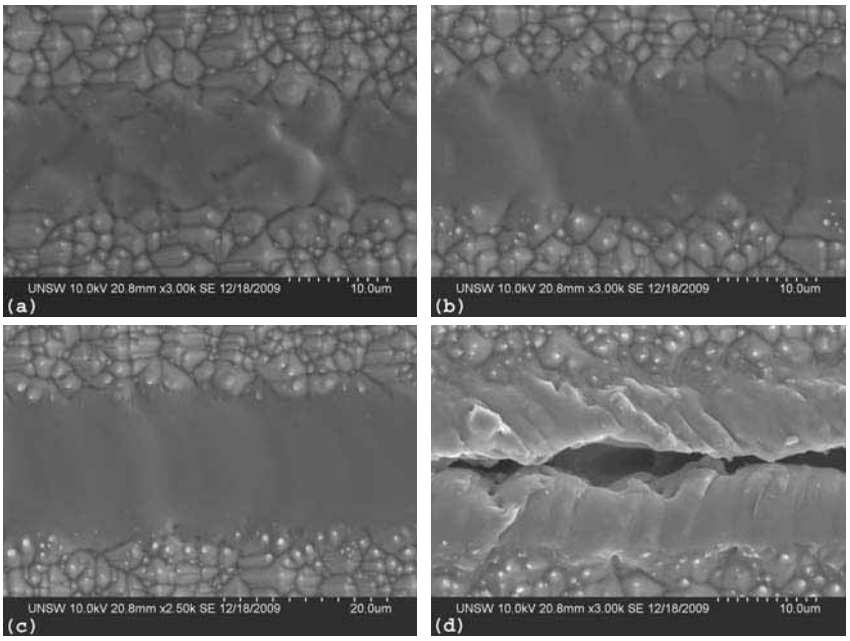

Figure 7-4: SEM planar view of LD lines fabricated using different laser powers on bare textured surface. Laser power is increasing from (a)-(d).

Figure 7-5 shows images of LD lines produced on a bare planar surface. At low laser intensity the LD region is barely noticeable using an optical microscope or SEM (image (a)). However, surface roughness appears after the laser treatment, as indicated by the atomic force microscopy (AFM) scan shown in image (b). Occasional holes that appear at higher laser powers are probably caused by fluctuation in the laser power (image (c)). It was found that the transition from melting to evaporation/ablation is faster on planar surfaces.

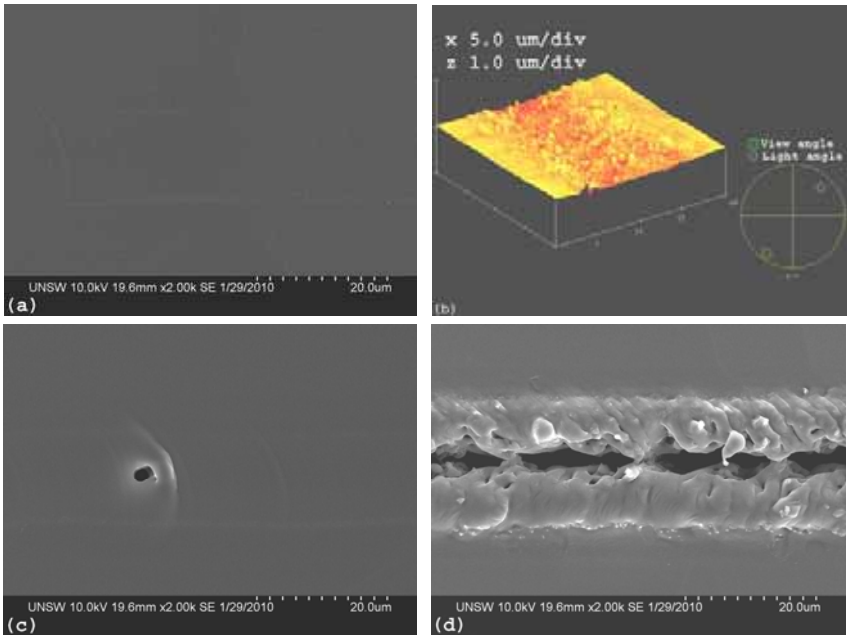

Figure 7-5: Planar view of LD line fabricated using different laser powers on bare planar surface (a, c and d) and AFM scan (b) of the laser-doped line created under similar laser conditions to that shown in (a).

Cross-sectional images of the textured lines (Figure 7-4) are presented in Figure 7-6. An FIB system was employed to create the cross sections, while an SEM was used for imaging. It is interesting to track the development of the LD line morphology as the power increases, especially the deformation of the surface pyramids. As can be seen in image (a), the use of low laser power only rounds the pyramids, while their general shape is still noticeable. Increased laser power enhances the melting process, as shown in later images and hence modifies the textured surface. The localised nature of the laser process is very clear, as can be seen by the perfect pyramids adjacent to the melted regions, in all images, irrespective of the laser power used.

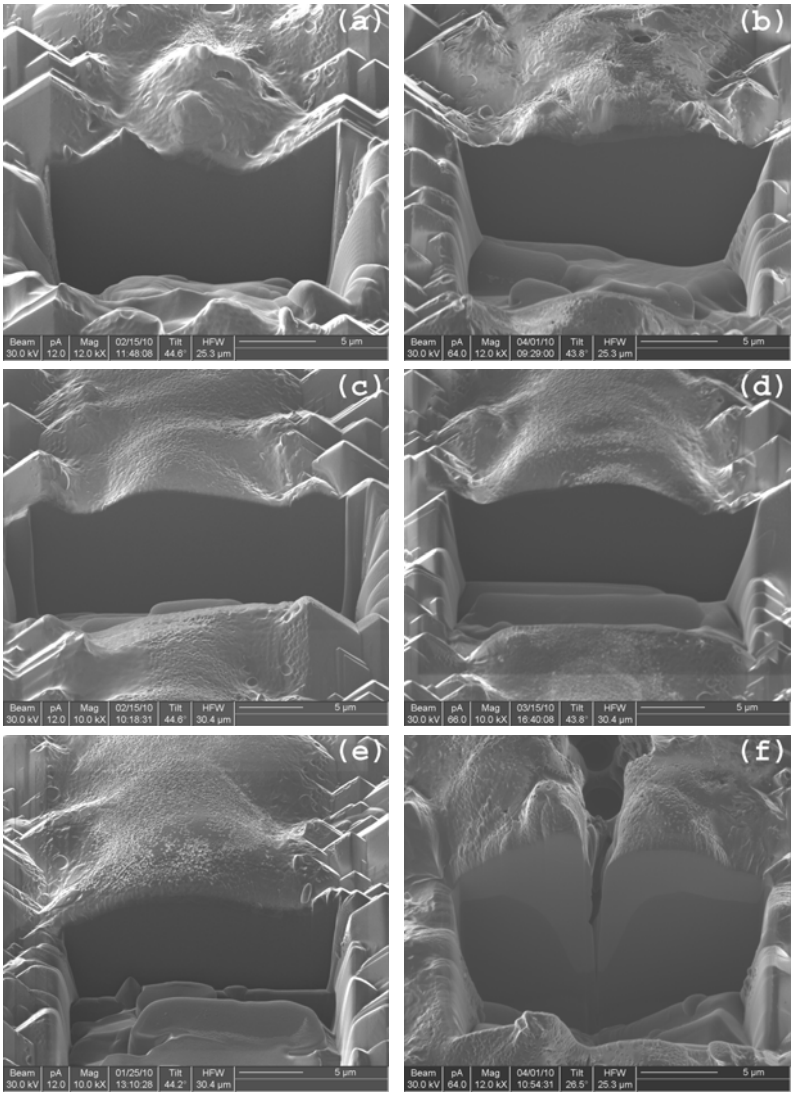

Figure 7-6: Cross-sectional SEM images of LD lines fabricated using different laser powers, with laser power increasing from (a)-(f).

7.3 Influence of Laser Power on Junction Parameters

In this section the influence of laser power on the laser-doped junction is studied. A heat transfer simulation is used to calculate the melting depth and duration. The dependence of the sheet resistivity on the laser power, scanning speed, sample surface and the presence of a PSG layer is studied using the four-point probe method, while the surface concentration and the junction depth are investigated using SIMS. At the end of the section, EBIC is employed to inspect the formed junctions.

7.3.1 Heat Transfer Simulation

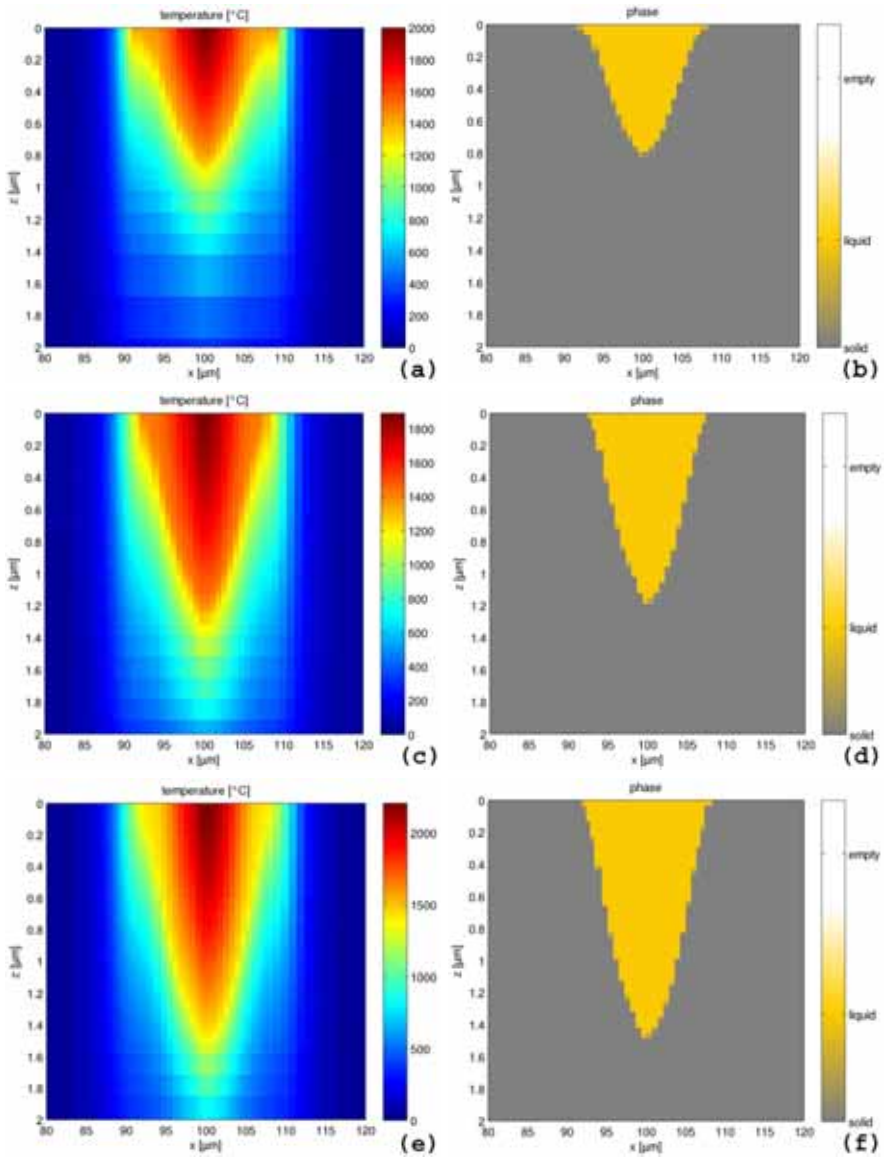

Figure 7-7: Heat transfer simulation results: spatial temperature distribution at maximum melting depth (left) and spatial phase diagram (right). Laser power: 400 mW (a, b), 500 mW (c, d) and 600 mW (e, f).

The influence of laser power on the melting depth and duration was investigated using the heat transfer simulation, developed by Fell [338]. The simulated parameters are summarised in Table A14-1. Figure 7-7 presents the results of these simulations. The left column shows the spatial temperature distribution at the maximum melting depth, while the spatial phase diagram is given in the right column.

As expected the melting depth increases with increasing laser power. Table 7-2 summarises the maximum depth, melting duration and maximum temperature as a function of the laser power as calculated by the simulation. Increased melting time and depth are obtained by larger laser power. Similar trends were found in the literature (for example see Ref. [341]).

Table 7-2: Maximum melt depth, maximum melting duration and maximum temperature as calculated by the heat transfer simulation for different laser powers.

Power [mW]	Max Depth [µm]	Melting Duration [µs]	Max Temp. [°C]
400	0.83	0.4	2500
500	1.19	0.6	3130
600	1.49	0.8	3770

7.3.2 Sheet Resistivity and Dopant Concentration

In this section the influence of the laser power, scanning speed and sample surface on the sheet resistivity (SHR) is investigated using the four-point probe method, while the surface concentration and the junction depth are studied using SIMS.

Sample preparation

Both planar and textured *p*-type wafers were used. After a saw damage etch (or alkaline texturing) and full RCA clean, a thin (~18 nm) dry oxide was thermally grown in a conventional open tube furnace, followed by 15 min annealing at 1000˚C in nitrogen. An ARC SiN_x (n_r = 2.1, d = 75 nm) was then deposited onto the front surface using the laboratory PECVD system (see Table 5-1 for deposition parameters). After applying SOD onto the SiN_x film, laser doping was performed using different laser diode currents and different laser scanning speeds. In each laser condition three lines and one measurement pad (15 mm × 2 mm) were created. The measurement pad consisted of closely spaced lines. The interval between the lines was adjusted according to the LD line width in order to maintain a similar overlap between adjacent lines**.** The four-point probe method [409] was employed for the sheet resistivity measurements using an appropriate correction factor [410].

SIMS [379] was used to detect the level of phosphorus in the laser-doped lines. A SIMS system with a resolution capability of 10 µm was used to detect the atomic concentration in a single LD line. The SOD was removed by a short dip in HF solution prior to the measurement.

Results and discussion

Figure 7-8 (a) shows the SHR as a function of the diode current for three different laser scanning speeds (textured surface). Regardless of the speed, the SHR decreases for increasing diode current until a threshold current is reached. Above this threshold current, which increases for increasing scanning speed, the SHR saturates for scanning speeds of 10 and 50 mm/s and increases for 100 mm/s. As shown by the heat transfer simulation, increasing the diode current increases the melting time and the melting depth, so that more dopants diffuse into the melt to reduce the SHR. Decreasing the scanning speed increases the number of melting cycles of each sub-area, hence increasing the total melting time and therefore decreasing the SHR. Saturation occurs when the process becomes source limited: under these conditions the number of dopant atoms and not the melting time limits the diffusion process. Increased SHR for increasing diode current (above some threshold current) was observed by others [103] and could be explained by evaporation of silicon with dopants during ablation or a decrease of doping homogeneity.

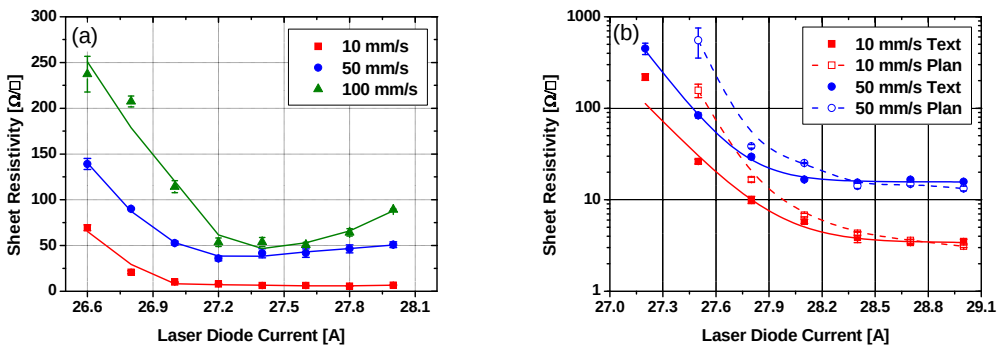

Figure 7-8: SHR as a function of the laser diode current for: (a) different laser scanning speeds on textured surfaces and (b) planar and textured surfaces. The solid and the dashed lines are given as guides to the eyes. The error bars represent the standard deviation of ten measurements.

Figure 7-8 (b) presents the SHR as a function of the diode current for planar and textured surfaces at two different scanning speeds. A similar trend as that seen in Figure 7-8 (a) can be observed for both the textured and planar samples, although planar samples demonstrate higher SHR at low diode currents. Higher reflectance at the laser wavelength (5% and 10% for textured and planar surfaces, respectively – see Figure 6-6) is assumed to be the reason for the higher SHR of the planar surfaces at low diode currents. However, when the diffusion process is changed to source limited,

the reflectance difference no longer influences the SHR. Thus similar values of SHR are obtained for both surfaces.

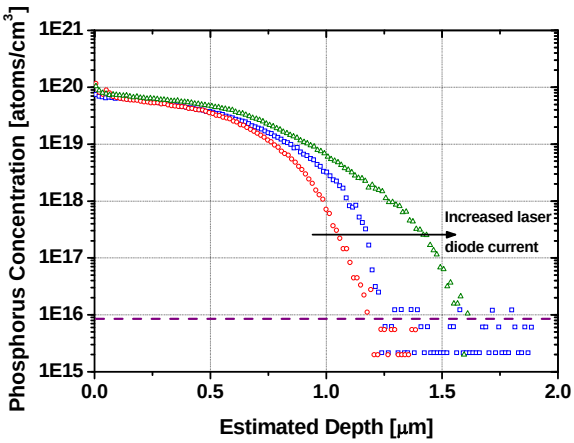

Figure 7-9: SIMS measurements of LD lines created by three different laser diode currents. The dashed line represents the boron level in the substrate.

Figure 7-9 shows the results of the SIMS measurements for three different laser diode currents; the background boron concentration is presented as a dashed line. Similar to previously reported results [67, 105], and agreeing with the findings of the heat transfer simulation, it was found that the junction depth increases when increasing the diode current. Comparable concentrations were detected near the surface for all the currents, which is in good agreement with recent results [411]. These high concentrations - above 1×10^{19} atoms/cm^3 - ensure ohmic contact between the silicon and the plated metal [230, 412]. It is assumed that the concentration level of $\sim7\times10^{19}$ atoms/cm^3 is fairly constant up to the junction location. The observed decrease in concentration for depths greater than 0.5 μm is due to the Gaussian shape of the laser beam and the resolution limitation of the SIMS measurement system. At depths greater than 0.5 μm, the width of the LD lines are smaller than 10 μm, therefore the SIMS system begins detecting signal from the adjacent silicon substrate that has not been melted reducing the average detected concentration.

Although SIMS detects the total phosphorus concentration, in the case of laser doping this concentration is similar to the active dopant concentration [69, 88, 95]. This conclusion is also supported by the very low obtained SHR values of less than 5 Ω/□ (see Figure 7-8).

Comparison between the results of the SIMS measurement and heat transfer simulation provides insight into the influence of the number of melting cycles on the junction depth. The heat transfer simulation predicts a melting depth of 1.5 μm (for 600 mW laser power), comparable to the junction depth measured by SIMS. However, the junction depth cannot be explained by the very short melting duration (0.8 μs for the same laser power) predicted by the simulation, as in this period of time the dopants diffuse only 0.1-0.2 μm (using diffusion coefficient values from Table

7-1). The deeper junction is explained by the large number of melting cycles. At each cycle the dopants diffuse deeper into the melt region until they reach the melt front. The number of melting cycles can be estimated using the following expression:

$$\textbf{7-1)} \quad Melting \quad Cycles = \frac{(Q-switch \quad frequency)\times(LD \quad line \quad width)}{Scanning \quad speed}$$

Inserting the typical parameters of the laser system (see Table 6-3), estimations for 50-100 melting cycles were calculated. This relatively large number of cycles allows the dopants to diffuse up to 2.5 µm (if the melt depth permits that), hence under this condition melting and junction depths are similar.

Using PC1D modelling and the results of the SIMS measurement, the sheet resistivity can be calculated. Sheet resistivities in the range 7-10 Ω/□ were obtained, which are in good agreement with measured values (see Figure 7-8).

7.3.3 Influence of PSG Removal

In the previous section the phosphosilicate glass (PSG) layer was not removed from the sample surfaces prior to the laser doping process. This layer is formed on the wafer surface during phosphorus diffusion. It mainly consists of SiO_2:P_2O_5 with a ratio that depends on the process duration, process temperature, gas composition and gas flow in the furnace [413]. This layer can be used as a dopant source. In this section the influence of the PSG layer on the achieved SHR is evaluated.

Sample preparation

Six CZ *p*-type wafers with resistivity of 5 Ω.cm were textured using an anisotropic alkaline solution prior to a full RCA clean. The wafers were diffused in an open tube furnace using solid sources. The PSG was removed from three of the wafers using an HF dip. All six wafers were then dry oxidised and annealed at 1000°C for 15 min. An ARC SiN_x was deposited onto the front surface using the laboratory PECVD system. Prior to the laser doping process, phosphorus SOD was applied to two samples from each group while the third was left as a reference. Five different laser diode currents were used to create measurement pads with dimensions of 15 × 2 mm^2. The sheet resistivity was measured using the four-point probe technique with an appropriate correction factor.

Results

Figure 7-10 presents the average sheet resistivity as a function of the laser diode current for the two groups. The emitter sheet resistivity was measured prior to the laser doping process and found to be 90 Ω/□ and 240 Ω/□ for the samples with and without PSG, respectively. Figure 7-10 (a) shows the sheet resistivity of the

samples which were processed without SOD. The sheet resistivity of the sample with PSG is in the range 45-55 Ω/□ - roughly half the background emitter resistivity - with a minimum at a medium laser diode current (28.2 A). Evaporation of dopants is assumed to occur above this current level. This assumption is supported by the sheet resistivity of the sample without PSG. At low laser diode current, the sheet resistivity is quite steady and similar to the emitter sheet resistivity. However, at higher diode current the resistivity increases significantly due to the evaporation of doped Si. Note that the same diode current leads to an increase in the sheet resistivity in both cases.

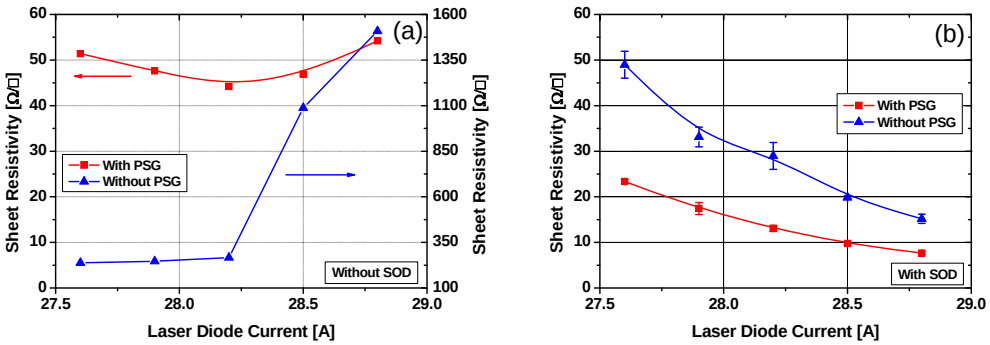

Figure 7-10: Sheet resistivity as a function of laser diode current for samples with and without PSG: without SOD (a) and with SOD (b). The solid lines are given as a guide for the eye, while the error bars represent the STD of 10 measurements ((b) only).

Figure 7-10 (b) presents the sheet resistivity as a function of the laser diode current for the samples, which were processed with SOD. It can be seen that the sheet resistivity values of the PSG group are roughly half of those without PSG. These results agree with results published by Morilla *et al*. [414], but they conflict with those obtained by Carlsson *et al*. which found only negligible difference between the SHR of samples with and without PSG [109].

Conclusions

It was shown that the PSG layer can be used as a phosphorus source, which significantly reduces the obtained SHR. However retaining the PSG layer is not suitable for some fabrication sequences that employ wet rear etching prior to the laser doping process.

7.3.4 Electron Beam Induced Current

In this part of the work EBIC based on an SEM system was used to examine the laser-doped junctions. The interaction volume, formed by a 4 keV electron beam, was found to be ~220 nm deep using CASINO simulation [415] - see Figure 7-11. This beam was employed to scan the cross section as well as the planar view of the junction region.

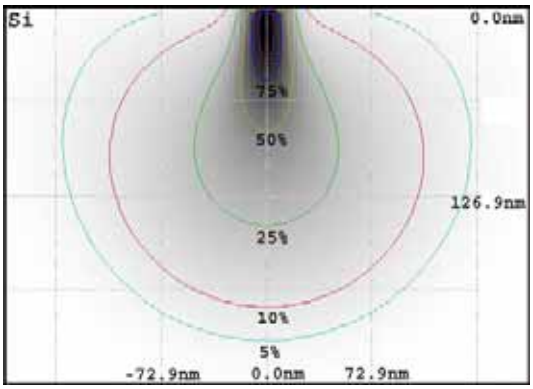

Figure 7-11: CASINO simulation result presents the interaction volume of a 4 keV electron beam in Si. The solid lines indicate the percentages of the initial beam energy.

Sample preparation

P-type wafers with resistivity of 1-3 Ω.cm were used. The laser doping was performed using seven different laser diode currents. Three closely-spaced LD lines were formed at each laser condition on the same wafer. Subsequently, the SOD was removed by a short dip in HF solution prior to a clean in Piranha etch. The rear contact was formed by evaporating Al on the back surface and sintering it for 30 min at 850˚C. Finally an EBIC scan was performed for the cross and the planar sections of each line to determine the junction location and associated parameters.

Results and discussion

Figure 7-12 presents a series of superimposed SE and EBIC images that demonstrate the formation of LD lines on a *p*-type planar substrate using phosphorus SOD. The prominent white line is the EBIC signal, which indicates the location of the *p-n* junction. One side of the junction, below the EBIC line, is the unmelted *p*-type silicon substrate, on the other side of the line is the melted and recrystallised area. Note that no thermal diffusion was done; all the junctions were created by the laser doping process. Image (a) shows a cross sectional scan of the LD line formed with a low diode current. Under this laser condition a shallow, 22-24 μm-wide junction was created. Image (b) presents a planar scan of the same line. The bright EBIC signal indicates that the junction is at a shallower depth than the interaction volume; therefore, the junction is less than 220 nm deep. Image (e) shows a cross sectional scan of the LD line formed with higher diode current. Under this condition the Gaussian shape of the laser beam became apparent. The junction shape, which follows the shape of the laser beam, is deep (~0.8 μm) in the centre and shallow at the edges (see Figure 7-7). The variation in the junction depth is more pronounced in image (f), which presents a planar view of the same line. The central area of the scanned line is dark, indicating that only a weak EBIC signal was measured from this region. Hence the depth of the junction in this region is greater than the depth of the interaction

volume. A shallow junction is observed at the edges of the line, which can be attributed to the Gaussian shape of the laser beam.

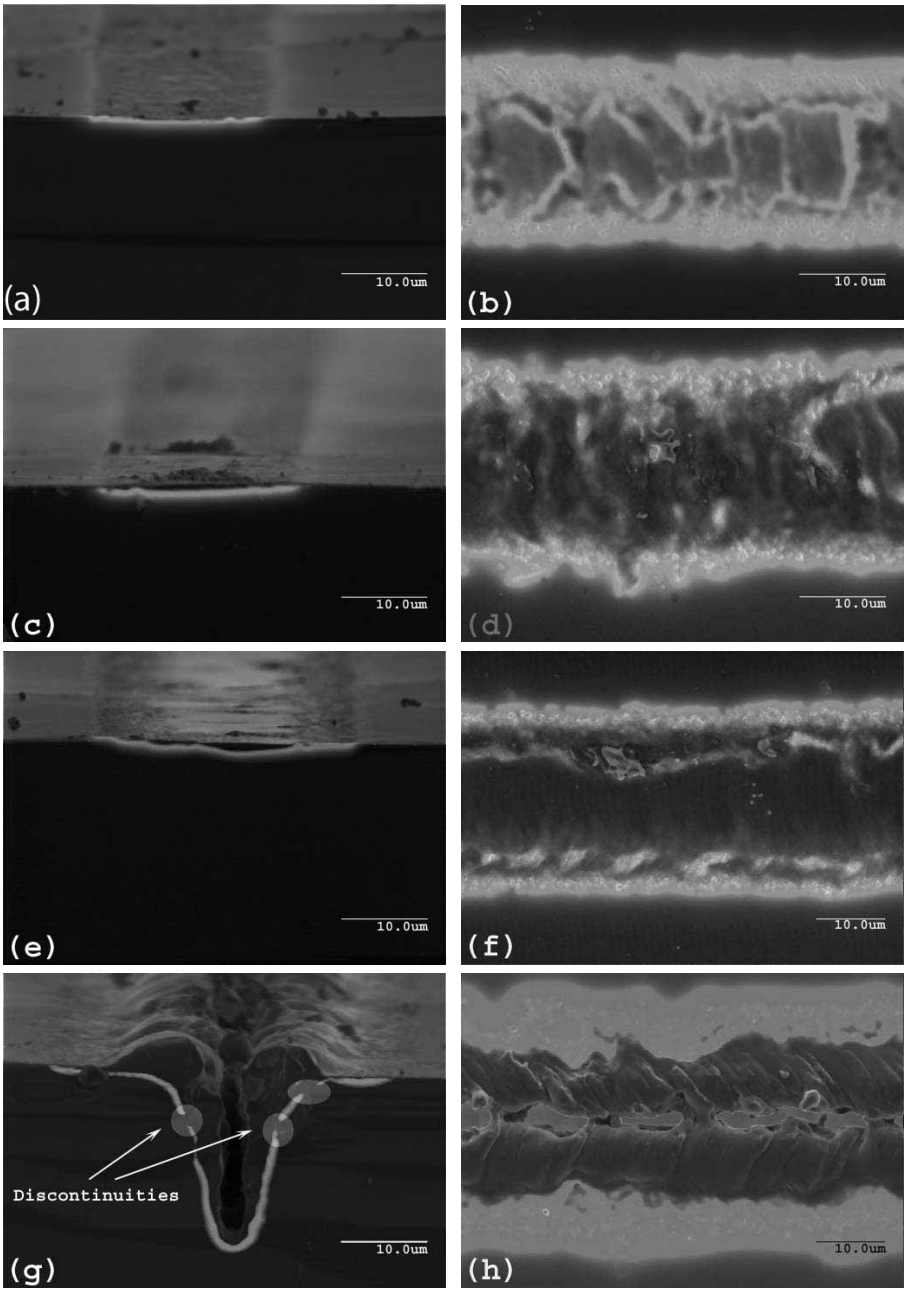

Figure 7-12: EBIC scan of cross-sectional (left) and planar (right) views of LD lines formed by different laser diode currents: 26.4 A (a, b), 26.9 A (c, d), 27.4 A (e, f) and 28.6 A (g, h).

Image (g) shows a junction that was formed using a diode current sufficient to cause laser-induced ablation. Despite the ablation a *p-n* junction was formed, although discontinuities in the junction exist at some locations. As concluded in the previous chapter, it is possible that micro-cracks, which were most likely formed during the cooling process, electrically isolate some of the junction region, making it impossible to collect any EBIC signal when such regions are exposed to the electron beam. A

planar view of the same line is given in image (h). A shallow junction can be observed at the edges and at the centre of the LD line and are evidence of the Gaussian shaped laser beam and the ablation, respectively. A large number of cross-sections were investigated and it was found that these discontinuities occur more frequently with high diode current, although they do not commonly appear.

Figure 7-13 shows the width of the LD line as a function of the laser diode current for a *p*-type, planar substrate doped with phosphorus SOD as measured by the EBIC images. Due to the Gaussian shape of the laser beam, the width of the line increases with increasing diode current.

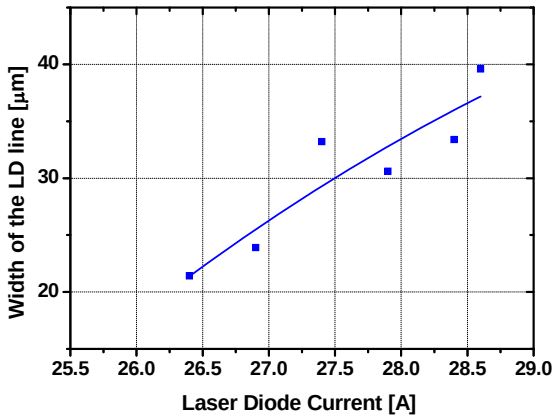

Figure 7-13: Laser-doped line width as a function of the laser diode current (*p*-type, planar substrate with phosphorus SOD).

Figure 7-14 shows the results of the laser doping process when performed on a textured surface. Image (a) presents an SEM image of the LD line created with low diode current. Although very limited melting occurred as indicated by the existence of the pyramids after the laser doping process, the junction was formed as demonstrated by image (b). Creation of a junction without significant damage to the texturing is desirable when using laser doping to form large area *p*-*n* junctions as indicated also by others [125]. Image (f) presents the case where medium diode current was used. As noted previously, the effect of the Gaussian shape of the laser beam is more visible in this image, where a ~1.65 µm-deep junction can be observed in the centre of the line. Image (h) demonstrates near-perfect junction formation despite strong ablation.

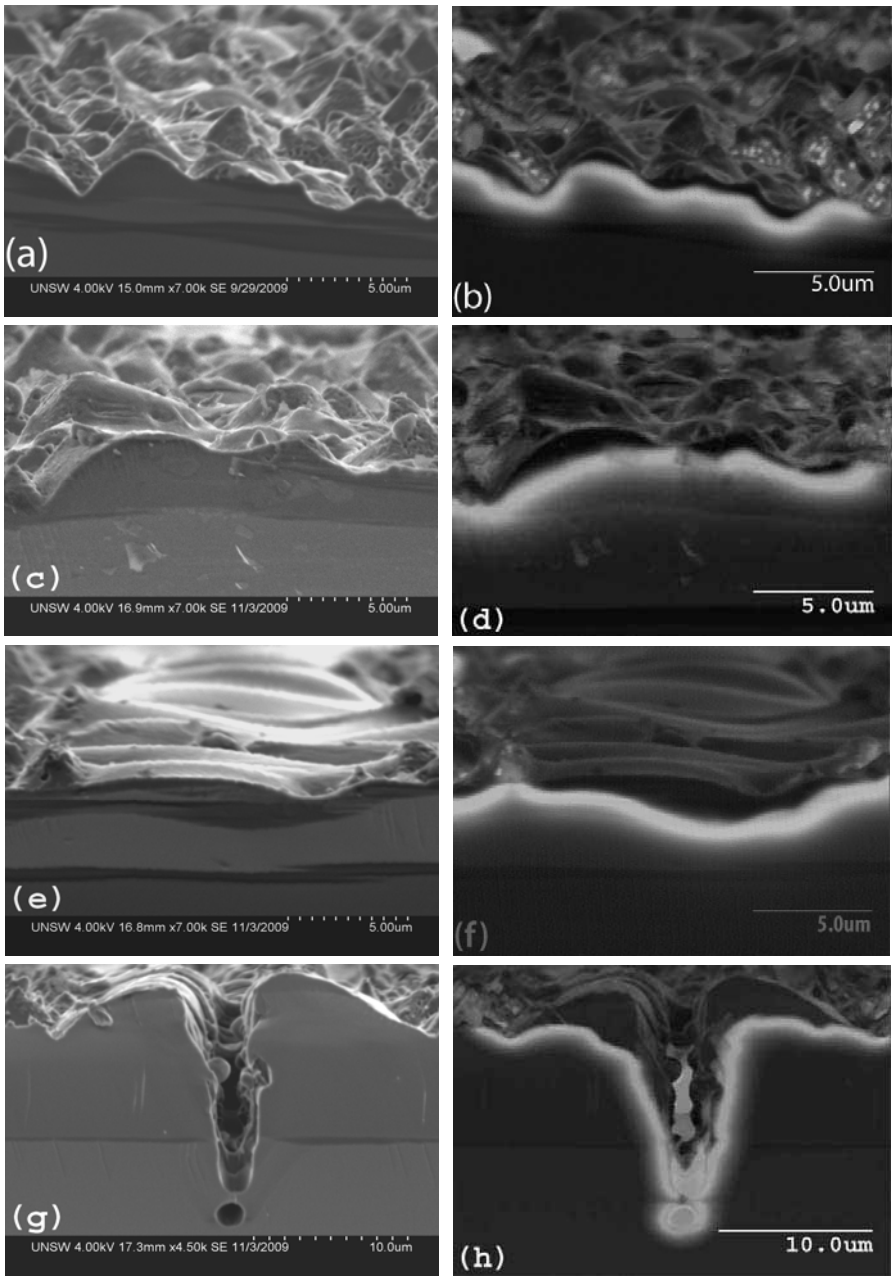

Figure 7-14: SEM (left) and SE+EBIC (right) of LD line formed with different laser diode current on *p*-type, textured substrate with phosphorus SOD: 25.9 A (a, b), 27.4 A (c, d), 27.9 A (e, f) and 28.4 A (g, h).

A wide range of laser diode currents have been shown to create a *p-n* junction. As demonstrated by the EBIC images, junctions can be formed by a diode current that is too weak to completely melt the pyramids on the top surface as well as one that is sufficiently high to create ablation. From the perspective of plating to the exposed laser-doped silicon surface, metal adhesion is significantly increased for the groove geometry achieved by ablation (for example Figure 7-12 (g)), compared to the relatively flat surfaces (Figure 7-12 (a) or (c)).

Although some discontinuities were observed when using the highest laser powers, it seems there is scope to still achieve some ablation that can be used to

improve the adhesion between the silicon and the metal without significantly degrading the cell performance.

7.3.5 Contact Resistance

In order to investigate the influence of the laser diode currents on the specific contact resistance (ρ_c), the transmission line model (TLM) method [416-417] was used.

Sample preparation

Five CZ *p*-type textured wafers with resistivity of 1-3 Ω.cm were RCA cleaned prior to emitter diffusion (120 Ω/□) in a tube furnace and short dry oxidation (18 nm). An ARC SiN_x was then deposited onto the front surface using the laboratory PECVD system, followed by laser doping at five different laser diode currents. The laser pattern on each wafer consisted of five parallel LD lines and one measurement pad (15 mm × 2 mm). The interval between the lines was varied in the range of 22-105 mm, while the length of the lines was set to 20 mm (see Figure 7-15). Electroless plating was employed to form the metal contacts; see Table 7-6 for details regarding the plating. At the completion of the metallisation process, the TLM pattern was separated from the host wafer by laser cleaving from the rear (according to the dashed lines in Figure 7-15).

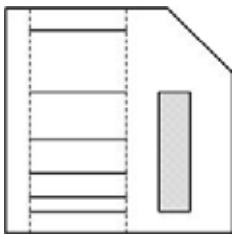

Figure 7-15: Planar view of the TLM wafer. The drawing is not to scale.

The resistance between each pair of neighbouring LD lines was extracted from a dark *I-V* measurement. Plotting the resistance as a function of the spacing between the lines can be used to extract the specific contact resistance (from the *y*-intercept) and the effective emitter (from the slope) [416]. Figure 7-16 presents the resistance-spacing graph for the highest and lowest laser diode current.

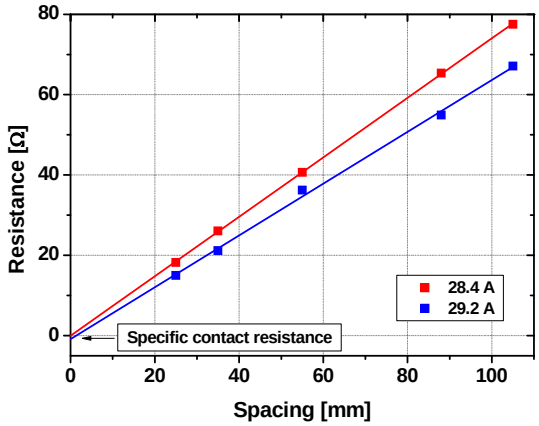

Figure 7-16: Resistance as a function of the spacing between the LD lines.

Table 7-3 provides the SHR (extracted using the measurement pad), as well as the extracted specific contact resistance and the effective emitter resistivity. For all the investigated laser diode currents a negative value of ρ_c was obtained, indicating that the real contact resistance was too small to be measured [418]. Note that the effective emitter resistivity agrees well with the measured SHR.

Table 7-3: Measured SHR, extracted specific contact resistance and effective emitter resistivity.

Diode current [A]	Measured SHR [Ω/□]	Specific contact resistance [Ω/cm^2]	Effective emitter SHR [Ω/□]
28.4	18.7	< 0	14.8
28.6	14.6	< 0	14.2
28.8	9.5	< 0	14.0
29.0	6.7	< 0	13.0
29.2	5.0	< 0	12.9

A very low specific contact resistance was measured for a wide range of laser diode currents. This is in good agreement with the measured SHR (Figure 7-8) and the SIMS measurement (Figure 7-9).

7.4 Improved Metal Adhesion through Laser Power Control

The adhesion between the metal and the shallow LD areas could be a possible drawback to laser-doped solar cells [66]. However, this problem can be avoided by increasing the roughness or creating holes in the laser-doped areas to at least 5 µm depth to act as anchor points [419]. This section examines the influence of the laser

power on the solar cell electrical parameters to ascertain the tradeoff between surface roughness and electrical performance.

7.4.1 Sample preparation

To investigate the influence of laser diode current on solar cell performance, four groups of five SSLD solar cells on a large area (154 cm^2), commercial grade *p*-type CZ substrate (1-3 Ω.cm) were fabricated. After alkaline texturing and cleaning, a 40 Ω/□ emitter was formed in a conventional diffusion tube furnace. PSG removal and edge isolation increased the emitter sheet resistivity to a value of 80 Ω/□. After a short dry oxidation, an ARC SiN_x was deposited using an industrial remote PECVD system from Roth & Rau (see Table A13-1 for deposition parameters). The rear contact was formed by firing screen-printed Al paste prior to the laser doping process. The optimum laser diode current (29.5 A), ablation current (30.2 A) and two other currents were used to create a wide range of melting profiles, as shown in Figure 7-17. Finally, nickel and copper photo-plating were used to form the front grid and contact pads. The nickel sintering was performed using a belt furnace at a peak temperature of 400°C and a belt speed of 6000 mm/min (~55 sec at peak temperature).

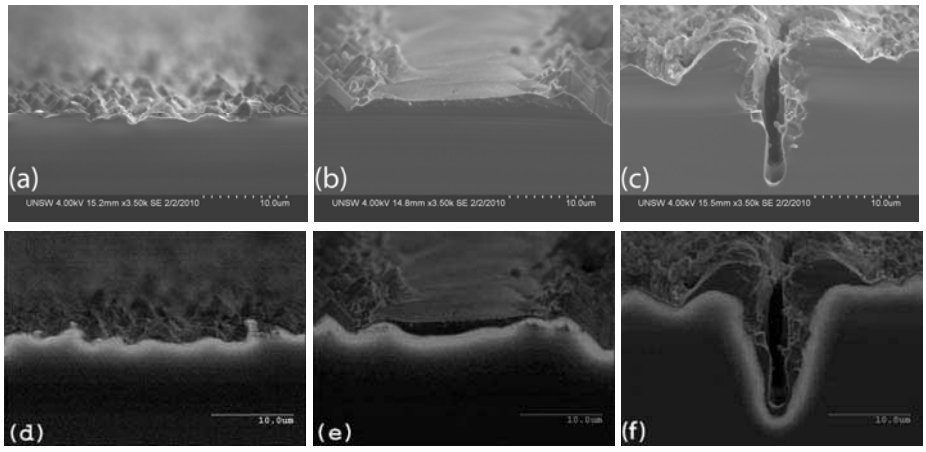

Figure 7-17: SEM (a-c) and SE+EBIC (d-f) images of LD lines formed by different laser diode currents: 28.2 A (a, d), 29.5 A (b, e) and 30.2 A (c, f).

7.4.2 Results

Table 7-4 summarises the average values of the electrical parameters of the different groups. The measurements were done using the QuickSun solar simulator, according to the procedure described in Section 6.5. The low values of the V_{oc} and the *FF* significantly reduce the efficiency of the group created by the highest diode current (the "ablation group") by 4% absolute. Interestingly similar electrical parameters were obtained by the other three groups, although they were fabricated using different laser conditions. The reduction of the J_{sc} with increasing diode current

can be explained by the increased shading due to the variation of the LD line width (see Figure 7-13).

To further investigate the influence of the diode current on the *FF*, Suns-V_{oc} measurements [202] were done before and after the metallisation process. Table 7-4 includes the average *p-FF* of the different groups. Comparison between the *FF* and the *p-FF* before and after the metallisation process highlights the fact that the *FF* of the ablation group is limited by shunt resistance induced by the metal.

Table 7-4 : Summary of the average electrical parameters of the different groups (AM 1.5G, 100 mW/cm^2, 25°C).

Diode current [A]	V_{oc} [mV]	J_{sc} [mA/cm^2]	*p-FF* [%] Before metal	*p-FF* [%] After metal	*FF* [%]	Eff. [%]
28.2	629.8	36.6	86.0	80.8	74.3	17.2
29.2	627.7	36.1	86.4	81.4	75.2	17.1
29.5	628.5	36.1	86.8	81.8	75.5	17.2
30.2	600.0	35.1	84.6	70.9	62.4	13.2

Lock-in thermography (LIT) images give visual evidence for the variation in the shunt resistance due to the laser diode current. In this method, the surface temperature is sensed by infra-red camera and enables the detection of shunted regions in the cells due to their local heating [420]. Figure 7-18 presents LIT images of representative cells from selected groups. All the images were taken under the same conditions and are presented in the same scale. Warm colours indicate higher temperatures and therefore shunted regions. The worst shunts can be observed in the cells fabricated with the highest diode current. This is especially true in the busbars, where the impact of defects is magnified by the closeness of the lines although the same laser conditions as for the fingers were used. It is possible that despite the continuous junction observed in Figure 7-17 (c), discontinuities exist in other locations along the LD lines which lead to shunting when metallised.

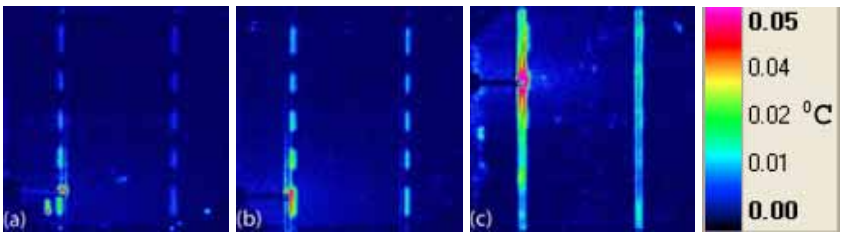

Figure 7-18: Lock-in thermography of representative cells: 28.2 A (a), 29.5 A (b) and 30.2 A (c). All images were taken under the same conditions and presented in the same scale. The scale indicates the variation in temperature.

The lower average V_{oc} value of the group made with the highest diode current, is probably due to several contributing factors including: increased shunting, the presence of defects, loss of heavily doped material isolating the junction region from the Si-metal interface and the large Si-metal interface created by the ablation. The significant degradation of the solar cell performance, as indicated by the electrical parameters (Table 7-4) and the current-voltage characteristics (see Figure 7-19) limits the extent to which ablation can be used to improve adhesion between the silicon and the metal. However, the satisfactory and consistent electrical parameter values for the wide range of laser diode currents indicate that intermediate amounts of ablation or *semi-ablation* can be used without significantly degrading cell performance. More severe ablation might be used to produce individual holes and therefore anchor points for the metallisation while simultaneously minimising the electrical performance degradation.

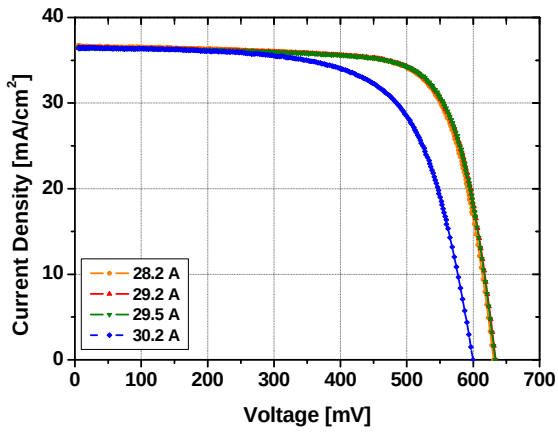

Figure 7-19: The current – voltage characteristics of representative cells from each group (AM 1.5G, 100 mW/cm^2, 25°C).

To further investigate the influence of the diode current on solar cell performance, a second batch was prepared. A similar laser system was used, with repetition rate of 200 kHz and scanning speed of 300 mm/s. This system extends the diode current range that allows laser doping to occur. Hence, laser diode conditions for creating intermediate amounts of ablation were found. Apart from the different laser conditions, the fabrication process was similar to that used for the first experiment, with some minor modifications. The thickness of the ARC was optimised to increase the cell's current density and the spacing between the laser lines was reduced to minimise the emitter resistive losses and therefore improve the *FF*. Five groups of five SSLD solar cells were fabricated, using optimum current (16.8 A), semi-ablation current (19.5 A) and three other currents. Figure 7-20 presents the SEM and the SE+EBIC images of selected lines.

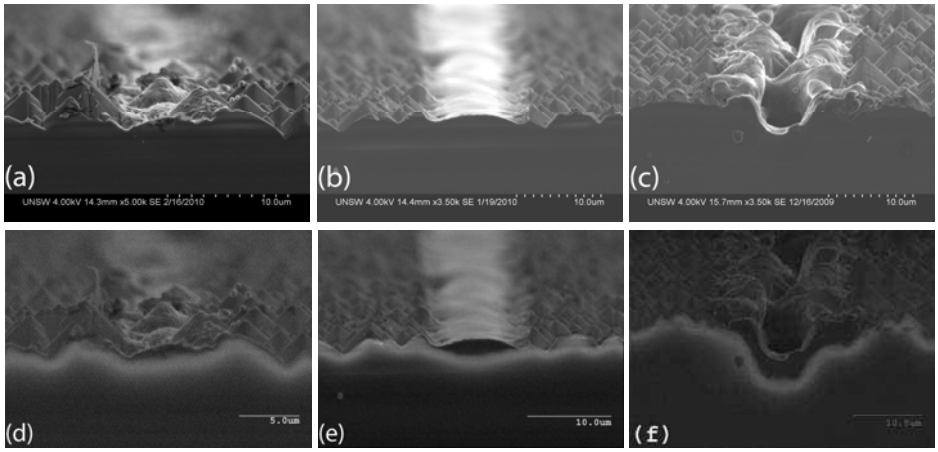

Figure 7-20: SEM (a-c) and SE+EBIC (d-f) images of LD lines formed by different laser diode currents: 14.1 A (a, d), 16.8 A (b, e) and 19.5 A (c, f).

Table 7-5 summarises the average values of the electrical parameters of the different groups in this batch. In contrast to the first batch, similar J_{sc} and *FF* values were obtained for all groups, including the group fabricated with the highest current. Note that both parameters were improved compared to the previous batch. The main difference between the groups is the V_{oc}, which reduces as expected, when increasing the diode current. This drop in the V_{oc} results in a reduction of the overall solar cell efficiency. Although the efficiency is reduced with increasing diode current, an efficiency above 18.1% was achieved even for the highest diode current.

Table 7-5: Summary of the average electrical parameters of the different groups (AM 1.5G, 100 mW/cm^2, 25°C)**.**

Diode current [A]	V_{oc} [mV]	J_{sc} [mA/cm^2]	*p-FF* [%] After metal	*FF* [%]	Eff. [%]
14.10	627.6	37.9	83.1	78.0	18.6
15.45	625.7	37.9	83.1	76.8	18.2
16.80	629.4	38.0	83.3	77.7	18.6
18.15	622.8	38.0	83.3	77.4	18.3
19.50	616.5	37.9	81.8	77.7	18.1

The data in Table 7-5 is plotted below in Figure 7-21. From the four presented graphs it is clear that the decrease in efficiency is due to a reduction in the V_{oc}. The steady value of the *FF*, even when semi-ablation occurred, was surprising. To provide more information regarding the *FF*, Table 7-5 and Figure 7-21 include the *p-FF* values as well. The lower *p-FF* value of the group fabricated with the highest diode current indicates that the average shunt resistance of this group is lower. Despite this,

a *p-FF* value of almost 82% indicates that not even this group suffers from a severe shunt problem.

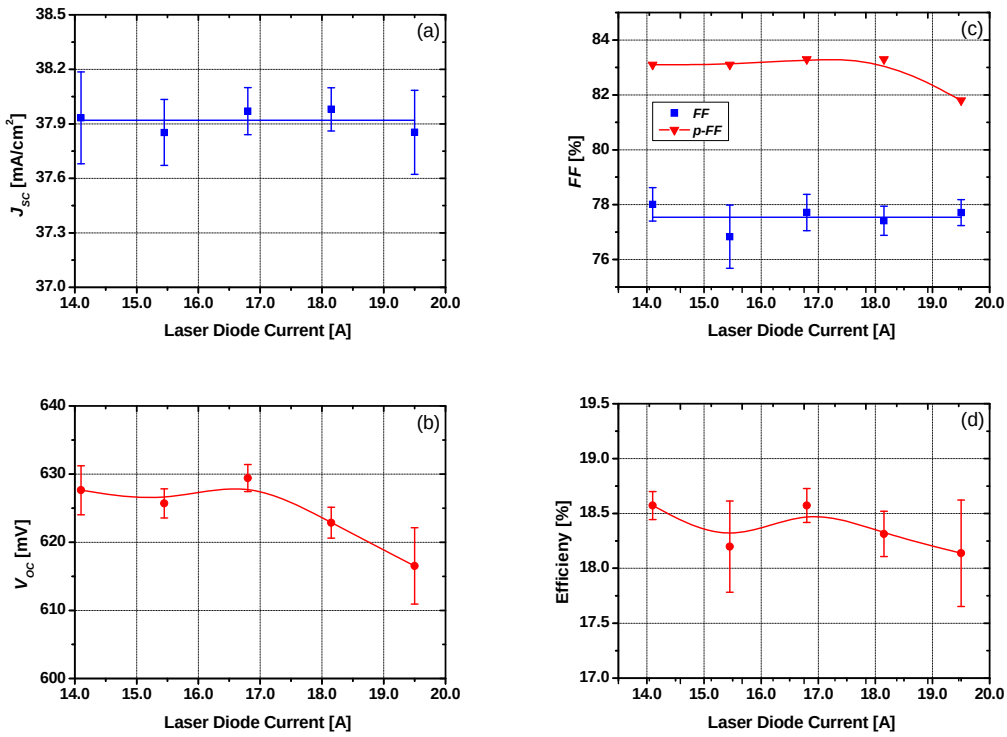

Figure 7-21: The average electrical parameters as a function of the laser diode current: (a) J_{sc}, (b) V_{oc}, (c) *FF* + *p-FF* and (d) Efficiency. The solid lines are given as guides to the eyes. The error bars represent the standard deviation of five solar cells.

To demonstrate visually the influence of the diode current on the shunt resistance, both PL imaging and LIT were employed. Figure 7-22 presents PL and LIT images of representative cells from different groups. The two dark strips in the PL images are the front busbars. Also visible are the ten rear silver soldering pads. A uniform V_{oc}, except for at the busbars and the contact pads, can be observed in all the images. Image (c) shows the PL image of one of the cells fabricated with the highest diode current. This image is slightly darker than the other PL images (images (a) and (b)), as predicted by the V_{oc} values. Images (d)-(f) present the LIT images of selected cells. All the images were taken under the same conditions and are presented using the same scale. In contrast to the first batch, no significant difference can be observed between the images. These images support the conclusion that for intermediate levels of ablation, the SSLD solar cells are not limited by the shunt resistance.

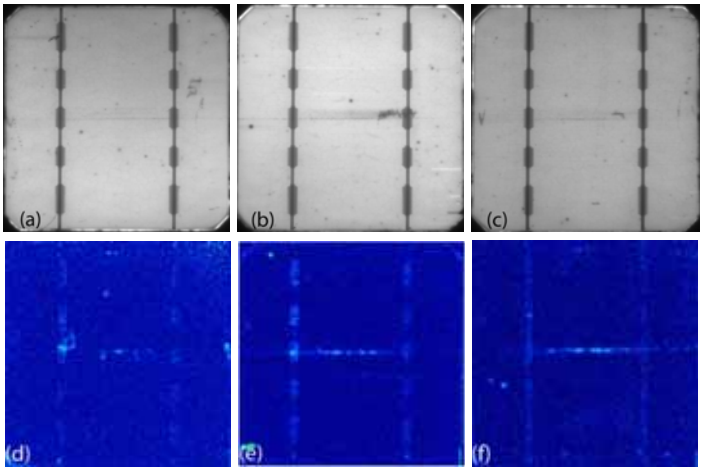

Figure 7-22: PL imaging (a-c) and lock-in thermography (d-f) of representative cells: 14.1A (a, d), 16.8 A (b, e) and 19.1 A (c, f). All the images were taken under the same conditions and are presented in the same scale.

Figure 7-23 shows the current-voltage characteristics and the spectral response of representative cells from each group. The spectral response measurements were performed using a calibrated Optronic Laboratories spectrophotometer. No significant difference between the different groups can be observed.

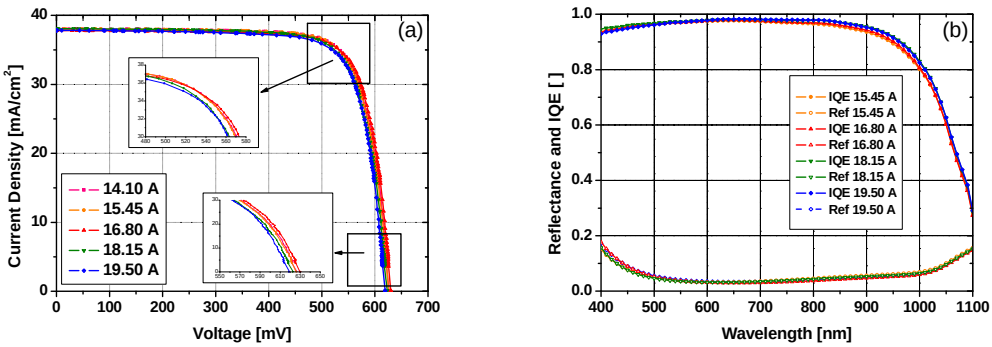

Figure 7-23: The current-voltage characteristics (a) and the reflectance and internal quantum efficiency (b) of representative cells from each group.

Figure 7-24 presents the current-voltage characteristics of the best solar cells fabricated in this experiment. An efficiency of 18.7% was achieved on a large area commercial grade *p*-type CZ substrate. This is believed to be the highest efficiency ever reported for a laser-doped solar cell using commercial grade wafers.

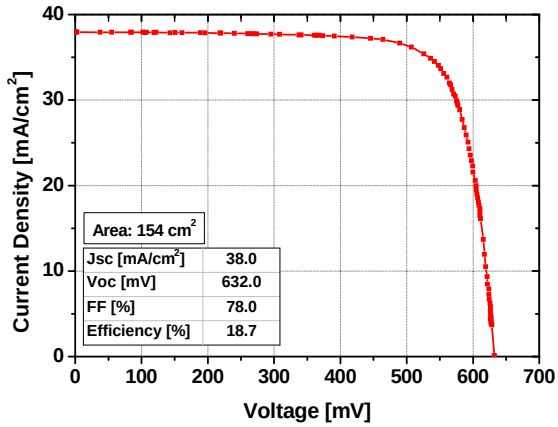

Figure 7-24: The current-voltage characteristics of the best solar cells fabricated during this work (AM 1.5G, 100 mW/cm^2, 25°C).

7.4.3 Discussion

It seems that the main influence of the laser diode current is on the V_{oc} of the solar cells. The *FF* and the *p-FF* values indicate that intermediate levels of silicon ablation do not create significant shunting, with the conclusion that the lower V_{oc} values are not shunt-limited. In the previous chapter it was shown that the laser diode current has limited influence on the formation of laser-induced defects in the laser-doped area when a stack layer of SiO_2/SiN_x is used. It was also found that the implied V_{oc} of these areas is not influenced by the diode current when it is passivated with SiN_x. Hence it is possible that the large Si-metal interface and loss of heavily-doped silicon, which isolates this interface from the junction, are the limiting factors of the V_{oc} for intermediate levels of silicon ablation. The interface area when ablation or semi-ablation occurs is significantly larger than the relatively smooth lines that are produced in the absence of ablation. The large standard deviation of the electrical parameters of the ablation group (see Figure 7-21 (b)) supports this conclusion as well. Control of the ablation process under the experimental conditions of this study was limited. Therefore variation in the groove depth and in the Si-metal interface was high, leading to a large variation of the V_{oc} within the group. When increased ablation occurs, extended shunts – presumably created from metal penetration into regions near the junction – acts to further increase the loss in V_{oc} caused by the large metal interface area.

It was demonstrated by different methods that the laser diode current surprisingly, has minimal influence on the *FF* and the shunt resistance of the cells up to intermediate levels of ablation. It will be shown in the next section that this unique behaviour is due to the photo-plating process. Different behaviours were observed when using other plating techniques.

By performing an adhesion test, Wenham *et al.* showed that intermediate amounts of ablation greatly improve the adhesion strength of the plated metal [419].

This is true for ablation that forms holes or grooves at least 5 μm deep, similar to that demonstrated in this work (see Figure 7-20 (c)). It is therefore concluded that intermediate levels of ablation can be used as a possible solution for poor adhesion between the metal and the silicon without significant loss of efficiency.

Efficiencies above 18.1% for large area commercial grade *p*-type, CZ wafers were demonstrated, despite the presence of intermediate levels of silicon ablation. Note that this solution can be applied only to cell structures like the SSLD. For cell structures with higher V_{oc}, such as double-sided laser-doped solar cells, where the V_{oc} is higher than 665 mV (see next chapter or Ref. [421]), the dark saturation current (I_0) associated with the observed voltage drop will reduce the V_{oc} of the cell to the 630 mV range, significantly degrading the cell efficiency.

7.5 The Influence of Metallisation Methods

To benefit fully from the self-aligned pattern, electroless [422] or photo-plating [389-390, 423] can be used. While electroless plating has long been used in diverse solar cell structures such as the BC cell [424], photoplating has been only recently employed. In this technique, which is also known as light induced plating (LIP), the plating process is driven by the internal voltage of the solar cells. Under illumination, carriers are generated and drift across the junction, creating an internal current. This current is used to induce plating, similar to the principle of the conventional electroplating method [425]. Note that in the photoplating technique plating occurs only on the *n*-type surfaces which can be beneficial in certain applications.

One of the major challenges in both the electroless and photo-plating techniques is the nickel (Ni) sintering step. The chemical composition, and therefore the resistivity, of the Ni silicide formed in this step is influenced by the sintering temperature [426-427]. The Ni silicide has three main purposes: to reduce the contact resistance at the Si-metal interface; to improve adhesion of the subsequent thick copper (Cu) layer and; to prevent diffusion of Cu into the junction region. Due to its high diffusion coefficient in silicon, Cu can easily penetrate into the junction region to create a shunt even at low temperatures. The Ni silicide provides a barrier to Cu diffusion and prevents its penetration. It was found that Ni sintering in the 350-400°C range provides thermally stable silicide with low contact resistance [424]. However, the sintering process often degrades the electrical performance of the device due to Ni being driven into defected regions in the vicinity of the junction.

This section investigates the influence of the plating techniques on the shunt resistance using the Suns-V_{oc} and LIT methods. The formation of resistance-limited enhanced recombination regions is investigated using the local ideality factor.

7.5.1 Sample Preparation

Five groups each consisting of five SSLD solar cells were fabricated on large area (154 cm^2) commercial grade *p*-type CZ substrate (1-3 Ω.cm). The fabrication process was identical to the one described in the previous section. A diode-pumped, Q-switched, frequency-doubled Nd:YVO_4 laser with a repetition rate of 200 kHz and scanning speed of 300 mm/s was employed to create the LD areas. Five different laser diode currents were used to create a wide range of melting profiles. One wafer from each group was cleaved into six similar samples (16 cm^2). Three samples from each wafer were electrolessly plated with Ni and Cu, while photoplating was performed on the other three with the aim of evaluating the potential benefits of the selectivity offered by photoplating. The Ni sintering was carried out in a conventional tube furnace at 350°C in a nitrogen environment for all samples. Details regarding the metallisation processes are given in Table 7-6.

The rest of the wafers, four from each group, were photoplated in similar conditions, but the Ni sintering was carried out in an open air belt furnace with set peak temperature of 400°C and a belt speed of ~6000 mm/min (~55 sec at peak temperature). Such belt furnaces offer better temperature control than tube furnaces in terms of ramping up and down, minimising the possible negative impact of laser-induced damage on device performance. Due to equipment limitations it was not possible to sinter electroless plated samples in the belt furnace. Therefore, only samples that were sintered in the tube furnace can be directly compared. However, results of the wafers sintered in the belt furnace are given to demonstrate the full potential of the photoplating technique. The complete fabrication sequence is presented in Figure 7-25.

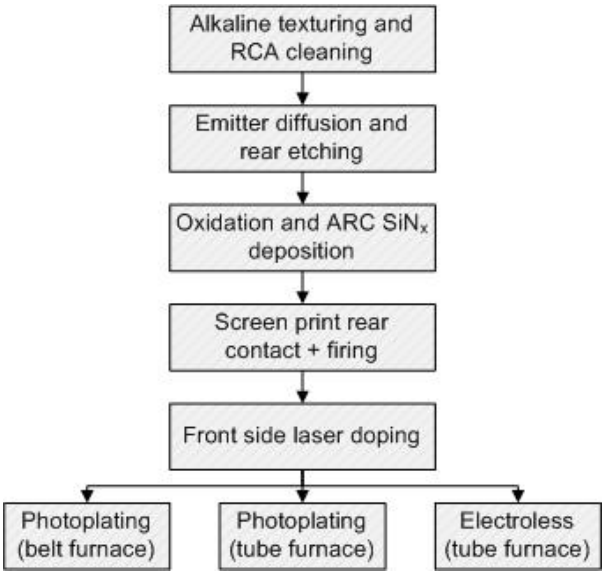

Figure 7-25: Device fabrication sequence.

Table 7-6: Details of the metallisation process.

	Electroless plating solutions	Photoplating solutions
Nickel plating	Ammonia based solution (from Transene).	Watts nickel electroplating solution [428].
Copper plating	Acid copper sulphate solution (from Enthone).	Acid copper sulphate solution.

	Electroless plating		Photoplating	
	Temperature [°C]	Duration [min]	Temperature [°C]	Duration [min]
Nickel Plating	85	5	30	3
Nickel Sintering	350	3	350	3
Copper Plating	48	120	30	8

7.5.2 Results

Suns-V_{oc} measurements were carried out after the metallisation process. Figure 7-26 presents the *p-FF* as a function of the laser diode current for electroless and photo-plated cells. The photoplated cells demonstrate higher *p-FF* for the entire laser diode range. The superiority of the photoplated cells is even more prevalent at higher diode current. It is interesting to note that the *p-FF* of the photoplated cells sintered in the belt furnace is almost constant over the entire diode current range, indicating minimal impact on device performances from variations in laser-induced damage. The high *p-FF* value, of more than 81%, indicates these cells do not suffer from significant performance loss due to either shunt resistance, or junction recombination.

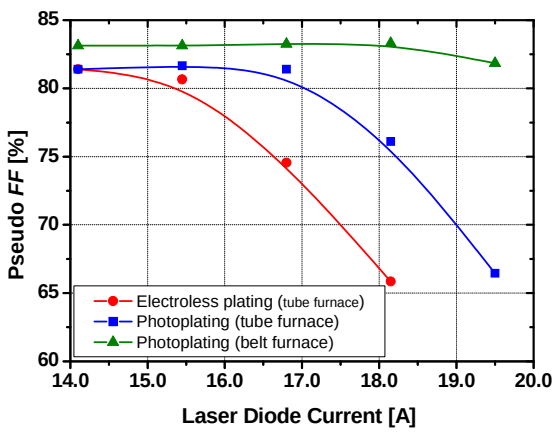

Figure 7-26: Pseudo *FF* as a function of the laser diode current of solar cells plated with electroless and photoplating methods. The solid lines are given as a guide to the eyes.

Figure 7-27 gives a visual presentation of the shunts using LIT. The same scale was used for all images. The two narrow black lines observed in some of the images, are the two probes which feed the current into the cell. Due to the lateral

resistance of the metal fingers, the regions near the probes are heated more. Figure 7-27 (a) and (b) are images of photoplated cells (sintered in the tube furnace), fabricated using a diode current of 14.1 A and 16.8 A, respectively. No significant difference between the images can be observed, which indicates similar shunt resistances. Similar behaviour can be seen in the case of photoplated cells sintered in a belt furnace, shown in images (c) and (d). Images (e) and (f) are of electroless plated cells, using the same laser diode currents and sintered in the tube furnace. Significant variation in the measured temperature, especially in and around the busbar, indicates areas of increased shunting. These images are in good agreement with the results presented in Figure 7-26.

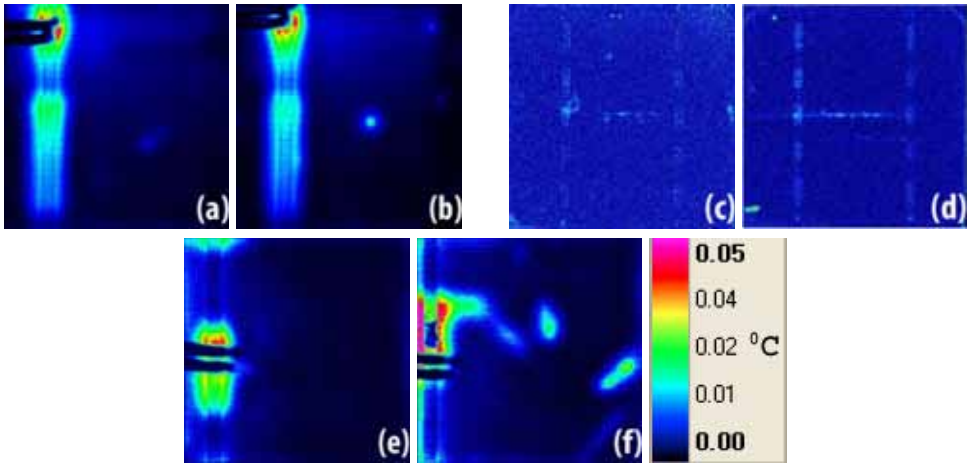

Figure 7-27: Lock-in Thermography of cells plated with the photoplating method + tube furnace (a, b), photoplating method + belt furnace (c, d) and electroless plating + tube furnace (e, f) at different laser diode currents: 14.1 A (a, c and e) and 16.8 A (b, d and f). The scale indicates the variation in temperature.

Another method to investigate the influence of the metallisation on the *FF* is by extracting the local ideality factor from the dark *I-V* curve. The shape of this graph has been found to be a very useful characterisation tool, especially in the identification of different performance-limiting mechanisms in solar cells [429]. Figure 7-28 (a) shows the dark *I-V* curves of solar cells fabricated using the same laser diode current (16.8 A) but plated by different methods, whereas Figure 7-28 (b) presents the extracted local ideality factor as a function of the voltage. The humps, clearly observed in these graphs, were identified by Hernando *et al*. to be due to breakage of the texturisation pyramids [430], while McIntosh attributed it to resistance–limited regions of high recombination [429]. It was found that a high ideality factor value at the MPP indicates reduced *FF* [431]. Figure 7-28 (b) also shows the MPPs of these cells, although an ideality factor above unity was calculated for all cases, a significant variation was noted between electroless and photo-plated cells.

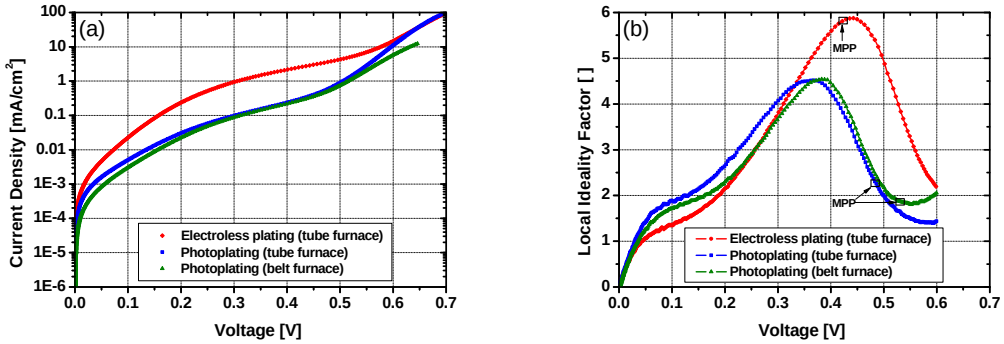

Figure 7-28: Dark *I-V* curves (a) and local ideality factor as a function of the voltage (b) of solar cells plated with electroless and photoplating methods, using laser diode current of 16.8 A. The MPP of each cell is marked on its corresponding curve.

7.5.3 Discussion

At a low laser diode current of 14.1 A, the *p-FF* values of electroless and photo-plated cells are similar, however for higher diode currents the *p-FF* of the photoplated cells is higher. Hence, the solar cell parameters are influenced differently by the laser diode current when different plating methods are used.

In a previous section (7.3.4), junction discontinuities were observed especially when high laser diode current was used (Figure 7-12). Due to the damage in these regions and possible exposure of *p*-type material via micro-cracks, these regions are more likely to induce shunts after plating.

The plating rate of the photoplating method is highly dependent on the internal voltage: it is lower in regions with low voltages (such as around micro-cracks), resulting in little or no metal plated in these areas. Furthermore, the selective plating only to *n*-type surfaces reduces the probability of shunt formation. In contrast to the photoplating technique, the cell parameters have limited influence on the plating rate in the electroless method; the metal is plated onto any exposed silicon regardless of the local voltage and whether it is *n*- or *p*-type. Therefore metal is plated in the micro-cracks when this method is employed, hence a direct path between the *n*- and *p*-type regions is created to form a shunt. Reduction of *p-FF* of electroless plated solar cells at increasing laser power was also reported by Kray *et al*. when comparing electroless Ni plating to evaporated metal contacts [121].

It can be seen in Figure 7-28 (b) that the local ideality factor between electroless and photo-plated cells differed significantly. Although breakage of pyramids occurred during the laser doping process (see Figure 7-6), this possibility is discarded as the main reason for the variation since identical laser conditions were used for all the samples. It was pointed out that a Schottky contact resulting from metal contacting the exposed *p*-type silicon increases recombination [432]. These Schottky contacts were identified as a possible cause for humps in the local ideality factor curves for BC solar cells [429]. In the previous chapter, laser-induced defects

especially at the interface between the molten and un-molten regions were observed. These defects, which may expose *p*-type areas, are plated when electroless plating is employed but not when photoplating is used. It is believed that increased saturation current from these resistance-limited enhanced recombination regions is the main reason for the high ideality factor of the electroplated cells. A high local ideality factor at the maximum power point leads to a reduction in the *FF*.

It is interesting to compare the effects of Ni sintering on the photoplated cells, in spite of their different sizes and possible variation in the plating process. The high and steady *p-FF* of the samples sintered in the belt furnace is most likely due to better Ni sintering conditions. It is possible that the significantly longer ramp up and ramp down conditions during sintering in the tube furnace, despite the lower set temperature, drives the Ni deeper than in the belt furnace. Up to laser diode current of 16.8 A, a range where junction discontinuities and ablation of material rarely occur, the depth of Ni silicide has only limited influence on the *p-FF*. The observed difference in the *p-FF* in this current range is attributed to increased junction recombination. At higher laser diode currents, the increased density of junction discontinuities and ablated areas tends to create a shallower local junction. The thickness of the Ni silicide under these conditions is more significant, as the Ni can be localised in the vicinity of the junction or can even penetrate through it, both of which further decrease the *p-FF* by junction recombination and shunting, respectively.

These results emphasise the advantage of the photoplating technique especially when combined with laser doping where occasional problematic regions are created by the laser. Such regions will not be plated, thereby avoiding the formation of shunts and/or high recombination Schottky contacts. To emphasise the advantage of the photoplating even more, Figure 7-29 presents the *I-V* curve of one of the large area photoplated cells, which was sintered in the belt furnace. Although the highest laser diode current (19.5 A) was employed to fabricate this cell, an efficiency of 18.2% is demonstrated.

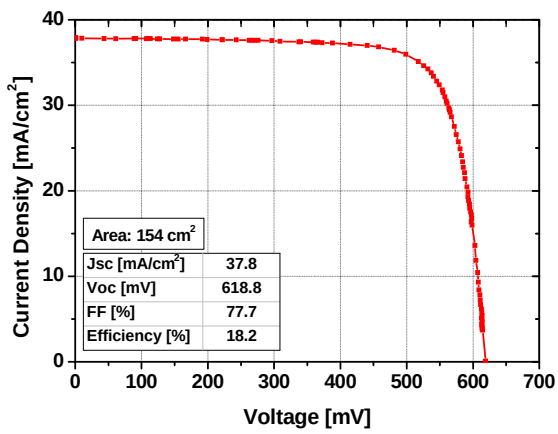

Figure 7-29: The current-voltage characteristic of one of the cells fabricated using laser diode of 19.5 A (AM 1.5G, 100 mW/cm^2, 25°C).

7.6 Chapter Summary

It has been shown that a wide range of laser diode currents can be used to create a *p-n* junction by laser doping. As demonstrated by EBIC imaging, the junctions can be formed by using a diode current that is too weak to completely melt the pyramids on the top surface as well as one that is sufficiently high to ablate the silicon. Although some discontinuities were observed in the latter case, it appears that grooves formed through intermediate levels of ablation can be used to improve the adhesion between the silicon and the metal without significantly degrading the cell performance.

It was found that the sheet resistivity is reduced with increasing laser diode current up to a threshold current level, above which it assumes a steady value when low scanning speeds are used. It was concluded that above the threshold current, a source-limited diffusion process occurs: the finite availability of dopants, not the melting time, is the limiting factor. High surface dopant concentration was found for a wide range of diode currents. This concentration, higher than 1×10^{19} cm^{-3}, ensures ohmic contact between the silicon and the plated metal for the entire range, including when ablation occurs.

It was shown that similar V_{oc}, J_{sc} and *FF* values are obtained for a wide range of laser diode currents. At intermediate levels of silicon ablation, the V_{oc} is the first cell parameter to be reduced, due primarily to the large Si-metal interface. This reduction decreases the efficiency, although efficiencies above 18.1% are still achievable. At higher levels of ablation, shunts reduce the *FF* and the V_{oc} as confirmed by Suns-V_{oc} measurements and LIT images. Under these conditions, significant efficiency degradation was observed. However, it was concluded that there are intermediate levels of ablation for which improved Si-metal adhesion can be achieved without significant damage to solar cell performance. An efficiency of 18.7% was achieved on a large area commercial grade *p*-type CZ industrial size substrate.

The influence of different plating methods on shunt and enhanced recombination regions was investigated. Higher pseudo-*FF*s were achieved for photoplated laser-doped solar cells, compared to those that were electroless plated.

If the photoplating technique is combined with well-optimised Ni sintering, the *p-FF* is almost independent of the laser diode current. High *p-FF* values above 81% indicate that cells fabricated under this condition are not limited by shunts. It was concluded that the superior performance of the photoplated cells is the result of the plating rate being dependent on the local voltage and the fact that only *n*-type surfaces are plated. Both of these phenomena reduce the potential of shunts and resistance-limited enhanced recombination regions. These advantages of the photoplating

method explain the achievement of efficiencies above 18.1% for a large range of laser diode currents.

Chapter 8 : Double Sided Laser-Doped Solar Cell

This chapter investigates the loss mechanisms of the single sided laser-doped (SSLD) solar cell presented in the previous chapter; methods to reduce these losses are proposed and evaluated with the aim of further improving the achieved efficiency of 18.7%. The main part of this chapter presents a novel solar cell structure: the *double* sided laser-doped (DSLD) solar cell. This structure is based on SiN_x passivation of the rear surface and the formation of a selective emitter and local BSF by laser doping. The fabrication sequence of this new structure is outlined and preliminary results are presented. Some problems, especially in the metallisation process, are identified and possible solutions are given.

8.1 Losses in SSLD

In order to gain insight into the loss mechanisms in SSLD solar cells, a PC1D model was developed to simulate the performance of these devices. In addition, test samples were fabricated to evaluate the voltage and the J_0 after different processing steps.

8.1.1 Front Surface

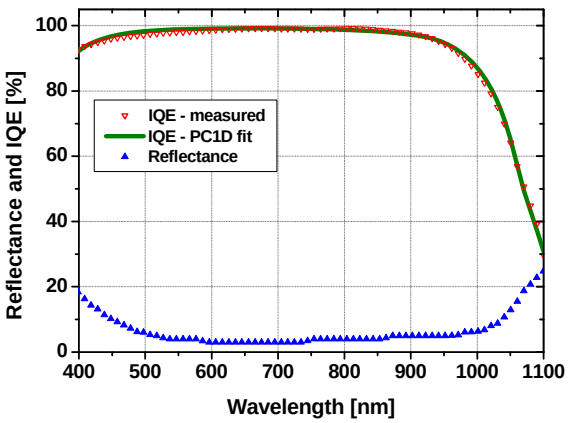

Figure 8-1: Measured IQE and reflectance curves of 18.7% efficient SSLD. The solid line is the PC1D fit (for modelling parameters, see Table A11-3).

Figure 8-1 presents the IQE of the 18.7% efficient SSLD solar cell, together with the modelled data derived from its PC1D fit. The fit parameters are given in Table A11-3. As can be seen in Figure 8-1, the cell's response to short wavelengths (< 550 nm) is lower than unity and indicates losses in both the J_{sc} and V_{oc} of the device. The relatively low emitter sheet resistivity and the high front SRV both contribute to this loss. However, increasing the emitter sheet resistivity reduces the *FF* and thus reduces the cell efficiency.

In order to identify the optimum emitter sheet resistivity, the SSLD PC1D modelling was employed, varying only the emitter resistivity and the front SRV to obtain the modified J_{sc} and V_{oc}. The variation in the *FF* was estimated using the expression for the normalised power loss P_{em} due to emitter resistivity given by [135]:

8-1)
$$P_{em} = \frac{\rho_s}{12}\frac{J_{mp}}{V_{mp}}S^2$$

where J_{mp} and V_{mp} are the current and the voltage at the maximum power point (MPP), ρ_s is the emitter sheet resistivity and S is the spacing between the metal fingers. Figure 8-2 shows the solar cell efficiency as a function of the emitter sheet resistivity. The curve illustrates the trade-off between the improvement in J_{sc} and V_{oc} and the degradation of the *FF* when increasing the resistivity. A maximum efficiency is achieved for cells with a 120-140 Ω/□ emitter.

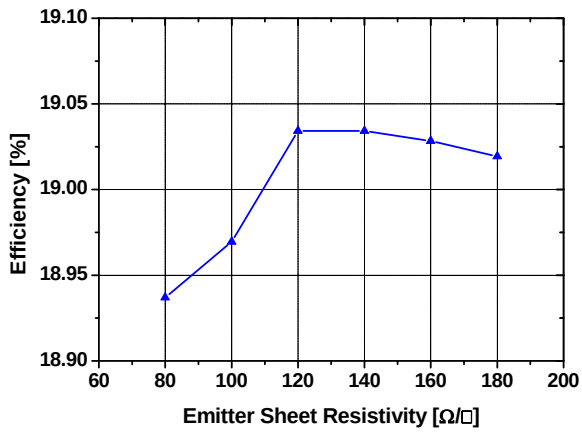

Figure 8-2: Modelled efficiency as a function of the emitter sheet resistivity. The solid line is given as a guide for the eye.

Figure 8-3 compares the IQE of a 70 Ω/□ and 120 Ω/□ SSLD solar cell emitter, as obtained from the PC1D simulation. The superiority of the 120 Ω/□ emitter cell is demonstrated by the unity spectral response at short wavelengths.

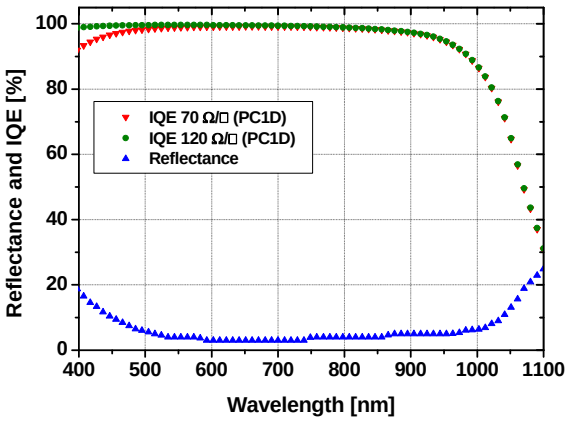

Figure 8-3: IQE of 70 and 120 Ω/□ SSLD solar cells as obtained from PC1D simulation.

Table 8-1 compares the electrical parameters of the solar cell, its fitted values and the predicted parameters of a 120 Ω/□ emitter cell. For the 120 Ω/□ cell, a front SRV of 200 cm/s was assumed; this value is based on a measurement that will be presented in Section 8.3.2 below. A 0.3% absolute increase in the solar cell efficiency is predicted for a modified emitter, mainly due to enhancement of the V_{oc}, but also by increasing the J_{sc}. It was found that reducing the front SRV without increasing the emitter resistivity has a limited impact.

Table 8-1: Electrical parameters of the 18.7% SSLD solar cell, together with the parameters obtained from the PC1D fit. The predicted parameters of a SSLD solar cell with lighter emitter (120 Ω/□) are given as well.

	Measured	**PC1D – 70 Ω/□**	**PC1D – 120 Ω/□**
J_{sc} **[mA/cm^2]**	38.0	37.9	38.3
V_{oc} **[mV]**	632.0	630.8	640.7
FF **[%]**	78.0	78.0	77.6
Efficiency [%]	18.7	18.6	19.0

It seems that some manufacturers who fabricate selective-emitter solar cells, prefer slightly heavier-doped emitters (< 90 Ω/□), under the assumption that absorption in the EVA (ethylene vinyl acetate - used for encapsulation of cells in standard modules) negates any improvement in device spectral response at short wavelengths [433]. Details relating to the absorption of light by EVA can be found for example, in Ref. [434]. Under these conditions low emitter sheet resistivity seems beneficial due to reduced resistive loss. However, the PC1D simulation predicts only a small degradation of the *FF* (-0.5%), smaller than the enhancement of the V_{oc} (+1.6%). Hence increasing the emitter resistivity to the range of 120 Ω/□ enhances the solar cell efficiency, even without improvement of the current. Development of a new EVA with lower absorption will improve solar cell efficiency even further.

Note that the minimum of the reflectance curve reveals the shading loss due to the front contacts can be estimated as ~3.2%.

8.1.2 J_0 Contribution

To gain better insight into the recombination losses, the contribution of each fabrication step to the total dark saturation current was investigated.

Sample Preparation

Commercial grade CZ *p*-type wafers with resistivity of 2 Ω.cm were used in this experiment. In order to estimate the wafer quality, one of the wafers was saw damage etched and RCA cleaned before SiN_x deposition onto both surfaces. A Si-rich SiN_x film was chosen due to its high quality of passivation. An upper-bound SRV of ~10 cm/s was measured on FZ wafers, which were fabricated in conjunction with the CZ substrate. The effective lifetime and the implied V_{oc} were measured using the QSS-PC system (generalised analysis). The dark saturation current density (J_0) associated with the implied V_{oc} was calculated using:

8-2)
$$J_0 = \frac{J_{sc}}{\exp(\frac{V_{oc}}{kT/q})}$$

A second sample was used to calculate the J_0 associated with the front surface after an emitter diffusion and subsequent processing. After alkaline texturing and full RCA cleaning, a 40 Ω/□ emitter was diffused using a conventional tube furnace. PSG removal and edge isolation increased the emitter sheet resistivity to 70-75 Ω/□. After a short dry oxidation an ARC SiN_x was deposited onto the front surface using the industrial remote PECVD system, while a Si-rich SiN_x film (identical to that used previously) was deposited onto the rear surface as a passivation layer using the laboratory PECVD system. After implied V_{oc} measurements, the total J_0 was calculated using Eq. (8-2), while the J_0 associated with the front surface was found as the difference between the total J_0 values (total J_0 after this stage and J_0 of the well passivated un-diffused wafer – see Table 8-2). The contribution of the emitter and the texturing to the total J_0 and to the reduction in the implied V_{oc} was calculated using PC1D.

A third experiment was carried out to determine the contribution of the rear Si-Al interface to J_0. To do this, the Si-rich film was removed from the rear surface and was replaced by screen printed Al. The V_{oc} of the device was then measured using a multimeter under one-sun conditions after firing the Al. It was then remeasured after the formation of a selective emitter by laser doping. Finally, Ni and Cu photo-plating were used to form the front grid and contact pads. The Ni sintering was performed at

400°C using an open air belt furnace. The V_{oc} of the finished solar cells was measured under one-sun illumination. Table 8-2 summarises the V_{oc} and J_0 values after each fabrication step and the contribution of each step to the total J_0. Note that the calculation is carried out under the assumption that J_{01} (ideality factor of unity) is the dominant recombination process. This assumption is reasonably accurate due the small percentage of LD regions, which contribute also to J_{02}. It can be seen that the rear surface contributes more than 50% of the total dark saturation current of the finished solar cell. A similar rear side contribution was calculated for the BC solar cell fabricated on a similar 1 Ω.cm CZ *p*-type substrate by Wenham [44]. The post-metallisation improvement is explained by an improved front surface and bulk passivation due to hydrogenation. As shown in the previous chapter, the degradation typically associated with metallisation is minimised by the use of photoplating. Furthermore, the heavy doping beneath the metal isolates this high recombination interface from the active area of the cell, thus minimising its influence. These results emphasise the importance of high quality rear passivation in order to boost the electrical performance of these cells.

Table 8-2: Calculated J_0 of different fabrication steps

Process	V_{oc} / Implied V_{oc} [mV]	Total J_0 [A/cm^2]	J_0 of the process [A/cm^2]	% of total J_0
Wafer	688.4 [a]	4.2×10^{-14}	4.2×10^{-14}	8
Texturing and emitter	666.3 [b]	1.0×10^{-13}	5.9×10^{-14}	11
SiO_2/SiN_x passivation	653.7 [a]	1.7×10^{-13}	6.6×10^{-14}	13
Rear contact	628.6	4.6×10^{-13}	2.9×10^{-13}	**56**
Front laser doping	624.6	5.4×10^{-13}	7.9×10^{-14}	----
Metallisation	625.5	5.2×10^{-13}	-1.9×10^{-14}	12 [c]

[a] Implied V_{oc}.

[b] PC1D calculation.

[c] For both laser doping and metallisation.

8.1.3 Summary

Two main loss mechanisms were identified in the 18.7% efficient SSLD solar cell. The first one is the relatively heavily-diffused emitter and the corresponding poor front surface passivation. Both were found to degrade the efficiency by 0.3-0.4% absolute. The second is attributed to the rear surface design, as indicated by its contribution to the total dark saturation current. Reducing the rear surface recombiantion was shown to enhance the efficiency to above 20% (see Chapter 5). The following sections present preliminary work performed to achieve this goal.

8.2 Local BSF Formation

Local BSF (LBSF) beneath metal contacts improves solar cell performance by isolating the high recombination Si-metal interface from the active regions of the cell and by reducing the contact resistance between the Si and the metal. Furthermore, when SiN_x is used for rear surface passivation, the LBSF plays a critical role in reducing possible shunts. It was found that the J_{sc} of SiN_x passivated solar cells is lower than that obtained for SiO_2 passivated cells [299]. Initially this phenomenon was attributed to the injection level dependence of the SRV obtained by SiN_x passivation [299] or to reduced internal reflectivity [298]. However, it was soon realised that shunting between the *n*-type inversion layer beneath the SiN_x and the rear contact is the source of this reduction [435-436]. It was shown that this shunting can be eliminated by a potential barrier such as that created by an LBSF [303, 436]. This section investigates a new method to form an LBSF using laser doping.

8.2.1 Sheet Resistivity and Dopant Concentration

Obtaining high doping concentration using boron SOD is challenging, mainly due to the relatively low boron concentration in these solutions (4-10% compared to > 30% in the phosphorus SODs [437]). In this section four commercially available boron SODs are compared and evaluated.

Sample preparation

Textured *p*-type wafers were used to evaluate the sheet resistivity. After an alkaline texturing and full RCA clean, an ARC SiN_x (n_r = 2.1, d = 75 nm) was deposited onto the front surface using the industrial PECVD system. After applying different boron SODs onto the SiN_x film, laser doping was performed using three different laser diode currents. In each laser condition three lines and one measurement pad (15 mm × 2 mm) were created. The four-point probe method was employed for the sheet resistivity measurements using an appropriate correction factor.

Results and discussion

Figure 8-4 presents the sheet resistivity as a function of the laser diode current for the four tested boron SODs. A significant difference between the solutions is apparent. However, SHR below 20 Ω/□ was obtained by two solutions, which is adequate for LBSF formation. It is interesting that the lowest sheet resistivity was obtained by the B155 solution, which contained the lowest boron concentration (4%, compared to 8% and 10% in B200 and B219, respectively [437]). It was found that special additives in this solution allow more boron to be driven into the silicon [438].

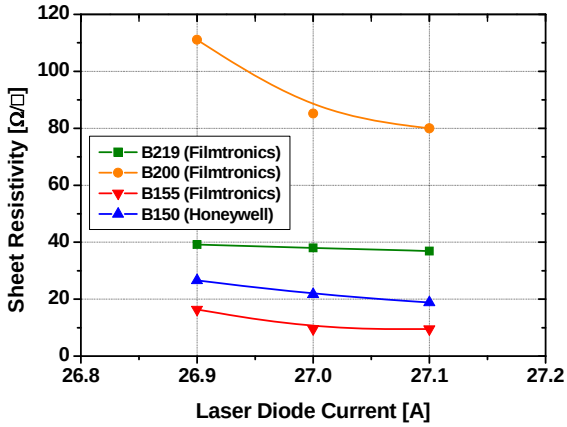

Figure 8-4: Sheet resistivity as a function of the laser diode currents for the four boron SODs. The solid lines are given as a guide for the eye.

In order to detect the surface concentration and the junction depth, SIMS measurements were taken using two CZ *p*-type wafers. After saw damage etch and full RCA clean, ARC SiN_x was deposited onto one surface as described previously. Two different SODs (B150 and B155) were spun onto the surface prior to the laser doping process. Due to the limited resolution of the SIMS system used, the measurement was carried out on a 15 mm × 2 mm measurement pad. Figure 8-5 shows the results of this measurement: a surface concentration exceeding 1×10^{19} cm^{-3} was achieved with both SODs, which is sufficient for an ohmic contact between the Si and the plated metal [230, 412] and to eliminate the shunt between the *n*-type inversion layer and the metal contact. The SHR was calculated using the SIMS data and PC1D modelling and found to be in good agreement with the measurements presented in Figure 8-4. Due to the lower SHR achieved with the B155, it was used in this thesis as a boron SOD.

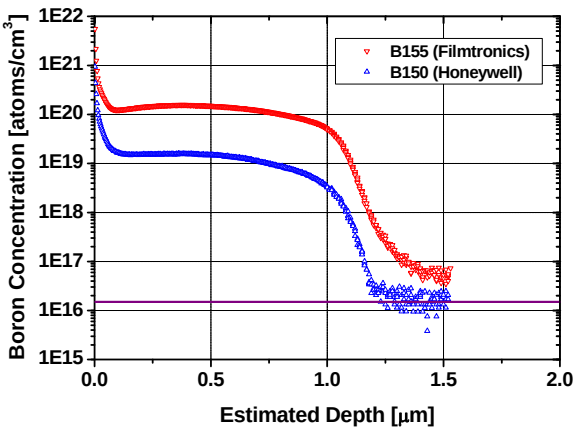

Figure 8-5: SIMS measurements of two different boron SODs. The solid line represents the boron level in the substrate.

The influence of the laser power on the surface concentration and the junction depth was studied using planar *n*-type (2.1 Ω.cm) samples prepared with the phosphorus samples presented in Section 7.3.2.

Sample preparation

After a saw damage etch and full RCA clean, a thin (~18 nm) dry oxide was thermally grown in a conventional open tube furnace, followed by 15 min annealing at 1000˚C in nitrogen. An ARC SiN_x (n_r = 2.1, d = 75 nm) was then deposited onto the front surface using the laboratory PECVD system (see Table 5-1 for deposition parameters). After applying boron SOD onto the SiN_x film (B155), laser doping was performed using different laser diode currents. In each laser condition three lines and one measurement pad were created. A SIMS system with a resolution capability of 10 μm was employed and therefore was able to detect the atomic concentration in a single LD line. The SOD was removed by a short dip in HF solution prior to the measurement.

Results and discussion

The measurement results are given in Figure 8-6. Similar to the results obtained with phosphorus SOD (see Figure 7-9), increased laser power increases the junction depth, with almost no variation of the surface concentration. The deeper junction achieved by the phosphorus dopants is attributed to the larger diffusion coefficient of phosphorus in molten Si (see Table 7-1). Note the contrast between the shapes of the graphs presented in Figure 8-6 and in Figure 8-5. The observed decrease in concentration for depths greater than 0.5 μm (in Figure 8-6) may be attributed to the Gaussian shape of the laser beam and the resolution limitation of the SIMS measurement system. As explained previously, at depths greater than 0.5 μm below the surface the SIMS system begins detecting signal from the adjacent silicon substrate that has not been melted, reducing the average detected concentration. This effect does not arise when a wide measurement pad is used (Figure 8-5). However, forming a measurement pad requires overlap between the LD lines, which may modify the atoms concentration and reduce the sheet resistivity.

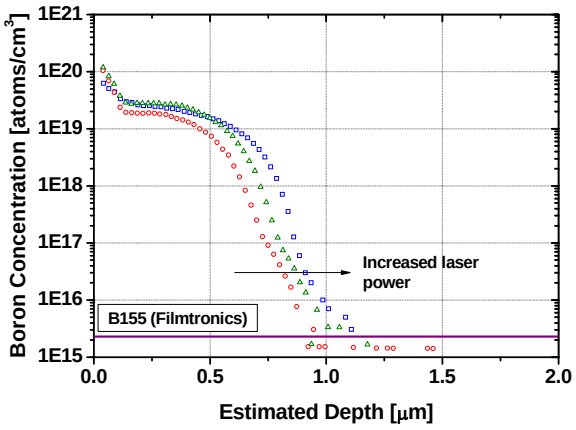

Figure 8-6: SIMS measurements of LD lines created by three different laser diode currents. The solid line represents the phosphorus level in the substrate.

8.2.2 Electron Beam Induced Current

An EBIC system was employed to image the junction formed by the boron SOD.

Sample preparation

A textured CZ *n*-type wafer with resistivity of 6 Ω.cm was used in this part of the study. The laser doping was performed using boron SOD (B155) with seven different laser diode currents. Three closely-spaced LD lines were formed at each laser condition on the same wafer. Subsequently, the SOD was removed by a short dip in HF solution prior to a Piranha etch cleaning. The rear contact was formed by evaporating Al on the back surface and sintering it for 30 min at 850˚C. Finally, an EBIC scan employing a 4 keV electron beam was performed for the cross section and planar section of each line to determine the junction location and associated parameters.

Results

Figure 8-7 presents superimposed SE+EBIC images of representative LD lines. It is clear that *p*-*n* junctions were formed for the entire range of diode currents. Image (a) shows an SE+EBIC image of LD lines created with low diode current. The EBIC signal is strong in the entire doped area, indicating a shallow junction (< 220 nm). Image (c) presents the LD lines formed with higher diode current. The dark area in the middle of the line indicates a deeper junction in this region. Image (d) demonstrates near-perfect junction formation despite strong ablation.

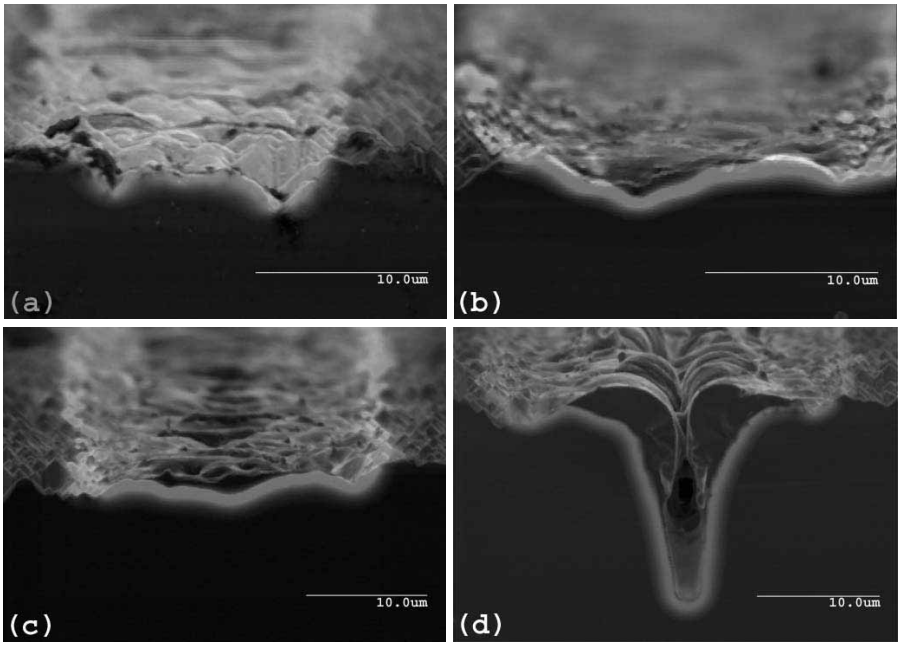

Figure 8-7: SE+EBIC images of LD lines formed with different laser diode currents on *n*-type, textured substrate with boron SOD: 25.9 A (a), 26.9 A (b), 27.4 A (c) and 28.6 A (d).

8.2.3 Summary

It was shown that LBSF can be formed by laser doping. High surface concentrations - above 1×10^{19} cm^{-3} - were detected at different laser diode currents, ensuring the formation of ohmic contacts with very low contact resistance [439]. Note that these concentrations are higher than those reported by others [66] and are assumed to prevent formation of shunts between the inversion layer beneath the SiN_x layer and the rear metal contacts. EBIC images demonstrate the formation of uniform laser-doped junctions at a wide range of laser diode currents, even when ablation occurs.

8.3 The Double Sided Laser-Doped Solar Cell

It was shown in the previous section that the rear surface contributes more than 50% of the total dark saturation current of the SSLD. It was shown that improving the rear surface passivation can enhance the cell efficiency to above 20%. This section presents preliminary work to develop a novel SiN_x-passivated DSLD solar cell structure. Due to equipment limitations it was not possible to perform the metallisation of the developed structure until a later phase of the project. Therefore the fabrication process was optimised up to the metallisation. It is assumed that due to the heavy diffusion beneath the contacts the device performance will be independent of the SRV at the Si-metal interface and therefore, the metallisation process will not significantly affect the total device dark saturation current or degrade the device performance.

8.3.1 Fabrication Sequence

The fabrication sequence of the novel DSLD solar cell has been developed based on conclusions drawn from experiments presented in previous chapters and sections.

Figure 8-8 presents a schematic of the DSLD solar cell structure. The main features of this structure are the well-passivated rear surface, the laser-doped selective emitter and the LBSF beneath the rear metal contact, also created by laser doping.

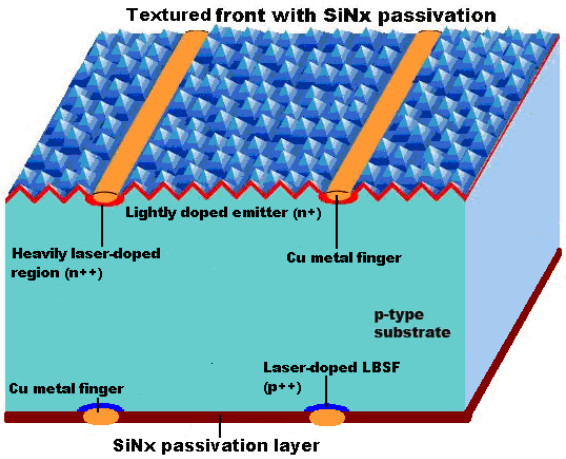

Figure 8-8: The DSLD solar cell structure schematic.

The wafers were alkaline textured prior a full RCA clean and ~120 Ω/□ emitter diffusion. After a short dry oxidation and annealing at 1000°C for 15 min, an ARC SiN_x was deposited onto the front surface. NaOH (12.5%, 55°C, 10 min) was used to etch the lightly doped *n*-type layer from the edges and the rear. Note that the SiO_2/SiN_x stack layer serves as a mask for this process; hence the emitter profile is not influenced by it. Following an RCA clean, a SiN_x layer was deposited onto the rear surface as a passivation layer, as it was shown previously to provide superior passivation quality for the low resistivity *p*-type substrate. Front and rear laser doping were carried out to create the selective emitter and LBSF, respectively. Finally, Ni and Cu were electrolessly plated to form the front and rear metal contact simultaneously. It was not possible to apply photoplating to the DSLD structure due to the selective plating on *n*-type surfaces only. Note that the relatively short high-temperature processes make this cell structure very suitable for commercial application and for mc-Si substrates.

In industrial applications, there are some benefits to performing the edge isolation prior to the oxidation, mainly due to commonly-available wet rear isolation systems. Figure 8-9 provides the fabrication sequence both in laboratory and commercial environments, while Table A15-1 summarises the process parameters.

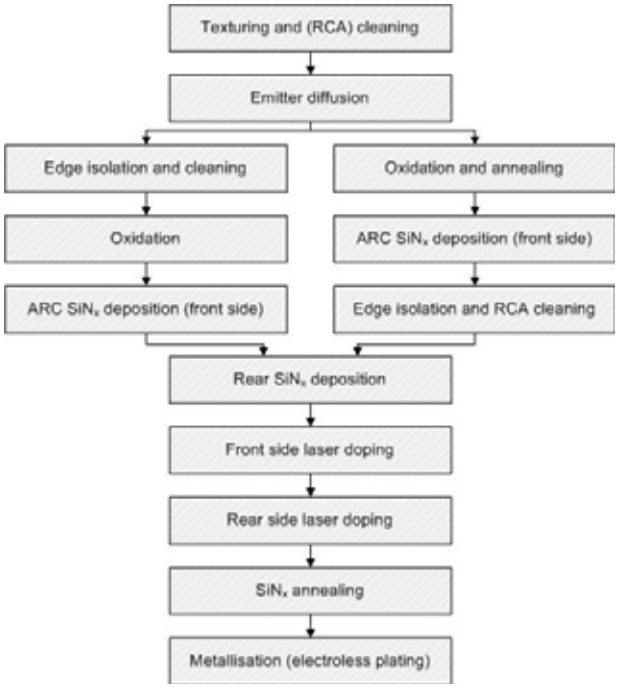

Figure 8-9: Industrial (left) and laboratory (right) DSLD fabrication sequences.

8.3.2 Front Surface Passivation

The front passivation of the SSLD solar cells presented in previous chapters is based on SiO_2/SiN_x stack layer. It was shown in Chapter 6 that this stack layer reduces the formation of laser-induced defects. Furthermore, it was shown that this layer minimises over-plating of metal during electroless plating [391]. Comparisons between SiN_x and the SiO_2/SiN_x stack as passivation layers for n^+ emitters can be found in the literature; however, contrary results were reported for emitters with resistivities in the vicinity of 100 Ω/□ [271, 288-289]. In order to verify the published results and to assess the passivation quality, this section compares the passivation quality of SiN_x and the SiO_2/SiN_x stack layer for a 120 Ω/□ emitter. The calculated SRV is then used in PC1D modelling of DSLD and SSLD solar cells. Note that due its poor ARC properties and incompatibility with industrial environments, SiO_2 as a single layer was not included in this comparison.

Sample Preparation

Ten CZ *p*-type wafers with resistivity of 1 Ω.cm were used to evaluate the passivation quality. After saw damage etch and full RCA clean, both of the surfaces were diffused to create a similar ~120 Ω/□ layer using an open tube furnace and solid phosphorus sources. A short dry oxidation followed by 15 min annealing in N_2 ambient was used to grow a thin oxide (~18 nm) and to drive in the dopants. The wafers were then split into two groups:

1. SON group: ARC SiN_x ($n_r \sim 2.1$, $d = 75$ nm) was deposited onto both surfaces using the laboratory PECVD system (see Table 5-1 for deposition parameters).
2. SIN group: the SiO_2 layer was removed using an HF dip prior to ARC SiN_x deposition.

The effective lifetime and the implied V_{oc} were measured before and after annealing at 680°C in an open air belt furnace. Table A12-1 summarises the zone settings.

Results

Table 8-3 summarises the average one-sun implied V_{oc} of both of the groups, before and after the annealing process. The SON group demonstrates a slightly higher implied V_{oc} in both cases (6-8 mV). Superiority of the stack layer as an n^+ emitter passivation layer was found in the literature [270]. However, it was shown that both layers provide similar passivation for emitters with resistivities below 100 Ω/□ [271, 288-289].

Table 8-3: Average one-sun implied V_{oc} of both groups, before and after annealing.

	SON Group	SiN Group
As-deposited [mV]	654.5	648.4
Post annealing [mV]	674.1	666.3

Figure 8-10 presents the effective lifetime as a function of the injection level of representative samples from both groups after annealing.

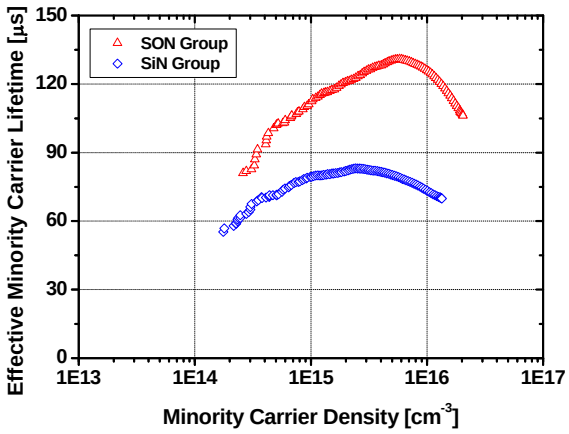

Figure 8-10: Effective lifetime as a function of injection level of representative samples from the SiN and the SON groups (post-anneal).

In order to estimate the SRV of the SiO_2/SiN_x stack layer on textured n^+ emitters, four FZ p-type wafers with resistivity of 1 Ω.cm were used. The wafers were

textured using an anisotropic alkaline etch solution, which formed 1-2 µm-high pyramids and resulted in a wafer thickness in the 200-210 µm range. The rest of the process was similar to that described above.

Figure 8-11 shows a sheet resistivity mapping of representative sample as obtained using a Semilab WD-2000, while Table 8-4 summarises the average one-sun implied V_{oc}, effective lifetime (at one-sun) and the maximum SRV (at injection level of 1×10^{15} cm^{-3}) values before and after annealing.

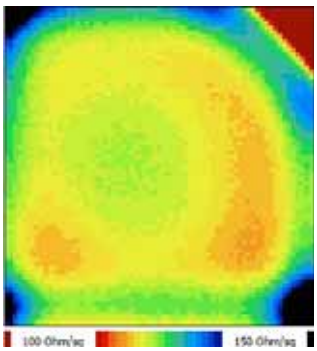

Figure 8-11: Semilab sheet resistivity mapping of a representative sample.

Table 8-4: Average one-sun implied V_{oc}, effective lifetime and SRV values, before and after annealing. STD values are given in brackets.

	One-sun implied V_{oc} [mV]	**Effective lifetime [µm]**	**Max SRV at 1×10^{15} cm^{-3} [cm/s]**
As-deposited [mV]	671.0 (2.6)	95.7 (9.1)	121
Post annealing [mV]	684.2 (4.0)	149.0 (19.0)	59

Summary

It was shown that the SiO_2/SiN_x stack layer provides better passivation than an ARC SiN_x film for an n^+ emitter. Better passivation together with reduced laser-induced defects and over-plating makes the stack layer the preferred option for front surface passivation films for LD solar cells.

8.3.3 Initial Batch

A first batch of DSLD solar cells was fabricated on CZ *p*-type 2 Ω.cm substrates following the fabrication sequence described above (Figure 8-9). Table 8-5 provides the average one-sun implied V_{oc} after rear SiN_x deposition and front-side laser doping. The significant drop in the implied V_{oc} was unexpected, as the typical voltage drop for SSLD cells was only ~5 mV. Though a high defect density within the LD lines might explain this decrease, investigation of the lines using an optical microscope, as shown in Figure 8-12 (a), did not reveal an unusual defect density.

Degradation of the rear surface passivation during the baking of the phosphorus SOD (P512) might instead explain this behaviour.

After spinning the SOD on the front surface, the wafer was placed in the oven on a sheet of Al foil and baked at 120°C in air ambient to dry out the solvents and any moisture in the SOD. It is known that phosphoric acid at high temperature etches SiN_x [331]; however, according to the data sheet, P512 does not contain phosphoric acid [437]. Furthermore, no change of the ARC SiN_x was observed previously, when the P512 was employed as a SOD for SSLD. It was suspected that during the spinning some of the P512 wrapped some region of the rear surface as well. Due to the high temperature between the wafer and the Al sheet, which is higher than the ambient temperature, the etch rate of the SiN_x by the high concentration phosphorus solution is enhanced significantly. To confirm this suspicion, P512 was spun onto the rear surface of two wafers. The wafers were then baked at 120°C for 30 min with the rear surface facing downward. Figure 8-12 (b) presents a digital image of the wafers after this process. The SiN_x was etched away from most of the surface, indicating that during standard SOD baking, the rear passivation may be degraded. As a result, wafers were placed on small pins during subsequent baking to ensure that some gap exists between them and the Al sheet. Note that the film etch rate by phosphoric acid at room temperature is negligible and is therefore suitable for use as a SOD provided the wafers are not heated up and the equipment allows that.

Table 8-5: Average one-sun implied V_{oc}, after rear deposition and front LD.

	Implied V_{oc} [mV]
After rear deposition	657.7
After front laser doping	646.6
Change compared to previous	*-11.1*

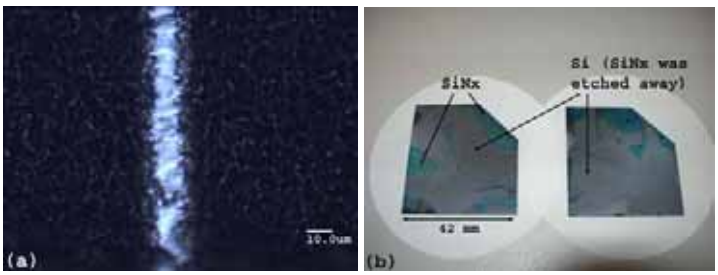

Figure 8-12: Micrograph image of LD line on front surface (a) and digital image of the rear side of SiN_x passivated samples after baking with P512.

The chemical compositions of commercial SOD solutions are often unknown due to confidentiality. Therefore, in addition to the SHR and dopant concentration, a test needs to be performed to determine the effects of the SOD on the surface coating, if any.

8.3.4 Influence of SiN_x film Parameters

In Chapter 5, it was found, using a test structure, that Si-rich SiN_x films provide better passivation than N-rich films. This section verifies the results using the DSLD solar cell structure. The influence of the rear SiN_x film parameters on the laser process is studied as well.

Sample preparation

Four groups of four 16 cm^2 wafers were fabricated according to the standard sequence (Figure 8-9). The only difference between the groups was the rear surface SiN_x film: four gas ratios were used to deposit SiN_x with refractive indices between 2.12 and 2.6, as measured by dual mode ellipsometer at 632.8 nm. The thickness of all the films was in the 74-76 nm range. Prior to the rear laser doping process, the dependence of the obtained SHR on the refractive index was tested using two laser diode currents. The measurement was taken using the four-point probe technique with the appropriate correction factor for a 15 mm × 2 mm measurement pad.

Results

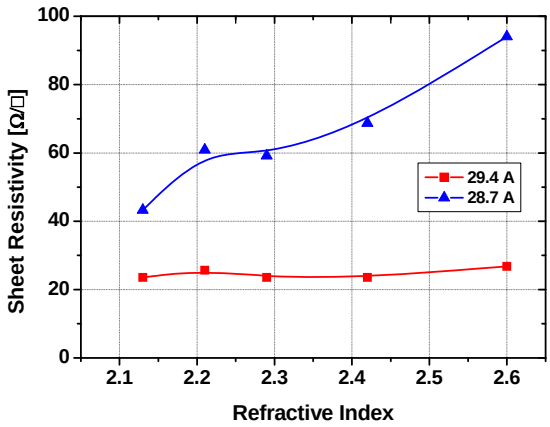

Figure 8-13: Sheet resistivity as a function of the refractive index of the SiN_x for two laser diode currents. The lines are given as a guide for the eye.

Figure 8-13 presents the results of these measurements, while Table 8-6 includes the reflectance of each film, coated with SOD, at 532 nm. At low laser diode current, a clear correlation between the reflectance and the SHR can be seen. High reflectance reduces the laser energy absorbed by the substrate, decreasing the melting time and the amount of dopants that are able to diffuse into the molten region. Furthermore, when a Si-rich film is employed, some laser energy is absorbed in the film in addition to the reflectance loss. At high diode current, the SHR is quite steady across all the indices. It is assumed that at this diode current, the process becomes source limited, so the available laser energy no longer influences the obtained SHR.

Table 8-6: Reflectance at 532 nm for different refractive index SiN_x films (with SOD).

SiN_x index	Reflectance [%]
2.21	5.4
2.29	8.7
2.42	22.7
2.61	27.1

Figure 8-14 shows micrographs of representative LD lines on the front (a) and the rear (b) surfaces, while image (c) provides a three dimensional (3D) image of the LD line presented in (a). As can be seen a uniform and continuous melting was obtained on both surfaces.

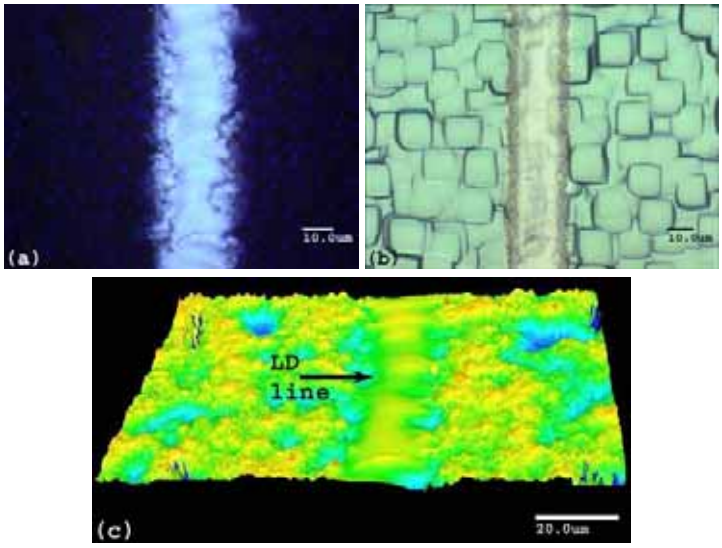

Figure 8-14: Micrographs of laser-doped lines: front surface (a) and rear surface (b). Image (c) is the 3D image of the LD line presented in (a).

Table 8-7 summarises the average one-sun implied V_{oc} after different fabrication steps of the four groups. Similar to the results presented in Chapter 5, it seems that Si-rich films provide better as-deposited passivation. The contributions of the front and rear laser doping processes to the total dark saturation current is similar across all the groups, thus is not influenced by the SiN_x parameters. The final average one-sun implied V_{oc} follows the trend of the as-deposited values; that is, Si-rich SiN_x-passivated solar cells demonstrate higher implied V_{oc}. Note that one-sun implied V_{oc} in the range of 660 mV after the LD processes was obtained for two groups.

Table 8-7: Average one-sun implied V_{oc}, after different fabrication steps, for four different rear passivation SiN_x films.

	GR = 1.14 [mV]	GR = 1.07 [mV]	GR = 0.88 [mV]	GR = 0.77 [mV]
After rear deposition	640.9	642.6	663.6	660.8
After front laser doping	635.1	639.2	657.6	658.1
Change compared to previous	*-5.8*	*-3.4*	*-6.0*	*-2.7*
After rear laser doping	628.8	633.2	647.7	650.3
Change compared to previous	*-6.3*	*-6.0*	*-9.9*	*-7.8*
After SiN_x annealing	**636.1**	**638.3**	**660.3**	**660.3**
Change compared to previous	*+7.3*	*+5.1*	*+12.6*	*+10.0*

Figure 8-15 presents the effective lifetime as a function of the injection level of representative sample from the GR = 0.77 group. The annealing process enhances the effective lifetime to a value similar to the un-processed wafer. Figure 8-16 demonstrates the same by providing the PL images of the same wafer at different points in the fabrication process. All the images were taken under the same conditions and are presented in the same scale.

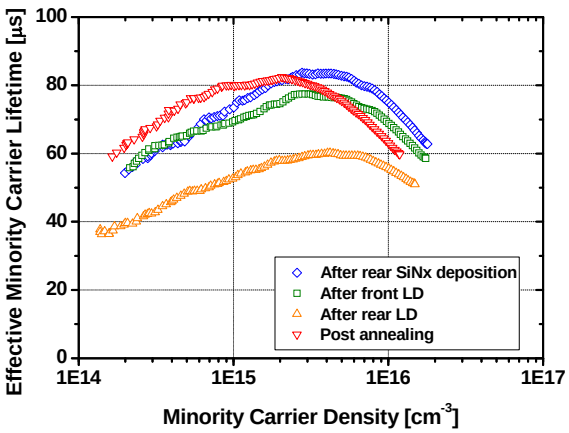

Figure 8-15: Effective lifetime as a function of the injection level after different fabrication steps.

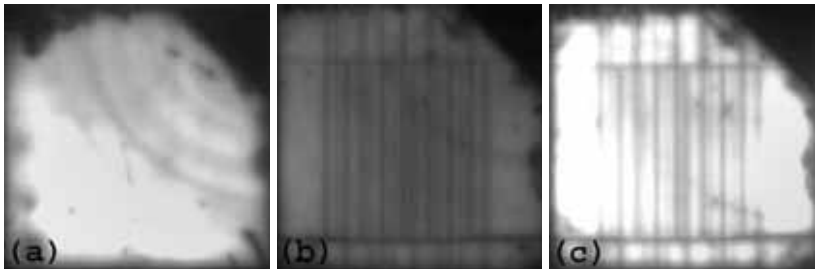

Figure 8-16: PL images after rear SiN_x deposition (a), after front and rear laser doping (b) and after annealing at 680°C (c).

A similar experiment was performed to investigate the influence of the rear SiN_x thickness on the solar cell parameters. The fabrication sequence is similar to previous one. The only modification is the rear SiN_x deposition: in this experiment the GR was kept constant at 0.88 ($n_r \sim 2.4$), while the deposition time was varied in the range of 60-105 sec. Table 8-8 summarises the average one-sun implied V_{oc} after different fabrication steps. Similar to results presented in Chapter 5, the as-deposited implied V_{oc} values are similar, but the post-annealing results indicate that it may be beneficial to employ a thicker film.

Table 8-8: Average one-sun implied V_{oc} after different fabrication steps for three different thicknesses of rear passivation SiN_x film.

	60 sec [mV]	**82 sec [mV]**	**105 sec [mV]**
After rear deposition	654.5	654.8	654.0
After front laser doping	651.8	652.6	648.2
Change compared to previous	*-2.7*	*-2.2*	*-5.8*
After rear laser doping	644.0	646.0	641.2
Change compared to previous	*-7.8*	*-6.5*	*-7.0*
After SiN_x annealing	**656.2**	**661.8**	**663.5**
Change compared to previous	*+12.2*	*+15.8*	*+22.3*

Summary

The first batches of DSLD demonstrated implied V_{oc} values above 660 mV before metallisation, which is an improvement of 25-30 mV over SSLD cells at the same stage. The implied V_{oc} after annealing was found to be similar to the initial value, hence to balance the losses due to front and rear laser doping processes. Similar to the finding in Chapter 5, it was found that devices passivated with Si-rich SiN_x and with thicker films demonstrate higher one-sun implied V_{oc}.

8.3.5 Optimised Cells

Two batches of DSLD solar cells (16 cm^2) were fabricated according to the standard sequence outlined before. In accordance with conclusions from previous experiments, a thick Si-rich SiN_x film (GR = 0.77, 105 sec) was used as rear surface passivation. Note that both of the batches were fabricated according to the same sequence.

Results

An electrochemical capacitor-voltage (ECV) profiler (Dage CVP21) was employed to profile the emitter [440]. The result of this measurement together with its PC1D fit is presented in Figure 8-17. The difference between the measurement and

the fit is assumed to arise from the so-called *emitter-push effect*, where stress induced by high phosphorus concentration enhances the diffusion velocity above that expected from isoconcentration studies [441-443]. Good agreement was found between the profile and the 120 Ω/□ value obtained by the four-point probe measurement.

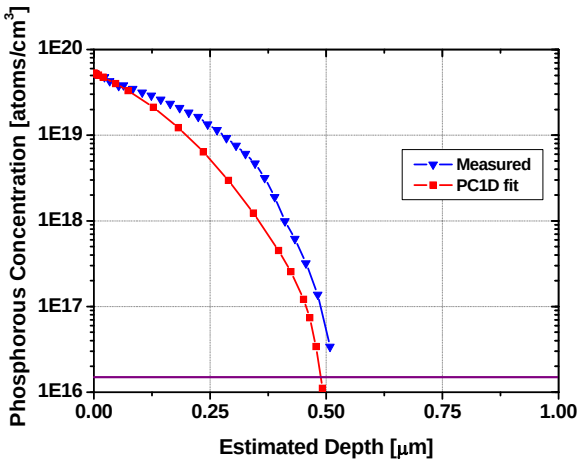

Figure 8-17: Emitter profile – atomic concentration as a function of estimated depth, as obtained by electrochemical CV profiler. The solid line represents the substrate doping level.

The laser conditions were chosen to provide uniform and continuous melting as shown in Figure 8-18 micrographs. The sheet resistivity was measured using the measurement pads and was estimated to be 9 Ω/□ and 22 Ω/□ for the front and the rear LD lines, respectively.

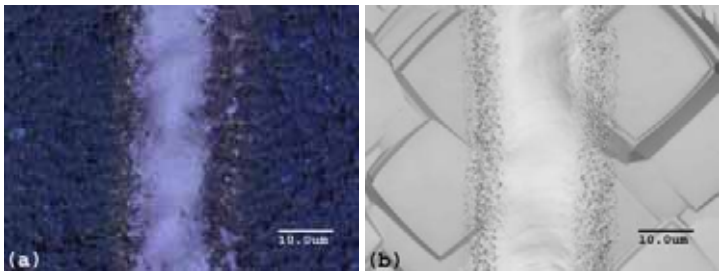

Figure 8-18: Micrographs of laser-doped lines: front surface (a) and rear surface (b).

Table 8-9 summarises the average one-sun implied V_{oc} of the two batches after different fabrication steps. The variation of the as-deposited implied V_{oc} is due to process variation (probably PECVD). Although the drops in the implied V_{oc} after the front and the rear laser doping seem similar, they represent different contributions to the total J_0, due to the different implied V_{oc}. Table 8-9 also includes the contribution of each fabrication step to the total J_{01}. It is assumed that J_{01} is the main contributor for the total dark saturation current, due to the large distance between the rear LD regions and the junction and the small percentage of LD areas on the front surface. Note that the calculated value after the front laser doping provides the upper

boundary, due to addition contribution from the J_{02} component. The significant post-annealing enhancement demonstrates the ability of this process to improve solar cell performance, even in cases where the as-deposited passivation quality is relatively low (for example batch B). The high implied V_{oc} at the end of the fabrication process (prior to the metallisation) demonstrates the capability of the DSLD structure to achieve high efficiencies exceeding 20%. Due to heavy doping beneath the metal contacts, it is assumed that the metallisation process does not significantly degrade the performance of the device. This assumption is also supported by the conclusions of the previous chapter.

Table 8-9: Average one-sun implied V_{oc} *and* J_{01} after different fabrication steps for two batches with the same process sequence.

	Batch A		**Batch B**	
	Implied V_{oc} [mV]	**J_{01} [A/cm^2]**	**Implied V_{oc} [mV]**	**J_{01} [A/cm^2]**
After rear deposition	671.7	8.2×10^{-14}	648.7	2.0×10^{-13}
After front laser doping	664.9	1.1×10^{-13}	640.9	2.8×10^{-13}
Change compared to previous	*-6.8*	*$+2.5\times10^{-14}$*	*-7.8*	*$+7.5\times10^{-14}$*
After rear laser doping	657.4	1.4×10^{-13}	633.7	3.7×10^{-13}
Change compared to previous	*-7.5*	*$+3.7\times10^{-14}$*	*-7.2*	*$+9.3\times10^{-14}$*
After SiN_x annealing	**671.4**	8.2×10^{-14}	**682.0**	5.4×10^{-14}
Change compared to previous	*+14.0*		*+48.3*	

Figure 8-19 presents the effective lifetime as a function of the injection level of representative samples from each batch. The impressive post annealing enhancement is clearly shown, especially in image (b).

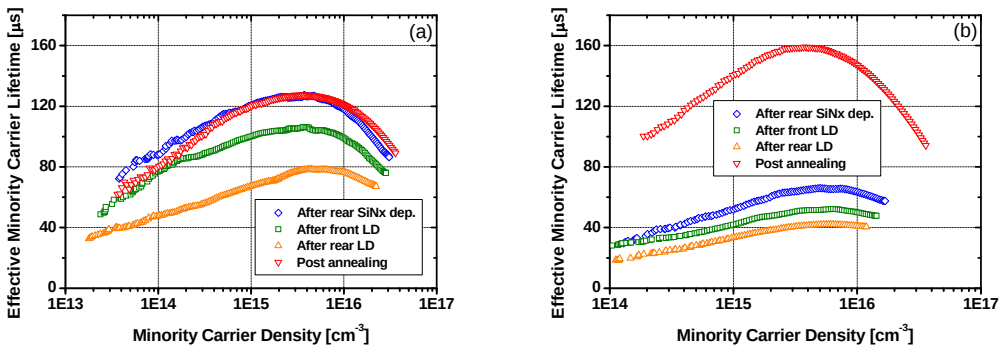

Figure 8-19: Effective lifetime of representative samples as a function of the injection level after different fabrication steps: batch A (a) and batch B (b).

Figure 8-20 shows PL images of a representative cell from batch B after different fabrication steps. All the images were taken under similar conditions and are

presented in the same scale. Note the clear degradation after the rear laser doping process and the significant improvement due to the annealing.

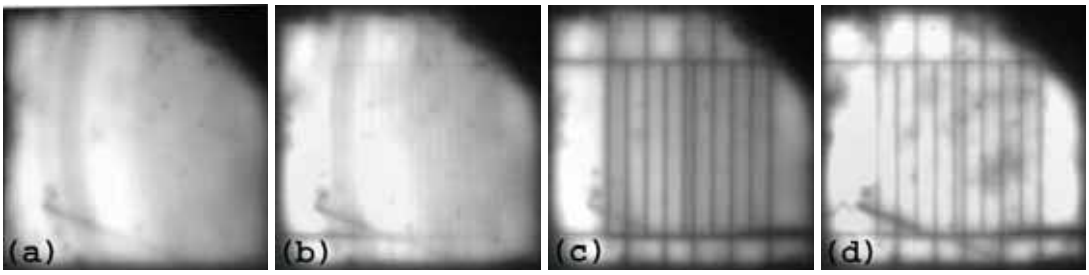

Figure 8-20: PL images of rear SiN_x deposition (a), after front laser doping (b), after rear laser doping (c) and after annealing at 680°C (d).

Summary

The initial results of the new DSLD structure yield an implied V_{oc} exceeding 680 mV before the metallisation, demonstrating the potential of this cell design to achieve efficiencies above 20%. Low SHR both for selective emitter and LBSF were demonstrated. These low values ensure low contact resistance and isolation of the bulk from the high recombination Si-metal interface.

It was noted that the degradation after the rear laser doping is greater than that seen after front-side doping; the next section investigates the source of this difference.

8.3.6 Degradation of the Passivation

Though laser-induced defects were investigated in Chapter 6, the influence of laser doping on the passivation layer has not been discussed. Furthermore, an implied V_{oc} drop above 7 mV was measured after rear laser doping (see Table 8-9), which is above the expected value from PC1D simulation. This section therefore investigates the influence of the laser doping process on the adjacent passivation layer.

A PC1D simulation was used to estimate the maximum drop of the implied V_{oc} after the rear laser doping process. As a starting point, a device with 120 Ω/□ emitter and an SRV of 100 cm/s for both surfaces was simulated. The bulk lifetime was chosen so as to match the implied V_{oc} measured after the front laser doping process (according to Table 8-9). These parameters are summarised in Table 8-10 in the "Region 1 – Before" column. The post-rear-LD case was simulated by adding a second region to the model ("Region 2"). In order to estimate the worst case scenario the effective lifetime of this region was chosen to be 1 μs and the rear SRV to 1×10^7 cm/s. The predicted drop in the V_{oc} was calculated under the assumption that the laser doping area covers 3% of the total device area. A drop of ~3 mV was predicted, less than the measured one.

Interestingly rear laser doping had a greater negative impact on the implied V_{oc} than front-side doping, although the latter may increase the J_{02} due to the short distance to the *p-n* junction.

Table 8-10: PC1D simulation parameters.

	Region 1 Before	Region 1 After	Region 2
Thickness [μm]	180	178.5	1.5
Resistivity [Ω.cm]	2	2	20
Emitter sheet resistivity [Ω/□]	120	120	----
Effective lifetime [μs]	209	209	1
SRV front [cm/s]	100	100	0
SRV rear [cm/s]	100	0	1×10^{7}

PL imaging system with a magnification lens was used to investigate the influence of the laser doping on the passivation layer. The resolution of the obtained image was found to be 30 μm/pixel. Localised degradation of surface passivation influences the voltage (and thus the PL signal) not only in the degraded region, but also in surrounding areas, due to carrier diffusion. In order to minimise the latter effect, a very low-quality boron-doped (N_A = ~1×10^{18} cm^{-3}) *p*-type wafer was used. After a full RCA clean, SiN_x was deposited (GR = 1.14, 105 sec) onto the front surface using the laboratory PECVD system. The effective lifetime was too low to be measured and is assumed to be less than 1 μs; therefore, the diffusion length in this type of wafer is estimated to be below 40 μm. A single laser line was defined in the middle of the wafer without applying any SOD. Figure 8-21 presents a micrograph of the 28 μm-wide laser line.

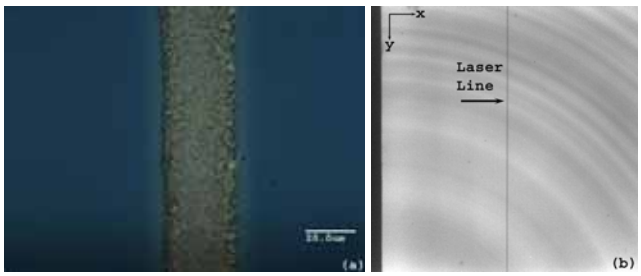

Figure 8-21: Micrograph (a) and PL image (b) of the laser line.

The PL image was then analysed using MATLAB code, which sums and normalises the PL counts in each column (*y*-axis - see Figure 8-21 (b)). Figure 8-22 presents the normalised PL counts as a function of the distance from the centre of the laser line (x = 0). It is clear that the degraded region (150 μm) is much wider than the laser line width (28 μm). Furthermore, the region width is also larger than the

calculated diffusion length. This indicates that the laser process influences the passivation quality in an area much wider than the melting zone.

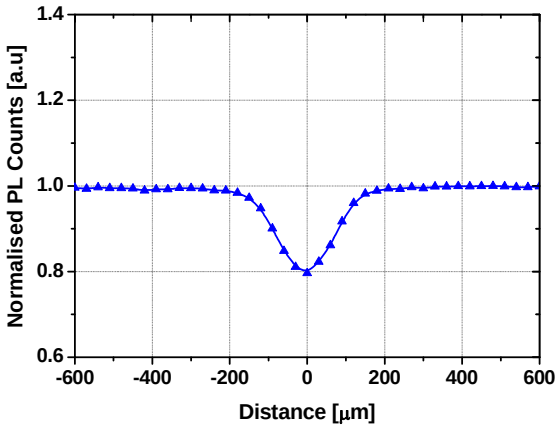

Figure 8-22: Normalised PL counts as a function of the distance from the centre of the laser line.

In order to compare between different passivation methods the same procedure was repeated, this time with commercial grade *p*-type CZ wafers (2 Ω.cm). SiN_x and a SiO_2/SiN_x stack layer on *p*-type and on n^+-diffused surfaces were both investigated after annealing. Wafers with similar effective lifetime and thus similar minority carrier diffusion length were chosen to be compared. The results of these measurements are presented in Figure 8-23. The most striking result is the wide degraded region, more than four **millimetres** from each side of the laser line. This large distance is mainly due to the large diffusion length. No significant difference was observed between the two passivation methods on either the *p*-type or n^+-diffused surfaces. Due to a difference in the effective lifetime values, direct comparison between the *p*-type and n^+-surface is not possible.

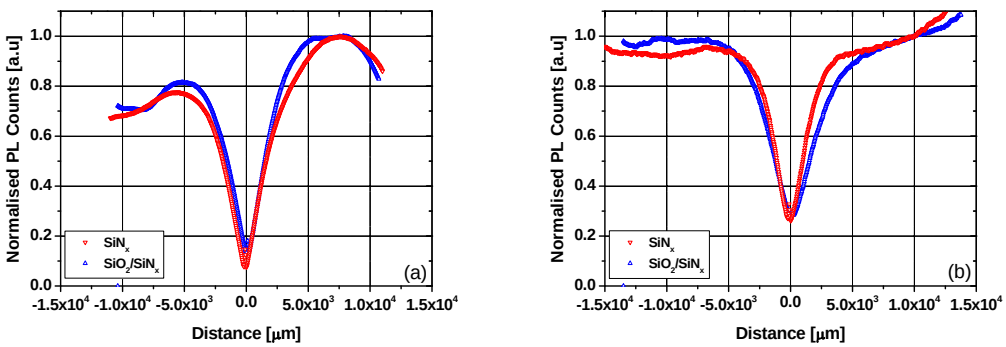

Figure 8-23: Normalised PL counts as a function of the distance from the laser line: on *p*-type surface (a) and on n^+ diffused surface (b).

Summary

Due to the laser doping process the passivation quality is degraded in a wide region adjacent to the molten areas. It is possible that the high temperature, even in the un-melted regions, damages the passivation. One possible degradation mechanism

could be the diffusion of hydrogen out of the passivation film, leaving un-passivated dangling bonds. According to this assumption, passivation methods based on hydrogen passivation, such as SiN_x, are more sensitive to the laser process. This can explain the bigger implied V_{oc} drop after the rear laser doping process. However, a higher density of laser-induced defects (due to the absence of a SiO_2 layer) or the fact that the rear is an un-diffused surface could also contribute to this behaviour. Further investigation is necessary.

8.3.7 Optical Loss

A possible limitation of the DSLD structure is the reduction in device current due to the absence of Al, which is often used as a rear reflector in solar cells [32]. This section employs a PC1D model to estimate the possible current loss arising from replacing the Al with SiN_x.

Figure 8-24 presents the transmission (T) and reflectance (R) as a function of the wavelength of representative DSLD solar cell, as measured using a Cary 500 spectrophotometer.

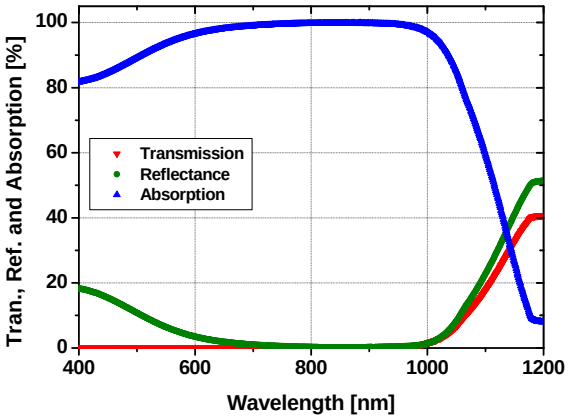

Figure 8-24: Transmission, reflectance and absorption as a function of the wavelength.

Also presented is the absorption (A), which was calculated using the following expression:

8-3) $$A = 1 - (T + R)$$

The calculated absorption below 550 nm includes absorption within the ARC SiN_x, though for wavelengths longer than 450 nm this absorption is relatively small (see Figure 5-38). Above 1000 nm the calculated absorption decreases rapidly, due to significant increase in both reflectance and transmission. It is assumed that only ~5% of the incident light is reflected directly from the front surface, while the rest is

reflected after a number of bounces in the cell [444]. Note that at 1200 nm 40% of the light is transmitted and more than 50% is reflected.

In order to estimate the reduction in the current, the reflectance measurement was fitted with a PC1D model; the reflectance of a representative SSLD solar cell was also simulated for comparison. Figure 8-25 shows the measured reflectance, together with the PC1D fits, as a function of the wavelength. Good agreement was achieved between the SSLD measurement and the PC1D fit; however, it was challenging to fit the DSLD measurement for the entire wavelength range. Therefore, Figure 8-25 includes two fit curves, which provide a lower (fit (a)) and upper (fit (b)) boundary for this measurement. Table 8-11 presents the fit parameters of the three curves. Despite the fact that both structures have a similar front surface, it was found that different parameters need to be used to fit the measurements. For the SSLD measurement, a good fit was obtained using the value that characterises a Lambertian surface. It was shown by Yablonovitch and Cody that $1/(n_r)^2$ of the light striking this type of surface will be coupled out [31, 445]; for Si at 1200 nm, this amounts to ~8% (n_r = 3.52). However, this value was found to be too low to fit the DSLD measurement. The reflectance from the DSLD rear surface was chosen to fit the transmission measurement (see Figure 8-24). Due to the fact that no absorption occurs within the SiN_x at these wavelengths, light that is not transmitted is reflected by the surface (~60%).

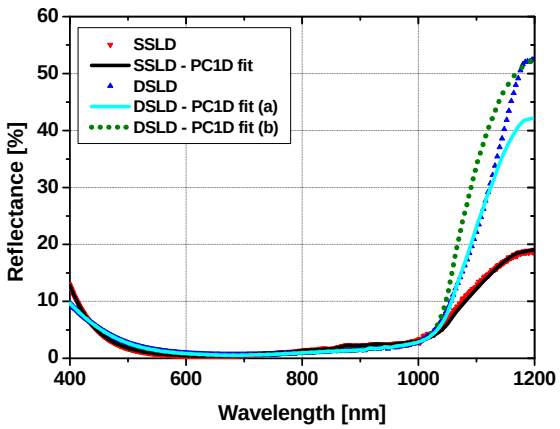

Figure 8-25: Comparison between the reflectance of DSLD and SSLD as a function of the wavelength. The solid and dotted lines are PC1D fits to the measurements.

The difference in the front surface parameters is assumed to arise from the diverse optical paths taken by light rays in different structures. Although a comparable amount of light reflects from the rear surface of both of the structures, less light escapes from the front surface in the case of the Al rear surface since it reflects light in a diffuse fashion [444]. According to the fit and the reflectance measurements more light is reflected from the front surface of the DSLD structure, although less light is

reflected from the Si-SiN_x interface. Thus the percentage of light escaping from the front surface in the Si-SiN_x case is significantly higher.

Table 8-11: PC1D parameters used to fit the reflectance measurements.

		Rear – Al	Rear – SiN_x Fit (a)	Rear – SiN_x Fit (b)
Front surface (diffuse):	First bounce [%]	92	89	90
	Subsequent bounces [%]	92	77	30
Rear surface (diffuse):	First bounce [%]	69	56	55
	Subsequent bounces [%]	69	90	92

The PC1D model of the SSLD solar cell (see Table A11-3) was employed to estimate the variation in J_{sc}. The internal reflectance parameters in the model were modified according to Table 8-11. For the DSLD solar cell, rear SRV of 100 cm/s was simulated. As can be seen in Table 8-12, a drop of 0.2-0.4 mA/cm^2 is predicted by the model when SiN_x replaces the Al at the rear surface.

Table 8-12: Comparison between the J_{sc} of DSLD and SSLD solar cells.

	J_{sc} [mA/cm^2]
SSLD (Al rear)	38.1
DSLD (SiN_x rear, SRV rear = 100 cm/s) – (a)	37.9
DSLD (SiN_x rear, SRV rear = 100 cm/s) – (b)	37.7

The WVASE software package was used to gain a better understanding of the internal reflectance properties of Al and SiN_x. The internal reflectance was modelled for both Si-Al and Si-SiN_x (Si-rich) interfaces. The optical properties of Al were taken from a data file included in the software package, while the model developed in Chapter 5 was used for the SiN_x film. Figure 8-26 presents the internal reflectance as a function of the wavelength for light beams of varying incident angle. Note that a beam of light entering the cell at normal incidence to the plane strikes the rear surface at ~41°, after being diverted by the textured front surface (see Figure 8-26 (c)). It can be seen that SiN_x is a perfect reflector for light beams which are incident on the rear surface at an angle greater than 40°. In comparison, Al reflects only 80-90% of the light at this angle (for relevant wavelengths, longer than 950 nm). Hence, SiN_x can be employed as a suitable rear reflector.

The difference between the measurement presented in Figure 8-24 and the model is assumed to be due to the high level of roughness at the cell's rear surface (see Figure 8-27). Due to this roughness, some of the light strikes the rear surface at

angles smaller than 40°, so a high portion of it is transmitted. The 40% transmitted light, as indicated in Figure 8-24, is therefore a mixture of perfect and relatively poor (~8%) internal reflectance. However, even in the case of perfect internal reflectance, focus needs to be given to the device optical design in order to minimise the amount of light escaping from the front surface.

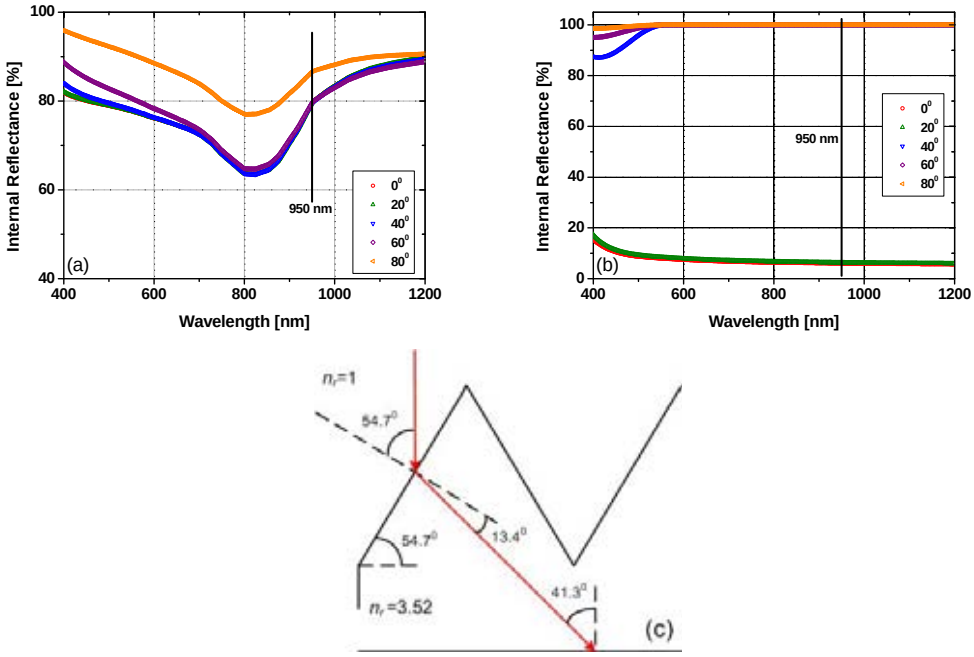

Figure 8-26: Internal reflectance of Al (a) and SiN_x (b) as a function of the wavelength for different incidence angles (with respect to the rear surface normal) and ray tracing (c) (not to scale).

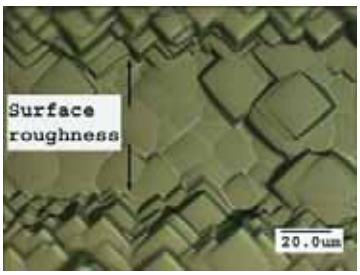

Figure 8-27: Micrograph of the rear surface of the DSLD used for transmission measurement.

Summary

Transmission and reflectance measurements together with PC1D modelling were used to estimate the current lost due to the replacement of the rear Al by SiN_x. A reduction of up to 0.4 mA/cm^2 was found for the DSLD structure, mainly due to light escaping via the front surface. Part of this loss can be regained if the cell is placed on a reflective material such as white polymer during encapsulation into a module [31], or if light is allowed to enter the cell from the rear.

WVASE was employed to compare Al and SiN_x as rear reflectors; it was shown that SiN_x is a perfect reflector for light beams striking the rear surface at angles greater than 40° but is quite poor for smaller angles. Optimisation of the optical

design of the DSLD structure will allow for the full utilisation of this internal reflectance capability.

8.3.8 Summary

Preliminary results for the new DSLD solar cell demonstrated the potential of this structure to obtain efficiencies exceeding 20% due to the high V_{oc}. One-sun implied V_{oc} above 680 mV was achieved using commercial grade CZ *p*-type wafers when measured after laser doping and prior to the metallisation. This is ~50 mV higher than the V_{oc} obtained for the SSLD at the same stage. It was shown that the laser doping process degrades the passivation quality in a wide region, significantly wider than the molten area. It is assumed that this degradation is result of the high temperature, which leads to out-diffusion of hydrogen from the SiN_x to the ambient.

A PC1D simulation was carried out to assess the current loss due to the absence of Al at the rear. It was found that up to 0.4 mA/cm^2 can be lost, though different methods can be employed to minimise this reduction.

8.4 Problems with the Metallisation of DSLD

As mentioned previously the metallisation process was done only at the end of the research, due to equipment limitations. This section presents initial results and identified problems. Possible solutions are suggested in order to solve the problems.

8.4.1 Metallisation Process

The metallisation process employed during this study was based on the electroless plating process developed for BC solar cells [424]. Besides offering low contact resistance and high conductivity, the electroless method provides selective plating, which maximises the benefits of the laser doping process. In this method metal does not plate on the dielectric layers, such as SiO_2 and SiN_x, but only on the contact areas. Note that at this stage photoplating is not possible as it selectively plates *n*-type regions.

The standard metallisation process begins with deglazing, which etches any type of oxide layer (such as PSG) formed during the laser doping process and prepares the surface for the subsequent plating. While buffered HF can be used in the case of conventional BC, in the case of double sided BC (DSBC) solar cells a modified solution needs to be used in order to etch both the PSG and the borosilicate glass (BSG) simultaneously [418]. Next, Ni is plated into the exposed contact regions. The Ni deposition process favours deposition on n^{++} Si, so the nucleation of the initial Ni layer is relatively easy and reliable for *n*-type contacts [418]. However, the plating

of *p*-type contacts is more challenging. Following the plating, the Ni is sintered to form Ni-silicide in tube furnace filled with N_2. The composition of the formed silicide is influenced by the sintering temperature. Ni_2Si is formed at a low temperature range (200-350°C), while NiSi and $NiSi_2$ are formed at elevated temperatures, NiSi at 350-750°C and $NiSi_2$ above 750°C [446]. Although it has been shown that the contact resistance is almost independent of the sintering temperature in the range 240-400°C [447], it was shown in the previous chapter that the sintering conditions (duration, ramping up/down, etc) have a significant influence on the formation of shunts and junction recombination. If done correctly, the formed silicide reduces the contact resistance, improves adhesion of the subsequent thick Cu layer and prevents diffusion of Cu into the junction region. Finally, Cu is plated from an aqueous solution into the Ni/Ni-silicide regions, forming the metal contacts. The last step relies heavily on a fully nucleated Ni/Ni-silicide layer to ensure uniform and stable Cu plating [418]. Table 8-13 summarises the metallisation process.

Table 8-13: Summary of the electroless plating process.

	Duration	Temperature
Deglazing	30 sec	Room Temp.
Ni plating	5 min	85°C
Ni sintering	2.5 min	350°C
Ni flash	1.5 min	85°C
Cu plating	60 min	45°C

The standard process is relatively straightforward, due to the fact that only phosphorus-doped regions need to be plated. However, as highlighted by Guo [418], simultaneous plating of both polarities is challenging as electrons are rare in heavily-doped *p*-type regions.

8.4.2 Palladium Activation

Four DSLD solar cells, fabricated according to the sequence described in Figure 8-9 (N-rich SiN_x film as rear passivation, GR= 1.14) were used to evaluate the challenges in the metallisation process. The standard metallisation process (see Table 8-13) was employed. Optical microscope examinations were performed after the Ni and the Cu plating to assess the plating. It was seen that Ni plated into both surfaces, although some isolated un-plated regions were observed. However, only a small amount of Cu was plated, as indicated by micrographs in Figure 8-28.

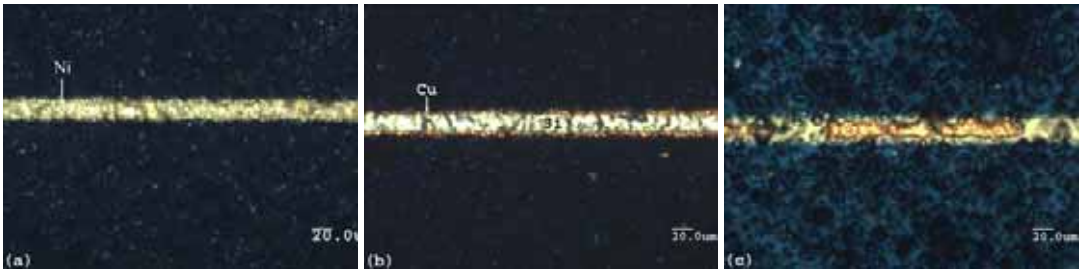

Figure 8-28: Micrographs of LD lines after Ni plating (a) and after Cu plating - front surface (b) and rear surface (c).

Due to the fact that plated Ni was observed, it was first suspected that in-activation of the Cu plating solution is the source of the poor plating. The Cu plating solution is self-catalytic and can be activated by generation of hydrogen by initial plating into metal, such as Al. However, repeating the experiment with wafers with a screen-printed Al rear contact and with Al wires did not seem to improve the reaction, although plating was observed on the Al wires and partly on the screen-printed solar cells.

Formation of Ni-oxide can prevent Cu plating. However, the sintering was carried out in an N_2 environment and the samples were stored in an elephant tube filled with N_2 during cooling to prevent Ni oxidation. Furthermore, Ni-flash step was performed prior to the Cu plating to form a thin, fresh Ni layer on which the Cu may plate easily.

Palladium (Pd) activation prior to Ni plating was proven to facilitate nucleation during the Ni plating process and improve Ni coverage and adhesion to the Si [446, 448]. It was also integrated into the advanced metallisation sequence developed by Guo for the DSBC solar cell [418]. Recently, Fisher reported improved uniformity of Ni plated on a *p*-type surface after Pd-activation [449]. In this reaction the Pd displaces a single atomic layer of Si, forming an ideal nucleation layer for the subsequent Ni plating [418, 448]. Although it seems that Ni plated onto both surfaces, it was decided to investigate if Pd activation can improve the poor Cu plating.

A second batch of DSLD devices was fabricated in a similar fashion to that described previously (GR= 1.14). The metallisation process was similar to the one presented in Table 8-13, with one modification: Pd activation was carried out between the deglazing and the Ni plating. The Pd solution was based on $PdCl_2$ and ammonia as proposed by Karmalkar and Banerjee [448] and the activation was done at room temperature for six minutes. Figure 8-29 presents micrographs of LD lines after Cu plating. A significant improvement can be observed for both surfaces. However, the plated Cu lines were still very thin (< 3 μm) and rough. Furthermore, it seems that occasionally the Pd activates parts of the dielectric layer, which causes a severe over-plating problem: see image (c). Figure 8-30 shows an extreme case where the entire surface was activated, resulting in almost complete coverage of the surface by Ni.

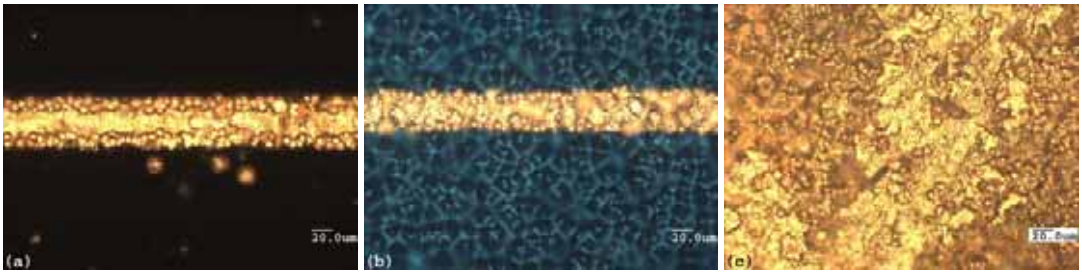

Figure 8-29: Micrographs of LD lines after Cu plating using Pd activation: front surface (a) and rear surface (b-c).

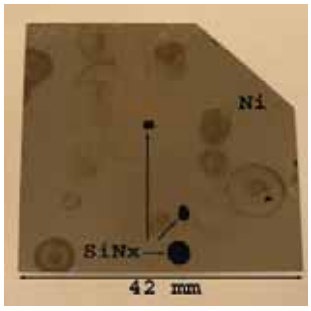

Figure 8-30: Digital image of DSLD after Pd activation and Ni plating.

8.4.3 Degradation of the Rear Passivation

Another problem which was identified is degradation of the rear passivation during the metallisation, even in cases where metal was not plated. This phenomenon is clearly demonstrated in Figure 8-31, where PL images of the same DSLD solar cell are presented before and after the metallisation process. The cell was fabricated according to the process given in Figure 8-9 and Table A15-1. Si-rich SiN_x film was employed as rear passivation layer.

The post-metallisation degradation is easily observed. Note that the exposure time of image (b) was double that of image (a). This degradation occurred despite the fact that the metallisation process was not successful, as no metal was plated into either of the surfaces as shown in image (c). Similar degradation was observed for a number of batches. It was also noticed that the colour of the rear SiN_x changed during the process. For example, the initial colour of the SiN_x shown in image (c) was silvery prior to the metallisation (not shown) and changed to blue, as can be seen in the digital image.

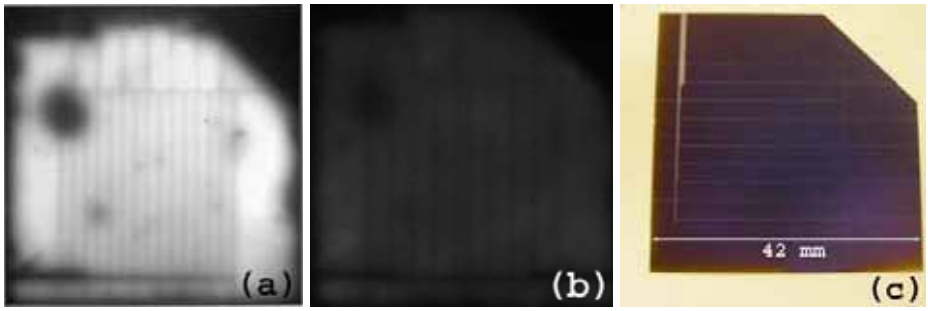

Figure 8-31: PL images of the same DSLD solar cell: before metallisation (a) and after metallisation (b). A digital image of the rear surface after the metallisation is given as well (c).

In order to investigate the source of the degradation a test structure was employed. Six *p*-type 1 Ω.cm CZ wafers were saw damage etched to a thickness of 220 μm prior to a full RCA cleaning. The wafers were then split into two groups of three wafers each. Si-rich SiN_x (GR = 0.77, n_r ~ 2.6) was deposited onto both surfaces of one group, while N-rich SiN_x (GR = 1.07, n_r ~ 2.2) was deposited onto the second group. No laser doping process was carried out before the metallisation. The effective lifetime and the implied V_{oc} were measured after each step using the QSS-PC system. Table 8-14 summarises the average one-sun implied V_{oc} after each metallisation step. Although reductions were observed after the Ni and the Cu plating steps, the final implied V_{oc} is higher than the initial value. Hence, the source of the degradation is still unknown.

Note that no metal was plated during this experiment due to lack of exposed Si (no LD lines). It is possible that the degradation process is initiated by plating.

Table 8-14: Average one-sun implied V_{oc} after different metallisation steps.

	GR = 0.77 [mV]	**GR = 1.07 [mV]**
After deglazing	642.6	642.4
After Ni plating	632.4	638.4
Change compared to previous	*-10.2*	*-4.0*
After Ni sintering	646.4	657.0
Change compared to previous	*+14.0*	*+18.6*
After Cu plating	**648.6**	**648.1**
Change compared to previous	*+2.3*	*-8.9*
Total change	**+6.0**	**+5.7**

Further experiments indicated that N-rich SiN_x films are more stable than Si-rich films during the metallisation. It is possible that some of the plating solutions contain NaOH, which was found in Chapter 5 to etch Si-rich SiN_x film very quickly. However, this remains to be investigated.

8.4.4 Summary

Preliminary experiments were carried out to evaluate the electroless plating process for DSLD solar cells. Two main problems were identified. The first was insufficient Cu plating on both surfaces. It was shown that Pd activation improved the plating process; however, it was found occasionally to activate large surface regions, which resulted in over-plating.

A second problem is degradation of the rear passivation during the process. It seems that the degradation is smaller for N-rich than for Si-rich SiN_x layers. Therefore, one possible solution to the degradation problem can be employing N-rich film as rear passivation, although Si-rich films provide better passivation. A second solution could be evaporation of Al onto the rear surface. In this case only the front surface needs to be plated, which can be done using the photoplating method.

8.5 Chapter Summary

Two main loss mechanisms in the SSLD solar cell were identified; the first is the relatively heavy emitter and the corresponding poor front surface passivation. Both were found to degrade the efficiency by 0.3-0.4% absolute. The second loss mechanism is the rear surface design as indicated by its contribution to the total dark saturation current.

An optimum emitter resistivity was identified in the range 120-140 Ω/□. It was shown that the SiO_2/SiN_x stack layer provides better passivation than SiN_x film for this range of emitters, although they are comparable. However, the stack layer is the preferred option due to reduced laser-induced defects and over-plating.

The formation of LBSF plays a critical role in the SiN_x passivated DSLD solar cell. It was shown that LBSF can be formed by the laser doping method. High surface concentrations, above 1×10^{19} cm^{-3} were detected at different laser diode currents, which ensure the formation of an ohmic contact with very low contact resistance. These concentrations are higher than those reported previously and are assumed to prevent formation of shunt between the inversion layer beneath the SiN_x layer and the rear metal contacts.

Preliminary results of the new DSLD solar cell structure were presented. One-sun implied V_{oc} above 680 mV was achieved using commercial grade CZ *p*-type wafers, at the end of the laser doping process, prior to the metallisation. This is ~50 mV higher than the V_{oc} obtained by the SSLD at the same stage. This high V_{oc} demonstrates the potential of this structure to achieve efficiencies exceeding 20%. However, complete device fabrication was challenging due to problems in the metallisation process.

Two main problems were identified during initial metallisation processes. The first was insufficient Cu plating on both surfaces. It was shown that Pd activation can

improve the plating process; however it was found occasionally to activate large surface regions, which resulted with over plating. A second problem is degradation of the rear passivation quality during the process. Possible solutions for these problems were presented, however more work needs to be done to fully solve them.

Chapter 9 : Conclusions

The primary aim of this thesis was to improve the efficiency of the SSLD solar cell, focusing on two important aspects of device design. The first was modification of the rear surface, which was achieved mainly by replacing the standard Al contact with localised contacts and high-quality SiN_x passivation. The second was optimisation of the laser doping process and the laser operation condition.

In the first part of this thesis, several passivation methods were compared. As SiN_x was found to provide the best passivation for un-diffused low resistivity *p*-type substrate, the impact of the film parameters and annealing conditions on the obtained passivation was investigated. The main conclusions from this component of the thesis are:

1. Si-rich layers provide lower S_{eff} values than N-rich films before and after annealing. No influence of the film thickness on the as-deposited one-sun implied V_{oc} was observed, but a strong post-annealing correlation was found, where a thicker film provides better passivation.

2. Annealing in the 600-820°C range significantly improves the passivation of different SiN_x films on different surfaces. An optimal annealing temperature was identified in the 680-700°C range. An S_{eff} value in the range of 2-7 cm/s was calculated for 1 Ω.cm *p*-type substrate at an injection level of 1×10^{15} cm^{-3}.

3. Annealing produces significant enhancement of the bulk lifetime in SiN_x passivated CZ wafers. Using an optimal annealing condition, the implied V_{oc} of CZ substrates increased to a value comparable to that of FZ wafers: almost 720 mV.

4. It was shown that the injection level dependence of the S_{eff} can reduce the theoretical *FF* by up to 3%, similar to the value calculated for PERL solar cells. Despite this dependence, very low S_{eff} values were calculated under both one-sun and MPP operating conditions.

5. SiN_x passivation is highly suitable for laser-doped solar cell fabrication sequences. In addition to having good passivation properties, SiN_x films also demonstrated excellent tolerance to all processing conditions. Good thermal

stability was shown under Ni sintering conditions. No influence of annealing on the optical parameters of the ARC layer was observed. Slow etch rates in aqueous HF solutions ensure no degradation during the deglazing process, prior to metallisation. However, care needs to be taken when a NaOH-based solution is used as it was found to etch the film and degrade its passivation quality.

Laser doping is a promising method for creating selective emitters. Its main advantage is the localised nature of the laser beam, which allows melting of the surface area without heating the bulk. However, laser-induced defects, contaminations and discontinuities in the laser-doped junctions degrade the solar cell performance. In **Chapter 6,** laser-induced defects were investigated using a wide range of characterisation techniques. The main focus was given to studying the impacts of dielectric film on defect formation. The main conclusions from this chapter are:

1. Laser doping degrades the electrical performance of the device. This degradation is more pronounced when a dielectric layer is present on the surface of the silicon during the laser process, possibly due to the thermal expansion mismatch between the silicon and the overlying dielectric layer.

2. No crystalline disorientation resulting from the epitaxial regrowth process was observed using a combination of EBIC and EBSD microscopy. Near-surface defects caused by laser doping were observed both in TEM images and after Yang etching. A higher density of defects was revealed by the etch when a dielectric film was present on the surface prior to laser doping.

3. It was concluded that near-surface laser-induced defects and a high level of oxygen in the molten area are the source of the electrical performance degradation. Although not directly observed, a high point defect density may also contribute to this degradation. The high concentrations of nitrogen detected near the surface can possibly degrade the subsequent metallisation process.

4. It appears that the dominant mechanism for the observed electrical performance degradation is the formation of defects when a dielectric layer is used, whereas contaminations and point defects are the predominant defects in the case of bare wafers.

5. Using cross-sectional EBIC analysis of laser-doped lines it was found that a continuous and uniform *p-n* junction is formed even when ablation occurs,

although discontinuities in the junction are more frequently observed for high laser powers.

6. It was shown that SiO_2/SiN_x stack is able to reduce the defect density. It seems that the well-known ability of the oxide to relieve stress in the SiN_x together with its low thermal expansion coefficient are the reasons for the reduced defect density.

7. SSLD solar cells with SiO_2/SiN_x stack layer demonstrate higher V_{oc} and *FF* than those with SiN_x only. It was shown by a spectral response measurement that the observed change in the V_{oc} is not due to differences in the front surface passivation, but is more likely due to formation of defects adjacent to the laser-doped lines. An efficiency of 18.4% on commercial grade CZ substrates demonstrates that high efficiencies are achievable despite the laser-induced defects if an optimum dielectric layer and laser power are chosen.

Chapter 7 investigates the influence of laser parameters on the electrical performance of laser-doped solar cells. The main conclusions from this chapter are:

1. A wide range of laser diode currents can be used to create a *p-n* junction by laser doping. Laser-doped junctions can be formed by using a diode current that is too weak to completely melt the pyramids on the top surface as well as one that is sufficiently high to ablate the silicon.

2. Grooves formed through intermediate levels of ablation can be used to improve the adhesion between the silicon and the metal without significantly degrading the cell performance. It was shown that similar V_{oc}, J_{sc} and *FF* values are obtained for a wide range of laser diode currents. At intermediate levels of silicon ablation, the V_{oc} is the first cell parameter to be reduced, primarily due to the large Si-metal interface. This reduction decreases the efficiency, although efficiencies above 18.1% are still achievable. At higher levels of ablation, shunts reduce the *FF* and the V_{oc}. Under these conditions significant efficiency degradation was observed.

3. An efficiency of 18.7% was achieved on a large area commercial grade *p*-type CZ industrial size substrate. This demonstrates the potential of the laser doping method to fabricate high-efficiency solar cells on a relatively low quality of substrate using commercial equipment and processes.

4. Electroless and photo-plating were compared; higher pseudo-*FF*s were achieved for photoplated laser-doped solar cells. If the photoplating technique is combined with well-optimised Ni sintering, the pseudo-*FF* is almost independent of the laser diode current. The superior performance of the photoplated cells results from the dependence of the plating rate on the local voltage and the fact that only *n*-type surfaces are plated. Both of these phenomena reduce the prominence of shunts and resistance-limited enhanced recombination regions.

The starting point of **Chapter 8** is an investigation of loss mechanisms in the SSLD solar cell. As a conclusion from this investigation a new structure – the DSLD solar cell – was developed and preliminary results were presented. The main conclusions from this chapter are:

1. Two main loss mechanisms limit the performance of the SSLD solar cell. The first is the relatively heavy emitter and the corresponding poor front surface passivation. It was shown that by increasing the emitter sheet resistivity to the 120-140 Ω/□ range, the efficiency can be increased by 0.3-0.4% absolute. The second loss mechanism is the rear surface design as indicated by its contribution to the total dark saturation current.

2. A local back surface field can be formed by the laser doping method. Surface concentrations above 1×10^{19} cm^{-3} were detected at different laser diode currents, ensuring the formation of an ohmic contact with very low contact resistance. These concentrations are higher than previously reported and are assumed to prevent formation of shunts between the rear metal contacts and the inversion layer that lies beneath the SiN_x layer.

3. One-sun implied V_{oc} above 680 mV was achieved using the DSLD structure on commercial grade CZ *p*-type wafers, at the end of the laser doping process and prior the metallisation. This is ~50 mV higher than the V_{oc} obtained for the SSLD at the same stage. This high V_{oc} demonstrates the potential of this structure to achieve efficiencies exceeding 20%.

4. Two main problems were identified during initial metallisation processes. The first was insufficient Cu plating on both surfaces. It was shown that Pd activation can improve the plating process; however, it was found to occasionally activate large surface regions, which resulted in over-plating. A second problem is degradation of the rear passivation during metallisation.

Possible solutions for these problems were presented, however more work needs to be done to fully solve them.

9.1 Original Contributions

The following are the original contributions made by the author .in this thesis:

1. A comprehensive study regarding the influence of the annealing temperature on the obtained passivation was carried out. This study completes an existing gap in the published literature.

2. It was demonstrated that when CZ substrates are annealed, significant bulk lifetime enhancement occurs. Using an optimal annealing condition the implied V_{oc} of CZ substrate increased to a value comparable to that of FZ wafers.

3. Laser-induced defects were comprehensively studied. Special attention was given to the influence of a dielectric film on the generation of defects. This study completes an existing gap in the published literature.

4. A new laser pulse shaping method to increase the melting duration and to slow the recrystallisation velocity was developed. A reduction of the laser-induced defect density and improvement of dopant mixing can be achieved using this approach. A patent application has been filed by the university to protect this novel method.

5. The influence of laser power on the laser-doped solar cell performance was investigated. It was demonstrated that grooves formed through intermediate levels of ablation can be used to improve the adhesion between the silicon and the metal without significantly degrading the cell performance.

6. Electroless and photo-plating were compared for the first time, regarding the formation of shunts and enhanced recombination regions in laser-doped solar cells. The superiority of the photoplating method was demonstrated by higher pseudo-*FF* values.

7. A new DSLD solar cell structure has been developed. One-sun implied V_{oc} above 680 mV was achieved using commercial grade CZ *p*-type wafers when measured after laser doping, prior to metallisation. This is ~50 mV higher than

the V_{oc} obtained by the SSLD at the same stage. This high V_{oc} demonstrates the potential of this structure to achieve efficiencies exceeding 20%.

9.2 Future Work

During this thesis a number of topics were identified for further work:

1. A comprehensive study should be performed regarding the source of the post-annealing enhancement. Focus needs to be given to the variation in the charge, the surface state density and the capture cross section after annealing.

2. The influence of the laser process on the surrounding passivation was only briefly investigated during this thesis. Further work is needed to evaluate the impact of this degradation mechanism on the solar cell performance. This degradation process may limit the benefits of SiN_x passivation of the rear surface. Furthermore, it is suspected that use of a CW laser enhances this degradation effect, due to the longer heating duration. This can limit the use of this type of laser for rear laser doping.

3. Development of rear surface passivation based on negative fixed charge for the DSLD on a *p*-type substrate can be very beneficial due to reduced dependence of the passivation on the injection level and on hydrogen passivation of dangling bonds. While Al_2O_3 appears promising, investigation is needed to assess its suitability for the laser-doped solar cell fabrication sequence and for the industrial environment.

4. While equipment limitations prevented its practical realisation, a new pulse shaping system was designed and a theoretical study was carried out to investigate its potential. The proposed pulse shaping method seems to provide many advantages when employed during the laser doping process, including the reduction of the defect density and improvement of the dopant mixture.

5. Two main problems were identified regarding the metallisation of DSLD solar cells. Much more work is needed to optimise this process. As a first step it is recommended to use SiN_x with a lower refractive index as rear surface passivation. It seems that the etching rate of this film by the metallisation solutions is relatively slow. Modification of the solution baths in order to accommodate Si-rich SiN_x is also recommended as this film demonstrated a higher passivation quality. Al evaporation onto the rear SiN_x can be used as another possible solution. In this case photoplating can be employed as the metallisation method. However, care needs to be given to evaporation and

annealing processes in order to minimise any possible degradation effects of it on the passivation quality.

6. It was shown that when photoplating and optimised Ni sintering conditions are used, the pseudo-*FF* is independent of the laser diode current. It was also shown that photoplated solar cells demonstrated higher pseudo-*FF* than electroless plated cells. A plating method which selectively plates not only the *n*-type regions of the front, but also the *p*-type regions of the rear should be developed. This can be carried out by applying voltage during the plating or by using selective solutions.

Appendix 1: Publications List

Journal Articles

Hameiri Z, Puzzer T, Mai L, Sproul AB, Wenham SR. Laser induced defects in laser doped solar cells. *Progress in Photovoltaics: Research and Applications* (DOI: 10.1002/pip.1043).

Hameiri Z, Mai L, Puzzer T, Wenham SR. Influence of laser power on the properties of laser doped solar cells. *Solar Energy Materials and Solar Cells* (DOI: 10.1016/j.solmat.2010.12.006).

Hameiri Z, Mai L, Wenham SR. Advantages of photoplating for laser doped solar cells. *Progress in Photovoltaics: Research and Applications* (DOI: 10.1002/pip.1072).

Hameiri Z, Mai L, Sproul, AB, Wenham SR. 18.7% efficient laser doped solar cell on CZ *p*-type silicon. *Applied Physics Letters*, 2010; **97**: 222111-222113.

Conference Proceedings

Tjahjono BS, Guo JH, **Hameiri Z**, Mai L, Sugianto A, Wang S, Wenham SR. High efficiency solar cells structures through the use of laser doping. *22nd European Photovoltaic Solar Energy Conference*, 2007: 966-969.

Tjahjono B, Wang S, Sugianto A, Mai L, **Hameiri Z**, Borojevic N, Ho-Baillei A, Wenham S. Application of laser doped contact structure on multicrystalline solar cells. *23rd European Photovoltaic Solar Energy Conference*, 2008: 1995-2000.

Hameiri Z, Mai L, Borojevic N, Javid S, Tjahjono BS, Sugianto A, Wang S, Sproul AB, Wenham SR. The influence of silicon nitride annealing temperature on the implied Voc of CZ silicon wafers. *18th International Photovoltaic Science and Engineering Conference*, 2009.

Hameiri Z, Tjahjono BS, Mai L, Wang S, Sugianto A, Javid S, Wenham SR. Double sided laser doped solar cells. *18th International Photovoltaic Science and Engineering Conference*, 2009.

Mai L, Sugianto A, Tjahjono T, Edwards M, **Hameiri Z**, Wenham S. Aluminium alloyed rear junction laser doped contact solar cells on CZ n-type silicon. *18th International Photovoltaic Science and Engineering Conference*, 2009.

Hameiri Z, Mai L, Borojevic N, Javid S, Tjahjono B, Wang S, Sproul A, Wenham S. The influence of silicon nitride layer parameters on the implied Voc of CZ silicon wafers after annealing. *34th IEEE Photovoltaic Specialists Conference (PVSC)*, 2009: 1795-1800.

Mai L, **Hameiri Z**, Tjahjono BS, Wenham SR, Sugianto A, Edwards MB. Rear junction laser doped solar cells on CZ n-type silicon. *34th IEEE Photovoltaic Specialists Conference (PVSC)*, 2009: 1811-1815.

Wang S, Puzzer T, Vogl B, Tjahjono B, Hallam B, Eadie M, Borojevic N, **Hameiri Z**, Wenham S. Overcoming over-plating problems on acid textured multicrystalline wafers with silicon nitride coated surfaces. *24th European Photovoltaic Solar Energy Conference*, 2009: 1449-1452.

Wang S, Tjahjono B, Hallam B, Vogl B, Eadie M, Sugianto A, Mai L, **Hameiri Z**, Wenham S. The use of silicon oxynitride on laser doped multicrystalline solar cells. *24th European Photovoltaic Solar Energy Conference*, 2009: 1632-1635.

Borojevic N, **Hameiri Z**, Tjahjono B, Lennon A, Wenham S. Development of Inkjet texturing for multicrystalline silicon laser doped selective emitter solar cells. *19th International Photovoltaic Science and Engineering Conference*, 2009.

Patent Application

Mai L, Edwards MB, Green MA, Hallam B, **Hameiri Z**, Kupper NB, Sugianto A, Tjahjono BS, Wang S, Wenham AM, Wenham SR. Solar cell methods and structure. *Patent Application PCT/AU2010/000036* 2007.

Wenham A, **Hameiri Z**. Improved laser operation for laser doping of silicon. *Patent Application PCT/AU10/00145* 2008.

High Efficiency Water Pump System

Hameiri Z, Spooner T, Sproul AB. Experimental results for a high efficiency pool pump system. *44th ANZSES Conference*, 2006.

Hameiri Z, Spooner T, Sproul AB. High efficiency pool filtering systems utilising variable frequency drives. *Renewable Energy* 2009; **34**: 450-455.

Appendix 2: Abbreviations List

3D	Three Dimensional
AC	Alternating Current
AFM	Atomic Force Microscopy
APCVD	Atmospheric Pressure Chemical Vapour Deposition
ARC	Anti Reflection Coating
a.u	Arbitrary Unit
BC	Buried Contact
BHF	Buffered Hydrofluoric acid
BKD	Backscatter Kikuchi Diffraction
BOE	Buffered Oxide Etch
BSF	Back Surface Field
BSG	Boronsilicate Glass
CCD	Charge-Coupled Device
CV	Capacitor-Voltage
CVD	Chemical Vapour Deposition
CW	Continuous Wave
CZ	Czochralski
DC	Direct Current
DCD	Double Crystal X-ray Diffractometry
DI H_2O	Distilled water
DLTS	Deep Level Transient Spectroscopy
DRM	Depletion-Region Modulation
DSBC	Double Sided Buried Contact
DSLD	Double Sided Laser Doped
EBIC	Electron Beam Induced Current
EBSD	Electron Backscattering Diffraction
ECN	Energy Centre of the Netherlands
ECV	Electrochemical Capacitor-Voltage
eeh	Electron-electron-hole
EFG	Edge-defined Film-fed Grown
ehh	Electron-hole-hole
EVA	Ethylene Vinyl Acetate
EWT	Emitter Wrap-Through
FGA	Forming Gas Anneal
FIB	Focused Ion Beam

FWHM	Full Width at Half Maximum
FZ	Float Zone
GILD	Gas Immersion Laser Doping
GR	Gas Ratio
HIT	Heterojunction with Intrinsic Thin film
HMI	Hahn Meitner Institut (Berlin)
IBBC	Interdigitated Buried Backside Contact
IQE	Internal Quantum Efficiency
ISE	Instituts für Solare Energiesysteme in Fraunhofer
ISFH	Institut für Solarenergieforschung in Hameln/Emmerthal
Laser	Light Amplification by Stimulated Emission of Radiation
LBSF	Local Back Surface Field
LCE	Laser Chemical Etching
LCP	Laser Chemical Processing
LD	Laser Doped
LED	Light Emitting Diode
LFC	Laser Fired Contact
LIMPID	Laser Induced Melting of Pre-deposited Impurities Doping
LIP	Light Induced Plating
LIT	Lock-in Thermography
LPCVD	Low Pressure Chemical Vapour Deposition
MIS/IL	Metal-Insulator-Semiconductor Inversion Layer
MOSFET	Metal-Oxide-Semiconductor Field-Effect Transistor
MPP	Maximum Power Point
MWT	Metal Wrap-Through
N/A	Not Applicable
NI	National Instruments
PA-ALD	Plasma-Assisted Atomic Layer Deposition
PCD	Photoconductance Decay
PECVD	Plasma Enhanced Chemical Vapour Deposition
PERC	Passivated Emitter and Rear Contacts
PERL	Passivated Emitter Rear Locally diffused
PL	Photoluminescence
PSG	Phosphosilicate Glass
PV	Photovoltaic
QSS	Quasi Stead-State
OSS-PC	Quasi Stead-State Photoconductance
OSS-PL	Quasi Stead-State Photoluminescence
RF	Radio Frequency
RISE	Rear Interdigitated Single Evaporation

RT	Room Temperature
RTO	Rapid Thermal Oxide
SCF	Semiconductor Finger
SE	Secondary Electron
SHR	Sheet Resistivity
SIMS	Secondary Ion Mass Spectrometry
SOD	Spin on Dopant
SRH	Shockley-Read-Hall recombination
SRV	Surface Recombination Velocity
SSLD	Single Sided Laser Doped
STD	Standard Deviation
TCA	Trichloroethane
TEM	Transmission Electron Microscopy
TLM	Transmission Line Model
UNSW	University of New South Wales
UV	Ultraviolet
WD	Working Distance

Appendix 3: Symbols List

Symbol	Description	Unit
A	Resonator cross section	cm^2
A	Absorption	---
A_i	Scaling factor	---
B	Radiative recombination coefficient	cm^3/s
C	Speed of light	cm/s
Cn	Auger coefficient	cm^6/s
Cp	Auger coefficient	cm^6/s
D	Minority carrier diffusion constant	cm^2/s
$D_{it}(E)$	Interface state at given energy	cm^{-3}-eV^{-1}
d	Dielectric film thickness	nm
E	Young's modulus of elasticity	Pa
E_c / E_v	Energy of conduction / valance bands	eV
E_e	Electron kinetic energy	eV
E_t	Energy level of recombination centre	eV
FF	Fill factor	%
f_{abs}	Optical constant	---
f_s	Scaling factor	---
G	Generation rate	cm^{-3}-s^{-1}
G_0	Measured illumination	sun
$h\upsilon$	Photon energy	J
I_0	Dark saturation current	A
I_{PL_rel}	Relative PL signal	---
J_0	Dark saturation current density	A/cm^2
J_{01}	Bulk and surface dark saturation current density	A/cm^2
J_{02}	Junction dark saturation current density	A/cm^2
J_{0e}	Emitter saturation current density	mA/cm^2
J_{mp}	Maximum power point current density	mA/cm^2
J_{rec}	Recombination current density	mA/cm^2
J_{sc}	Short circuit current density	mA/cm^2
k	Boltzmann constant	J/K
k	Extinction coefficient	---
L(t)	Optical pumping	cm^{-3}-s^{-1}
L_{eff}	Effective diffusion length	cm
l	Length of the laser rod	cm

l^*	Length of the laser resonator	cm
$N_{A/D}$	Acceptor / donor concentration in the substrate	cm^{-3}
N_c / N_v	Effective densities of states in conduction / valance bands	cm^{-3}
N_{it}	Surface states density	cm^{-2}
N_{st}	Surface state density	cm^{-2}
N_t	Defect concentration	cm^{-3}
n / p	Electron / hole concentration	cm^{-3}
n_0 / p_0	Electron / hole thermal equilibrium concentration	cm^{-3}
n_1 / p_1	Electron / hole SRH densities	cm^{-3}
n_i	Intrinsic carrier concentration.	cm^{-3}
n_r	Refractive index	---
n_s / p_s	Electron / hole concentrations at the surface	cm^{-3}
P(t)	Power	W
P_{em}	Normalised power loss due to emitter resistivity	---
p-FF	Pseudo fill factor	%
Q_f	Density of fixed charges	C/cm^2
Q_{it}	Charge density in interface states	C/cm^2
Q_m	Density of mobile charge	C/cm^2
q	Elementary charge of electron	C
R	Reflectance	---
R_{sh}	Shunt resistance	Ω-cm^2
S	Spacing between metal fingers	cm
S_{eff}	Effective surface recombination velocity	cm/s
S_{n0} / S_{p0}	Surface recombination velocity parameters (SRV parameters)	cm/s
T	Temperature	K
T	Transmission	---
t	Time	sec
U	Net recombination rate	cm^{-3}-s^{-1}
U_s	Net recombination rate at the surface	cm^{-2}-s^{-1}
V	Voltage	mV
V_{mp}	Voltage at MPP	mV
V_{oc}	Open circuit voltage	mV
W	Wafer thickness	μm
α	Absorption coefficient	cm^{-1}
γ	Inversion reduction factor	---
Δn	Excess minority carrier concentration	cm^{-3}
Δn_s	Excess minority carrier concentration at the surface	cm^{-3}
ΔT	Change of temperature,	K
$\Delta\alpha_t$	Difference in thermal expansion coefficients	K^{-1}

$\Delta\eta$	Separation of the quasi Fermi level	eV
$\zeta(t)$	Losses in laser cavity	---
λ	Wavelength	cm or nm
$\mu_{n/p}$	Mobility of electron / hole	cm^2/V-s
ν	Poisson's ratio	---
ρ_c	Specific contact resistance	Ω/cm^2
ρ_s	Emitter sheet resistivity	Ω
σ	Conductivity	S/cm
σ_{em}	Stimulated emission cross section	cm^2
$\sigma_{n/p}$	Capture cross section of electron / hole	cm^2
σ_s	Stress	Pa
τ	Carrier lifetime	µs
τ_{bulk}	Bulk lifetime	µs
τ_{eff}	Effective minority carrier lifetime	µs
τ_{n0} / τ_{p0}	Capture time constant of electron / hole	µs
τ_s	Carrier lifetime at the surface	µs
τ_{sp}	Spontaneous emission decay time constant	µs
υ_{th}	Thermal velocity of carriers	cm/s
Φ	Photon density	cm^{-3}

Symbol	Description
Ag	Silver
Al	Aluminium
Ar	Argon
B	Boron
Cu	Copper
H_2	Hydrogen gas
N_2	Nitrogen gas
Ni	Nickel
O_2	Oxygen gas
O_i	Interstitial oxygen
P	Phosphorus
Pd	Palladium
Pt	Platinum
Si	Silicon
a-Si	Hydrogenated amorphous Si
mc-Si	Multi-crystalline Si
Al_2O_3	Aluminium oxide
CO_2	Carbon dioxide
CrO_3	Chromium trioxide
HF	Hydrofluoric acid
KOH	Potassium hydroxide
NaOH	Sodium hydroxide
$Nd:YVO_4$	Neodymium doped Yttrium Vanadate
NH_3	Ammonia
NH_4F	Ammonium Fluoride
PH_3	Phosphine
P_2O_5	Phosphorus pentoxide
PCl_3	Phosphorus trichloride
$PdCl_2$	Palladium chloride
SiH_4	Silane
SiN_x	Amorphous hydrogenated silicon nitride
Si_3N_4	Stoichiometric silicon nitride
SiO_2	Silicon dioxide
TiO_2	Titanium dioxide

Appendix 4: System of Units

Quantity	Unit	Symbol
Conductance	Siemens	S
Current[1]	Ampere	A
Electric charge	Coulomb	C
	Elementary charge	q
Energy	Joule	J
	Electron-volt	eV
Flow rate	Standard cubic centimetres per minute	sccm
Frequency[2]	Hertz	Hz
	Revolutions per minute	RPM
Length[3]	Meter	m
Mass	Gram	g
Power[4]	Watt	W
Pressure	Bar (milli)	mbar
	Pascal	Pa
	Torr (milli)	mTorr
Resistivity	Ohm	Ω
Temperature	Kelvin	K
	Degree Celsius	°C
Time[5]	Second	s or sec
Voltage[6]	Volt	V

[1] Milliampere (10^{-3} A) is often used in this thesis for current.
[2] In this thesis kHz (10^{3} Hz) and MHz (10^{6} Hz) are often used.
[3] In semiconductors it is more common to use centimetre (10^{-2} m), micrometer (10^{-6} m) and nanometre (10^{-9} m) for length.
[4] Milliwatt (10^{-3} W) is often used in this thesis for power.
[5] Microsecond (10^{-6} s) is often used in this thesis for time.
[6] Millivolt (10^{-3} V) is often used in this thesis for voltage.

Appendix 5: More about SiN_x

This appendix adds more information regarding SiN_x, which was not included in the main review. The first part reviews the influence of the deposition parameters on the obtained passivation, while the second part reviews SiN_x passivation of both n^+- and p^+-type emitters and *n*-type substrates.

A5.1 Optimisation of the Deposition Parameters

The deposition parameters determine the properties of the Si-SiN_x interface; therefore, they strongly influence the overall quality of the resulting passivation, as discussed in Section 4.2. This section briefly summarises the influence of these parameters on the obtained passivation.

A5.1.1 Deposition Temperature

Deposition temperature has a significant influence on the effective lifetime obtained after the deposition. Higher deposition temperature was found to provide better effective lifetime for both remote and direct PECVD methods [136, 245, 271], although it seems that the optimum temperature differs according to the reactant gases used. Kerr found that effective lifetime increased with temperature [136], while Lauinger *et al*. found an optimum temperature in the range of 350-400°C on a similar system [244]. Kerr suggested that changing the reactant gas from pure silane to dilute silane shifts the optimum temperature to higher values [136]. Better performance at a deposition temperature around 350°C was also reported by Schimdt *et al*. and by Moschner *et al*. using an inline remote PECVD system [237, 250].

A5.1.2 Plasma Pressure and Plasma Power

The relationship between plasma pressure and effective lifetime is unclear and disparate results have been reported. While Lauinger *et al*. reported an optimum pressure (in terms of effective lifetime) around 400 mTorr in their remote system [238], Moschner *et al*. found that deposition pressure had no influence on the effective lifetime in their remote industrial system [250]. Schmidt *et al*. found increased effective lifetime for decreased pressure in their direct (high frequency) system [159, 271]. In the last case it was emphasised that there is a lower limit to the pressure beyond which plasmas cannot be sustained [136].

Different trends were also found in the influence of the plasma power. While Lauinger *et al*. [238] and Moschner *et al*. [250] found improvement of the effective

lifetime for increased plasma powers, Schmidt *et al*. [159, 271] and Kerr [136] found the impact to be relatively weak.

A5.1.3 Gas Flow Rate and Gas Ratio

The gas flow rate was found to have a mild impact on the effective lifetime in several reviewed studies [136, 238, 250, 271]. However, it has been argued that the *ratio* between the reactant gases, and not the flow rate, is the important parameter [159, 271].

Lauinger *et al*. found that effective lifetime increases with the SiN_4/NH_3 ratio [238]. Mackel and Ludemann reported a similar behaviour for their $SiH_4/N_2/H_2$ mixture [251]. Furthermore, Lauinger *et al*. pointed out that the impact of all the deposition parameters on the refractive index n_r - which is directly related to the gas ratio - is similar to their impact on the effective lifetime [238]. It was found that the effective lifetime increases with increasing refractive index up to $n_r = 2.4$, above which the effective lifetime saturates [238]. Hence, Si-rich films (high n_r) give better passivation quality. The superiority of Si-rich films was also reported by other research groups, for both SiN_4/NH_3 and $SiH_4/N_2/H_2$ mixtures [237, 253, 267, 273]. However, Schmidt *et al*. [159, 271] and Kerr [136] found a different behaviour when dilute silane is used: a clear peak in the effective lifetime was observed for $n_r = 1.9$. De Wolf *et al*. found that while planar surfaces are passivated better by Si-rich films, lower refractive index films are preferable for textured wafers [261].

A5.2 Passivation of Emitters and *n*-Type Substrates

Up to this point, the discussion has been limited to the passivation of *p*-type substrates as the main focus of this thesis is the rear surface passivation of *p*-type solar cells. However, investigations were carried out to evaluate the passivation capability of SiN_x for *n*-type substrates and n^+ and p^+ emitters. This section briefly reviews the main conclusions of these investigations.

A5.2.1 Passivation of n^+ Emitter

The first investigations of SiN_x-passivated n^+-type emitters were carried out as recently as the mid-1990s. Ruby *et al*. and Chen *et al*. measured J_{0e} of 80 and 200 fA/cm^2 on 100 Ω/□ emitters, respectively [450-451]. Lenkeit *et al*. compared different PECVD systems and found that remote and high-frequency direct PECVD systems are superior to low-frequency ones for emitter passivation [452]. As is the case for *p*-type substrates, it was concluded that Si-rich films provide better passivation, hence lower J_{0e} [258, 267, 452]. The high passivation quality of these emitters before annealing was found to be stable and even improved after thermal treatment [258, 267, 452]. In his extensive work, Kerr measured J_{0e} of 20 and 120 fA/cm^2 on 400 and

30 Ω/□ emitters, respectively, for his optimised passivation film [136]. Although a thin SiO_2 provides better passivation than SiN_x of any thickness, it was shown that similar values of J_{0e} are obtained for emitters with sheet resistivity lower than 150 Ω/□ [288]. The J_{0e} value of textured surfaces was found to increase by a factor of 1.5-3 [136, 237, 453]. This increase is attributed to an increase in the surface area of the emitter and possible higher recombination on the (111) plane. Figure A5-1 summarises the key results achieved by different research groups. The effect of the sheet resistivity on J_{0e} is similar to that reported for SiO_2 passivated emitters [454].

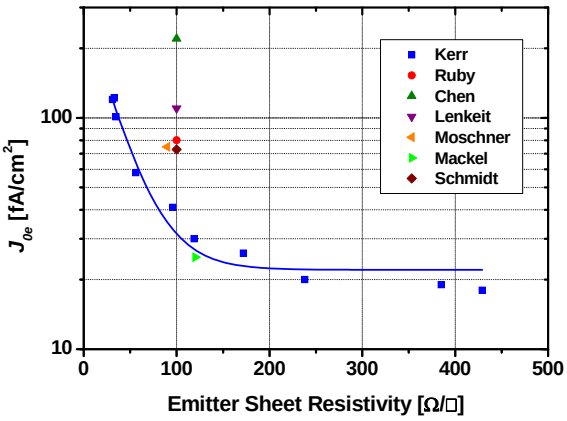

Figure A5-1: J_{0e} as a function of the emitter sheet resistivity as reported by different research groups. The fit is to Kerr's result [136]. References: Ruby [450], Chen [451], Lenkeit [452], Moschner [453], Mackel [267] and Schmidt [237]. The values serve as rough guide, as they were extracted from graphs.

A5.2.2 Passivation of *n*-Type Substrates

Experimental data for SiN_x passivated *n*-type substrates are less available. Schmidt *et al*. measured S_{eff} below 20 cm/s on an 11 Ω.cm *n*-type wafer [227], while Kunst *et al*. measured similar value on an 18 Ω.cm substrate [455]. Kerr *et al*. extended the available data to the range of 0.6–90 Ω.cm (see Table A5-1) [248, 296]. The influence of Δn on S_{eff} at low injection levels was found to be limited. $S_{eff}(\Delta n)$ has a constant value under these conditions; this behaviour is different from that observed with *p*-type substrates [248, 296]. Chen *et al*. obtained extremely low values of 7 and 2 cm/s for 1 Ω.cm *n*-type wafer (planar surfaces), using near-stoichiometric and Si-rich films, respectively [456]. However, the surface passivation of as-deposited SiN_x on textured surfaces was found to be quite poor, with some improvement after annealing [456].

Table A5-1: Summary of S_{eff} values achieved on *n*-type substrate by different research groups.

Substrate Resistivity [Ω.cm]	S_{eff} [cm/s]	Ref.	Substrate Resistivity [Ω.cm]	S_{eff} [cm/s]	Ref.
90	1.4	[248]	1.5	5.5	[248]
20	2.7	[248]	1.0	< 7	[305]
18	< 20	[455]	1.0	< 2	[305]
11	< 20	[227]	0.6	9.8	[248]

A5.2.3 Passivation of p^+ Emitter

It appears that Kerr was the first to investigate SiN_x-passivated p^+ emitters [136]. Emitters in the range of 40-500 Ω/□ on high-resistivity *n*-type wafers were studied. Kerr's results (see Figure A5-2) suggest that PECVD SiN_x film does not provide the high-quality passivation seen when using SiO_2. Similar results were reported by Petres *et al*. when passivating ~90 Ω/□ emitter on a 2.8 Ω.cm *n*-type substrate [457]. While the implied V_{oc} of the cell with a SiN_x-passivated emitter (at one-sun) was only 596 mV, up to 650 mV was achieved by SiO_2 passivation. It was also shown that this passivation is not thermally stable: a drop of 20 mV was observed after a firing process. The poor passivation capability of the SiN_x was explained by the high fixed positive charge within this film, which creates a depletion layer at the Si-SiN_x interface [136]. Recently, however, post-annealing implied V_{oc} values above 650 mV were achieved for a wide range of emitter resistivities on 1 Ω.cm *n*-type substrates [305]. Similar results were also reported by Mihailetchi *et al*.: 670 mV were obtained on a 50-65 Ω/□ emitter [458]. Figure A5-2 summarises the key results for p^+ emitters passivated by SiN_x.

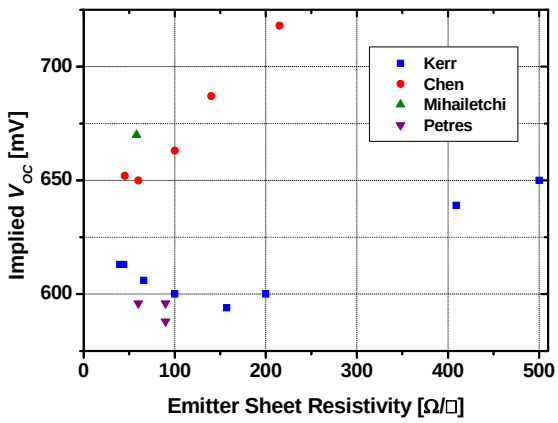

Figure A5-2: One-sun implied V_{oc} of SiN_x passivated emitters as reported by Kerr [136], Chen [305], Mihailetchi [458] and Petres [457].

Appendix 6: Other Passivation Methods

This appendix briefly reviews a variety of surface passivation techniques, which although were not used in this study, can be employed as rear surface passivation.

A6.1 Al_2O_3

In recent years attention has been given to the use of Al_2O_3 as a passivation layer in solar cell applications. Hoex *et al*. used Plasma-Assisted Atomic Layer Deposition (PA-ALD) of Al_2O_3 to obtained extremely low S_{eff} of 2 cm/s and 13 cm/s on *n*- and *p*-type substrates, respectively [459]. Due to the high *negative* fixed charge density within this layer, 1.2-1.4×10^{13} cm^{-2} [460], Al_2O_3 is capable of providing a high quality passivation even for the relativly challenging p^+ emitter surface. A low J_{0e} value of 10 fA/cm^2 was measured on an emitter with resistivity > 100 Ω/□, while 30 fA/cm^2 was measured on a 54 Ω/□ emitter. These values are lower than those obtained by SiO_2 or by SiN_x [461]. Another advantage of Al_2O_3 passivation is the weak dependence of S_{eff} on the injection level, even at low levels [459]. Interestingly, the high passivation quality is only obtained after annealing, typically at 450°C for 30 min. The as-deposited passivation is quite poor; for example, effective lifetime in the range of only 2-8 µs was measured for a 2 Ω.cm FZ *p*-type substrate [459]. However, after annealing the effective lifetime of the same sample improved up to 1.2 ms! The significant post-annealed improvement has been attributed to an increase of the negative charge density (from 3-20×10^{11} cm^{-2} to 5-8×10^{12} cm^{-2}) and to a reduced surface state density [460]. Similar to SiN_x, ~2 nm layer of SiO_x was found at the Si-Al_2O_3 interface, it was shown that this layer has a significant role in the demonstrated passivation quality of the Al_2O_3 layer [460].

A6.2 Hydrogenated Amorphous Si

The interest in hydrogenated amorphous-Si (a-Si) increased rapidly from the beginning of 1990s, when Sanyo introduced the Heterojunction with Intrinsic Thin film (HIT) solar cell [462]. This film – typically deposited by PECVD system at 200-250°C – has been proven to provide excellent passivation for both substrate polarities. Dauwe *et al*. reported S_{eff} values of 7 cm/s and 3 cm/s on *n*- and *p*-type wafers, respectively, which is better than what has been demonstrated with SiO_2 or SiN_x [463]. This superior passivation quality enables the HIT structure to achieve an impressive efficiency of 21.8%, with a V_{oc} of 718 mV on a CZ *n*-type substrate [464]. However a-Si has some drawbacks, one of them is thermal instability [465]. Severe

passivation degradation was reported after a short anneal at 350°C, although better stability was observed at 250°C [463]. The second drawback is the high absorption of the film, which limits its use as front surface passivation.

Appendix 7: High Intensity QSS-PL

This appendix presents the high intensity QSS-PL system developed in this thesis.

As mentioned in Chapter 3, the original setting of the QSS-PL system is limited to one-sun intensity [192]. In order to extend the system capacity, an 815 nm diode laser was employed to replace the LED-array package as the illumination source. This modification is able to increase the intensity up to 10 suns. Figure A7-1 presents the schematic of the new system set-up.

The main limitation of this set-up in its present form is the relatively complex method used to determine the scaling factors. As previously explained in Section 3.2.3, QSS-PL measurement involves two scaling factors. The first (f_s) relates to the system optics while the second (A_i) relates to the sample. In the traditional QSS-PL set-up, f_s is determined separately (by an additional calibrated detector) and only once for a system, whereas the self-consistent method is employed to determine the value of A_i. However, in the high intensity set-up both factors are unknown. In order to determine their values, the first measurement is performed using the traditional set-up. The value of A_i found in the low intensity measurement is then used in the high intensity measurement. This allows the value of f_s to be determined using the self-consistent method. The value of this factor was found to be in the range of 1.8-2.2×10^{18} and varied with to the sample position. A new system, based on a high intensity LED array is presently being built. In this new system f_s will need to be determined only once for the system.

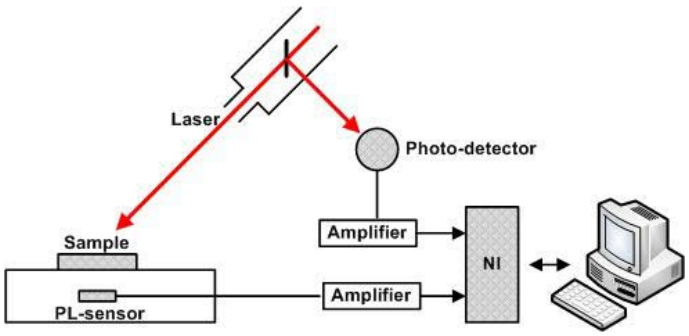

Figure A7-1: Schematic of the high intensity QSS-PL system.

Appendix 8: UNSW Q-switched Laser

This appendix presents the limitations of the diode-pumped, Q-switched, frequency-doubled Nd:YVO_4 laser system employed in this thesis. While the laser head was manufactured by Advanced-Optowave Corporation, all the other system components were manufactured and assembled by Yuemao. As this system does not contain an integrated power/energy meter, the relationship between the laser diode current and the average laser output power were established using an optical power meter located on the *X*-*Y* stage. Despite using identical laser settings (laser diode current and Q-switch frequency), the laser output was found to vary as shown in Figure A8-1.

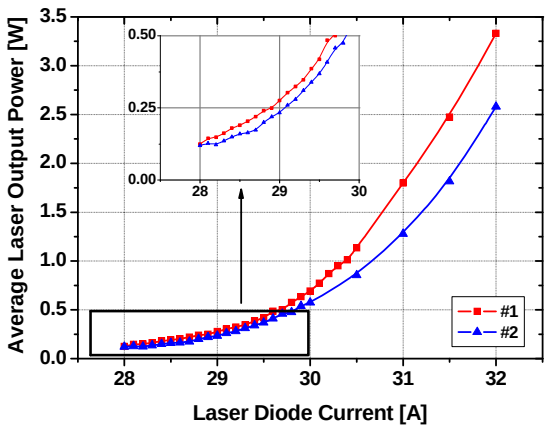

Figure A8-1: The average laser output power as a function of the laser diode current as measured on two different days. The solid lines are given as a guide to the eyes.

It is assumed that temperature fluctuation in the laser head is the cause for variation in the laser output power. In the present set-up, the laser head is air-cooled using fans without any active cooling element. Additionally the temperature of the laboratory is affected by changes in outdoor temperature and in equipment usage. This lack of control of the laser temperature causes the temperature of the laser head to vary, and hence also the power output as demonstrated in Figure A8-2. Therefore, the optimum laser diode current for laser doping had to be determined before each processing session, and effort was made to complete the processing within a short period of time. Note that this needs to be considered when comparing results from different processing days. In order to improve the temperature control, a water cooling system is recommended.

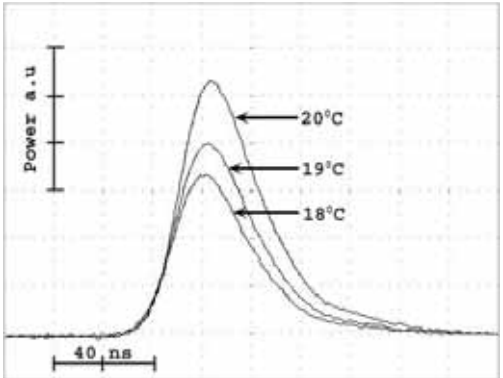

Figure A8-2: Oscilloscope images of laser pulses at different ambient temperatures (identical laser diode current and Q-switch frequency).

Another limitation of the employed laser system is variation of the laser power during operation. It seems the first sequence of pulses (> 500 pulses) is more powerful, although the laser system contains a first-pulse suppression mechanism. This power variation seems to be independence of the laser head temperature. Figure A8-3 demonstrates this problem by presenting two micrographs of LD lines. Image (a) was taken near the start of the outermost lines, while image (b) was taken 0.5 mm from this point. While ablation occurred near the starting point, a near-perfect melting was observed soon after. Similar behaviour was observed for all the lines created in this thesis. In order to minimise the influence of the first high-power pulses, all the LD lines were started outside the active area of the solar cells.

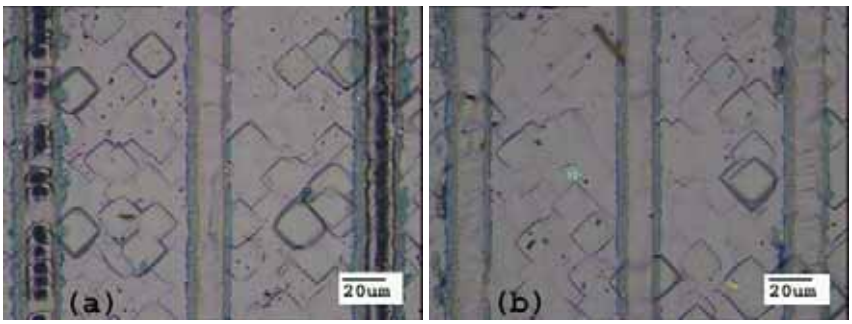

Figure A8-3: Micrographs of LD lines: near the starting point of the outermost lines (a) and 0.5 mm from this point (b)

Appendix 9: Effects of Spinning and Baking Conditions on the SHR

This appendix investigates the influence of the spinning and baking conditions on the obtained sheet resistivity.

In this part of the study, CZ *p*-type wafers with resistivity of 2 Ω.cm were employed. After an anisotropic alkaline texturing and RCA clean, SiN_x was deposited onto the front surface using industrial remote PECVD system. The refractive index and the thickness of the SiN_x film were found to be 2.05 and 75 nm, respectively (at 632.8 nm). Phosphorus SOD (P512) was used as a dopants source for all the wafers, while the spinning and baking conditions were varied. Only one parameter was varied each time, while the rest were set according to Table A9-2. On each sample, measurement pads were formed using 1-2 laser diode currents. The sheet resistivity was measured using the four-point probe method with an appropriate correction factor. Figure A9-1 presents the sheet resistivity as a function of the spinning conditions, while Figure A9-2 demonstrates the influence of the baking conditions.

As predicted, increasing the spinning speed decreases the SOD film thickness (see Figure A9-1 and Table A9-1). A thinner film contains fewer dopants [411], therefore the obtained SHR is increased. However, film uniformity improved with increasing rotation frequency. Therefore, in this study, it was found that rotation frequency of 3000 RPM provides a uniform film with relative low SHR. No influence of the spinning duration on the obtained SHR was observed as indicated by Figure A9-1 (b).

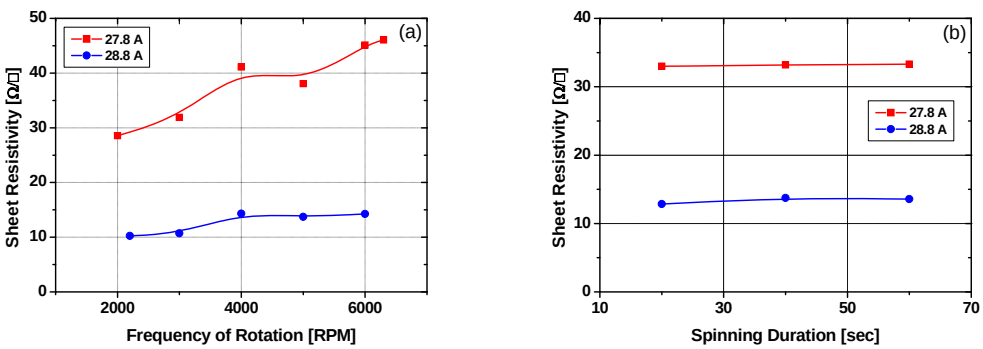

Figure A9-1: The sheet resistivity as a function of the rotation frequency (a) and spinning duration (b). The solid lines are given as a guide to the eyes.

Table A9-1: SOD film thickness for different rotation frequencies as measured by Dektak surface profiler.

RPM	Thickness [nm]
2000	~450
3000	~350
6000	~250

Figure A9-2 presents increasing SHR values when the baking duration and/or baking temperature are increased. It is assumed that both make the SOD film brittle and hence easy to be removed during laser irradiation [66].

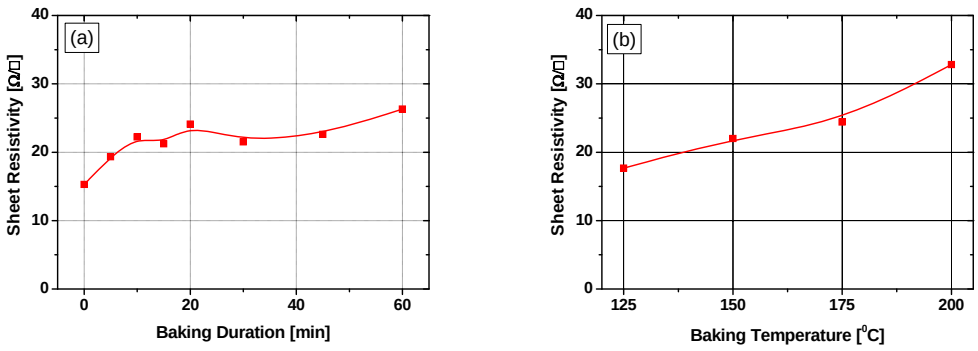

Figure A9-2: The sheet resistivity as a function of the baking duration (a) and baking temperature (b). The solid lines are given as a guide to the eyes.

Table A9-2 summarises the spinning and baking conditions, which were used in this thesis, as concluded from the investigation presented in this appendix.

Table A9-2: Spinning and baking conditions which were used in this thesis.

Rotation frequency	3000 RPM
Spinning duration	20 sec
Baking temperature	120°C
Baking duration	10 min

Appendix 10: Capture Cross Section

The following tables summarise the influence of variation in the capture cross sections on the minority carrier effective lifetime. Both low and high injection levels were considered, for different σ_n/σ_p ratios.

For a *p*-type substrate, σ_p mainly influences the effective lifetime at high injection level, while σ_n impacts the effective lifetime at low injection level. The ratio σ_n/σ_p determines the transition point between the two cases. For *n*-type, due to the positive fixed charge within the SiN_x, the effective lifetime is influenced mainly by σ_p in both low and high injection levels.

For *p*-type substrate:

		$\sigma_p \uparrow$	$\sigma_p \downarrow$	$\sigma_n \uparrow$	$\sigma_n \downarrow$
$\sigma_n/\sigma_p =$	Low injection	Decrease	Increase	Decrease	Increase
	High injection	Decrease	Increase	Decrease	Increase
$\sigma_n/\sigma_p \uparrow$	Low injection	Decrease	D/I	Decrease	D/I
	High injection	Decrease	Increase	=	=
$\sigma_n/\sigma_p \downarrow$	Low injection	D/I	Increase	D/I	Increase
	High injection	Decrease	Increase	=	=

For *n*-type substrate:

		$\sigma_p \uparrow$	$\sigma_p \downarrow$	$\sigma_n \uparrow$	$\sigma_n \downarrow$
$\sigma_n/\sigma_p \uparrow$	Low injection	Decrease	Increase	=	=
	High injection	Decrease	Increase	=	=
$\sigma_n/\sigma_p \downarrow$	Low injection	Decrease	Increase	=	=
	High injection	Decrease	Increase	=	=

↓ = decrease, ↑ = increase.

D/I: decrease or increase according to the specific parameters.

=: No change is predicated.

Appendix 11: PC1D Modelling Parameters

Table A11-1: Summary of the PC1D simulated parameters (Figure 5-2).

Parameter	Value
Thickness [μm]	170
Resistivity [Ω.cm]	1.0
Emitter sheet resistivity [Ω/□]	150
Bulk effective lifetime [μs]	100
Fill Factor [%]	79
Reflectance	Measured reflectance

Table A11-2: Summary of the PC1D simulated parameters (Figure 5-13).

Parameter	Value
Thickness [μm]	160
Resistivity [Ω.cm]	2.5
Emitter sheet resistivity [Ω/□]	1000
Bulk effective lifetime [μs]	160
Reflectance [%]	10

Table A11-3: Summary of the PC1D simulated parameters (Chapter 8).

Parameter		Value
Thickness [μm]		170
Resistivity [Ω.cm]		2.0
Reflectance		Measured reflectance
Front surface textured depth [μm]		1
Internal optical reflectance [%]		
Front:	First bounce	92
	Subsequent bounce	92
Rear :	First bounce	75
	Subsequent bounce	75
Emitter contact [Ω]		0.55
Internal conductor [S]		2.2×10^{-3}
Internal diode [A]		1×10^{-9}
	Ideality factor	2
Emitter sheet resistivity [Ω/□]		70
Emitter depth [μm]		0.4
Rear diffusion [cm^{-3}]		5×10^{18}
	Depth [μm]	5
	Profile	Uniform
Bulk effective lifetime [μs]		60
Front SRV [cm/s]		2.5×10^{4}
Rear SRV [cm/s]		1×10^{7}

Appendix 12: The Belt Furnace

Table A12-1: Summary of the belt furnace temperature setting.

Zone		Set temperature [°C]
HTO	Zone 1	300
	Zone 2	350
	Zone 3	400
	Zone 4	400
Heating	Zone 1	400
	Zone 2	500
	Zone 3	550
	Zone 4	650
	Zone 5	680
	Zone 6	687

Table A12-2: Summary of the belt furnace temperature setting (Sections 5.5.1, 5.5.2).

Zone		Set temperature [°C]
HTO	Zone 1	300
	Zone 2	350
	Zone 3	400
	Zone 4	400
Heating	Zone 1	400
	Zone 2	500
	Zone 3	550
	Zone 4	600 if zone 5 < 700°C 650 if zone 5 > 700°C
	Zone 5	Vary
	Zone 6	Vary

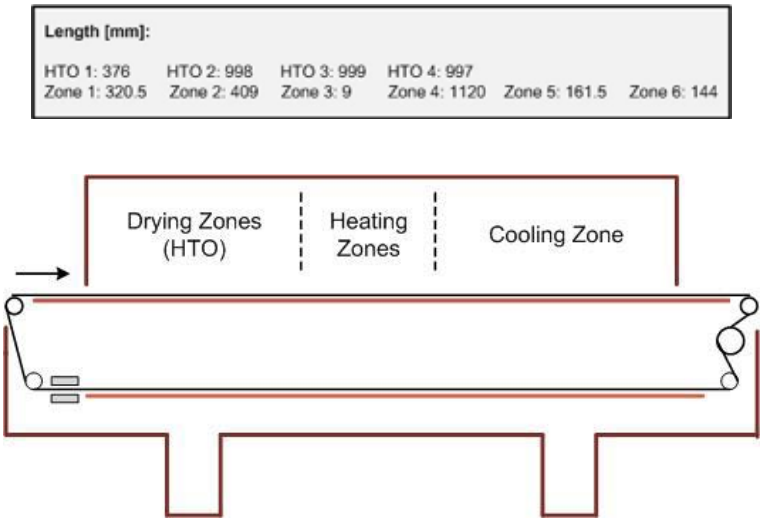

Figure A12-1: Diagram of the belt furnace.

Appendix 13: Industrial Remote PECVD System

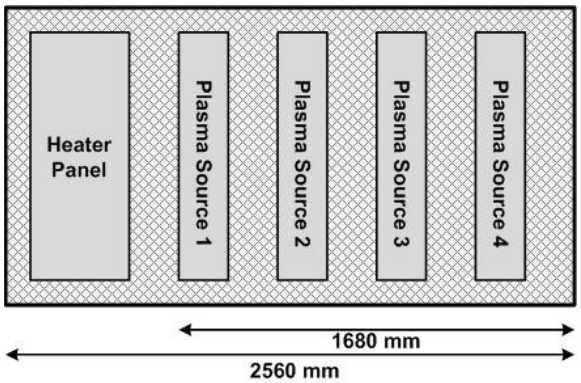

Figure A13-1: Diagram of the industrial remote PECVD system deposition chamber diagram (Roth & Rau – SINA).

Table A13-1: Deposition parameters of the industrial remote PECVD system.

Parameter	Value
Deposition temperature [°C]	350
Ammonia flow rate [sccm]	1600
Silane flow rate [sccm]	420
Total pressure [mbar]	0.17
Microwave power [W]	1300
RF power [W]	2000
Deposition speed [mm/min]	76

Appendix 14: Heat Transfer Simulation Parameters

Table A14-1: Summary of the heat transfer simulation parameters (Sections 6.2.2 and 7.3.1).

Parameter	Value
Wavelength [nm]	532
Average Power [mW]	500
Pulse Duration (FWHM) [ns]	40
Spatial Beam Profile	Gaussian
Gaussian Width [μm]	5
Temporal Pulse Shape	Typical Smooth Pulse
Reflectance at 532 nm [%]	10

Appendix 15: Fabrication Process Parameters

Table A15-1: Fabrication Process Parameters.

Process		Duration	Temperature
Emitter diffusion	(120 Ω/□)	12 min	850°C
Dry oxidation	(18 nm)	5 min	1060°C
Annealing		15 min	1000°C
ARC SiN_x deposition	GR = 1.14	105 sec	
Rear isolation	NaOH (12.5%)	10 min	55°C
Rear SiN_x deposition	GR = 0.77	105 sec	
Front side laser doping:			
Spinning condition	3000 RPM	20 sec	
Baking condition		10 min	120°C
Laser condition	Vary		
Rear side laser doping:			
Spinning condition	3000 RPM	20 sec	
Baking condition		10 min	120°C
Laser condition	Vary		
SiN_x annealing	4600 mm/s		680°C

Bibliography

[1] Houghton J. Global warming. *Reports on Progress in Physics* 2005; **68**: 1343-1403.
[2] *Copenhagen Diagnosis*, The Climate Change Research Centre - UNSW, 2009.
[3] Service RF. Is it time to shoot for the sun? *Science* 2005; **309**: 548-551.
[4] *Global Status Report*, REN21, 2010.
[5] *The Energy Challenge for Achieving the Millennium Development Goals*, UN-Energy, United Nations, 2005.
[6] Blackburn J, Cunninngham S, *Solar and Nuclear Costs —The Historic Crossover*, Renewable Energy World, 2010.
[7] *The Case Against Nuclear Power*, Greenpeace, 2008.
[8] http://www.solarbuzz.com, last accessed: 12 August, 2010.
[9] Lide D. *CRC Handbook of Chemistry and Physics*. 90th ed., 2009.
[10] Bruton TM. General trends about photovoltaics based on crystalline silicon. *Solar Energy Materials and Solar Cells* 2002; **72**: 3-10.
[11] Jester TL. Crystalline silicon manufacturing progress. *Progress in Photovoltaics: Research and Applications* 2002; **10**: 99-106.
[12] *The Oxford English Dictionary*. Oxford University Press, 1989.
[13] *The Macquarie Concise Dictionary*. The Macquarie Library, 2004.
[14] Becquerel AE. Mémoire sur les effets électriques produits sous l'influence des rayons solaires. *Comptes Rendus des Séances Hebdomadaires* 1839; **9**: 561-567.
[15] Green M. Photovoltaic principles. *Physica E: Low-dimensional Systems and Nanostructures* 2002; **14**: 11-17.
[16] Fritts CE. On a New Form of Selenium Photocell. *Proceedings of the American Association for the Advancement of Science*, 1883: 97.
[17] Fritts CE. A new form of selenium cell. *American Journal of Science* 1883; **26**: 465.
[18] Ohl RS. Light sensitive electric device. *US Patent Number 2402662* 1941.
[19] Chapin DM, Fuller CS, Pearson GL. A New Silicon p-n Junction Photocell for Converting Solar Radiation into Electrical Power. *Journal of Applied Physics* 1954; **25**: 676-677.
[20] Willeke GP. The crystalline silicon solar cell—history, achievements and perspectives. *19th European Photovoltaic Solar Energy Conference*, 2004: 383-386.
[21] Mandelkorn J, McAfee C, Kesperis J, Schwartz L, Pharo W. Fabrication and Characteristics of Phosphorous-Diffused Silicon Solar Cells. *Journal of The Electrochemical Society* 1962; **109**: 313-318.
[22] Green MA. The path to 25% silicon solar cell efficiency: History of silicon cell evolution. *Progress in Photovoltaics: Research and Applications* 2009; **17**: 183-189.
[23] Lindmayer J, Allison JF. The violet cell: An improved silicon solar cell. *Comsat Technical Review* 1973; **3**: 1-22.
[24] Shockley W, Queisser H. Detailed Balance Limit of Efficiency of p-n Junction Solar Cells. *Journal of Applied Physics* 1961; **32**: 510-519.
[25] Zhao J, Wang A, Green MA. 24·5% Efficiency silicon PERT cells on MCZ substrates and 24·7% efficiency PERL cells on FZ substrates. *Progress in Photovoltaics: Research and Applications* 1999; **7**: 471-474.

[26] Mai L. *Overcoming The Performance and Limitation of Comercial Screen-Printed Solar Cells*. PhD dissertation, University of New South Wales, Sydney, Australia, 2010.
[27] Ralph EL. Recent advancements in low cost solar cell processing. *11th IEEE Photovoltaic Specialists Conference (PVSC)*, 1975: 315-316.
[28] Hilali M, To B, Rohatgi A. A review and understanding of screen-printed contacts and selective-emitter formation. *14th Workshop on Crystalline Silicon Solar Cells and Modules*, 2004.
[29] Mandelkorn J, Lamneck J. Simplified fabrication of back surface electric field silicon cells and novel characteristics of such cells. *9th IEEE Photovoltaic Specialists Conference*, 1972: 66-71.
[30] Mandelkorn J, Lamneck JH. A new electric field effect in silicon solar cells. *Journal of Applied Physics* 1973; **44**: 4785-4787.
[31] Green MA. *Silicon Solar Cells: Advanced Principles & Practice*. University of New South Wales: Sydney, Australia, 1995.
[32] Zhao J, Wang A, Altermatt P, Wenham S, Green M. 24% efficient PERL silicon solar cell: Recent improvements in high efficiency silicon cell research. *Solar Energy Materials and Solar Cells* 1996; **41-42**: 87-99.
[33] Zhao J, Wang A, Altermatt PP, Wenham SR, Green MA. 24% efficient silicon solar cells. *24th IEEE Photovoltaic Specialists Conference, First WCPEC*, 1994: 1477-1480.
[34] Zhao J, Wang A, Altermatt P, Green MA. Twenty-four percent efficient silicon solar cells with double layer antireflection coatings and reduced resistance loss. *Applied Physics Letters* 1995; **66**: 3636-3638.
[35] Green MA, Zhao J, Wang A, Wenham SR. Very high efficiency silicon solar cells-science and technology. *IEEE Transactions on Electron Devices* 1999; **46**: 1940-1947.
[36] Wang A. *High Efficiency PERC and PERL Silicon Solar Cells*. PhD dissertation, University of New South Wales, Sydney, Australia, 1992.
[37] Zhao J, Wang A, Green M. Performance degradation in CZ(B) cells and improved stability high efficiency PERT and PERL silicon cells on a variety of SEH MCZ(B), FZ(B) and CZ(Ga) substrates. *Progress in Photovoltaics: Research and Applications* 2000; **8**: 549-558.
[38] Wenham SR, Green MA. Laser grooved solar cell. *US Patent 4,626,613* 1986.
[39] Wenham SR, Green MA. Buried contact solar cell. *US Patent 4,726,850* 1988.
[40] Chong C, Wenham S, Green M. High-efficiency, laser grooved, buried contact silicon solar cells. *Applied Physics Letters* 1988; **52**: 407-409.
[41] Myers SM, Seibt M, Schroter W. Mechanisms of transition-metal gettering in silicon. *Journal of Applied Physics* 2000; **88**: 3795-3819.
[42] Ourmazd A, Schroter W. Phosphorus gettering and intrinsic gettering of nickel in silicon. *Applied Physics Letters* 1984; **45**: 781-783.
[43] Green MA, Chong CM, Zhang F, Sproul A, Zolper J, Wenham SR. 20% efficient laser grooved, buried contact silicon solar cells. *20th IEEE Photovoltaic Specialists Conference*, 1988: 411-414.
[44] Wenham S. Buried-contact silicon solar cells. *Progress in Photovoltaics: Research and Applications* 1993; **1**: 3-10.
[45] Wenham SR, Honsberg CB, Green MA. Buried contact silicon solar cells. *Solar Energy Materials and Solar Cells* 1994; **34**: 101-110.

[46] Honsberg CB, Yun F, Ebong A, Taouk M, Wenham SR, Green MA. 685 mV open-circuit voltage laser grooved silicon solar cell. *Solar Energy Materials and Solar Cells* 1994; **34**: 117-123.
[47] Tang YH, Dai XM, Zhao JH, Wang AH, Wenham SR, Honsberg CB. Rear surface passivation in buried contact solar cells. *26th IEEE Photovoltaic Specialists Conference*, 1997: 251-254.
[48] Ebong A, Lee S, Honsberg C, Wenham S. High Efficiency Double Sided Buried Contact Silicon Solar Cells. *Japanese Journal of Applied Physics* 1996; **35**: 2077-2080.
[49] Guo J-H, Cotter JE. Laser-grooved backside contact solar cells with 680-mV open-circuit voltage. *IEEE Transactions on Electron Devices* 2004; **51**: 2186-2192.
[50] Cousins PJ. *High Efficiency, Thin Double-Sided Buried Contact Solar Cells on Commercial Monocrystalline Silicon Wafers*. PhD dissertation, University of New South Wales, Sydney, Australia, 2004.
[51] Guo J-H, Tjahjono BS, Cotter JE. 19.2% efficiency n-type laser-grooved silicon solar cells. *31st IEEE Photovoltaic Specialists Conference*, 2005: 983-986.
[52] Green MA, Wenham SR, Honsberg CB, Hogg D. Transfer of buried contact cell laboratory sequences into commercial production. *Solar Energy Materials and Solar Cells* 1994; **34**: 83-89.
[53] Bruton TM, Heasman KC, Nagle JP, Cunningham DW, Mason NB, Russell R, Balbuena MA. Large area high efficiency silicon solar cells made by the laser grooved buried grid process. *12th European Photovoltaic Solar Energy Conference*, 1994: 761-762.
[54] Bruton T, Mason N, Roberts S, Hartley ON, Gledhill S, Fernandez J, Russell R, Warta W, Glunz S, Schultz O, Hermle M, Willeke G. Towards 20% efficient silicon solar cells manufactured at 60 MWp per annum. *3rd World Conference on Photovoltaic Energy Conversion*, 2003: 899-902.
[55] Mason NB, Jordan D. A high efficiency silicon solar cell production technology. *10th European Photovoltaic Solar Energy Conference*, 1991: 280-283.
[56] Wenham SR, Mai L, Ji J, Shi Z. Low area contacts for screen-printed solar cells. *PCT/AU2006/001603* 2007.
[57] Wenham SR, Mai L, Tjahjono B, Ji J, Shi Z. Innovative emitter design and metal contact for screen-printed solar cells. *15th International Photovoltaic Science and Engineering Conference*, 2005: 804-805.
[58] Mai L, Wenham SR, Tjahjono B, Ji J, Shi Z. New Emitter Design and Metal Contact for Screen-Printed Solar Cell Front Surfaces. *4th IEEE World Conference on Photovoltaic Energy Conversion*, 2006: 890-893.
[59] Hauser A, Hahn G, Spiegel M, Feist H, Breitenstein O, Rakotoniaina JP, Fath P, Bucher E. Comparison of different techniques for edge isolation. *17th European Photovoltaic Solar Energy Conference*, 2001: 1739-1742.
[60] Guo JH, Cotter E, McIntosh KR, Fisher K, Chen FW, Karpour A. Edge passivation for small-area, high-efficiency solar cells. *22nd European Photovoltaic Solar Energy Conference*, 2007: 1348-1351.
[61] Abbott MD, Trupke T, Hartmann HP, Gupta R, Breitenstein O. Laser isolation of shunted regions in industrial solar cells. *Progress in Photovoltaics: Research and Applications* 2007; **15**: 613-620.
[62] Knorz A, Peters M, Grohe A, Harmel C, Preu R. Selective laser ablation of SiNx layers on textured surfaces for low temperature front side metallizations. *Progress in Photovoltaics: Research and Applications* 2009; **17**: 127-136.

[63] Hermann S, Harder N, Brendel R, Herzog D, Haferkamp H. Picosecond laser ablation of SiO2 layers on silicon substrates. *Applied Physics A: Materials Science & Processing* 2010; **99**: 151-158.
[64] Engelhart P, Hermann S, Neubert T, Plagwitz H, Grischke R, Meyer R, Klug U, Schoonderbeek A, Stute U, Brendel R. Laser ablation of SiO2 for locally contacted Si solar cells with ultra-short pulses. *Progress in Photovoltaics: Research and Applications* 2007; **15**: 521-527.
[65] Pirozzi L, Vetrella UB, Falconieri M, Salza E. A laser system for silicon solar cell processing: design, setup and operation. *Materials Science Forum* 1995; **173-174**: 319-324.
[66] Abbott MD. *Advanced Laser Processing and Photoluminescence Characterisation of High Efficiency Silicon Solar Cells*. PhD dissertation, University of New South Wales, Sydney, Australia, 2006.
[67] Pirozzi L, Vetrella U, Salza E. Innovative applications of laser technology in photovoltaics. *Laser Applications in Microelectronic and Optoelectronic Manufacturing II*, 1997: 119-128.
[68] Kray D, Baumann S, Mayer K, Eyer A, Willeke GP. Novel techniques for low-damage microstructuring of silicon. *20th European Photovoltaic Solar Energy Conference*, 2005: 156-159.
[69] Muller JC, Fogarassy E, Salles D, Stuck R, Siffert PM. Laser processing in the preparation of silicon solar cells. *IEEE Transactions on Electron Devices* 1980; **27**: 815-821.
[70] Van Kerschaver E, Einhaus R, Szlufcik J, Nijs J, Mertens R. A novel silicon solar cell structure with both external polarity contacts on the back surface. *2nd World Conference on Photovoltaic Solar Energy Conversion*, 1998: 1479-1482.
[71] Gee JM, Schubert WK, Basore PA. Emitter wrap-through solar cell. *23rd IEEE Photovoltaic Specialists Conference*, 1993: 265-270.
[72] Jooss W, Neu W, Faika K, Knauss H, Kress A, Keller S, Fath P, Bucher E. Process and technology development for back contact silicon solar cells. *29th IEEE Photovoltaic Specialists Conference*, 2002: 122-125.
[73] Gee JM, Buck ME, Schubert WK, Basore PA. Progress on the emitter wrap-through silicon solar cell. *12th European Photovoltaic Solar Energy Conference*, 1994: 743-746.
[74] Knauss H, Jooss W, Roberts S, Bruton TM, Toelle R, Fath P, Bucher E. Emitter wrap through solar cells using electroless plating metallisation. *17th European Photovoltaic Solar Energy Conference*, 2001.
[75] Kray D, Dicker J, Osswald D, Leimenstoll A, Glunz SW, Zimmermann W, Tentscher KH, Strobl G. Progress in high-efficiency emitter-wrap-through cells on medium quality substrates. *3rd World Conference on Photovoltaic Energy Conversion*, 2003: 1340-1343.
[76] Fellmeth T, Menkoe M, Clement F, Biro D, Preu R. Highly efficient industrially feasible metal wrap through (MWT) silicon solar cells. *Solar Energy Materials and Solar Cells* 2010; **94**: 1996-2001.
[77] Schneiderlöchner E, Preu R, Lüdemann R, Glunz SW. Laser-fired rear contacts for crystalline silicon solar cells. *Progress in Photovoltaics: Research and Applications* 2002; **10**: 29-34.
[78] Harper FE, Cohen MI. Properties of Si diodes prepared by alloying Al into n-type Si with heat pulses from a Nd:YAG laser. *Solid-State Electronics* 1970; **13**: 1103-1109.

[79] Glunz SW, Schneiderlöchner E, Kray D, Grohe A, Hermle M, Kempwerth H, Preu R, Willeke G. Laser-fired contact solar cells on p-and n-type substrates. *19th European Photovoltaic Solar Energy Conference*, 2004: 408-411.
[80] Mason NB, Schultz O, Russell R, Glunz SW, Warta W. 20.1% efficient large area cell on 140 micron thin silicon wafer. *21st European Photovoltaic Solar Energy Conference*, 2006: 521-523.
[81] Schultz O, Glunz SW, Warta W, Preu R, Grohe A, Köber M, Willeke GP, Russel R, Fernandez J, Morilla C, Bueno R, Vincuería I. High-efficiency solar cells with laser-grooved buried contact front and laser-fired rear for industrial production. *21st European Photovoltaic Solar Energy Conference*, 2006: 826-829.
[82] Schultz O, Glunz SW, Willeke GP. Multicrystalline silicon solar cells exceeding 20% efficiency. *Progress in Photovoltaics: Research and Applications* 2004; **12**: 553-558.
[83] Hofmann M, Saint-Cast P, Suwito D, Seiffe J, Schmidt C, Kambor S, Gautero L, Kohn N, Nekarda J, Leimenstoll A, Wagenmann D, Erath D, Catoir J, Wolke W, Janz S, Biro D, Grohe A, Rentsch J, Glunz S, Preu R. Overview on crystalline silicon solar cells using PECVD passivation and laser-fired contacts. *24th European Photovoltaic Solar Energy Conference*, 2009.
[84] Engelhart P, Teppe A, Merkle A, Grischke R, Meyer R, Harder N-P, Brendel R. The RISE-EWT solar cell: new approach towards simple high efficiency silicon solar cells. *17th International Photovoltaic Science and Engineering Conference (PVSEC)*, 2005: 802-803.
[85] Engelhart P, Harder NP, Merkle A, Grischke R, Meyer R, Brendel R. RISE: 21.5% Efficient Back Junction Silicon Solar Cell with Laser Technology as a Key Processing Tool. *4th IEEE World Conference on Photovoltaic Energy Conversion*, 2006: 900-904.
[86] Engelhart P, Harder N, Grischke R, Merkle A, Meyer R, Brendel R. Laser structuring for back junction silicon solar cells. *Progress in Photovoltaics: Research and Applications* 2007; **15**: 237-243.
[87] Fairfield J, Schwuttke GH. Silicon diodes made by laser irradiation. *Solid State Electronics* 1968; **11**: 1175-1176.
[88] Young RT, Wood RF, Narayan J, White CW, Christie WH. Pulsed laser techniques for solar cell processing. *IEEE Transactions on Electron Devices* 1980; **27**: 807-815.
[89] Young RT, Wood RF, Christie WH, Jellison GE. Substrate heating and emitter dopant effects in laser-annealed solar cells. *Applied Physics Letters* 1981; **39**: 313-315.
[90] Young RT, Wood RF, Christie WH. Laser processing for high-efficiency Si solar cells. *Journal of Applied Physics* 1982; **53**: 1178-1189.
[91] Turner GB, Tarrant D, Pollock G, Pressley R, Press R. Solar cells made by laser-induced diffusion directly from phosphine gas. *Applied Physics Letters* 1981; **39**: 967-969.
[92] Besi-Vetrella U, Arabito G, Barbarossa V, Salza E, Artuso F, Belardinelli M, Grilli ML, Pirozzi L. Structural and electrcial characterization of laser doped silicon. *2nd World Conference and Exhibition on Photovoltaic Solar Energy Conversion*, 1998: 1366-1369.
[93] Deutsch TF, Fan JCC, Turner GW, Chapman RL, Ehrlich DJ, Osgood RM. Efficient Si solar cells by laser photochemical doping. *Applied Physics Letters* 1981; **38**: 144-146.

[94] Young RT, van der Leeden GA, Sandstrom RL, Wood RF, Westbrook RD. High-efficiency Si solar cells by beam processing. *Applied Physics Letters* 1983; **43**: 666-668.
[95] Stuck R, Fogarassy E, Muller JC, Hodeau M, Wattiaux A, Siffert P. Laser-induced diffusion by irradiation of silicon dipped into an organic solution of the dopant. *Applied Physics Letters* 1981; **38**: 715-717.
[96] Kray D, Fell A, Hopman S, Mayer K, Willeke G, Glunz S. Laser Chemical Processing (LCP) A versatile tool for microstructuring applications. *Applied Physics A: Materials Science & Processing* 2008; **93**: 99-103.
[97] Narayan J, Young RT, Wood RF, Christie WH. p-n junction formation in boron-deposited silicon by laser-induced diffusion. *Applied Physics Letters* 1978; **33**: 338-340.
[98] Fogarassy E, Stuck R, Grob JJ, Siffert P. Silicon solar cells realized by laser induced diffusion of vacuum-deposited dopants. *Journal of Applied Physics* 1981; **52**: 1076-1082.
[99] Eisele S, Bilger G, Ametowobla M, Kohler JR, Werner JH. Sputtered phosphorus precursors for laser doping. *17th International Photovoltaic Science and Engineering Conference (PVSEC)*, 2007: 715-716.
[100] Wong YW, Yang XQ, Chan PW, Tong KY. Excimer-laser doping of spin-on dopant in silicon. *Applied Surface Science* 1993; **64**: 259-263.
[101] Lo VC, Wong YW, Cho HC, Chen YQ, Ho SM, Chan PW, Tong KY. Excimer laser assisted spin-on doping of boron into silicon. *Semiconductor Science and Technology* 1996; **11**: 1285-1290.
[102] Ventura L, Schunck JP, Muller JC, Barthe S, Vetrella UB, Pirozzi L, Salza E. Influence of baking conditions of doped spin-on glass sources on the formation of laser assisted selective emitters. *25th IEEE Photovoltaic Specialists Conference*, 1996: 577-580.
[103] Ametowobla M, Esturo-Breton A, Kohler JR, Werner JH. Laser processing of crystalline silicon solar cells. *31st IEEE Photovoltaic Specialists Conference*, 2005: 1277-1280.
[104] Eisele SJ, Roder TC, Kohler JR, Werner JH. 18.9% efficient full area laser doped silicon solar cell. *Applied Physics Letters* 2009; **95**: 133501.
[105] Esturo-Breton A, Ametowobla M, Kohler JR, Werner JH. Laser doping for crystalline silicon solar cell emitters. *20th European Photovoltaic Solar Energy Conference*, 2005: 851-854.
[106] Grilli ML, Arabito G, Artuso F, Barbarossa V, Belardinelli M, Besi-Vetrella U, Ferrazza F, Ginocchietti G, Nacci R, Salza E, Pirozzi L. Screen priniting on laser doped selective emitter for large area production silicon solar cells. *2nd World Conference and Exhibition on Photovoltaic Solar Energy Conversion*, 1998: 1854-1857.
[107] Besi-Vetrella U, Pirozzi L, Salza E, Ginocchietti G, Ferrazza F, Ventura L, Slaoui A, Muller JC. Large area, screen printed silicon solar cells with selective emitter made by laser overdoping and RTA spin-on glasses. *26th IEEE Photovoltaic Specialists Conference*, 1997: 135-138.
[108] Besi-Vetrella U, Arabito G, Barbarossa V, Salza E, Artuso F, Grilli ML, Belardinelli M, Pirozzi L. A novel method to get localized BSF in silicon solar cells. *2nd World Conference and Exhibition on Photovoltaic Solar Energy Conversion*, 1998: 1562-1565.

[109] Carlsson C, Esturo-Breton A, Ametowobla M, Kohler JR, Werner JH. Laser doping for selective silicon solar cell emitter. *21st European Photovoltaic Solar Energy Conference*, 2006: 938-940.
[110] Röder TC, Eisele SJ, Grabitz P, Wagner C, Kulushich G, Köhler JR, Werner JH. Add-on laser tailored selective emitter solar cells. *Progress in Photovoltaics: Research and Applications* 2010; **18**: 505-510.
[111] Jager U, Okanovic M, Hortheis M, Grohe A, Preu R. Selective emitter by laser doping from phosphosilicate glass. *24th European Photovoltaic Solar Energy Conference*, 2009.
[112] Eisele S, Ametowobla M, Bilger G, Kohler JR, Werner JH. Phosphorus sputtered laser doped emitters. *23rd European Photovoltaic Solar Energy Conference*, 2008: 1737-1739.
[113] Willeke G, Kray D. A new route towards 50 um thin crystalline silicon wafer solar cells. *17th European Photovoltaic Solar Energy Conference*, 2001: 1621-1624.
[114] Kray D, Fell A, Hopman S, Mayer K, Mesec M, Glunz SW, Willeke GP. Progress in laser chemical processing (LCP) for innovative solar cell microstructuring and wafering applications. *22nd European Photovoltaic Solar Energy Conference*, 2007.
[115] Richerzhagen B, Delacrétaz G, Salathé R. Complete model to simulate the thermal defocusing of a laser beam focused in water. *Optical Engineering* 1996; **35**: 2058-2066.
[116] http://www.synova.ch, last accessed: 3 September, 2010.
[117] Hopman S, Fell A, Mayer K, Mesec M, Rodofili A, Kray D. Comparison of Laser Chemical Processing and LaserMicroJet for structuring and cutting silicon substrates. *Applied Physics A: Materials Science & Processing* 2009; **95**: 857-866.
[118] Hopman S, Fell A, Mayer K, Aleman M, Mesec M, Muller R, Kray D, Willeke GP. Characterization of laser doped silicon wafers with laser chemical processing. *22nd European Photovoltaic Solar Energy Conference*, 2007.
[119] Rodofili A, Fell A, Hopman S, Mayer K, Willeke GP, Kray D, Glunz SW. Local p-type back surface fields via laser chemical processing (LCP): first experiments. *23rd European Photovoltaic Solar Energy Conference*, 2008: 1808-1811.
[120] Rodofili A, Hopman S, Fell A, Mayer K, Mesec M, Granek F, Glunz SW. Characterization of doping via laser chemical processing (LCP). *24th European Photovoltaic Solar Energy Conference*, 2009.
[121] Kray D, Aleman M, Fell A, Hopman S, Mayer K, Mesec M, Muller R, Willeke GP, Glunz SW, Bitnar B, Neuhaus DH, Ludemann R, Schlenker T, Manz D, Bentzen A, Sauar E, Pauchard A, Richerzhagen B. Laser-doped silicon solar cells by Laser Chemical Processing (LCP) exceeding 20% efficiency. *33rd IEEE Photovoltaic Specialists Conference*, 2008: 1-3.
[122] Werner JH, Kohler J, Esturo-Breton A. Laser doping of solid bodies using a linear-focussed laser beam and production of solar-cell emitters based on said method. *US Patent Application 2008/0026550 A1* 2008.
[123] Kohler JR, Ametowobla M, Esturo-Breton A. Numerical modeling of pulsed laser doping of crystalline silicon solar cells. *20th European Photovoltaic Solar Energy Conference*, 2005.
[124] Esturo-Breton A, Ametowobla M, Carlsson C, Kohler J, Werner J. 15.4% efficiency silicon solar cells with laser doped emitter. *21st European Photovoltaic Solar Energy Conference*, 2006: 1247-1249.

[125] Carlsson C, Esturo-Breton A, Ametowobla M, Kohler JR, Werner JH. Laser doping of textured monocrystalline silicon wafers. *22nd European Photovoltaic Solar Energy Conference*, 2007: 1593-1595.
[126] Roder T, Esturo-Breton A, Eisele S, Wagner C, Kohler JR, Werner JH. Fill factor loss of laser doped textured silicon solar cells. *23rd European Photovoltaic Solar Energy Conference*, 2008: 1740-1742.
[127] Wenham SR, Green MA. Self aligning method for forming a selective emitter and metallization in a solar cell. *US Patent Application 6429037* 2002.
[128] Tjahjono BS, Guo JH, Hameiri Z, Mai L, Sugianto A, Wang S, Wenham SR. High efficiency solar cells structures through the use of laser doping. *22nd European Photovoltaic Solar Energy Conference*, 2007: 966-969.
[129] Abbott MD, Cotter JE, Fisher K. N-type bifacial solar cells with laser doped contacts. *4th IEEE World Conference on Photovoltaic Energy Conversion*, 2006: 988-991.
[130] Mai L, Hameiri Z, Tjahjono BS, Wenham SR, Sugianto A, Edwards MB. Rear junction laser doped solar cells on CZ n-type silicon. *34th IEEE Photovoltaic Specialists Conference (PVSC)*, 2009: 1811-1815.
[131] Hopman S, Fell A, Mayer K, Fleischmann C, Drew K, Kray D, Granek F. Study on Laser Parameters for Silicon Solar Cells with LCP Selective Emitters. *24th European Photovoltaic Solar Energy Conference*, 2009: 1072-1076.
[132] Tjahjono B, Wang S, Sugianto A, Mai L, Hameiri Z, Borojevic N, Ho-Baillei A, Wenham S. Application of laser doped contact structure on multicrystalline solar cells. *23rd European Photovoltaic Solar Energy Conference*, 2008: 1995-2000.
[133] Aberle AG. *Crystalline Silicon Solar Cells: Advanced Surface Passivation and Analysis*. University of New South Wales: Sydney, Australia, 2004.
[134] Aberle A. Surface passivation of crystalline silicon solar cells: a review. *Progress in Photovoltaics: Research and Applications* 2000; **8**: 473-487.
[135] Green MA. *Solar Cells: Operating Principles, Technology and System Application*. University of New South Wales: Sydney, Australia, 1998.
[136] Kerr MJ. *Surface, Emitter and Bulk Recombination in Silicon and Development of Silicon nitride Passivated Solar Cells*. PhD dissertation, Australian National University, 2002.
[137] Altermatt P, Schenk A, Geelhaar F, Heiser G. Reassessment of the intrinsic carrier density in crystalline silicon in view of band-gap narrowing. *Journal of Applied Physics* 2003; **93**: 1598-1604.
[138] Sproul AB, Green MA, Zhao J. Improved value for the silicon intrinsic carrier concentration at 300 K. *Applied Physics Letters* 1990; **57**: 255-257.
[139] Trupke T, Green MA, Wurfel P, Altermatt PP, Wang A, Zhao J, Corkish R. Temperature dependence of the radiative recombination coefficient of intrinsic crystalline silicon. *Journal of Applied Physics* 2003; **94**: 4930-4937.
[140] Schlangenotto H, Maeder H, Gerlach W. Temperature dependence of the radiative recombination coefficient in silicon. *Physica Status Solidi (a)* 1974; **21**: 357-367.
[141] Parks J, Brennan K, Smith A. Two-dimensional model of photon recycling in direct gap semiconductor devices. *Journal of Applied Physics* 1997; **82**: 3493-3498.
[142] Tyagi MS, Van Overstraeten R. Minority carrier recombination in heavily-doped silicon. *Solid-State Electronics* 1983; **26**: 577-597.
[143] Dziewior J, Schmid W. Auger coefficients for highly doped and highly excited silicon. *Applied Physics Letters* 1977; **31**: 346-348.

[144] Hangleiter A, Häcker R. Enhancement of band-to-band Auger recombination by electron-hole correlations. *Physical Review Letters* 1990; **65**: 215.
[145] Glunz SW, Biro D, Rein S, Warta W. Field-effect passivation of the SiO2-Si interface. *Journal of Applied Physics* 1999; **86**: 683-691.
[146] Kerr M, Cuevas A. General parameterization of Auger recombination in crystalline silicon. *Journal of Applied Physics* 2002; **91**: 2473-2480.
[147] Shockley W, Read WT. Statistics of the Recombinations of Holes and Electrons. *Physical Review* 1952; **87**: 835.
[148] Hall RN. Electron-Hole Recombination in Germanium. *Physical Review* 1952; **87**: 387.
[149] Rein S, Rehrl T, Warta W, Glunz SW. Lifetime spectroscopy for defect characterization: Systematic analysis of the possibilities and restrictions. *Journal of Applied Physics* 2002; **91**: 2059-2070.
[150] Schroder D. *Semiconductor Material and Device Characterization*. Wiley-IEEE Press, 2006.
[151] Otaredian T. Separate contactless measurement of the bulk lifetime and the surface recombination velocity by the harmonic optical generation of the excess carriers. *Solid-State Electronics* 1993; **36**: 153-162.
[152] Sproul AB. Dimensionless solution of the equation describing the effect of surface recombination on carrier decay in semiconductors. *Journal of Applied Physics* 1994; **76**: 2851-2854.
[153] Grove AS, Fitzgerald DJ. Surface effects on p-n junctions: Characteristics of surface space-charge regions under non-equilibrium conditions. *Solid-State Electronics* 1966; **9**: 783-806.
[154] Sze S, Ng K. *Physics of Semiconductor Devices*. John Wiley& Sons. Inc., 2007.
[155] Bennett H, Wilson C. Statistical comparisons of data on band-gap narrowing in heavily doped silicon: Electrical and optical measurements. *Journal of Applied Physics* 1984; **55**: 3582-3587.
[156] Dumke W. Quantum Theory of Free Carrier Absorption. *Physical Review* 1961; **124**: 1813.
[157] Kane DE, Swanson RM. Measurement of the emitter saturation current by a contactless photoconductivity decay method. *IEEE Photovoltaic Specialists Conference*, 1985.
[158] Schmidt J, Lauinger T, Aberle AG, Hezel R. Record low surface recombination velocities on low-resistivity silicon solar cell substrates. *25th IEEE Photovoltaic Specialists Conference*, 1996: 413-416.
[159] Schmidt J, Kerr M. Highest-quality surface passivation of low-resistivity p-type silicon using stoichiometric PECVD silicon nitride. *Solar Energy Materials and Solar Cells* 2001; **65**: 585-591.
[160] Lauinger T, Schmidt J, Aberle A, Hezel R. Record low surface recombination velocities on 1 ohm.cm p-silicon using remote plasma silicon nitride passivation. *Applied Physics Letters* 1996; **68**: 1232-1234.
[161] Leguijt C, Lolgen P, Eikelboom JA, Weeber AW, Schuurmans FM, Sinke WC, Alkemade PFA, Sarro PM, Maree CHM, Verhoef LA. Low temperature surface passivation for silicon solar cells. *Solar Energy Materials and Solar Cells* 1996; **40**: 297-345.
[162] Yablonovitch E, Allara DL, Chang CC, Gmitter T, Bright TB. Unusually low surface-recombination velocity on silicon and germanium surfaces. *Physical Review Letters* 1986; **57**: 249-252.

[163] Kampwerth H, Rein S, Glunz SW. Pure experimental determination of surface recombination properties with high reliability. *3rd World Conference on Photovoltaic Energy Conversion*, 2003: 1073-1076.
[164] Buczkowski A, Radzimski ZJ, Rozgonyi GA, Shimura F. Separation of the bulk and surface components of recombination lifetime obtained with a single laser/microwave photoconductance technique. *Journal of Applied Physics* 1992; **72**: 2873-2878.
[165] Cuevas A. The effect of emitter recombination on the effective lifetime of silicon wafers. *Solar Energy Materials and Solar Cells* 1999; **57**: 277-290.
[166] Markvart T. *Practical Handbook of Photovoltaics: Fundamentals and Applications*. Elsevier Science Ltd, 2003.
[167] Stevenson D, Keyes R. Measurement of Carrier Lifetimes in Germanium and Silicon. *Journal of Applied Physics* 1955; **26**: 190-195.
[168] Thurber WR, Mattis RL, Liu YM, Filliben JJ. Resistivity-Dopant Density Relationship for Phosphorus-Doped Silicon. *Journal of The Electrochemical Society* 1980; **127**: 1807-1812.
[169] Thurber WR, Mattis RL, Liu YM, Filliben JJ. Resistivity-Dopant Density Relationship for Boron-Doped Silicon. *Journal of The Electrochemical Society* 1980; **127**: 2291-2294.
[170] Sinton R, Macdonald D. *WCT-120 Photoconductance Lifetime Tester: User Manual*. Sinton Consulting, Inc, 2006.
[171] Cuevas A, Macdonald D. Measuring and interpreting the lifetime of silicon wafers. *Solar Energy* 2004; **76**: 255-262.
[172] Sinton RA, Cuevas A, Stuckings M. Quasi-steady-state photoconductance, a new method for solar cell material and device characterization. *25th IEEE Photovoltaic Specialists Conference*, 1996: 457-460.
[173] Sinton R, Cuevas A. Contactless determination of current--voltage characteristics and minority-carrier lifetimes in semiconductors from quasi-steady-state photoconductance data. *Applied Physics Letters* 1996; **69**: 2510-2512.
[174] Berge C, Schmidt J, Lenkeit B, Nagel H, Aberle AG. Comparison of effective carrier lifetimes in silicon determined by transient and quasi-steady-state photoconductance measurements. *2nd World Conference and Exhibition on Photovoltaic Solar Energy Conversion*, 1998: 1426-1429.
[175] Nagel H, Lenkeit B, Sinton RA, Metz A, Hezel R. Relationship between effective carrier lifetimes in silicon determined under transient and steady-state illumination. *16th European Photovoltaic Solar Energy Conference*, 2000.
[176] Nagel H, Berge C, Aberle A. Generalized analysis of quasi-steady-state and quasi-transient measurements of carrier lifetimes in semiconductors. *Journal of Applied Physics* 1999; **86**: 6218-6221.
[177] Tiedje T, Haberman JI, Francis RW, Ghosh AK. An rf bridge technique for contactless measurement of the carrier lifetime in silicon wafers. *Journal of Applied Physics* 1983; **54**: 2499-2503.
[178] Brody J, Rohatgi A, Ristow A. Guidelines for more accurate determination and interpretation of effective lifetime from measured quasi-steady-state photoconductance. *11th Workshop on Crystalline Silicon Solar Cell Materials & Processes*, 2001.
[179] Macdonald D, Cuevas A, McIntosh K, Barbosa L, De Ceuster D. Impact of Cr, Fe, Ni, Ti and W surface contamination on diffused and oxidised n-type crystalline silicon wafers. *20th European Photovoltaic Solar Energy Conference*, 2005: 627-630.

[180] Trupke T, Bardos RA. Self-consistent determination of the generation rate from photoconductance measurements. *Applied Physics Letters* 2004; **85**: 3611-3613.
[181] McIntosh KR, Sinton RA. Uncertainty in photoconductance lifetime measurements that use an inductive-coil detector. *23rd European Photovoltaic Solar Energy Conference*, 2008: 77-82.
[182] McIntosh K, Guo J-H, Abbott M, Bardos R. Calibration of the WCT-100 photoconductance instrument at low conductance. *Progress in Photovoltaics: Research and Applications* 2008; **16**: 279-287.
[183] Macdonald D, Cuevas A. Trapping of minority carriers in multicrystalline silicon. *Applied Physics Letters* 1999; **74**: 1710-1712.
[184] Cuevas A, Stocks M, McDonald D, Kerr M, Samundsett C. Recombination and trapping in multicrystalline silicon. *IEEE Transactions on Electron Devices* 1999; **46**: 2026-2034.
[185] Macdonald D, Sinton R, Cuevas A. On the use of a bias-light correction for trapping effects in photoconductance-based lifetime measurements of silicon. *Journal of Applied Physics* 2001; **89**: 2772-2778.
[186] Bail M, Schulz M, Brendel R. Space-charge region-dominated steady-state photoconductance in low-lifetime Si wafers. *Applied Physics Letters* 2003; **82**: 757-759.
[187] Cousins P, Neuhaus D, Cotter J. Experimental verification of the effect of depletion-region modulation on photoconductance lifetime measurements. *Journal of Applied Physics* 2004; **95**: 1854-1858.
[188] Cuevas A, Sinton RA. Prediction of the open-circuit voltage of solar cells from the steady-state photoconductance. *Progress in Photovoltaics: Research and Applications* 1997; **5**: 79-90.
[189] IEC 60904–3: Photovoltaic devices—Part 3: Measurement principles for terrestrial photovoltaic (PV) solar devices with reference spectral irradiance data. 2008.
[190] Roth T, Hohl-Ebinger J, Schmich E, Warta W, Glunz S, Sinton R. Improving the accuracy of Suns-Voc measurements using spectral mismatch correction. *33rd IEEE Photovoltaic Specialists Conference*, 2008: 1-5.
[191] Trupke T, Bardos RA, Hudert F, Wurfel P, Zhao J, Wang A, Green MA. Effective excess carrier lifetimes exceeding 100 milliseconds in float zone silicon determined from photoluminescence. *19th European Photovoltaic Solar Energy Conference*, 2004: 758-761.
[192] Trupke T, Bardos RA. Photoluminescence: a surprisingly sensitive lifetime technique. *31st IEEE Photovoltaic Specialists Conference*, 2005: 903-906.
[193] Abbott MD, Cotter JE, Trupke T, Bardos RA. Investigation of edge recombination effects in silicon solar cell structures using photoluminescence. *Applied Physics Letters* 2006; **88**: 114105.
[194] Trupke T, Bardos RA, Nyhus J. Photoluminescence characterization of silicon wafers and silicon solar cells. *18th Workshop on Crystalline Silicon Solar Cells and Modules: Materials and Processes (NREL)*, 2008.
[195] Trupke T, Bardos RA. Photoluminescence: A versatile characterisation technique for crystalline silicon. *15th Workshop on Crystalline Silicon Solar Cells & Modules*, 2005.
[196] Trupke T, Bardos RA, Abbott MD, Cotter JE. Suns-photoluminescence: Contactless determination of current-voltage characteristics of silicon wafers. *Applied Physics Letters* 2005; **87**: 093503.

[197] Trupke T. Influence of photon reabsorption on quasi-steady-state photoluminescence measurements on crystalline silicon. *Journal of Applied Physics* 2006; **100**: 063531.
[198] Bardos RA, Trupke T. Self-consistent determination of the generation rate in photoluminescence and photoconductance lifetime measurements. *31st IEEE Photovoltaic Specialists Conference*, 2005: 899-902.
[199] Trupke T, Bardos RA, Abbott MD. Self-consistent calibration of photoluminescence and photoconductance lifetime measurements. *Applied Physics Letters* 2005; **87**: 184102.
[200] Roth T, Rosenits P, Rudiger M, Warta W, Glunz SW. Comparison of photoconductance and photo-luminescence based lifetime measurement techniques. *IEEE Conference on Optoelectronic and Microelectronic Materials and Devices*, 2008: 249-252.
[201] Bardos RA, Trupke T, Schubert MC, Roth T. Trapping artifacts in quasi-steady-state photoluminescence and photoconductance lifetime measurements on silicon wafers. *Applied Physics Letters* 2006; **88**: 053504.
[202] Sinton RA, Cuevas A. A quasi-steady state open-circuit voltage method for solar cell characterization. *16th European Photovoltaic Solar Energy Conference*, 2000: 1152–1155.
[203] Trupke T, Bardos RA, Schubert MC, Warta W. Photoluminescence imaging of silicon wafers. *Applied Physics Letters* 2006; **89**: 044107.
[204] Trupke T, Bardos RA, Abbott MD, Chen FW, Cotter JE, Lorenz A. Fast Photoluminescence Imaging of Silicon Wafers. *4th IEEE World Conference on Photovoltaic Energy Conversion*, 2006: 928-931.
[205] Abbott MD, Cotter JE, Chen FW, Trupke T, Bardos RA, Fisher KC. Application of photoluminescence characterization to the development and manufacturing of high-efficiency silicon solar cells. *Journal of Applied Physics* 2006; **100**: 114514.
[206] Chen FW, Cotter JE, Trupke T, Bardos RA. Characterization of PECVD Silicon Nitride Passivation with Photoluminescence Imaging. *4th IEEE World Conference on Photovoltaic Energy Conversion*, 2006: 1372-1375.
[207] Abbott MD, Cotter JE, Trupke T, Fisher K, Bardos RA. Application of Photoluminescence to High-Efficiency Silicon Solar Cell Fabrication. *4th IEEE World Conference on Photovoltaic Energy Conversion*, 2006: 1211-1214.
[208] Trupke T, Pink E, Bardos RA, Abbott MD. Spatially resolved series resistance of silicon solar cells obtained from luminescence imaging. *Applied Physics Letters* 2007; **90**: 093506.
[209] Kampwerth H, Trupke T, Weber JW, Augarten Y. Advanced luminescence based effective series resistance imaging of silicon solar cells. *Applied Physics Letters* 2008; **93**: 202102.
[210] Trupke T, Bardos RA, Abbott MD, Fisher K, Bauer J, Breitenstein O. Luminescence imaging for fast shunt localisation in silicon solar cells and silicon wafers. *International Workshop on Science and Technology of Crystalline Silicon Solar Cells*, 2006.
[211] Ghannam MY. A new n+pn+ structure with back side floating junction for high efficiency silicon solar cells. *22nd IEEE Photovoltaic Specialists Conference*, 1991: 284-289.
[212] Fossum JG, Lindholm FA, Shibib MA. The importance of surface recombination and energy-bandgap arrowing in p-n-junction silicon solar cells. *IEEE Transactions on Electron Devices* 1979; **26**: 1294-1298.

[213] Balk P. *The Si-SiO2 System (Materials Science Monographs)*. Elsevier Science Ltd, 1988.
[214] Trapp OD, Blanchard RA, Shepherd WH. *Semiconductor Technology Handbook*. Technology Associates, 1980.
[215] Nicollian EH, Brews JR. *MOS (metal oxide semiconductor) Physics and Technology*. Wiley, 1982.
[216] Eades W, Swanson R. Calculation of surface generation and recombination velocities at the Si-SiO2 interface. *Journal of Applied Physics* 1985; **58**: 4267-4276.
[217] Snel J. The doped Si/SiO2 interface. *Solid-State Electronics* 1981; **24**: 135-139.
[218] Aberle A. Overview on SiN surface passivation of crystalline silicon solar cells. *Solar Energy Materials and Solar Cells* 2001; **65**: 239-248.
[219] Kerr M, Cuevas A. Very low bulk and surface recombination in oxidized silicon wafers. *Semiconductor Science and Technology* 2002; **17**: 35.
[220] Lai SK, Young DR, Calise JA, Feigl FJ. Reduction of electron trapping in silicon dioxide by high-temperature nitrogen anneal. *Journal of Applied Physics* 1981; **52**: 5691-5695.
[221] Hoex B, Peeters FJJ, Creatore M, Blauw MA, Kessels WMM, van de Sanden MCM. High-rate plasma-deposited SiO2 films for surface passivation of crystalline silicon. *Journal of Vacuum Science & Technology A: Vacuum, Surfaces, and Films* 2006; **24**: 1823-1830.
[222] Balk P. Low temperature annealing in the Al-SiO2-Si System. *Proceedings of the electrochemical society fall meeting*, 1965: 29.
[223] Cuevas A, Basore P, Matlakowski Ge, Dubois C. Surface recombination velocity of highly doped n-type silicon. *Journal of Applied Physics* 1996; **80**: 3370-3375.
[224] Reed M, Plummer J. Chemistry of Si-SiO2 interface trap annealing. *Journal of Applied Physics* 1988; **63**: 5776-5793.
[225] Wilkinson AR, Elliman RG. Passivation of Si nanocrystals in SiO2: Atomic versus molecular hydrogen. *Applied Physics Letters* 2003; **83**: 5512-5514.
[226] Aberle A, Hezel R. Progress in Low-temperature Surface Passivation of Silicon Solar Cells using Remote-plasma Silicon Nitride. *Progress in Photovoltaics: Research and Applications* 1997; **5**: 29-50.
[227] Schmidt J, Lauinger T, Aberle AG, Hezel R. Light-biased photoconductance decay measurements on silicon-nitride passivated silicon wafers. *13th European Photovoltaic Solar Energy Conference*, 1995: 1287-1290.
[228] Aberle A, Glunz S, Warta W. Impact of illumination level and oxide parameters on Shockley-Read-Hall recombination at the Si-SiO2 interface. *Journal of Applied Physics* 1992; **71**: 4422-4431.
[229] Kimure K. Recent developments in polycrystalline silicon solar cells. *First International Photovoltaic Science and Engineering Conference (PVSEC 1)*, 1984: 37-41.
[230] Sze SM, Stephen W. *VLSI Technology*. McGraw-Hill Book Company, 1988.
[231] Robinson SJ, Wenham SR, Altermatt PP, Aberle AG, Heiser G, Green MA. Recombination rate saturation mechanisms at oxidized surfaces of high-efficiency silicon solar cells. *Journal of Applied Physics* 1995; **78**: 4740-4754.
[232] Sterling HF, Swann RCG. Chemical vapour deposition promoted by r.f. discharge. *Solid-State Electronics* 1965; **8**: 653-654.
[233] Hezel R, Schorner R. Plasma Si nitride-A promising dielectric to achieve high-quality silicon MIS/IL solar cells. *Journal of Applied Physics* 1981; **52**: 3076-3079.

[234] Hezel R. Silicon nitride for the improvement of silicon inversion layer solar cells. *Solid-State Electronics* 1981; **24**: 863-868.
[235] Hezel R, Jaeger K. Low-Temperature Surface Passivation of Silicon for Solar Cells. *Journal of The Electrochemical Society* 1989; **136**: 518-523.
[236] Cuevas A, Kerr MJ, Schmidt J. Passivation of crystalline silicon using silicon nitride. *3rd World Conference on Photovoltaic Energy Conversion*, 2003: 913-918.
[237] Schmidt J, Moschner JD, Henze J, Dauwe S, Hezel R. Recent progress in the surface passivation of silicon solar cells using silicon nitride. *19th European Photovoltaic Solar Energy Conference*, 2004.
[238] Lauinger T, Moschner J, Aberle A, Hezel R. Optimization and characterization of remote plasma-enhanced chemical vapor deposition silicon nitride for the passivation of p-type crystalline silicon surfaces. *Journal of Vacuum Science & Technology A: Vacuum, Surfaces, and Films* 1998; **16**: 530-543.
[239] *Handbook of Plasma Processing Technology: Fundamentals, Etching, Deposition, and Surface Interactions*. William Andrew Publishing/Noyes, 1990.
[240] Smith D. *Thin-Film Deposition: Principles and Practice*. MacGraw-Hill, 1995.
[241] Smith D, Alimonda A, Chen C, Ready S, Wacker B. Mechanism of SiNxHy Deposition from NH3-SiH4 Plasma. *Journal of The Electrochemical Society* 1990; **137**: 614-623.
[242] Soppe W, Rieffe H, Weeber A. Bulk and surface passivation of silicon solar cells accomplished by silicon nitride deposited on industrial scale by microwave PECVD. *Progress in Photovoltaics: Research and Applications* 2005; **13**: 551-569.
[243] Franz G. Das Niederdruckplasma. *Vakkum in der Praxis (in German)* 1991; **4**: 274-280.
[244] Lauinger T, Aberle AG, Hezel R. Comparision of direct and remote PECVD silicon nitride films for low-temperature surface passivation of p-type crystalline silicon. *14th European Photovoltaic Solar Energy Conference*, 1997: 853-856.
[245] Soppe WJ, Devilee C, Schiermeier SEA, Hong J, Kessels WMM, Van De Sanden MCM, Arnoldbik WM, Weeber AW. Bulk and Surface Passivation by Silicon Nitride Grown by Remote Microwave PECVD. *17th European Photovoltaic Solar Energy Conference*, 2001.
[246] Lucovsky G, Tsu DV. Plasma enhanced chemical vapor deposition: Differences between direct and remote plasma excitation. *Journal of Vacuum Science & Technology A: Vacuum, Surfaces, and Films* 1987; **5**: 2231-2238.
[247] Lauinger T, Moschner J, Aberle A, Hezel R. UV stability of highest-quality plasma silicon nitride passivation if silicon solar cells. *25th IEEE Photovoltaic Specialists Conference*, 1996: 417-420.
[248] Kerr MJ, Cuevas A. Recombination at the interface between silicon and stoichiometric plasma silicon nitride. *Semiconductor Science and Technology* 2002; **17**: 166-172.
[249] Aberle A, Lauinger T, Schmidt J, Hezel R. Injection-level dependent surface recombination velocities at the silicon-plasma silicon nitride interface. *Applied Physics Letters* 1995; **66**: 2828-2830.
[250] Moschner JD, Henze J, Schmidt J, Hezel R. High-quality surface passivation of silicon solar cells in an industrial-type inline plasma silicon nitride deposition system. *Progress in Photovoltaics: Research and Applications* 2004; **12**: 21-31.
[251] Mackel H, Ludemann R. Detailed study of the composition of hydrogenated SiNx layers for high-quality silicon surface passivation. *Journal of Applied Physics* 2002; **92**: 2602-2609.

[252] Leguijt C, Lölgen P, Eikelboom JA, Amesz PH, Steeman RA, Sinke WC, Sarro PM, Verhoef LA, Michiels PP, Chen ZH, Rohatgi A. Very low surface recombination velocities on 2.5 ohm.cm Si wafers, obtained with low-temperature PECVD of Si-oxide and Si-nitride. *Solar Energy Materials and Solar Cells* 1994; **34**: 177-181.
[253] Weeber AW, Rieffe HC, Goris M, Hong J, Kessels WMM, van de Sanden MCM, Soppe WJ. Improved thermally stable surface and bulk passivation of PECVD SiNx:H using N2 and SiH4. *3rd World Conference on Photovoltaic Energy Conversion*, 2003: 1131-1134.
[254] Elmiger JR, Schieck R, Kunst M. Recombination at the silicon nitride/silicon interface. *Journal of Vacuum Science & Technology A: Vacuum, Surfaces, and Films* 1997; **15**: 2418-2425.
[255] Hezel R, Blumenstock K, Schörner R. Interface States and Fixed Charges in MNOS Structures with APCVD and Plasma Silicon Nitride. *Journal of The Electrochemical Society* 1984; **131**: 1679-1683.
[256] Elmiger JR, Kunst M. Investigation of the silicon-plasma silicon nitride interface with in situ transient photoconductivity measurements. *Applied Surface Science* 1996; **103**: 11-18.
[257] Elmiger JR, Kunst M. Investigation of charge carrier injection in silicon nitride/silicon junctions. *Applied Physics Letters* 1996; **69**: 517-519.
[258] Van Erven AJM, Bosch RCM, Bijker MD. Textured silicon surface passivation by high-rate expanding thermal plasma deposited SiN and thermal SiO2/SiN stacks for crystalline silicon solar cells. *Progress in Photovoltaics: Research and Applications* 2008; **16**: 615-627.
[259] Schmidt J, Aberle A. Carrier recombination at silicon-silicon nitride interfaces fabricated by plasma-enhanced chemical vapor deposition. *Journal of Applied Physics* 1999; **85**: 3626-3633.
[260] Dauwe S, Schmidt J, Metz A, Hezel R. Fixed charge density in silicon nitride films on crystalline silicon surfaces under illumination. *29th IEEE Photovoltaic Specialists Conference*, 2002: 162-165.
[261] De Wolf S, Agostinelli G, Beaucarne G, Vitanov P. Influence of stoichiometry of direct plasma-enhanced chemical vapor deposited SiNx films and silicon substrate surface roughness on surface passivation. *Journal of Applied Physics* 2005; **97**: 063303.
[262] Lanford WA, Rand MJ. The hydrogen content of plasma-deposited silicon nitride. *Journal of Applied Physics* 1978; **49**: 2473-2477.
[263] Szlufcik J, De Clercq K, De Schepper P, Poortmans J, Buczkowski A, Nijs J, Mertens R. Improvement in Multicrystalline Silicon Solar Cells after Thermal Treatment of PECVD Silicon Nitride AR Coating. *12th European Photovoltaic Solar Energy Conference*, 1994: 1018-1021.
[264] Nagel H, Schmidt J, Aberle AG, Hezel R. Exceptionally high bulk minority-carrier lifetimes in block-cast multicrystalline silicon. *14th European Photovoltaic Solar Energy Conference*, 1997: 762-765.
[265] Rohatgi A, Yelundur V, Jeong J, Ebong A, Rosenblum MD, Hanoka JI. Fundamental understanding and implementation of Al-enhanced PECVD SiNx hydrogenation in silicon ribbons. *Solar Energy Materials and Solar Cells* 2002; **74**: 117-126.
[266] Rohatgi A, Narasimha S, Ruby DS. Effective Passivation of the Low Resistivity Silicon Surface by a Rapid Thermal Oxide/PECVD Silicon Nitride Stack and Its Application to Passivated Rear and Bifacial Si Solar Cells. *2nd World Conference on Photovoltaic Solar Energy Conversion*, 1998.

[267] Mackel H, Huljic DM, Craff-Castillo C, Ludemann R. Passivation quality and thermal stability of silicon nitride layers on silicon and phosphorus-diffused silicon solar cell emitters. *ISES Solar World Congress*, 2001: 1665-1673.
[268] Winderbaum S, Cuevas A, Chen F, Tan J, Hanton K, Macdonald D, Roth K. Industrial PECVD silicon nitride: surface and bulk passivation of silicon. *19th European Photovoltaic Solar Energy Conference*, 2004.
[269] Lenkeit B, Auer R, Aberle AG, Hezel R. Bifacial silicon solar cells with screen-printed rear contacts. *14th European Photovoltaic Solar Energy Conference*, 1997: 838-841.
[270] Rohatgi A, Doshi P, Moschner J, Lauinger T, Aberle AG, Ruby DS. Comprehensive study of rapid, low-cost silicon surface passivation technologies. *IEEE Transactions on Electron Devices* 2000; **47**: 987-993.
[271] Schmidt J, Kerr M, Cuevas A. Surface passivation of silicon solar cells using plasma-enhanced chemical-vapour-deposited SiN films and thin thermal SiO2/plasma SiN stacks. *Semiconductor Science and Technology* 2001; **16**: 164-170.
[272] Lenkeit B, Steckemetz S, Artuso F, Hezel R. Excellent thermal stability of remote plasma-enhanced chemical vapour deposited silicon nitride films for the rear of screen-printed bifacial silicon solar cells. *Solar Energy Materials and Solar Cells* 2001; **65**: 317-323.
[273] Weeber AW, Rieffe HC, Sinke WC, Soppe WJ. Structural and passivating properties of SiNx: H deposited under different precursor gases. *19th European Photovoltaic Solar Energy Conference*, 2004.
[274] Weeber AW, Rieffe HC, Romijn IG, Sinke WC, Soppe WJ. The fundamental properties of SiNx:H that determine its passivating qualities. *21st IEEE Photovoltaic Specialists Conference*, 2005: 1043-1046.
[275] Van Erven AJM, Bosch RCM, Weeber AW, Bijker MD. Effects of different firing profiles on layer characteristics and passivation properties of industrial ETP deposited silicon nitride films. *19th European Photovoltaic Solar Energy Conference*, 2004.
[276] Maeda M, Itsumi M. Thermal dissociation process of hydrogen atoms in plasma-enhanced chemical vapor deposited silicon nitride films. *Journal of Applied Physics* 1998; **84**: 5243-5247.
[277] Robertson J. Defects and hydrogen in amorphous silicon nitride. *Philosophical Magazine Part B* 1994; **69**: 307-326.
[278] Smith FW, Yin Z. Free energy model for bonding in a-Si alloys. *Journal of Non-Crystalline Solids* 1991; **137-138**: 871-874.
[279] Boehme C, Lucovsky G. H loss mechanism during anneal of silicon nitride: Chemical dissociation. *Journal of Applied Physics* 2000; **88**: 6055-6059.
[280] Sopori B, Zhang Y, Reedy R, Jones K, Yan Y, Al-Jassim M, Bathey B, Kalejs J. A comprehensive model of hydrogen transport into a solar cell during silicon nitride processing for fire-through metallization. *31st IEEE Photovoltaic Specialists Conference*, 2005: 1039-1042.
[281] Hong J, Kessels WMM, Soppe WJ, Weeber AW, Arnoldbik WM, van de Sanden MCM. Influence of the high-temperature ``firing'' step on high-rate plasma deposited silicon nitride films used as bulk passivating antireflection coatings on silicon solar cells. *Journal of Vacuum Science & Technology B: Microelectronics and Nanometer Structures* 2003; **21**: 2123-2132.
[282] Kessels WMM, van den Oever PJ, Hoex B, Bosch RCM, van Erven AJM, Bijker MD, van de Sanden MCM. Controlling the silicon nitride film density for

ultrahigh-rate deposition of top quality antireflection coatings. *31st IEEE Photovoltaic Specialists Conference*, 2005: 1253-1256.
[283] Romijn IG, Soppe WJ, Rieffe HC, Sinke WC, Weeber AW. Passivating Multi Cristalline Si Solar Cells using SiNx: H. *15th Workshop on Crystalline Silicon Solar Cells & Modules*, 2005.
[284] Romijn IG, Soppe WJ, Rieffe HC, Burgers AR, Weeber AW. Passivating mc-Si solar cells using SiN:H: from magic to physics. *20th European Photovoltaic Solar Energy Conference*, 2005.
[285] Winderbaum S, Romijn IG, Sterk D, Van Straaten B. MW PECVD a-SixNyHz: The road to optimum silicon nitride coatings. *21st European Photovoltaic Solar Energy Conference*, 2006.
[286] Dekkers HFW, Beaucarne G, Hiller M, Charifi H, Slaoui A. Molecular hydrogen formation in hydrogenated silicon nitride. *Applied Physics Letters* 2006; **89**: 211914.
[287] Larionova Y, Mertens V, Harder N, Brendel R. Surface passivation of n-type Czochralski silicon substrates by thermal-SiO2/plasma-enhanced chemical vapor deposition SiN stacks. *Applied Physics Letters* 2010; **96**: 032105.
[288] Kerr MJ, Schmidt J, Cuevas A, Bultman JH. Surface recombination velocity of phosphorus-diffused silicon solar cell emitters passivated with plasma enhanced chemical vapor deposited silicon nitride and thermal silicon oxide. *Journal of Applied Physics* 2001; **89**: 3821-3826.
[289] Kerr MJ, Schmidt J, Cuevas A. Comparison of high quality surface passivation schemes for phosphorus diffused emitters. *16th European Photovoltaic Solar Energy Conference*, 2000.
[290] Hubner A, Aberle A, Hezel R. Novel cost-effective bifacial silicon solar cells with 19.4% front and 18.1% rear efficiency. *Applied Physics Letters* 1997; **70**: 1008-1010.
[291] Hubner A, Aberle AG, Hezel R. 20% efficient bifacial silicon solar cells. *14th European Photovoltaic Solar Energy Conference*, 1997: 92-92.
[292] Dauwe S, Mittelstadt L, Metz A, Schmidt J, Hezel R. Low-temperature rear surface passivation schemes for >20% efficient silicon solar cells. *3rd World Conference on Photovoltaic Energy Conversion*, 2003: 1395-1398.
[293] Mittelstädt L, Dauwe S, Metz A, Hezel R. Highly efficient all silicon nitride passivated multicrystalline silicon solar cells. *17th European Photovoltaic Solar Energy Conference*, 2001: 1311-1314.
[294] Mittelstadt L, Dauwe S, Metz A, Hezel R, Habler C. Front and rear silicon-nitride-passivated multicrystalline silicon solar cells with an efficiency of 18.1%. *Progress in Photovoltaics: Research and Applications* 2002; **10**: 35-39.
[295] Green MA, Blakers AW, Zhao J, Milne AM, Wang A, Dai X. Characterization of 23-precent efficient silicon solar cells. *IEEE Transactions on Electron Devices* 1990; **37**: 331-336.
[296] Kerr MJ, Cuevas A. Comprehensive study of the doping and injection-level dependence of stoichiometric silicon nitride passivation for silicon solar cells. *29th IEEE Photovoltaic Specialists Conference*, 2002: 102-105.
[297] Janßen L, Windgassen H, Bätzner DL, Bitnar B, Neuhaus H. Silicon nitride passivated bifacial Cz-silicon solar cells. *Solar Energy Materials and Solar Cells* 2009; **93**: 1435-1439.
[298] Glunz SW, Preu R, Schaefer S, Schneiderlochner E, Pfleging W, Ludemann R, Willeke G. New simplified methods for patterning the rear contact of RP-PERC high-efficiency solar cells. *28th IEEE Photovoltaic Specialists Conference*, 2000: 168-171.

[299] Dauwe S, Metz A, Hezel R. A novel mask-free low-temperature rear surface passivation scheme based on PECVD silicon nitride for high-efficiency silicon solar cells. *16th European Photovoltaic Solar Energy Conference*, 2000: 1747-1750.
[300] Stocks M, Blakers A, Cuevas A. High efficiency reduced rear contact area mc-Si solar cells. *14th European Photovoltaic Solar Energy Conference*, 1997: 766-769.
[301] Basore PA. Numerical modeling of textured silicon solar cells using PC-1D. *IEEE Transactions on Electron Devices* 1990; **37**: 337-343.
[302] Kern W. The Evolution of Silicon Wafer Cleaning Technology. *Journal of The Electrochemical Society* 1990; **137**: 1887-1892.
[303] Romijn IG, Koppes M, Kossen EJ, Tool CJJ, Weeber AW. High efficiencies on mc-Si solar cells enabled by industrial firing through rear side passivating SiNx: H. *21st European Photovoltaic Solar Energy Conference*, 2006.
[304] Ghandhi SK. *VLSI Fabrication Principles: Silicon and Gallium Arsenide*. John Wiley& Sons. Inc. : New York, 1994.
[305] Chen W. *PECVD Silicon Nitride for n-type Silicon Solar Cells*. PhD dissertation, University of New South Wales, Sydney, Australia, 2008.
[306] Tool CJJ, Koppes M, Fleuster M, Van Straaten BHM, Weeber AW. Almost 1% absolute efficiency increase in mc-Si solar cell manufacturing with simple adjustments to the processing sequence. *21st European Photovoltaic Solar Energy Conference*, 2006.
[307] Schuurmans FM, Schonecker A, Eikelboom JA, Sinke WC. Crystal-orientation dependence of surface recombination velocity for silicon nitride passivated silicon wafers. *25th IEEE Photovoltaic Specialists Conference*, 1996: 485-488.
[308] Aberle A, Robinson S, Wang A, Zhao J, Wenham S, Green M. High-efficiency silicon solar cells: Fill factor limitations and non-ideal diode behaviour due to voltage-dependent rear surface recombination velocity. *Progress in Photovoltaics: Research and Applications* 1993; **1**: 133-143.
[309] Aberle A, Glunz S, Warta W. Field effect passivation of high efficiency silicon solar cells. *Solar Energy Materials and Solar Cells* 1993; **29**: 175-182.
[310] Green M. General solar cell curve factors including the effects of ideality factor, temperature and series resistance. *Solid-State Electronics* 1977; **20**: 265-266.
[311] Saitoh T, Hashigami H, Rein S, Glunz S. Overview of light degradation research on crystalline silicon solar cells. *Progress in Photovoltaics: Research and Applications* 2000; **8**: 537-547.
[312] Schmidt J, Aberle AG, Hezel R. Investigation of carrier lifetime instabilities in Cz-grown silicon. *26th IEEE Photovoltaic Specialists Conference*, 1997: 13-18.
[313] Glunz SW, Rein S, Warta W, Knobloch J, Wettling W. Degradation of carrier lifetime in Cz silicon solar cells. *Solar Energy Materials and Solar Cells* 2001; **65**: 219-229.
[314] Schmidt J, Bothe K, Hezel R. Formation and annihilation of the metastable defect in boron-doped Czochralski silicon. *29th IEEE Photovoltaic Specialists Conference*, 2002: 178-181.
[315] Bothe K, Schmidt J, Hezel R. Effective reduction of the metastable defect concentration in boron-doped Czochralski silicon for solar cells. *29th IEEE Photovoltaic Specialists Conference*, 2002: 194-197.
[316] Rein S, Glunz SW. Electronic properties of the metastable defect in boron-doped Czochralski silicon: Unambiguous determination by advanced lifetime spectroscopy. *Applied Physics Letters* 2003; **82**: 1054-1056.

[317] Reiss JH, King RR, Mitchell KW. Characterization of diffusion length degradation in Czochralski silicon solar cells. *Applied Physics Letters* 1996; **68**: 3302-3304.
[318] Graff K, Pieper H. The Properties of Iron in Silicon. *Journal of The Electrochemical Society* 1981; **128**: 669-674.
[319] Series RW, Barraclough KG. Carbon contamination during growth of Czochralski silicon. *Journal of Crystal Growth* 1982; **60**: 212-218.
[320] de Kock AJR, Stacy WT, van de Wijgert WM. The effect of doping on microdefect formation in as-grown dislocation-free Czochralski silicon crystals. *Applied Physics Letters* 1979; **34**: 611-613.
[321] Pimentel CA, Filho. Point defect aggregates in boron doped dislocation-free Czochralski silicon crystals. *Journal of Crystal Growth* 1983; **62**: 129-140.
[322] Verezub N, Prostomolotov A, Mezhennyi M, Milvidskii M, Reznik V. Theoretical and experimental study of the formation of grown-in and as-grown microdefects in dislocation-free silicon single crystals grown by the Czochralski method. *Crystallography Reports* 2005; **50**: S159-S167.
[323] Sopori BL, Deng X, Benner JP, Rohatgi A, Sana P, Estreicher SK, Park YK, Roberson MA. Hydrogen in silicon: A discussion of diffusion and passivation mechanisms. *Solar Energy Materials and Solar Cells* 1996; **41-42**: 159-169.
[324] Duerinckx F, Szlufcik J. Defect passivation of industrial multicrystalline solar cells based on PECVD silicon nitride. *Solar Energy Materials and Solar Cells* 2002; **72**: 231-246.
[325] Winderbaum S, Leo AJ, Shea SP, Koval TD, Kumar B. Characterisation of industrial-scale remote PECVD SiN depositions. *3rd World Conference on Photovoltaic Energy Conversion*, 2003: 1128-1130.
[326] Wright D, Marstein E, Rognmo A, Holt A. Plasma-enhanced chemical vapour-deposited silicon nitride films; The effect of annealing on optical properties and etch rates. *Solar Energy Materials and Solar Cells* 2008; **92**: 1091-1098.
[327] Janßen L, Rinio M, Borchert D, Windgassen H, Bätzner DL, Kurz H. Passivating thin bifacial silicon solar cells for industrial production. *Progress in Photovoltaics: Research and Applications* 2007; **15**: 469-475.
[328] Jellison GE, Modine FA. Parameterization of the optical functions of amorphous materials in the interband region. *Applied Physics Letters* 1996; **69**: 371-373.
[329] Wooten F. *Optical Properties of Solids*. Academic Press, 1972.
[330] Williams KR, Gupta K, Wasilik M. Etch rates for micromachining processing-Part II. *Journal of Microelectromechanical Systems* 2003; **12**: 761-778.
[331] Williams KR, Muller RS. Etch rates for micromachining processing. *Journal of Microelectromechanical Systems* 1996; **5**: 256-269.
[332] Baba-Kishi KZ. Review Electron backscatter Kikuchi diffraction in the scanning electron microscope for crystallographic analysis. *Journal of Materials Science* 2002; **37**: 1715-1746.
[333] Yang KH. An Etch for Delineation of Defects in Silicon. *Journal of The Electrochemical Society* 1984; **131**: 1140-1145.
[334] Leamy HJ. Charge collection scanning electron microscopy. *Journal of Applied Physics* 1982; **53**: R51-R80.
[335] Koechner W. *Solid-State Laser Engineering*. Springer, 2006.
[336] www.sintecoptronics.com, last accessed: 4 July, 2010.
[337] Wood RF, Geist GA. Modeling of nonequilibrium melting and solidification in laser-irradiated materials. *Physical Review B* 1986; **34**: 2606.

[338] Fell A, Kray D, Willeke G. Transient 3D/2D simulation of laser-induced ablation of silicon. *Applied Physics A: Materials Science & Processing* 2008; **92**: 987-991.
[339] Bell R, Toulemonde M, Siffert P. Calculated temperature distribution during laser annealing in silicon and cadmium telluride. *Applied Physics A: Materials Science & Processing* 1979; **19**: 313-319.
[340] Wang JC, Wood RF, Pronko PP. Theoretical analysis of thermal and mass transport in ion-implanted laser-annealed silicon. *Applied Physics Letters* 1978; **33**: 455-458.
[341] Wood RF, Giles GE. Macroscopic theory of pulsed-laser annealing. I. Thermal transport and melting. *Physical Review B* 1981; **23**: 2923-2942.
[342] Hull R. *Properties of crystalline silicon*. INSPEC, The Institution of Electrical Engineers, 1999.
[343] Riley FL. Silicon Nitride and Related Materials. *Journal of the American Ceramic Society* 2000; **83**: 245-265.
[344] Thompson M, Mayer JW, Cullis AG, Webber HC, Chew NG, Poate JM, Jacobson DC. Silicon Melt, Regrowth, and Amorphization Velocities During Pulsed Laser Irradiation. *Physical Review Letters* 1983; **50**: 896.
[345] *CRC Materials Science and Engineering Handbook*. 3rd ed. CRC Press, 2001.
[346] Jiang JZ, Lindelov H, Gerward L, Staahl K, Recio JM, Mori-Sanchez P, Carlson S, Mezouar M, Dooryhee E, Fitch A, Frost DJ. Compressibility and thermal expansion of cubic silicon nitride. *Physical Review B* 2002; **65**: 161202.
[347] von Allemen M, Lüthy W, Siregar MT, Affolter K, Nicolet MA. Annealing of silicon with 1.06 um laser pulses. *AIP Conference Proceedings* 1979; **50**: 43-47.
[348] Jellison GE, Modine FA. Optical absorption of silicon between 1.6 and 4.7 eV at elevated temperatures. *Applied Physics Letters* 1982; **41**: 180-182.
[349] Lowndes DH, Wood RF, Westbrook RD. Pulsed neodymium: yttrium aluminum garnet laser (532 nm) melting of crystalline silicon: Experiment and theory. *Applied Physics Letters* 1983; **43**: 258-260.
[350] Adachi S. *Optical Properties of Crystalline Amorphous Semiconductors: Materials and Fundamental Principles*. Kluwer Academic Publishers: Massachusetts, USA, 1999.
[351] van Bueren HG. *Imperfection in Crystals*. North-Holland Pub. Co: Amsterdam, 1960.
[352] Boer KW. *Survey of Semiconductor Physics: Electrons and Other Particles in Semiconductors*. Van Nostrand Reinhold: New York, 1990.
[353] Chan B. *Defects in Silicon Solar Cell Materials*. PhD dissertation, University of New South Wales, Sydney, Australia, 1993.
[354] Hayafuji Y, Yanada T, Aoki Y. Laser Damage Gettering and Its Application to Lifetime Improvement in Silicon. *Journal of The Electrochemical Society* 1981; **128**: 1975-1980.
[355] Mooney PM, Young RT, Karins J, Lee YH, Corbett JW. Defects in laser damaged silicon observed by DLTS. *Physica Status Solidi (a)* 1978; **48**: K31-K34.
[356] Young RT, Narayan J, Westbrook RD, Wood RF. Transmission electron microscopy and electrical properties measurements of laser doped silicon and GaAs. *AIP Conference Proceedings* 1979; **50**: 579-584.
[357] Young RT, Narayan J, Wood RF. Electrical and structural characteristics of laser-induced epitaxial layers in silicon. *Applied Physics Letters* 1979; **35**: 447-449.
[358] Benton JL, Kimerling LC, Miller GL, Robinson DAH, Celler GK. Electrical properties of laser annealed silicon. *AIP Conference Proceedings* 1979; **50**: 543-549.

[359] Benton JL, Doherty CJ, Ferris SD, Flamm DL, Kimerling LC, Leamy HJ. Hydrogen passivation of point defects in silicon. *Applied Physics Letters* 1980; **36**: 670-671.
[360] Liu PL, Yen R, Bloembergen N, Hodgson RT. Picosecond laser-induced melting and resolidification morphology on Si. *Applied Physics Letters* 1979; **34**: 864-866.
[361] Parker DL, Lin FY, Zhu SJ, Zhang DK, Porter WA. Selective lifetime doping in silicon by laser scanning. *IEEE Transactions on Electron Devices* 1982; **29**: 1718-1722.
[362] Ametowobla M, Kohler JR, Estru-Breton A, Werner JH. Characterization of a laser doping process for crystalline silicon solar cells. *21st European Photovoltaic Solar Energy Conference*, 2006.
[363] de Unamuno S, Fogarassy E. A thermal description of the melting of c- and a-silicon under pulsed excimer lasers. *Applied Surface Science* 1989; **36**: 1-11.
[364] Tong X, Chen L, Wang Y. Effect of Si-substrate heating during laser-induced B-doping. *Applied Physics A: Materials Science & Processing* 1994; **59**: 189-191.
[365] Matsuoka Y, Usami A. Normal laser damage of silicon solar cells without phase change. *Applied Physics Letters* 1974; **25**: 574-576.
[366] Parker DL, Lin FY, Zhu SJ, Zhang DK, Porter WA. A comparison of Nd:YAG fundamental and second-harmonic Q-switched laser-beam lifetime doping in single-crystal silicon. *IEEE Transactions on Electron Devices* 1983; **30**: 1322-1326.
[367] Ametowobla M, Kohler JR, Esturo-Breton A. Improved laser doping for silicon solar cells. *22nd European Photovoltaic Solar Energy Conference* 2007.
[368] Hoh K, Koyama H, Uda K, Miura Y. Incorporation of Oxygen into Silicon during Pulsed-Laser Irradiation. *Japanese Journal of Applied Physics* 1980; **19**: L375-L378.
[369] Mada Y, Inoue N. p-n junction formation using laser induced donors in silicon. *Applied Physics Letters* 1986; **48**: 1205-1207.
[370] Kishino S, Kanamori M, Yoshihiro N, Tajima M, Iizuka T. Heat-treatment behavior of microdefects and residual impurities in CZ silicon crystals. *Journal of Applied Physics* 1979; **50**: 8240-8243.
[371] Jourdan J, Veschetti Y, Dubois S, Desrues T, Monna R. Formation of Boron-doped region using spin-on dopant: investigation on the impact of metallic impurities. *Progress in Photovoltaics: Research and Applications* 2008; **16**: 379-387.
[372] Arora VK, Dawar AL. Laser-induced damage studies in silicon and silicon-based photodetectors. *Applied Optics* 1996; **35**: 7061-7065.
[373] Sugianto A, Tjahjono BS, Guo JH, Wenham SR. Impact of laser induced defects on the performance of solar cells using localised laser doped regions beneath the metal contact. *22nd European Photovoltaic Solar Energy Conference*, 2007: 1759-1762.
[374] Fell A, Hopman S, Kray D, Willeke GP. Transient 3D-simulation of laser-induced ablation of silicon. *22nd European Photovoltaic Solar Energy Conference*, 2007.
[375] Fell A, Kray D, Wutherich T, Muller R, Willeke GP, Glunz SW. Simulation of phase changes and dopant diffusion in silicon for the manufacturing of selective emitters via laser chemical processing. *23rd European Photovoltaic Solar Energy Conference*, 2008.
[376] Tan HS, Ong CK. Calculations on the laser-induced diffusion of surface-deposited dopants on silicon. *Journal of Physics C: Solid State Physics* 1983; **16**: 5063.

[377] Fogarassy E, Stuck R, Toulemonde M, Salles D, Siffert P. A model for laser induced diffusion. *Journal of Applied Physics* 1983; **54**: 5059-5063.
[378] Giannuzzi LA, Stevie FA. A review of focused ion beam milling techniques for TEM specimen preparation. *Micron* 1999; **30**: 197-204.
[379] Williams P. Secondary Ion Mass Spectrometry. *Annual Review of Materials Science* 1985; **15**: 517-548.
[380] Everhart TE, Wells OC, Matta RK. A novel method of semiconductor device measurements (Semiconductor doped region boundary, junction uniformity and depth from electron beam induced electrical signals). *Proceedings of the IEEE* 1964; **52**: 1642-1647.
[381] Donolato C. Evaluation of diffusion lengths and surface recombination velocities from electron beam induced current scans. *Applied Physics Letters* 1983; **43**: 120-122.
[382] Luke K, Cheng L. Characterization of the heavily doped emitter and junction regions of silicon solar cells using an electron beam. *Journal of Applied Physics* 1986; **60**: 2589-2595.
[383] Kurniawan O, Ong VKS. Choice of generation volume models for electron beam induced current computation. *IEEE Transactions on Electron Devices* 2009; **56**: 1094-1099.
[384] Karg D, Pensl G, Schulz M, Hassler C, Koch W. Oxygen-Related Defect Centers in Solar-Grade, Multicrystalline Silicon. A Reservoir of Lifetime Killers. *physica status solidi (b)* 2000; **222**: 379-387.
[385] Hu SM. Stress-related problems in silicon technology. *Journal of Applied Physics* 1991; **70**: R53-R80.
[386] Tada H, Kumpel A, Lathrop R, Slanina J, Nieva P, Zavracky P, Miaoulis I, Wong P. Thermal expansion coefficient of polycrystalline silicon and silicon dioxide thin films at high temperatures. *Journal of Applied Physics* 2000; **87**: 4189-4193.
[387] Petersen KE. Silicon as a Mechanical Material. *Proceedings of the IEEE* 1982; **70**: 420.
[388] Amer M, Dosser L, LeClair S, Maguire J. Induced stresses and structural changes in silicon wafers as a result of laser micro-machining. *Applied Surface Science* 2002; **187**: 291-296.
[389] Durkee LF. Method of plating by means of light. *US Patent 4,144,139*, 1979.
[390] Morishita S. Photo-plating solution and process. *US Patent 5,424,252* 1995.
[391] Sugianto A, *Development and Analysis of Laser-Doped Solar Cells (Bachelor of Engineering Undergraduate Thesis)*, University of New South Wales, Sydney, Australia, 2007.
[392] Wenham A, Hameiri Z. Improved laser operation for laser doping of silicon. *Patent Application PCT/AU10/00145* 2008.
[393] Windsor L, Controlled Laser Multiple Pulsing for Solar Cell Processing (Bachelor of Engineering Undergraduate Thesis), 1997, Unpublised work.
[394] Sameshima T, Usui S. Laser beam shaping system for semiconductor processing. *Optics Communications* 1992; **88**: 59-62.
[395] Jager U, Oesterlin P, Kimmerle A, Preu R. Beam shaping - the key to high throughput selective emitter laser processing with a single laser system. *35th IEEE Photovoltaic Specialists Conference (PVSC)*, 2010.
[396] Wagner W, Lengyel B. Evolution of the Giant Pulse in a Laser. *Journal of Applied Physics* 1963; **34**: 2040-2046.

[397] Kay RB, Waldman GS. Complete Solutions to the Rate Equations Describing Q-Spoiled and PTM Laser Operation. *Journal of Applied Physics* 1965; **36**: 1319-1323.
[398] Degnan JJ. Theory of the optimally coupled Q-switched laser. *IEEE Journal of Quantum Electronics* 1989; **25**: 214-220.
[399] Turri G, Jenssen H, Cornacchia F, Tonelli M, Bass M. Temperature-dependent stimulated emission cross section in Nd3+:YVO4 crystals. *Journal of the Optical Society of America B* 2009; **26**: 2084-2088.
[400] Zagumennyi AI, Mikhailov VA, Shcherbakov IA. Crystals for End-Diode-Pumped Lasers. *Laser Physics* 1996; **6**: 582-588.
[401] Coyle DB, Guerra DV, Kay RB. An interactive numerical model of diode-pumped, Q-switched/cavity-dumped lasers. *Journal of Physics D: Applied Physics* 1995; **28**: 452.
[402] Meilhac L, Pauliat G, Roosen G. Determination of the energy diffusion and of the Auger upconversion constants in a Nd:YVO4 standing-wave laser. *Optics Communications* 2002; **203**: 341-347.
[403] Sameshima T, Usui S. Analysis of dopant diffusion in molten silicon induced by a pulsed excimer laser. *Japanese journal of applied physics* 1987; **26**: 1208-1210.
[404] Stuck R, Fogarassy E, Grob J, Siffert P. Solubility limit of impurities in silicon after laser induced melting. *Applied Physics A: Materials Science & Processing* 1980; **23**: 15-19.
[405] Kodera H. Diffusion Coefficients of Impurities in Silicon Melt. *Japanese Journal of Applied Physics* 1963; **2**: 212-219.
[406] Garandet J. New Determinations of Diffusion Coefficients for Various Dopants in Liquid Silicon. *International Journal of Thermophysics* 2007; **28**: 1285-1303.
[407] Wood RF. Macroscopic theory of pulsed-laser annealing. III. Nonequilibrium segregation effects. *Physical Review B* 1982; **25**: 2786.
[408] Wood RF, Kirkpatrick JR, Giles GE. Macroscopic theory of pulsed-laser annealing. II. Dopant diffusion and segregation. *Physical Review B* 1981; **23**: 5555.
[409] Valdes LB. Resistivity measurements on Germanium for transistors. *Proceeding of the IRE*, 1954: 420-427.
[410] Smits FM. Measurement of sheet resistivities with the 4-point probe. *The Bell System Technical Journal* 1958: 711-718.
[411] Köhler JR, Eisele S. Influence of precursor layer ablation on laser doping of silicon. *Progress in Photovoltaics: Research and Applications* 2010; **18**: 334-339.
[412] Pierret RF, Harutunian K. *Semiconductor Device Fundamentals*. Addison-Wesley Publishing Company, 1996.
[413] Kooi E. Formation and Composition of Surface Layers and Solubility Limits of Phosphorus During Diffusion in Silicon. *Journal of The Electrochemical Society* 1964; **111**: 1383-1387.
[414] Morilla MC, Russell R, Fernandez JM. Laser induced ablation and doping processes on high efficiency silicon solar cells. *23rd European Photovoltaic Solar Energy Conference*, 2008: 1506-1509.
[415] Dominique D, Alexandre Réal C, Dany J, Xavier T, Vincent A, Raynald G. CASINO V2.42 - A fast and easy-to-use modeling tool for scanning electron microscopy and microanalysis users. *Scanning* 2007; **29**: 92-101.
[416] Reeves GK, Harrison HB. Obtaining the specific contact resistance from transmission line model measurements. *IEEE Electron Device Letters* 1982; **3**: 111-113.

[417] Mak LK, Rogers CM, Northrop DC. Specific contact resistance measurements on semiconductors. *Journal of Physics E: Scientific Instruments* 1989; **22**: 317-321.
[418] Guo J. *High Efficiency N-Type Laser-Grooved Buried Contact Silicon Solar Cells*. PhD dissertation, University of New South Wales, Sydney, Australia, 2004.
[419] Wenham A, Wenham S, Green MA. Improved Metal Adhesion. *Patent Application WO 2010/099564 A1* 2009.
[420] Breitenstein O, Rakotoniaina JP, Al Rifai MH. Quantitative evaluation of shunts in solar cells by lock-in thermography. *Progress in Photovoltaics: Research and Applications* 2003; **11**: 515-526.
[421] Hameiri Z, Mai L, Borojevic N, Javid S, Tjahjono B, Wang S, Sproul A, Wenham S. The influence of silicon nitride layer parameters on the implied Voc of CZ silicon wafers after annealing. *34th IEEE Photovoltaic Specialists Conference (PVSC)*, 2009: 1795-1800.
[422] Mallory G, Hajdu J. *Electroless Plating: Fundamentals and Applications*. William Andrew Publishing/Noyes Publication, New York, 1990.
[423] Glunz SW, Aleman M, Bartsch J, Bay J, Bayer K, Bergander R, Filipovic A, Greil S, Grohe A, Hörteis M, Knorz A, Menkö M, Pysch D, Radtke V, Rudolph D, Rublack T, Schetter C, Schmidt D, Woehl R, Mette A, Richter P, Schultz O. Progress in advanced metallization technology at Fraunhofer ISE. *33rd IEEE Photovoltaic Specialists Conference*, 2008.
[424] Wenham S. *Laser Grooved Silicon Solar Cells*. PhD dissertation, University of New South Wales, Sydney, Australia, 1986.
[425] Ollard EA, Smith EB. *Handbook of Industrial Electroplating*. New York, American Elsevier Pub. Co, 1964.
[426] Deng F, Johnson RA, Asbeck PM, Lau SS, Dubbelday WB, Hsiao T, Woo J. Salicidation process using NiSi and its device application. *Journal of Applied Physics* 1997; **81**: 8047-8051.
[427] dos Santos RE, Doi I, Diniz JA, Swart JW, dos Santos Filho SG. Investigation of Ni silicides formation on (100) Si by X-Ray diffraction (XRD). *Revista Brasileira de Aplicações de Vácuo* 2004; **23**: 32-35.
[428] Dennis JK, Such TE. *Nickel and Chromium Plating*. Woodhead Publishing Ltd. (UK), 1993.
[429] McIntosh KR. *Lumps, Humps and Bumps: Three Detrimental Effects in the Current-Voltage Curve of Silicon Solar Cells*. PhD dissertation, University of New South Wales, Sydney, Australia, 2001.
[430] Hernando F, Gutierrez R, Bueno G, Recant F, Rodriguez V. Humps, a surface damage explanation. *2nd World Conference on Photovoltaic Solar Energy Conversion*, 1998: 1321-1323.
[431] Wenham SR, Robinson SJ, Dai X, Zhao J, Wang A, Tang YH, Ebong A, Honsberg CB, Green MA. Rear Surface Effects in High Efficiency Silicon Solar Cells. *IEEE 1st World Conference on Photovoltaic Energy Conversion*, 1994: 1278-1282.
[432] Cotter JE, Mehrvarz HR, McIntosh KR, Honsberg CB, Wenham SR. Combined emitter and groove diffusion in buried contact solar cells. *16th European Photovoltaic Solar Energy Conference*, 2000.
[433] Wenham S. Personal Communication, UNSW, Sydney, July 2010.
[434] McIntosh K, Powell N, Norris A, Cotsell J, Ketola B. The effect of damp-heat and UV aging tests on the optical properties of silicone and EVA encapsulants. *Progress in Photovoltaics: Research and Applications* 2010; **DOI:10.1002/pip.1025**.

[435] Dauwe S, Mittelstadt L, Metz A, Hezel R. Loss mechanisms in silicon nitride rear surface passivation for silicon solar cells. *17th European Photovoltaic Solar Energy Conference*, 2001: 339-342.
[436] Dauwe S, Mittelstädt L, Metz A, Hezel R. Experimental evidence of parasitic shunting in silicon nitride rear surface passivated solar cells. *Progress in Photovoltaics: Research and Applications* 2002; **10**: 271-278.
[437] Filmtronics. *SOD - Product Information*. 2004.
[438] Burtner S. Personal Communication, March 2009.
[439] Schroder DK, Meier DL. Solar cell contact resistance — A review. *IEEE Transactions on Electron Devices* 1984; **31**: 637-647.
[440] Peiner E, Schlachetzki A, Krüger D. Doping Profile Analysis in Si by Electrochemical Capacitance-Voltage Measurements. *Journal of The Electrochemical Society* 1995; **142**: 576-580.
[441] Hu SM, Yeh TH. Approximate Theory of Emitter-Push Effect. *Journal of Applied Physics* 1969; **40**: 4615-4620.
[442] Fair RB, Tsai JCC. A Quantitative Model for the Diffusion of Phosphorus in Silicon and the Emitter Dip Effect. *Journal of The Electrochemical Society* 1977; **124**: 1107-1118.
[443] Nicholas KH. Studies of anomalous diffusion of impurities in silicon. *Solid-State Electronics* 1966; **9**: 35-47.
[444] Sproul A. Personal Communication, UNSW, Sydney, July 2010.
[445] Yablonovitch E, Cody GD. Intensity enhancement in textured optical sheets for solar cells. *IEEE Transactions on Electron Devices* 1982; **29**: 300-305.
[446] Coleman MG, Pryor RA, Sparks TG. The Pd2Si-(Pd)- Ni - solder plated metallization system for silicon solar cells. *13th IEEE Photovoltaic Specialists Conference (PVSC)*, 1978: 597-602.
[447] Arabito G, Artuso F, Belardinelli M, Barbarossa V, Besi Vetrella U, Gentilin L, Grilli ML, Mangiapane P, Pirozzi L. Electroless metallizations for contacts in buried structures. *2nd World Conference on Photovoltaic Solar Energy Conversion*, 1998: 1558-1561.
[448] Karmalkar S, Banerjee J. A Study of Immersion Processes of Activating Polished Crystalline Silicon for Autocatalytic Electroless Deposition of Palladium and Other Metals. *Journal of The Electrochemical Society* 1999; **146**: 580-584.
[449] Fisher K, *The Pitfalls of Pit Contacts: Electroless Metallisation for c-Si Solar Cells (Master Thesis)*, University of New South Wales, Sydney, Australia, 2007.
[450] Ruby DS, Wilbanks WL, Fieddermann CB. A statistical analysis of the effect of PECVD deposition parameterson surface and bulk recombination in silicon solar cells. *IEEE 1st World Conference on Photovoltaic Energy Conversion*, 1994: 1335-1338.
[451] Chen Z, Rohatgi A, Ruby D. Silicon surface and bulk defect passivation by low temperature PECVD oxides and nitrides. *IEEE 1st World Conference on Photovoltaic Energy Conversion*, 1994: 1331-1334.
[452] Lenkeit B, Lauinger T, Aberle AG, Hezel R. Comparison of remote versus direct PECVD silicon nitride passivation of phosphorus-diffused emitters of silicon solar cells. *2nd World Conference on Photovoltaic Solar Energy Conversion*, 1998: 1434-1437.
[453] Moschner JD, Doshi P, Ruby DS, Lauinger T, Aberle AG, Rohatgi A. Comparison of Front and Back Surface Passivation Schemes for Silicon Solar Cells. *2nd World Conference on Photovoltaic Solar Energy Conversion*, 1998: 1894-1897.

[454] King RR, Sinton RA, Swanson RM. Studies of diffused phosphorus emitters: saturation current, surface recombination velocity, and quantum efficiency. *IEEE Transactions on Electron Devices* 1990; **37**: 365-371.
[455] Kunst M, Abdallah O, Wunsch F. Passivation of silicon by silicon nitride films. *Solar Energy Materials and Solar Cells* 2002; **72**: 335-341.
[456] Chen F, Li T-T, Cotter J. PECVD Silicon Nitride Surface Passivation for High-Efficiency N-Type Silicon Solar Cells. *IEEE 4th World Conference on Photovoltaic Energy Conversion*, 2006: 1020-1023.
[457] Petres R, Libal J, Buck T, Kopecek R, Vetter M, Ferre R, Martin I, Borchert D, Fath P. Improvements in the Passivation of P+ Si Surfaces by PECVD Silicon Carbide Films. *IEEE 4th World Conference on Photovoltaic Energy Conference*, 2006: 1012-1015.
[458] Mihailetchi VD, Geerligs LJ, Komatsu Y, Buck T, Rover I, Wambach K, Knopf C, Kopecek R. High Efficiency Industrial Screen Printed n-Type mc-Si Solar Cells With Front Boron Emitter. *22nd European Photovoltaic Solar Energy Conference*, 2007: 1581-1585.
[459] Hoex B, Heil SBS, Langereis E, van de Sanden MCM, Kessels WMM. Ultralow surface recombination of c-Si substrates passivated by plasma-assisted atomic layer deposited Al2O3. *Applied Physics Letters* 2006; **89**: 042112-042113.
[460] Hoex B, Gielis JJH, van de Sanden MCM, Kessels WMM. On the c-Si surface passivation mechanism by the negative-charge-dielectric Al2O3. *Journal of Applied Physics* 2008; **104**: 113703-113707.
[461] Hoex B, Schmidt J, Bock R, Altermatt PP, van de Sanden MCM, Kessels WMM. Excellent passivation of highly doped p-type Si surfaces by the negative-charge-dielectric Al2O3. *Applied Physics Letters* 2007; **91**: 112107-112103.
[462] Wakisaka K, Taguchi M, Sawada T, Tanaka M, Matsuyama T, Matsuoka T, Tsuda S, Nakano S, Kishi Y, Kuwano Y. More than 16% solar cells with a new 'HIT' (doped a-Si/nondoped a-Si/crystalline Si) structure. *22nd IEEE Photovoltaic Specialists Conference*, 1991: 887-892.
[463] Dauwe S, Schmidt J, Hezel R. Very low surface recombination velocities on p- and n-type silicon wafers passivated with hydrogenated amorphous silicon films. *29th IEEE Photovoltaic Specialists Conference*, 2002: 1246-1249.
[464] Maruyama E, Terakawa A, Taguchi M, Yoshimine Y, Ide D, Baba T, Shima M, Sakata H, Tanaka M. Sanyo's Challenges to the Development of High-efficiency HIT Solar Cells and the Expansion of HIT Business. *4th IEEE World Conference on Photovoltaic Energy Conversion*, 2006: 1455-1458.
[465] Hofmann M, Janz S, Schmidt C, Kambor S, Suwito D, Kohn N, Rentsch J, Preu R, Glunz S. Recent developments in rear-surface passivation at Fraunhofer ISE. *Solar Energy Materials and Solar Cells* 2009; **93**: 1074-1078.